Structure and functional analysis of a recombinant endo-*β*-1,4-xylanase (*Ac*Xyn30B_12) from *Acetivibrio clariflavus* DSM 19732 and its application in deinking of waste papers

A thesis submitted for the partial fulfillment

of requirements for the award

of

DOCTOR OF PHILOSOPHY

by

BIPASHA CHOUDHURY

Under supervision of

Professor Arun Goyal

June 2025

BIOSCIENCES AND BIOENGINEERING

INDIAN INSTITUTE OF TECHNOLOGY GUWAHATI

GUWAHATI 781039, ASSAM, INDIA

Dedicated to my

Papa

&

Maa

Structure and functional analysis of a recombinant endo-*β*-1,4-xylanase (*Ac*Xyn30B_12) from *Acetivibrio clariflavus* DSM 19732 and its application in deinking of waste papers

PhD Thesis

by

BIPASHA CHOUDHURY

JUNE 2025

DEPARTMENT OF BIOSCIENCES AND BIOENGINEERING

INDIAN INSTITUTE OF TECHNOLOGY GUWAHATI

GUWAHATI 781039, ASSAM, INDIA

INDIAN INSTITUTE OF TECHNOLOGY GUWAHATI

DEPARTMENT OF BIOSCIENCES & BIOENGINEERING

STATEMENT

I do hereby declare that the content embodied in this thesis entitled as **"Structure and functional analysis of a recombinant endo-*β*-1,4-xylanase (*Ac*Xyn30B_12) from *Acetivibrio clariflavus* DSM 19732 and its application in deinking of waste papers"** is the result of investigations carried out by me in the Department of Biosciences and Bioengineering, Indian Institute of Technology Guwahati, Guwahati, India under the guidance of Professor Arun Goyal.

In keeping with the general practice of reporting scientific observations, due acknowledgements have been made wherever the work described is based on the findings of other investigators.

Bipasha Choudhury

June, 2025 ***Bipasha Choudhury***
(226106007)

INDIAN INSTITUTE OF TECHNOLOGY GUWAHATI

DEPARTMENT OF BIOSCIENCES & BIOENGINEERING

CERTIFICATE

It is certified that the work described in this thesis entitled "**Structure and functional analysis of a recombinant endo-β-1,4-xylanase (*Ac*Xyn30B_12) from *Acetivibrio clariflavus* DSM 19732 and its application in deinking of waste papers**" by Bipasha Choudhury (Roll No. 226106007) for the award of degree of Doctor of Philosophy is an authentic record of the results obtained from the research work carried out under my supervision at the Department of Biosciences & Bioengineering, Indian Institute of Technology Guwahati, Guwahati, India and this work has not been submitted elsewhere for a degree.

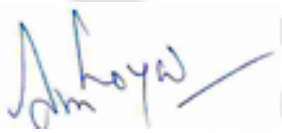

Dr. Arun Goyal *(MSc, MTech, PhD)*
(FAMI, FBRS, FABAP, FNABS, FNAAS, FIFIB, FMBI, FACCTI, FSEES)
(Thesis Supervisor)
Professor (HAG) and Former Head,
Department of Biosciences & Bioengineering
Indian Institute of Technology Guwahati
Guwahati, 781 039, India

ACKNOWLEDGEMENTS

The Ph.D. journey has been one of immense growth, learning and self-discovery. Completing this thesis marks not just the end of years of rigorous academic pursuit, but also reflects the collective support, guidance and encouragement I have received along the way. This work is a testament to the unwavering contributions of many individuals, each of whom has played an important role in shaping both my research and personal journey.

First and foremost, I extend my deepest gratitude to my supervisor, Prof. Arun Goyal, Department of Biosciences and Bioengineering, IIT Guwahati. His steadfast support, insightful guidance and consistent encouragement have been pivotal to the progress and completion of this research. I am sincerely thankful for the critical feedback and opportunities he provided, which greatly enriched my research experience. His patience, leadership and belief in my potential have been a constant source of motivation and his passion for scientific inquiry has inspired me deeply. The perspective and analytical thinking he imparted have not only enhanced the quality of this work but have also equipped me with the tools to tackle challenges beyond the academic sphere.

I would also like to express my sincere gratitude to my doctoral committee members, Prof. Nitin Chaudhary, Prof. Ranjan Tamuli, Dr. Shirisha Nagatu and Prof. Arun Goyal, for their insightful suggestions and constructive criticism, which have been instrumental in refining my research and guiding me toward the successful completion of my thesis.

I am deeply thankful to the Department of Biosciences & Bioengineering, Department of Physics and Central Instrumentation Facility (CIF), IITG, for providing infrastructural support and instruments for my research work. I am also thankful to IIT Guwahati for the Param-Kamrupa Supercomputing facility. I want to thank Dr. Ravishankar Ramachandran, Principal Scientist and his team members at CSIR-Central Drug Research Institute (CDRI), Lucknow, India, for providing the SAXS facility and to

my senior, Dr. Kedar Sharma for collecting the SAXS data. I also want to thank Prof. Carlos M.G.A. Fontes, CIISA-Faculdade de Medicina Veterinária, Universidade de Lisboa, Avenida da Universidade Técnica, Lisbon, Portugal for his expert suggestions.

I would also like to thank the present and former Heads of the Department of Biosciences & Bioengineering, IIT Guwahati, Prof. Utpal Bora, Prof. Rakhi Chaturvedi and Prof. Latha Rangan for providing the necessary facilities. I am highly thankful for the support received from all the other teaching and non-teaching staff members of the Department of Biosciences and Bioengineering, IIT Guwahati.

I wish to acknowledge the Ministry of Education (MoE), Govt. of India, for providing financial assistance through the research work.

I extend my deepest gratitude to all the members of my lab, Carbohydrate Enzyme Biotechnology Laboratory (CEBL). I am especially thankful to my seniors Dr. Kaustubh khaire, Dr. Maibam Premeshworii Devi, Dr. Jebin Ahmed, Dr. Yumnan Robinson Singh, Dr. Madhulika Srivastava, Shreya and Akshita for their cooperation and suggestions and my juniors, Akshay, Shushruta, Ashwani, Tiyasa, Deblina, Nilakshi, Shubhada and Shruti for their assistance in the lab.

I am deeply grateful to all my friends Gurleen, Sabari. Epshita, Kiran, Kaustav, Siddharth bhaiya, Neelave bhaiya and Kangana didi for their unwavering support and encouragement throughout this journey.

Finally, I wish to extend my deepest gratitude to my family, who have been my unwavering pillar of strength throughout this journey. Their constant love, faith, encouragement, countless sacrifices, silent prayers and unconditional support have formed the foundation upon which this work stands.

Above all, I bow in reverence to Lord Shri Krishna, whose divine wisdom, grace and presence have been my guiding force throughout this journey. This milestone would not have been possible without His constant support and silent companionship on the path.

Bipasha Choudhury
June, 2025

SYNOPSIS

Introduction

The increasing concerns regarding the depletion of fossil fuels and the environmental impact associated with their combustion have intensified the global pursuit of sustainable alternatives. Among the viable renewable resources, lignocellulosic biomass (LCB) has emerged as a pivotal candidate for the establishment of a green bioeconomy. LCB, composed of cellulose, hemicellulose and lignin, forms the structural framework of plant cell walls and is abundantly available from agricultural residues, forestry byproducts and energy crops (Saini *et al*., 2015; Mankar *et al*., 2021). Within LCB, hemicellulose and particularly its major component xylan, holds substantial promise due to its high abundance and the presence of fermentable sugars such as D-xylose. Xylan is a structurally complex heteropolymer characterized by *β*-1,4-linked xylose backbone and diverse side-chain substitutions, including arabinofuranosyl, glucuronic acid and acetyl groups (Razeq *et al*., 2017; Sohail *et al*., 2022). These structural features impart functional resilience to plant materials but also contribute to the recalcitrance of biomass toward enzymatic hydrolysis, necessitating the action of specialized enzyme systems.

The deconstruction of xylan involves a consortium of carbohydrate-active enzymes (CAZymes), that synergistically degrade the polymer into oligosaccharides and ultimately into xylose monomers (Henrissat *et al*., 1991; Drula *et al*., 2022). Among those, endo-*β*-1,4-xylanases, *β*-xylosidases, *α*-glucuronidases and arabinofuranosidases

play integral roles in cleaving the xylan backbone and removing the side groups, respectively (Choudhury *et al*., 2024). Endo-β-1,4-xylanases function on the xylan backbone by randomly cleaving at internal locations on β-1,4-glycosidic connections between xylopyranosyl residues and releasing a variety of products, such as xylobiose, xylotriose, xylotetraose, longer and/or branched xylo-oligomers (Bharadwaj *et al*., 2019). Among all the different classes of CAZy enzymes, GH30 family of glycoside hydrolases consists of both hemicellulose and cellulose degrading enzymes. It adopts a $(\beta/\alpha)_8$-barrel (TIM barrel) fold in their catalytic domain, featuring two conserved glutamic acid residues that mediate catalysis through a retaining double-displacement mechanism (St. John *et al*., 2010; Linares-Pastén *et al*., 2018). The enzymes under GH30 family are further divided into multiple subfamilies, with GH30_8 primarily comprising bacterial endo-xylanases that recognize glucuronic acid-substituted xylans. The structural complexity of these enzymes includes auxiliary carbohydrate-binding modules (e.g., CBM6 or CBM13), which facilitate substrate recognition and binding (Crooks *et al*., 2020; Biely *et al*., 2016).

Till date, a number of bacterial GH30_8 endo-xylanases have already been characterized. For example, *Bs*XynC from *Bacillus subtilis* showed optimal activity at 65°C and pH 6.0, releasing methylglucuronate-substituted oligosaccharides from glucuronoxylan (St. John *et al*., 2006). *Ec*Xyn30A from *Erwinia chrysanthemi* displayed endoxylanase hydrolytic activity (Hurlbert *et al*., 2001). Other characterized GH30_8 enzymes include Xyn30D from *Paenibacillus barcinonensis* (Valenzuela *et al*., 2012), *Cp*Xyn30A from *Clostridium papyrosolvens* (St. John *et al*., 2014) and

*Ca*Xyn30A from *Clostridium acetobutylicum* (St. John et al., 2018), each demonstrating endoxylanase activity but at different optimized conditions. Notably, fungal GH30 enzymes like *Tt*Xyn30A and *Tc*Xyn30C also contribute to endoxylanase activity along with broad pH stability and high catalytic activity on xylan polysaccharides (Šuchová *et al*., 2021; Nakamichi *et al*., 2019). The GH30 endo-xylanases are involved in different industrial applications like production of xylo-oligosaccharides (XOS) as anti-oxidants and for preparing cosmetic and nutraceuticals (Valls *et al*., 2018, Zerva *et al*., 2020), degradation of biomass waste for biofuel production (Rogowski *et al*., 2015), detoxification of animal feedstock (da Costa *et al*., 2019), fruit juice and brewing process (Bhardwaj *et al*., 2019, Liu *et al*., 2018), deinking of waste papers (Yang *et al*., 2023) and many more.

Among microbial sources, *Acetivibrio clariflavus* DSM 19732 stands out as a prolific producer of thermostable xylanolytic enzymes. This thermophilic and anaerobic bacterium, initially isolated from anaerobic sludge, is phylogenetically close to *Clostridium thermocellum* and is known to harbor both cell-free and cell-bound cellulosomes (Izquierdo *et al*., 2012; Shiratori *et al*., 2009). Its genome encodes an extensive array of 72 glycoside hydrolases, including a diverse collection of xylanases from GH families 10, 11, 30, 39, 43, 51, 67 and 74. Comparative genomics revealed that *A. clariflavus* has a greater diversity and abundance of xylanolytic enzymes than *C. thermocellum*, especially in the ability to completely degrade xylan to xylose, rather than stopping at xylo-oligomers (Izquierdo *et al*., 2012). This property makes it a

valuable candidate for biotechnological applications that require efficient hemicellulose deconstruction under high-temperature conditions.

A gene (GenBank accession no. AEV69300.1 and gene locus Clocl_2746) encoding a glycoside hydrolase family 30 (GH30) enzyme from *Acetivibrio clariflavus* was identified and designated as *Ac*Xyn30B_12. *Ac*Xyn30B_12 is an endo-*β*-1,4-xylanase enzyme that belongs to GH30_12 subfamily and is predicted to be part of the cellulosomal complex of *A. clariflavus*. In the present study, the gene encoding *Ac*Xyn30B_12 containing GH30 catalytic module, a carbohydrate-binding module 6 (CBM6) and a dockerin I domain was cloned, expressed and biochemically characterized (Fig. 1). Additionally, its 3D structure and functional dynamics were elucidated through in-silico modeling, small-angle X-ray scattering (SAXS) and dynamic light scattering (DLS) analyses, offering insights into its active-site architecture and conformational behavior in solution. The practical utility of *Ac*Xyn30B_12 was further assessed by evaluating its enzymatic deinking potential on different waste paper types (newspaper and notebook paper) under optimized reaction conditions, demonstrating its applicability as a green alternative to chemical-based waste paper deinking processes.

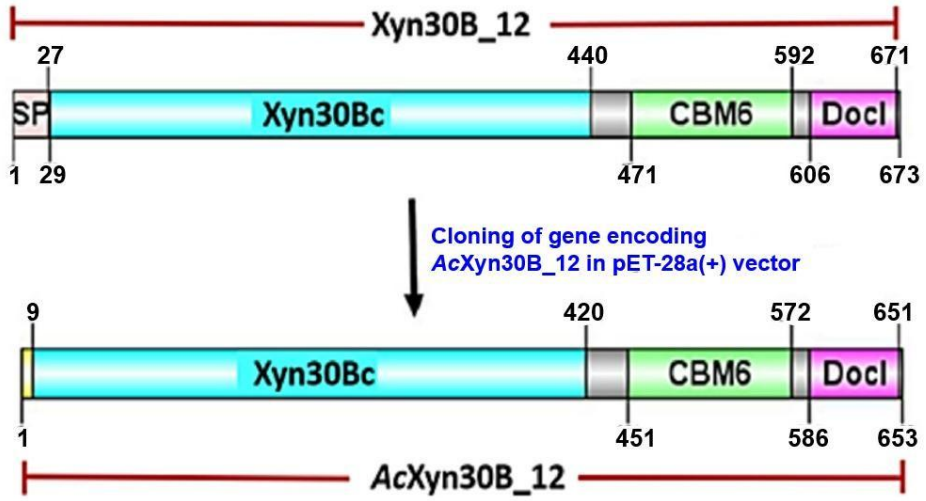

Fig. 1. Molecular architecture of *Ac*Xyn30B_12, developed by using DOG 2.0 software. The amino acid sequence of *Ac*Xyn30B_12 consists of 4 major domain sequences: (i) N-terminal signal peptide (residues 1-27, in pink color), (ii) catalytic module, Xyn30Bc (residues 29-440, in cyan color), (iii) family 6 carbohydrate binding module, CBM6 (residues 471-592, in green color) and (iv) C-terminal Type I dockerin domain, DocI (residues 606-671, in purple color).

Present work

The present work entitled as "**Structure and functional analysis of a recombinant endo-β-1,4-xylanase (*Ac*Xyn30B_12) from *Acetivibrio clariflavus* DSM 19732 and its application in deinking of waste papers.**" has been divided into 5 chapters.

Chapter 1 provides an in-depth overview of lignocellulosic biomass (LCB) as a renewable and sustainable resource with high potential for biofuel and bio-based chemical production. It discusses the structural organization of LCB, comprising cellulose, hemicellulose and lignin and highlights the role of hemicellulose, especially xylan, as a major source of fermentable pentose sugars. The various structural forms of xylan, such as arabinoxylan, glucuronoxylan and glucuronoarabinoxylan, are described

in detail along with their sources and complexity. The chapter introduces Carbohydrate-Active Enzymes (CAZymes), including glycoside hydrolases (GHs) and discusses the classification, mechanism of action and structural features of different enzymes under the GH30 family. In this chapter, emphasis is placed on endo-*β*-1,4-xylanases from GH30, their catalytic architecture (TIM barrel like structure), retaining mechanism of hydrolysis and industrial relevance. The potential of thermophilic bacterium *Acetivibrio clariflavus* DSM 19732, known for its complex cellulosome and high diversity of xylanases, is highlighted. The chapter concludes with the rationale and objectives of studying the GH30_12 enzyme *Ac*Xyn30B_12 from *A. clariflavus*, focusing on its characterization and application in waste paper deinking processes.

Chapter 2 describes the molecular cloning and expression of the gene (GenBank Accession No. AEV69300.1 and gene locus Clocl_2746) encoding endo-*β*-1,4-xylanase of GH30 family (*Ac*Xyn30B_12) from *Acetivibrio clariflavus* DSM 19732. Molecular architecture revealed that the full-length gene encoding *Ac*Xyn30B_12 contains a total of 673 amino acid residues and an N-terminal signal peptide, followed by a catalytic module, Xyn30Bc, CBM6 a C-terminal Type I dockerin domain, DocI. PCR amplification of the gene yielded a product approximately, 1.9kb in size. The amplified fragment was digested with restriction enzymes (*Nhe*I-*Xho*I) and ligated to the linearized pET-28a(+) expression vector. Upon transformation of ligated product using *E. coli* DH5α competent cells, positive clones harbouring the recombinant plasmid were verified *via* restriction digestion using enzymes, *Nhe*I and *Xho*I, which produced DNA bands of ~5.3 kb (vector) and ~1.9 kb (insert) as analysed by agarose gel electrophoresis

analysis. The confirmed recombinant plasmid was subsequently introduced into *E. coli* BL21 (DE3) cells for protein expression. The recombinant *Ac*Xyn30B_12 protein was expressed showing a band corresponding to molecular size, ~74 kDa as confirmed by SDS-PAGE analysis, which was corroborated with its theoretically known molecular mass (75 kDa). The optimum concentration of IPTG for expression of *Ac*Xyn30B_12 obtained was 1.0 mM and the optimum induction temperature determined for protein expression was 24°C.

Chapter 3 outlines the purification and functional characterization of the recombinant protein, *Ac*Xyn30B_12. The protein was purified using Ni-NTA affinity chromatography, followed by size-exclusion chromatography which displayed a molecular size of ~74 kDa. It displays optimal activity at pH 5.5 and 70°C. *Ac*Xyn30B_12 exhibited broad substrate specificity, with the highest catalytic efficiency against partially acetylated birchwood xylan (PABX), yielding a V_{max} of 133.3 U/mg and a K_M of 0.9 mg/mL. *Ac*Xyn30B_12 activity was enhanced by Ca^{2+} (10 %) and Mg^{2+} (7.3 %) ions. The enzyme also showed notable thermostability maintaining activity up to 60°C and pH tolerance within a pH range of 4.5-8.0 which makes it highly advantageous for industrial processes that demand robust enzymes capable of operating under harsh conditions. Time-course hydrolysis experiments revealed the ability of *Ac*Xyn30B_12 to release a variety of xylo-oligosaccharides (from xylopentaose to xylobiose) and xylose from PABX, confirming both its *endo and exo*- acting mechanisms. Additionally, *Ac*Xyn30B_12 effectively degraded lignocellulosic biomass, releasing significant amounts of xylo-oligosaccharides and xylose from

complex substrates which can be harnessed for diverse industrial purposes, including the production of biofuels, prebiotic oligosaccharides and other sustainable products. This study also demonstrated the synergistic action of *Ac*GH30A and *Ac*Xyn30B_12 in complex carbohydrate hydrolysis, with *Ac*Xyn30B_12 generating the non-reducing ends that serve as substrates for *Ac*GH30A. This cooperative activity highlights their potential for improving the efficiency of lignocellulosic biomass conversion, making them valuable assets in biofuel production and other biotechnological applications.

Chapter 4 focuses on the structural analysis of *Ac*Xyn30B_12 using computational and biophysical techniques. The sequence analysis of the cloned gene encoding *Ac*Xyn30B_12 along with pET-28a(+) vector sequence including N-terminal His6 tag revealed a total of 653 amino acids giving its molecular weight, 73.5 kDa and the isoelectric point of 4.79. Glu151 and Glu259 were the catalytic residues that were found to be conserved on multiple sequence alignment and superimposition with its homologous protein sequences. The distance between these catalytic residues was found to be 5.5 Å which revealed the retaining-type mechanism of hydrolysis followed by *Ac*Xyn30B_12. Circular dichroism analysis of *Ac*Xyn30B_12 showed 26.2% α-helices and 28.1% β-strands, corroborating with predictions from PSIPRED and SOPMA servers. 3D modelled structure of *Ac*Xyn30B_12 by Alphafold2 was the best showing 99.8% of amino acid residues in favorable region and only 0.2% in disallowed region of Ramachandran plot. The 3D model structure of *Ac*Xyn30B_12 showed the presence of $(\beta/\alpha)_8$ barrel and an associated a 'side-β structure', which is a characteristic feature of glycoside hydrolase family 30 (GH30) proteins. This structural arrangement aligns

with known features of GH30 enzymes, supporting its classification within this family. Molecular docking revealed the highest affinity of amino acids of catalytic cleft of *Ac*Xyn30B_12 with xylotriose (-11.2 kcal/mol). MD simulation analyses of both unbound *Ac*Xyn30B_12 and docked *Ac*Xyn30B_12-xylotriose complex, revealed that the docked complex had low RMSD value, lower fluctuation and lower flexibility at loop region (by RMSF value), lower surface area accessible on ligand binding (by SASA value) and higher compactness (by R_g value) as compared with unbound *Ac*Xyn30B_12. These results suggest that xylotriose binding induces structural stabilization in *Ac*Xyn30B_12, enhancing its rigidity and reducing flexibility, particularly in catalytically relevant regions. The R_g value of 3.9 nm found by MD simulation for unbound *Ac*Xyn30B_12 was similar with the results of SAXS and DLS. Small angle X-ray scattering (SAXS) analysis of *Ac*Xyn30B_12 confirmed the polydisperse and elongated structure of *Ac*Xyn30B_12 at 3 mg/mL and 5 mg/mL concentrations. Dummy atom model analysis of *Ac*Xyn30B_12 revealed monomeric form at 3 mg/mL and dimeric form at 5 mg/mL. Dynamic light scattering (DLS) analysis of *Ac*Xyn30B_12 confirmed the polydisperse nature at all concentrations (1, 3 and 5 mg/mL) and R_h values of 4.2 nm, 4.5 nm and 5.3 nm at 1, 3 and 5 mg/mL, respectively, matching the R_g results from SAXS analysis. A lower zeta potential of -4.0 mV at 5 mg/mL compared to -10.5 mV at 3 mg/mL indicated protein aggregation and dimerization at higher concentration which makes the enzyme valuable for production of different value-added products like prebiotics and biofuel.

Chapter 5 explores the application of purified GH30 family endo-*β*-1,4-xylanase (*Ac*Xyn30B_12) from *Acetivibrio clariflavus* DSM 19732 for the enzymatic deinking of waste papers *viz.* newspaper (NEPW) and notebook paper (NOPW). Among different types of waste papers analyzed, newspaper (NEPW) and notebook paper (NOPW) were selected based on their relatively high hemicellulose and low lignin content, making them suitable substrates for enzymatic deinking. Statistical optimization using response surface methodology (RSM) identified the ideal deinking conditions for both 5.0% (w/v) NEPW and NOPW with enzyme (*Ac*Xyn30B_12) loadings of 46.4 U/g and 58.6 U/g, respectively in 10 mL reaction mixture at 70°C for 90 min. Under these optimized conditions, *Ac*Xyn30B_12 achieved deinking efficiencies of 81.3% for NEPW and 77.2% for NOPW at 10 mL reaction scale, as determined by ERIC measurements. The deinking efficiency results obtained for *Ac*Xyn30B_12 were comparable to that of NaOH treated papers (87.3% for NEPW and 87.7% for NOPW) at 10 mL reaction scale. Although higher deinking efficiency was seen for NaOH treated papers, *Ac*Xyn30B_12 deinking preserved paper better than that of NaOH (68% (w/w) for NEPW and 72% (w/w) for NOPW), with 78% (w/w) recovery for NEPW and 76% (w/w) for NOPW indicating the retention of fiber integrity making it more suitable for paper recycling. At higher reaction volumes (20 mL and 50 mL), *Ac*Xyn30B_12 maintained consistent deinking efficiencies (79.0% for NEPW and 72.1% for NOPW) and biomass recovery (77% (w/w) for NEPW and 76% (w/w) for NOPW), demonstrating its scalability and suitability for large-scale deinking applications. Structural analysis revealed that *Ac*Xyn30B_12 treatment increased the

crystallinity index to 58.8% (NEPW) and 63.4% (NOPW), with corresponding increases in their apparent crystallite size (17.7% for NEPW and 22.8% for NOPW). ATR-FTIR analysis revealed that *Ac*Xyn30B_12 treatment significantly reduced the intensity of characteristic ink peaks (3025-3060 cm^{-1} for aromatic C-H and 1315 cm^{-1} for -OH in hemicellulose), confirming effective removal of ink and targeted hemicellulose hydrolysis, higher than that of crude enzyme and NaOH pretreated papers. FESEM imaging showed that *Ac*Xyn30B_12 treated fibers were more fragmented and exposed compared to untreated and crude enzyme-treated papers and comparable to that of NaOH treated papers. *Ac*Xyn30B_12 significantly improved deinked paper brightness up to 75.3% for NEPW and 48.0% for NOPW, representing 12.4% and 26.3% increases, respectively, over untreated samples. Water absorptivity (Cobb value) increased to 28.1 g/m^2 (NEPW) and 14.9 g/m^2 (NOPW) in case of *Ac*Xyn30B_12 as compared to that of NaOH (35.6% g/m^2 for NEPW and 24.6% g/m^2 for NOPW) showing higher fiber strength retention in papers deinked by *Ac*Xyn30B_12. The total reducing sugar (TRS) content in the effluent reached 1.8 mg/g for NEPW and 2.3 mg/g for NOPW with *Ac*Xyn30B_12, which was highest among all treatments, indicating superior xylan degradation. In contrast, the TRS released by NaOH was just 0.3 mg/g (NEPW) and 0.2 mg/g (NOPW). Effluent analysis showed *Ac*Xyn30B_12 generated lower Total Dissolved Solids (TDS: 10.0 mg/L NEPW, 8.5 mg/L NOPW) and Total Suspended Solids (TSS: 3.0 mg/L NEPW, 3.5 mg/L NOPW) compared to NaOH (TDS of 13.0 mg/L in NEPW and 10.5 mg/mL in NOPW; TSS of 4.5 mg/L in NEPW and 5.5 mg/mL in NOPW), demonstrating its eco-friendly nature. These results together conclude that

*Ac*Xyn30B_12 effectively removes ink, enhances fiber properties and produces environmentally effluent, making it an efficient and sustainable biocatalyst for waste paper recycling.

Chapter 1

General Introduction

1.1. Lignocellulosic biomass towards a green bioeconomy

Different non-renewable sources of energy like coal, petroleum products and natural gas have been extensively used since the Industrial Revolution for the socio-economic development of nations. However, excessive reliance on these fossil fuels is a primary driver of climate change due to the massive emission of greenhouse gases like CO_2, CH_4 and N_2O, leading to global warming and environmental degradation (IPCC, 2021). Consequently, there is an urgent need to explore renewable, biodegradable and eco-friendly energy sources to build a sustainable and green future. Bioethanol is one such promising renewable energy source that can be produced from plant-derived lignocellulosic biomass or in short LCB (Saini *et al*. 2015). Its availability from agricultural residues such as maize cobs, rice straw, sugarcane bagasse and pear pomace make it a cost-effective and sustainable feedstock (Saini *et al*. 2015; Kumar *et al*., 2009). LCB consists mainly of three polymers *viz*., cellulose, hemicellulose and lignin, that offers an abundant source of fermentable carbohydrates. Among these three polymers, hemicellulose is the second most abundant and holds great potential for producing bio-based fuels and chemicals. It is rich in pentose sugars, primarily xylose, which can be converted into bioethanol through genetically

engineered microbial platforms (Qaseem *et al*., 2021). The integration of metabolic engineering and synthetic biology has significantly improved xylose fermentation efficiency, expanding hemicellulose's role in the bio-based industry (Kim *et al*., 2019).

In addition to bioethanol, value-added chemicals such as furfural and 5-hydroxymethylfurfural (HMF) can be derived from hemicellulose, offering eco-friendly alternatives to petroleum-based industrial chemicals (Bozell & Petersen, 2010). These developments align with the concept of a bioeconomy, which emphasizes the use of biological resources to produce energy, materials and chemicals sustainably (European Commission, 2018). Thus, valorization of lignocellulosic biomass represents a pivotal strategy for reducing fossil fuel dependence, minimizing environmental pollution and advancing toward a circular and sustainable bioeconomy.

1.2. Lignocellulosic biomass

Lignocellulosic biomass (LCB), a major renewable resource, can be derived from a wide variety of agricultural residues and forest-based debris. It constitutes the dry, fibrous part of plants and is primarily composed of three major structural polymers arranged in a complex hetero-matrix: cellulose (35-50%), hemicellulose (20-35%) and lignin (5-30%) (Mankar *et al*., 2021; Yousuf *et al*., 2020), as illustrated in Fig. 1.1 (Waise *et al*., 2024). However, the exact proportion of cellulose, hemicellulose, and lignin can vary significantly depending on the type of biomass feedstock and its origin. These components form a rigid and recalcitrant matrix, making the biomass resistant to degradation, which is a key challenge in its bioconversion. LCB can be sourced from a range of materials, including hardwoods, softwoods, grasses and agricultural residues such as crop stalks, husks and shells (Mankar *et al*., 2021). Among these, forestlands and global plantation areas represent vast, sustainable reservoirs of woody

biomass, which is one of the most abundant types of lignocellulosic feedstock available worldwide. Woody biomass is typically categorized into two types, hardwood and softwood, which differ not only in anatomical features but also in their lignocellulosic composition and physical properties (Álvarez *et al*., 2016). Hardwoods generally have higher cellulose and lower lignin content as compared to the softwoods, making them somewhat more amenable to bioprocessing and enzymatic hydrolysis. Overall, the diversity and abundance of lignocellulosic feedstocks provide a robust foundation for developing sustainable and large-scale bio-based processes such as bioethanol production, biogas generation, paper recycling and bioplastic synthesis.

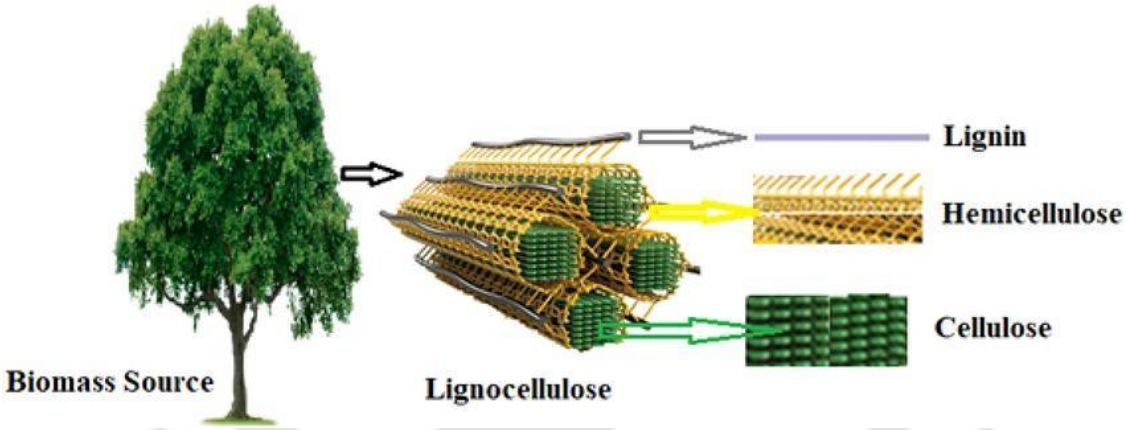

Fig. 1.1. Structure of lignocellulosic matrix along with its major components, cellulose, hemicellulose and lignin (Waise *et al*., 2024).

1.2.1. Hemicellulose

Hemicellulose is the second largest component of LCB after cellulose (Kumar *et al*., 2025). Hemicellulose plays a crucial structural role in lignocellulosic biomass by acting as a linkage between cellulose and lignin components, thereby contributing to the rigidity and integrity of the plant cell wall (Mankar *et al*., 2021). It is composed of various types of mono saccharides, including hexoses such as *α*-D-galactose, *β*-D-mannose and *β*-D-glucose; pentoses like *β*-D-xylose and *α*-L-arabinose and uronic

acids such as α-D-glucuronic acid and α-D-galacturonic acid. Structurally, hemicellulose is a branched heteropolymer with a single backbone. Based on its sugar composition, hemicellulose is classified into four primary types: xylan, mannan, xyloglucan (a polysaccharide whose main chain contain β-(1→4)-linked D-glucopyranose residues with side chain substitutions of β-(1→2)-linked D-xylopyranose residues) and β-1-3, β-1-4 mixed-linkage containing β-glucan (Devi *et al*. 2022; Qaseem *et al*. 2021). In hardwoods, hemicellulose mainly contains xylan, whereas in softwoods, most commonly found hemicellulose is glucomannan (Kumar *et al*., 2008).

1.2.1.1. Xylan

Xylan is the major component of hemicellulose and represents the second most abundant polysaccharide in the plant cell wall. It accounts for approximately, 30-35% of the dry weight of the plant cell wall, making it the most dominant form of hemicellulose. Xylan is found in both primary cell walls, particularly in monocotyledonous plants and secondary cell walls across various plant species (Collins *et al*., 2005). The primary sources of xylan include hardwoods from angiosperms (15-30%), softwoods from gymnosperms (7-10%) and annual plants (up to 30%) as reported by Collins *et al*., 2005. In terms of structure, wood-derived xylan exists in different forms, in softwoods, it is typically found as arabino-4-O-methylglucuronoxylan, whereas in hardwoods, it is mainly present as O-acetyl-4-O-methylglucuronoxylan. In contrast, arabinoxylans are the predominant xylan type in grasses and annual plants. The degree of polymerization of xylan varies with plant source, xylan in hardwoods generally contains 150-200 β-D-xylopyranose units, while softwood xylan comprises 70-130 units, indicating a wide range in chain length (Collins *et al*., 2005; Sohail *et al*., 2022).

Structurally, xylan consists of a homopolymeric backbone of *β*-1,4-linked D-xylopyranosyl units, which may be substituted to varying extents with different side-chain groups, such as *α*-L-arabinofuranosyl, acetyl, feruloyl, glucuronopyranosyl, 4-O-methyl-D-glucuronopyranosyl and *p*-coumaroyl groups (Collins *et al*., 2005; Sohail *et al*., 2022). Based on the nature and extent of these substitutions, xylan can be broadly classified into homoxylans which include homopolymers with *β*-1,4, *β*-1,3, or mixed linkages (Razeq *et al*., 2017) and heteroxylans, which include arabinoxylan, glucuronoxylan, glucuronoarabinoxylan and arabinoglucuronoxylan (Santibáñez *et al*., 2021).

1.2.1.1.1. Arabinoxylan

In arabinoxylan (AX), the xylose residues that are connected by the *β*-(1→4)-D-xylose linkage in the backbone xylan chain and have *α*-L-arabinofuranosyl (α-Araf) residues substituted at carbon 2 and/or 3 by *α*-(1→2) or *α*-(1→3) linkage as shown in Fig. 1.2 (Razeq *et al*., 2017). As shown in Fig. 1.2, there are also phenolic acids like ferulic acid and p-coumaric acid in certain AX that have been esterified to O-5 of *α*-L-arabinofuranosyl residues. These are frequently found in the starch and bran of cereal grains, seeds and grains.

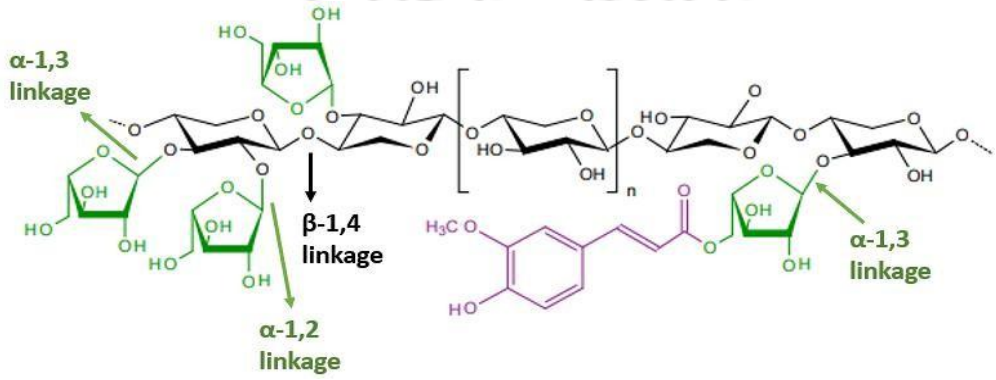

Fig. 1.2. Structure of arabinoxylan in cereal grain with its different side chain substitutions (Razeq *et al*., 2017). Here, black- xylan backbone chain and green- *α*-L-arabinofuranosyl and violet- ferulic acid.

1.2.1.1.2. Glucuronoxylan

In glucuronoxylan, the xylose residues that are connected by the *β*-(1→4)-D-xylose linkage in the backbone xylan chain and have single chain *α*-D-glucuronic acid (GA) and its 4-O-methyl derivative, 4-O-methyl glucuronic acid (MeGA), substituted at carbon 2 by *α*-(1→2) linkage as shown in Fig. 1.3.

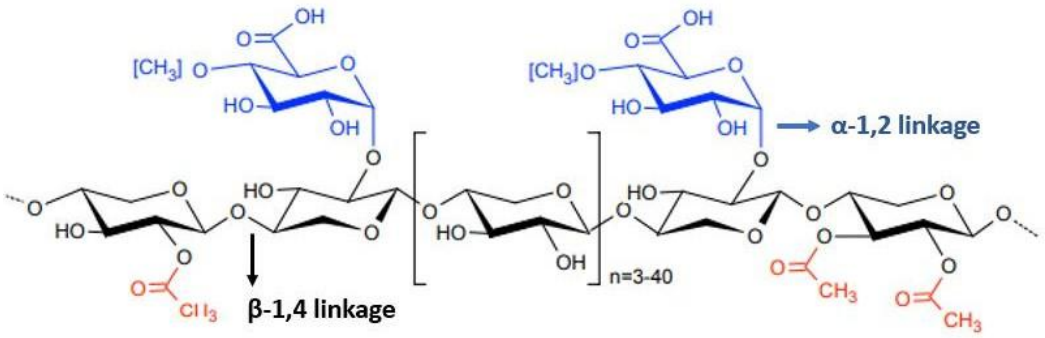

Fig. 1.3. Structure of glucuronoxylan in hardwood with its different side chain substitutions (Razeq *et al*., 2017). Here, black- xylan backbone chain, blue- 4-*O*-Methyl-D glucuronic acid and orange- acetyl groups.

1.2.1.1.3. Arabinoglucoronoxylan

Arabinoglucuronoxylan (AGX) resembles glucoronoxylan, however the xylose residues in the main backbone xylan chain, has α-Araf residues substituted at carbon 3 by *α*-(1→3) linkage as shown in Fig. 1.4. These polysaccharides are found in minimal quantities in softwood.

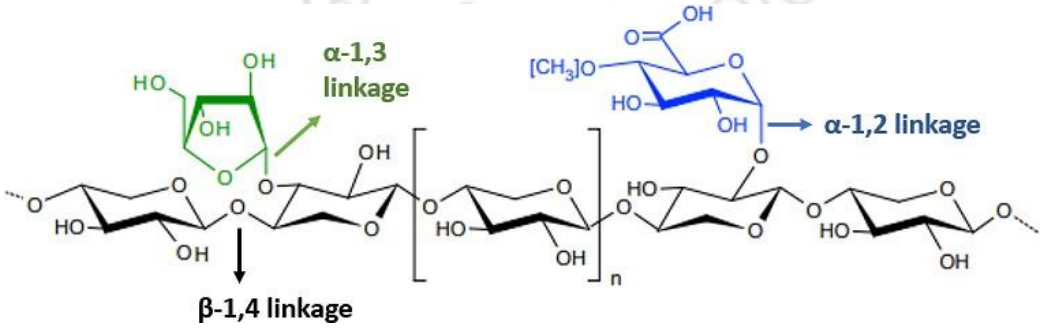

Fig. 1.4. Structure of arabinoglucuronoxylan in softwood with its different side chain substitutions (Razeq *et al*., 2017). Here, black- xylan backbone chain, green- *α*-L-arabinofuranosyl and blue- 4-*O*-Methyl-D glucuronic acid.

1.2.1.1.4. Glucuronoarabinoxylan

Glucuronoarabinoxylan (GAX) is similar to AGX, however the xylose residues in the main xylan backbone is disubstituted by *α*-Araf residues at carbon 2 and 3 by *α*-(1→2) and *α*-(1→3) linkages as shown in Fig. 1.5. It may also be substituted with ferulic acid. These polysaccharides are found in grasses and cereals like straw, stem etc.

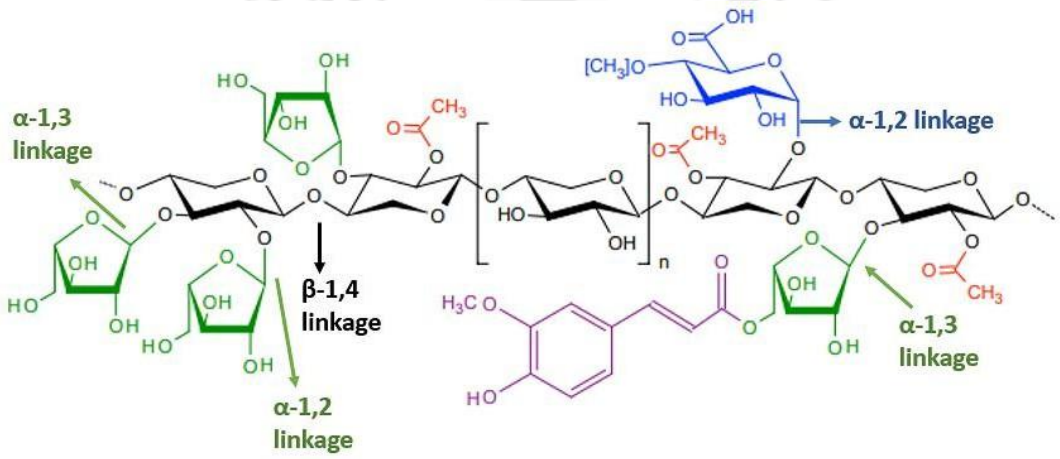

Fig. 1.5. Structure of glucuronoarabinoxylan in grasses and cereals with its different side chain substitutions (Razeq *et al*., 2017). Here, black- xylan backbone chain, green- *α*-L-arabinofuranosyl, blue- 4-*O*-Methyl-D glucuronic acid, violet- ferulic acid and orange- acetyl groups.

1.3. Carbohydrate active enzymes

Carbohydrate-Active Enzymes (CAZymes) are a diverse group of enzymes that catalyze the synthesis, modification, or breakdown of complex carbohydrates (Gavande *et al*., 2023). These enzymes play a crucial role in the degradation of structurally complex lignocellulosic biomass, which requires the concerted action of multiple, synergistically acting enzymes to achieve complete hydrolysis into monosaccharides. Initially, CAZymes such as glycoside hydrolases (GHs) and polysaccharide lyases (PLs) were grouped into different Clans based on structural

similarities and conserved catalytic residues. However, with the rapid increase in the number of characterized enzymes during the 1990s, a more systematic and functionally relevant classification became necessary (Gavande *et al*., 2023). To address this need, the Carbohydrate-Active enZymes database (CAZy) was established in 1998 (www.cazy.org), which now provides a comprehensive classification of CAZymes based on sequence similarity, structural features and conserved catalytic mechanisms (Drula *et al*., 2022). The database categorizes CAZymes into several classes, including glycoside hydrolases (GHs), polysaccharide lyases (PLs), glycosyl transferases (GTs), carbohydrate esterases (CEs) and auxiliary activities (AAs), each reflecting distinct enzymatic functions and structural motifs important for carbohydrate processing.

1.3.1. Glycoside hydrolase family 30

Glycoside hydrolases (GHs), often referred to as glycosidases, form a major category within the Carbohydrate-Active enZymes (CAZymes) and are responsible for cleaving glycosidic bonds that link sugar units in polysaccharides (Gavande *et al*., 2023). Glycoside hydrolases fall under the EC 3.2.1 classification and are also known to include transglycosidases, which facilitate transglycosylation reactions. They act on diverse glycosidic linkages, such as the β-1,4 bonds in cellulose between two D-glucose units, the α-1,4 bonds in starch and the β-1,4 bonds in xylan connecting D-xylose residues and produce different types of mono saccharides. Moreover, based on the substrate specificities the GH family enzymes are further classified into cellulolytic and hemicellulolytic enzymes (Collins *et al*.,2005, Henrissat *et al*.,1991). Presently, glycoside hydrolases are organized into 191 distinct families, reflecting their functional diversity and specificity (https://www.cazy.org/Glycoside-Hydrolases.html). The enzyme activities assigned to glycoside hydrolase family 30

(GH30) are: endo-β-1,4-xylanase (EC 3.2.1.8); β-glucuronidase (EC 3.2.1.31); glucuronoarabinoxylan endo-β-1,4-xylanase (EC 3.2.1.136); β-xylosidase (EC 3.2.1.37); glucosylceramidase (EC 3.2.1.45); β-1,6-glucanase (EC 3.2.1.75); endo-β-1,6-galactanase (EC:3.2.1.164), β-glucosidase (3.2.1.21); β-fucosidase (EC 3.2.1.38) and (reducing end) β-xylosidase (EC 3.2.1.-) (St John *et al*., 2010). GH30 family shows retaining mechanism. Moreover, the 3D structure of GH30 family enzymes shows the presence of $(\beta/\alpha)_8$ barrel fused to 9-stranded β-sandwich structure and Glutamate (Glu) is found to be the catalytic nucleophile/base (St John *et al*., 2010). Arrangement of this 9-stranded β-sandwich structure further divides GH30 into 12 subfamilies (Karlsson *et al*., 2018).

1.4. Xylan degrading enzymes

The most prevalent hemicelluloses in the cell walls of plants are known to be xylan polysaccharides. The β-1,4-linked xylose units make up the primary chain of xylan and can have variety of substitution by α-1,2- or α-1,3-linked arabinosyl units and/or α-1,2-linked (methyl)-glucuronic acid residues (Šuchová *et al*., 2022). The term xylanolytic enzymes is used for those hemicellulolytic enzymes that fully hydrolyze heteroxylans. Table 1.1 lists the different categories of xylan degrading enzymes, such as glycoside hydrolases (GH) and auxiliary activity enzymes, such as carbohydrate esterases (CE) and lytic polysaccharide monooxygenases (LPMOs), along with their mode of action.

Table 1.1. Xylan degrading enzymes classification in CAZy database.

Enzyme activity	EC number	CAZy family	Mode of action	References
Endo-*β*-1,4-xylanase	3.2.1.8	GH 5, 8, 10, 11, 30, 43, 98, 141	Breaks internal *β*-1,4-xylosidic bonds within the xylan polymer chain	Choudhury et al., 2024
β-Xylosidase	3.2.1.37	GH 3, 39, 43, 52	Releases individual xylose units by cleaving from the non-reducing ends of xylo-oligosaccharides	Ndata et al., 2021
Exo-*β*-1,4-xylanase	3.2.1.156	GH 8, 30	Acts on the terminal *β*-1,4-xylosidic bonds at the non-reducing ends of xylan chains	Chaudhary et al., 2021
α-L-Arabinofuranosidase	3.2.1.55	GH 43, 51, 54, 62	Removes *α*-L-arabinofuranosyl side chains from substituted xylan structures	Long et al., 2024
α-Glucuronidase	3.2.1.139	GH 67, 115	Eliminates α-glucuronic acid or related side groups attached to the xylan backbone	Anisha 2022
Acetylxylan esterase	3.1.1.72	CE 1, 4, 5, 6, 7, 16	Detaches acetyl groups from xylan by breaking ester linkages	Shrivastava et al., 2023
Feruloyl esterase	3.1.1.73	CE 1	Catalyzes the cleavage of ester bonds connecting ferulic acid to xylan	Shrivastava et al., 2023
Lytic polysaccharide monooxygenases (LPMO)	-	AA 9, 14	Cleaves glycosidic bonds of xylan polysaccharide in the crystalline and insoluble portion via an oxidative mechanism	Malgas *et al*., 2019

1.4.1. Endo-*β*-xylanase from GH30 family

Endo-*β*-xylanase plays a crucial role in the depolymerization of xylan, a primary constituent of hemicellulose. It specifically targets and cleaves *β*-1,4 xylosidic bonds within the xylan backbone, leading to the formation of xylo-oligosaccharides (Fu *et al*., 2023) as shown in Fig. 1.6. This enzyme is essential in several industrial applications, like the biofuel sector, paper and pulp industry, food industry and many more where effective degradation of biomass is vital.

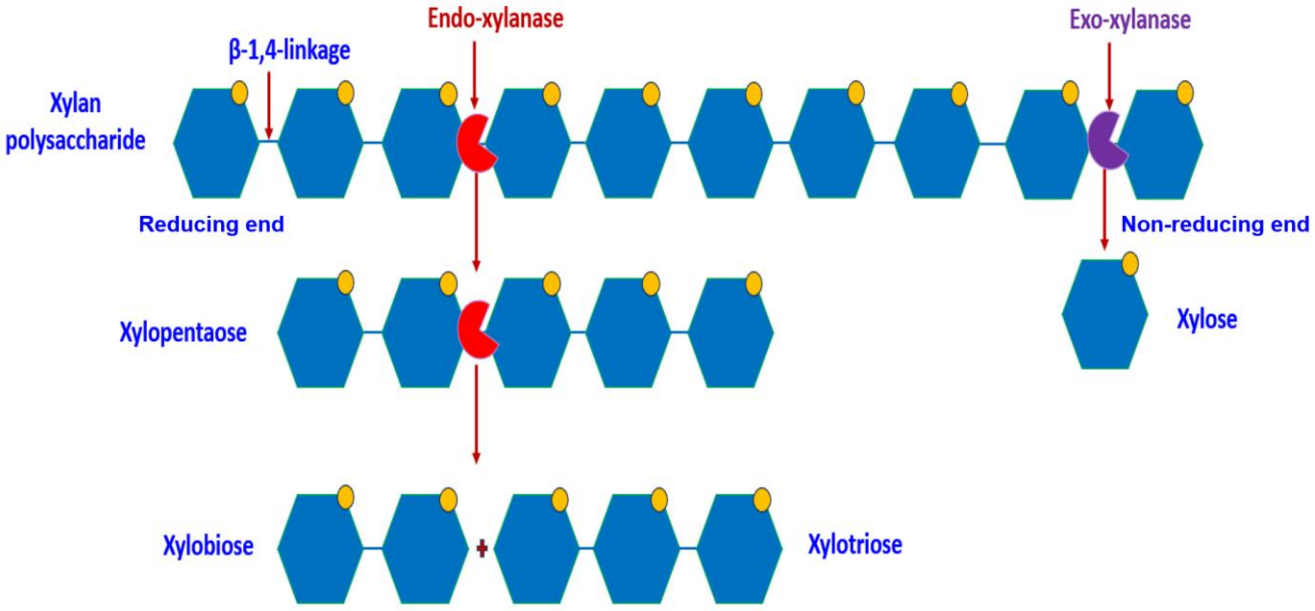

Fig. 1.6. Mode of action of endo- and exo-xylanases.

The catalytic domain of endo-*β*-xylanases of GH30 family, typically adopt a $(\beta/\alpha)_8$-barrel architecture which is commonly known as the TIM barrel (Puchart *et al*., 2021). This structure consists of eight parallel *β*-strands arranged in the core of the barrel, each followed by an outward-facing *α*-helix. The substrate-binding cleft is largely shaped by the loops connecting the *β*-strands and *α*-helices (*β*-*α* loops). The key catalytic residues usually a pair of aspartic or glutamic acids are positioned on the *β*-strands (Puchart *et al*., 2021). These residues act as the catalytic nucleophile and the acid/base in a two-step, double-displacement reaction mechanism (also called

retaining mechanism). In this reaction mechanism, a covalent bond containing intermediate, glycosyl-enzyme is formed, with the two catalytic carboxylic groups situated ~5.5 Å apart. In the first step (glycosylation), one of the residues acts as a nucleophile and attacks the anomeric carbon of the xylan backbone, while the other residue acts as an acid to protonate the leaving group, forming the glycosyl-enzyme, a covalent intermediate (Fig. 1.7). In the second step (deglycosylation), a water molecule, activated by the same residue now acting as a base, attacks the intermediate to release the product and regenerate the enzyme (Fig. 1.7). The overall reaction retains the anomeric configuration of the sugar. Transition states in both steps resemble an oxocarbenium ion, with GH30 enzymes often stabilizing a half-chair ($^4H_3$) conformation (Linares-Pasten *et al*., 2018).

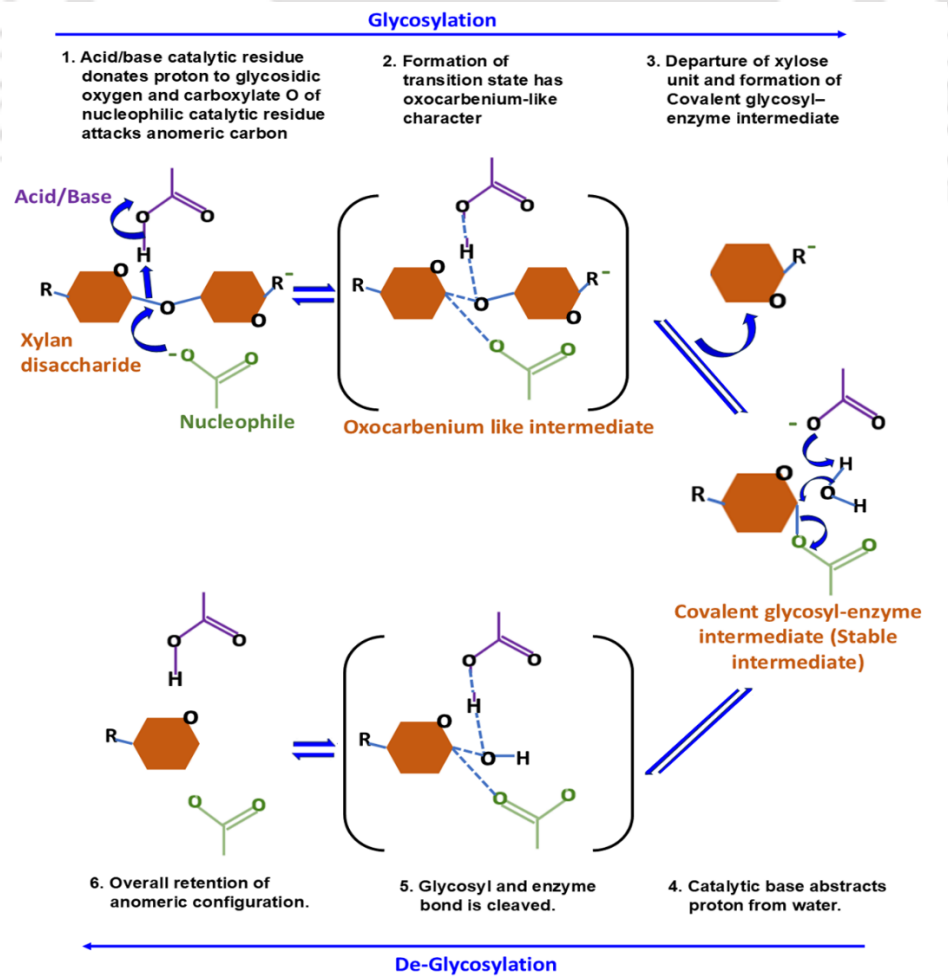

Fig. 1.7. Retaining mechanism of hydrolysis of endo-xylanase from GH30 family.

1.4.1.1. Biochemical properties of endo- *β*-xylanase from GH30 family

The first bacterial endo-xylanase from the GH30 family was *Bs*XynC from *Bacillus subtilis* reported in 1991 (St. John *et al*., 2006). The purified *Bs*XynC from *B. subtilis* was analysed to be a 43.9 kDa protein with an optimum temperature of 65°C and pH 6.0. The half-life ($t_{1/2}$) analysis of *Bs*XynC was 25h at 40°C and 5h at 50°C. The depolymerization of methylglucuronoxylan by *Bs*XynC resulted in the release of *β*-1,4-linked xylo-oligosaccharides containing single substitution of α-1,2-linked 4-O-methylglucuronate, according to MALDI-TOF MS and ^{1}H NMR analyses (St. John *et al*., 2006). Another GH30 bacterial endo-xylanase, *Ec*Xyn30A from *Erwinia chrysanthemi* showed a molecular mass of 42 kDa and optimum pH of 6.0 and temperature of 35°C (Hurlbert *et al*., 2001). The examination of *Ec*Xyn30A hydrolyzed products by MALDI-TOF data revealed that, its enzyme activity is highly dependent on the presence of D-glucuronic acid (GlcA) or (4-O-methyl-D-glucuronic acid) MeGlcA as side chain residues (Hurlbert *et al*., 2001). Other bacterial endo-xylanases including *Xy*n30D from *Paenibacillus barcinonensis* BP-23 (Valenzuela *et al*., 2012), *Ca*Xyn30B from *Clostridium acetobutylicum* ATCC824 (Crooks *et al*., 2020), *St*Xyn30A from *Streptomyces turgidiscabies* C56 (Maehara *et al*., 2018) are known to include mode of hydrolysis action similar to that of *Ec*Xyn30A (Puchart *et al*., 2021). Both *Cp*Xyn30A from *Clostridium papyrosolvens* DSM 2782 (Puchart *et al*., 2021, St John *et al*., 2014) and *Ca*Xyn30A from *C. acetobutylicum* ATCC 824 (Puchart *et al*., 2021, St John *et al*., 2018) each have optimum pH of 4.5 and both belong to the GH30_8 subfamily. Other biochemical properties like optimum pH, optimum temperature, pH stability, thermostability for different biochemically

characterized GH30 endo-xylanases from different prokaryotic organisms are mentioned in Table 1.2.

Table 1.2. Xylan degrading enzymes classification in CAZy database.

Organism/ Enzyme acronym	GH subfamily	Substrate	Opti-mum pH	Optimum Temperature	pH and thermostability (% enzyme activity retained)	References
Bacterial xylanases						
Streptomyces turgidiscabies, *St*Xyn30A	GH30_8	Beechwood xylan	6.5	55°C	pH 4.0-5.0, 40°C	Maehara et al., 2018
Clostridium acetobutylicum ATCC 824, *Ca*Xyn30A	GH30_8	Wheat arabinoxylan	4.5	40°C	pH 2.7-4.7 (68%), 4-50°C (85%)	St John et al., 2018
Clostridium papyrosolvens, *Cp*Xyn30A	GH30_8	Wheat arabinoxylan	4.5	30°C	-	St John et al., 2014
Paenibacillus barcinonensis, Xyn30D	GH30_8	Beechwood xylan	6.5	50°C	pH 6-8 (70%), 4-50°C (>80%)	Valenzuela et al., 2012
Bacillus subtilis, *Bs*XynC	GH30_8	Methylglucuron o-xylan	6	65°C	40°C (50%)	St. John et al., 2006
Erwinia chrysanthemi, *Ec*Xyn30A	GH30_8	Sweetgum xylan	6	35°C	25-60°C (>50%)	Hurlbert et al., 2001
Fungal xylanases						
Thermothelomyces thermophila ATCC 42464, *Tt*Xyn30A	GH30_7	Beechwood glucuronoxylan	4	50°C	pH 3-9 (97%), 45°C (88%)	Šuchová et al., 2021
T. cellulolyticus, *Tc*Xyn30C	GH30_7	Beechwood glucuronoxylan	4	55°C	pH 2.3-5.7 (>90%), 40-55°C (>90%)	Nakamichi et al., 2019

1.4.1.2. 3-Dimensional structure of endo-*β*-xylanases from GH30 family

The first 3D structure was solved in the year 2003 for endo-*β*-xylanase *Ec*Xyn30A, from *Erwinia chrysanthemi* as shown in Fig. 1.8 (Puchart *et al*., 2021). The enzyme consists of two domains, catalytic domain and small domain. The $(\beta/\alpha)_8$-barrel motif in the catalytic domain (residues 46 to 315) features a binding cleft along the C- terminal side of the *β*-barrel (Fig. 1.8A). The two catalytic residues were Glu165 and

Glu253 (Fig. 1.8B), having a distance of 4.22 Å located at the C-terminal of *β*-strands 4 and 7, respectively (Larson *et al*., 2003). The smaller domain (residues 31-43 and 323-413) is made up of 9 *β*-strands, five of which interact with *α*-helices 7 and 8 of the catalytic domain (Puchart *et al*., 2016). The three linkers between this smaller domain and the catalytic domain are composed of residues 44, 45 and residues 316 to 322 (Larson *et al*., 2003). The enzyme, *Ec*Xyn30A exhibits selectivity for glucuronoxylan because of ionic interactions between the guanidine group of the conserved arginine residue (R293) and the carboxyl group of MeGlcA. Other endo-xylanases like, *Cp*Xyn30A from

R. papyrosolvens (St. John *et al*., 2014) and *Ca*Xyn30A from *C. acetobutylicum* (St. John *et al*., 2018) were also structurally characterized.

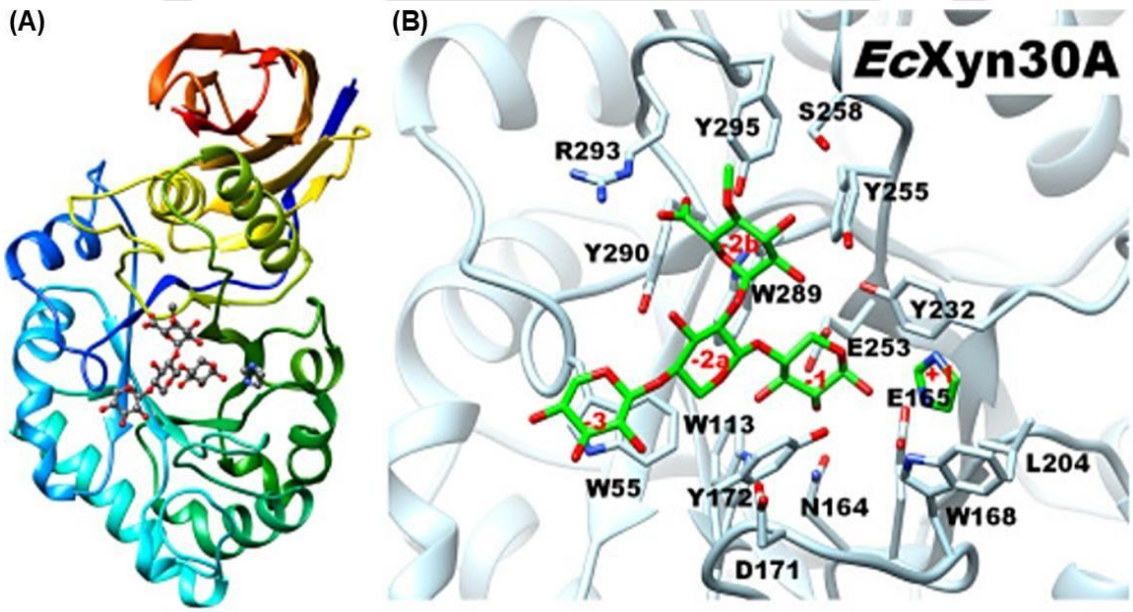

Fig. 1.8. (A) 3D structure for *Ec*Xyn30A (PDB ID: 2Y24) and **(B)** Detail view of active site of the enzyme *Ec*Xyn30A along with the ligand shown in green colour (Puchart *et al*., 2021).

1.4.2. Exo-xylanase

The enzyme, exo-*β*-xylanase acts by cleaving *β*-1,4-xylosidic linkages at the non-reducing ends of xylan chains as illustrated in Fig. 1.6, facilitating the sequential depolymerization of xylan (Chaudhary *et al*., 2021). These enzymes are particularly important for the complete breakdown of xylan, especially when functioning alongside endo-*β*-xylanase, which targets the *β*-1,4-xylosidic bonds within the main chain of xylan. The synergism between these enzymes enhances the overall performance in xylan degradation, making them important tools in a wide range of industries including biofuel production, paper and pulp processing and animal feed development (Yegin, 2023).

1.4.3. Carbohydrate binding modules

Carbohydrate-binding modules (CBMs) are non-catalytic modules associated with carbohydrate-active enzymes (CAZymes), particularly glycoside hydrolases (GHs), that facilitate the recognition and binding of complex carbohydrates (Henrissat, 1991). They enhance the catalytic efficiency of the associated with enzymes by bringing the catalytic domain into close proximity to the polysaccharide substrate, thereby enhancing the substrate accessibility and hydrolysis rates (Tomme *et al*., 2000). CBMs are categorized into different families based on their amino acid sequences and binding specificities, as curated in the CAZy database (Drula *et al*., 2022). CBMs typically function by recognizing specific structural motifs in polysaccharides, such as *β*-1,4-linked xylose in xylan or glucose units in cellulose. Xylanases from GH30 family, often possess a conserved CBM6 or CBM13 module located either at the N- or C-terminus (Linares-Pastén *et al*., 2018). The CBMs in GH30 enzymes are crucial for recognizing and binding to the complex, branched xylan

structures that these enzymes target (Crooks *et al*., 2020). The CBM6 family, commonly associated with GH30 xylanases, typically binds to non-crystalline regions of xylan and sometimes to cellulose (Henrissat, 1991). Its *β*-sandwich fold structure (as shown in Fig. 1.9) with a carbohydrate-binding cleft allows interaction through hydrophobic stacking and hydrogen bonds, recognizing specific patterns in the polysaccharide backbone (Henrissat, 1991). This selective recognition is particularly important in natural lignocellulosic environments, where polysaccharides are heterogeneous and often decorated with various substitutions (Biely *et al*., 2016).

Fig. 1.9. *β*-sandwich fold structure of carbohydrate binding module 6, CBM6 (Henshaw *et al*., 2004).

1.5. Xylanolytic microorganisms

An array of xylan degrading enzymes is identified in various microorganisms. This includes strains of yeast like *Pichia stiptis, Cryptococcus podzolicus, Fellomyces sp., Candida tropicalis* etc. Filamentous fungi under genera *Trichoderma, Aspergillu,* and *Fusarium* are some of the major producers of xylan degrading enzymes (Santibáñez *et al.*, 2021, Sohail *et al*., 2022). Bacteria like *Clostridium thermocellum, Bacillus stearothermophilus, Rhodotermus marinus* etc. have been reported to produce xylanases with high thermal stability compared to fungal xylanases (Santibáñez *et al*., 2021, Sohail *et al*., 2022). As compared to mesophilic microbes, thermophilic microbes are known to produce thermostable enzymes, as they can meet the industrial demands requiring thermostable enzymes having tolerance against high-pressure and greater resistance against denaturing agents (Bala *et al*., 2018). *Acetivibrio clariflavus* DSM 19732 (earlier known as *Clostridium clariflavum* DSM 19732), is a thermophilic anaerobe, chemoganotrophic, curved and rod-shaped bacterium as shown in Fig. 1.10 (Izquierdo *et al*., 2012) isolated from anaerobic sludge (Izquierdo *et al*., 2012, Shiratori *et al*., 2009). This organism has been found to utilize both hemicelluloses and cellulose

Izquierdo *et al*., 2010, Sizova *et al*., 2011). The analysis of the phylogenetic relationship of 16S rRNA gene of *A. clariflavus* with other cellulolytic clostridia from Cluster III showed its close homology to 16s rRNA gene of *Clostridium thermocellum* DSM 1313 followed by *Clostridium thermocellum* ATCC 20475 (Izquierdo *et al*., 2012). Its complete genome sequence was finished in July 2011, where the GenBank accession number for the project is CP003065 (Izquierdo *et al*., 2012). Its genome comprises one circular chromosome of length 4,897,678 bp with GC content of 35.6% but genome size was larger than its close relative *C. thermocellum* ATCC 20475. While analyzing the enzymes of *A. clariflavus* involved in lignocellulosic degradation, a total of 72 glycosyl hydrolases were identified, among which 27 represented known families. Comparison of the glycoside hydrolase inventory between *C. thermocellum* ATCC 20475 and *A. clariflavus*, showed 50 enzymes (69.4%) were found with closest match in *C. thermocellum* and of the remaining 22 enzymes, a total of 15 are found to be xylanases of glycosyl hydrolase (GH) families 10, 11, 39, 43, 51, 67 and 74. Also, it was found that *A. clariflavus* has a comparatively higher proportion and higher diversity of xylanolytic enzymes than *C. thermocellum* while cellulose-active GH families showed similar distribution between both the organisms. Moreover, *A. clariflavus* possesses a variety of xylanolytic enzymes that completely breaks down xylan to xylose, while xylanolytic enzymes in *C. thermocellum*, are only able to break xylan down to xylo-oligomers (Izquierdo *et al*., 2012). While lacking xylose isomerase, genome of *A. clariflavus* is found to have a putative xylulose kinase (Clocl_2440), which is a key difference from *C. thermocellum.*

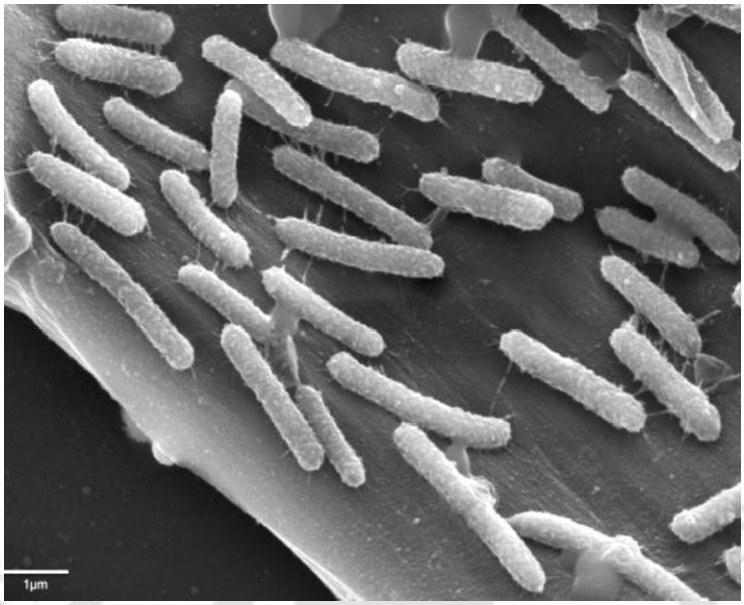

Fig. 1.10. Scanning electron micrograph of *Acetivibrio clariflavus* DSM 19732 (Izquierdo *et al*., 2012).

1.6. Applications of endo-xylanases from GH30 family

The broad substrate specificity and efficiency of endo-*β*-xylanases have made them indispensable in diverse of industrial and biotechnological applications (Fig 1.11). From pulp bleaching and biofuel production to animal feed improvement and the generation of bioactive xylo-oligosaccharides, endo-xylanases contribute significantly to sustainable biomass utilization. Additionally, their role in producing functional oligosaccharides with antioxidant, antimicrobial and prebiotic properties has opened up new avenues in food, pharmaceutical and cosmetic industries. The versatility of endo-xylanases, particularly from glycoside hydrolase family 30 (GH30), continues to drive innovation in biomass processing and valorization.

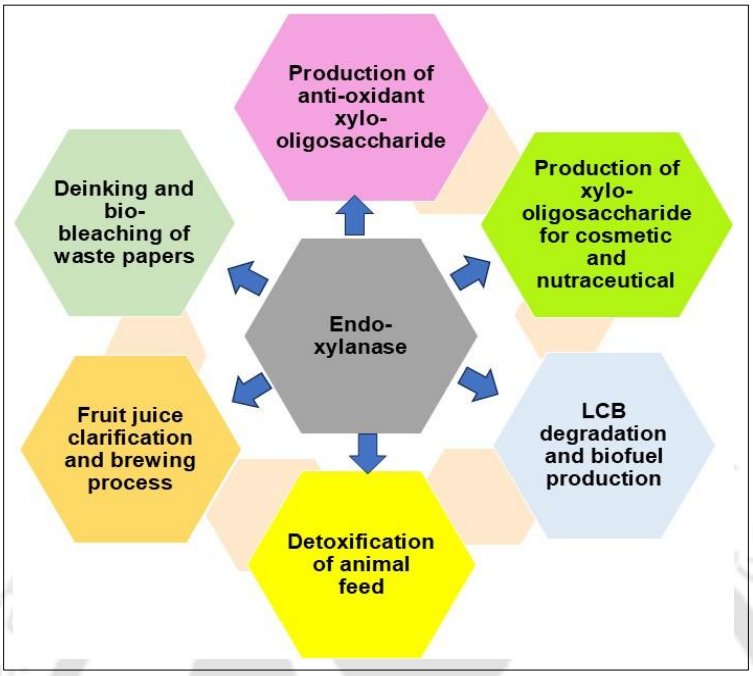

Fig. 1.11. Different applications of endo-*β*-xylanases.

1.6.1. Production of antioxidant xylo-oligosaccharides

Oxidative stress is a major factor in the development of chronic diseases and aging, that has prompted the interest in explaining natural antioxidants. Xylo-oligosaccharides, especially acidic forms containing uronic acid residues, have shown potential antioxidant properties. These compounds can be generated through endo-*β*-xylanase-catalyzed hydrolysis of glucuronoxylans. Their ability to scavenge free radicals and chelate metal ions make them as promising ingredient in health supplements and functional foods aimed at improving cellular defense mechanisms. GH30_8 xylanases release acidic xylo-oligosaccharides (AXOS) containing uronic acid residues, which functionally differ from the neutral XOS. These AXOS have potential bioactivities, such as antimicrobial properties, which may depend on the uronic acid content and oligosaccharide length (Katapodis *et al*., 2002; Christakopoulos *et al*., 2003). Another, GH30 endo-xylanase, Xyn30D from *P. barcinonensis* produced acidic XOS on hydrolysing birchwood and beechwood glucuronoxylan which displayed antioxidant activity (Valls *et al*., 2018).

1.6.2. Production of xylo-oligosaccharides for nutraceuticals and cosmetics

Xylo-oligosaccharide like xylobiose has drawn attention for its prebiotic, anti-inflammatory and antidiabetic effects. It also functions as a low-calorie sweetener and a moisturizing agent in cosmetics. Enzymatic production of xylobiose using endo-*β*-xylanases and accessory enzymes offers a natural and sustainable approach over chemical synthesis. With increasing demand for natural health and cosmetic products, the efficient bioproduction of xylobiose holds significant promise for diverse commercial applications. For example, the action of GH30 endo-xylanase enzyme, *Tt*Xyn30A from *Thermothelomyces thermophila* along with lytic polysaccharide monooxygenases (LPMOs) further boosts xylobiose yield (Zerva *et al*., 2020) used for prebiotic production.

1.6.3. Role in microbial ecology and plant biomass degradation

In natural ecosystems, microbial degradation of plant biomass is essential for carbon cycling. Endo-*β*-xylanases are one of the key enzymes involved in this process, enabling microorganisms to access energy by breaking down hemicellulose. Their action initiates the depolymerization of xylan, a major component of plant cell walls, facilitating further degradation by other enzymes. For example, the GH30 endo-xylanase enzyme, *St*Xyn30A from *Streptomyces thermoviolaceus* produced xylo-oligosaccharides with glucuronic acid substitutions upon hydrolysis of hardwood and crop residues (Maehara *et al*., 2018). Understanding the role of xylanases in microbial ecology provides insights into soil health, symbiotic digestion (e.g., in ruminants) and

strategies for efficient biomass utilization in biorefineries. Their presence in phytopathogens (e.g., *E. chrysanthemi*) suggests involvement in initial plant tissue degradation. Conversely, in rumen microbes, GH30 enzymes function in coordinated breakdown of plant-derived xylans, indicating their ecological importance varies with microbial habitat and substrate availability (Rogowski *et al*., 2015).

1.6.4. Detoxification of animal feedstock

Animal feed often contains plant-based materials that include anti-nutritional factors such as non-starch polysaccharides (NSPs), especially arabinoxylans and glucuronoxylans. These complex carbohydrates can increase gut viscosity, hinder nutrient absorption and promote the growth of pathogenic microbes in the gastrointestinal tract of animals like poultry and swine. Endo-β-xylanases play a crucial role in degrading these xylan-based NSPs, thereby reducing their anti-nutritional effects. The enzymatic breakdown of xylan not only improves the digestibility of the feed but also releases fermentable oligosaccharides that can serve as prebiotics (Choudhury *et al*., 2025). This contributes to better animal growth performance, improved feed conversion ratios and overall gut health, making xylanase supplementation an important strategy in modern livestock nutrition. For example, GH30 endo-xylanase from *Trichoderma piluliferum* and *T. viride* showed increase in the digestibility of hemicellulose-rich food like soyabean, corn cob and starch, rice peel and wheat bran (da Costa *et al*., 2019).

1.6.5. Fruit juice clarification and brewing process

Endo-xylanases play a significant role in the fruit juice and pulp industries by breaking down hemicellulosic polysaccharides, thereby enhancing juice yield and quality. Their enzymatic action reduces viscosity and facilitates the removal of

hemicellulose, improving juice clarity, aroma and color (Liu *et al*., 2018). For instance, endo-xylanase from *Pediococcus acidilactici* GC25 has been reported to enhance reducing sugar content and reduce turbidity in juices derived from fruits like kiwi, apple, peach, orange, apricot, grapes and pomegranate. Similarly, partially purified xylanase from *Streptomyces sp*. AOA40 improved the clarity of apple juice, while its application in orange, mousambi and pineapple juices showed clarity enhancements of 20.9%, 23.6%, and 27.9% respectively (Bhardwaj *et al*., 2019). In the brewing sector, cereals such as barley, wheat and rice, rich in non-starch polysaccharides, benefit from endo-xylanase treatment alongside cellulase and pectinase during mashing. This enzymatic combination promotes the release of pigments, fermentable sugars, minerals and nutrients, resulting in improved malt production, increased extract yield, reduced viscosity and enhanced stability of beverages like juice and wine (Bajaj *et al*., 2019).

1.6.6. Deinking in paper and pulp industry

Deinking is a critical process in the recycling of waste paper, as it facilitates the removal of printing inks and other surface contaminants to recover clean cellulose fibers suitable for reuse in papermaking. Traditionally, chemical deinking methods are employed, which rely on a combination of alkaline chemicals such as sodium hydroxide, hydrogen peroxide, surfactants and chelating agents to detach ink particles. Although effective, these processes often lead to fiber damage, high chemical usage and environmental pollution due to the discharge of toxic effluents. Physical deinking techniques such as flotation, washing, sonication and microwave irradiation are also in use and can enhance the efficiency of ink particle separation, though they may require high energy inputs and additional equipment for effective implementation

(Saxena and Chauhan, 2017). In contrast, enzymatic deinking offers an eco-friendly and efficient alternative. It utilizes specific classes of enzymes such as cellulases, hemicellulases (e.g. xylanases), pectinases, lipases and laccases to dislodge ink from fiber surfaces by selectively degrading the polysaccharide or proteinaceous matrices that bind ink particles. Among these, xylanases, particularly endo-xylanases, have gained attention for their role in deinking. These enzymes hydrolyze the β-1,4-xylosidic linkages in xylan, a key hemicellulose component of plant cell walls, thereby loosening the hemicellulosic matrix that often traps ink particles on the fiber surface. This enzymatic action enhances fiber porosity and disrupts lignin-carbohydrate complexes, facilitating more efficient ink removal during subsequent washing or flotation steps (Yang *et al*., 2023). Furthermore, enzymatic treatments preserve fiber integrity better than chemical processes and reduce the load on wastewater treatment systems, leading to lower operational costs and improved environmental outcomes (Saxena and Chauhan, 2017). The mechanism of deinking by endo-xylanase involves multiple synergistic effects. First, the enzyme weakens the physical and chemical interactions between ink and fiber by hydrolyzing xylan. This leads to fiber surface modification and detachment of ink particles. Secondly, by disrupting the lignin-hemicellulose matrix, the enzyme indirectly facilitates the removal of hydrophobic ink-bound lignin fragments (Yang *et al*., 2023). This not only improves ink release but also enhances the hydrophobicity contrast needed for efficient flotation. Xylanases can also increase the brightness and strength properties of the recycled pulp by improving the accessibility of residual bleaching agents. Notably, xylanases from glycoside hydrolase family 30 (GH30) have shown particular effectiveness in such applications. For example, GH30 endo-xylanase from *Bacillus halodurans* was reported to

significantly improve pulp brightness and reduce Effective Residual Ink Concentration (ERIC), especially when used in combination with laccase or cellulase. These GH30 enzymes are especially effective on substituted xylans, such as glucuronoxylan, found in hardwood pulps, making them suitable candidates for high-performance enzymatic deinking applications (Yang *et al*., 2023).

1.7. Significance and objectives of the proposed work

1.7.1. Significance of the proposed work

Enzymatic hydrolysis of different lignocellulosic biomass components is favored since it is ecofriendly, results in complete hydrolysis of LCB and yields a significant amount of reducing sugar. Xylanases play a critical role in degrading plant polysaccharides. Therefore, the studies on the xylanolytic enzymes from diverse sources has enormously increased over the world in the last decade. Around 72 glycosyl hydrolase enzymes were identified in the bacterium *Acetivibrio clariflavus* DSM 19732. Furthermore, as compared with *C. thermocellum, A. clariflavus* is known possess a large proportion and diverse types of xylanolytic enzymes. As *A. clariflavus* is a thermophilic microorganism, the endo-*β*-1,4-xylanase produced by it will have higher stability and optimum temperature which will help in fulfilling the industrial demands.

A gene encoding endo-*β*-1,4-xylanase (*Ac*Xyn30B_12) was located in the genome of *A. clariflavus* DSM 19732. *Ac*Xyn30B_12 is not biochemically and structurally characterized so far. Therefore, in this proposed work, the gene encoding a putative endo-*β*-1,4-xylanase (*Ac*Xyn30B_12) of family 30 glycoside hydrolase (Gene accession number- AEV69300.1) from *A. clariflavus* will be biochemically and structurally studied. The cloning, expression and purification and enzymatic assays of

*Ac*Xyn30B_12 can help in understanding the biochemical and functional properties of the enzyme. Structural characterization of *Ac*Xyn30B_12 using *in silico* techniques like: 3D structure prediction by modelling, molecular dynamics simulations, molecular docking can give information regarding its mechanism of catalysis and active-site pocket. Small angle X-ray scattering (SAXS) and dynamic light scattering (DLS) analysis will help understanding the molecular arrangement and conformation in solution form as well as solubility of the enzyme. These studies will give an overall idea about *Ac*Xyn30B_12 being potentially a relevant xylanase enzyme for various biochemical applications. The deinking efficiency of *Ac*Xyn30B_12 against different waste papers will also be analysed. Additionally, the environmental sustainability of the enzymatic deinking process will be examined by analyzing the effluent characteristics. These results will be compared with those obtained from conventional chemical deinking treatments to determine the relative eco-friendliness and potential of *Ac*Xyn30B_12 as a green alternative. The specific objectives of the present study are given below.

1.7.2. Specific objectives of the proposed work

1. Cloning, expression and purification endo-*β*-1,4-xylanase of family 30 Glycoside Hydrolase (*Ac*Xyn30B_12) from *Acetivibrio clariflavus.*
2. Biochemical and functional characterization of endo-*β*-1,4-xylanase (*Ac*Xyn30B_12).
3. 3-Dimensional structure modeling and molecular dynamic analyses of endo-*β*-1,4-xylanase (*Ac*Xyn30B_12).
4. Structure and molecular organization of *Ac*Xyn30B_12 in solution form by SAXS and DLS.
5. Enzymatic deinking of different waste papers using endo-*β*-1,4-xylanase *Ac*Xyn30B_12.

1.8. References

Álvarez, C., Reyes-Sosa, F.M., Díez, B. (2016) Enzymatic hydrolysis of biomass from wood. Microbial Biotechnology. 9(2), 149–156.

Anisha, G.S. (2022) Molecular advances in microbial α-galactosidases: Challenges and prospects. World Journal of Microbiology and Biotechnology. 38(9), 148.

Bala, A., Singh, B. (2019) Cellulolytic and xylanolytic enzymes of thermophiles for the production of renewable biofuels. Renewable Energy. 136, 1231–1244.

Bajaj, P., Mahajan, R. (2019) Cellulase and xylanase synergism in industrial biotechnology. Applied Microbiology and Biotechnology. 103(21-22), 8711–8724.

Bhardwaj, N., Kumar, B., Verma, P. (2019) A detailed overview of xylanases: an emerging biomolecule for current and future prospective. Bioresources and Bioprocessing. 6(1).

Biely, P., Singh, S., Puchart, V. (2016) Towards enzymatic breakdown of complex plant xylan structures: state of the art. Biotechnology Advances. 34(7), 1260–1274.

Bozell, J.J., Petersen, G.R. (2010) Technology development for the production of biobased products from biorefinery carbohydrates—the US Department of Energy's "Top 10" revisited. Green Chemistry. 12, 539–554.

Chaudhary, R., Kuthiala, T., Singh, G., Rarotra, S., Kaur, A., Arya, S.K., Kumar, P. (2021) Current status of xylanase for biofuel production: A review on classification and characterization. Biomass Conversion and Biorefinery. 13, 8773–8791.

Choudhury, B., Kumar, A., Goyal, A. (2025) Insights of Hemicellulolytic Enzymes for Detoxification of Biomass Used as Animal Feed. In: Lignocellulosic Biomass and Enzymes: Fundamentals, Emerging Technologies and Applications. Springer Nature Singapore, 211–236.

Christakopoulos, P., Katapodis, P., Kalogeris, E., Kekos, D., Macris, B.J., Stamatis, H., Skaltsa, H. (2003) Antimicrobial activity of acidic xylo-oligosaccharides produced by family 10 and 11 endoxylanases. International Journal of Biological Macromolecules. 31(4–5), 171–175.

Collins, T., Gerday, C., Feller, G. (2005) Xylanases, xylanase families and extremophilic xylanases. FEMS Microbiology Reviews. 29(1), 3–23.

Crooks, C., Long, L., St John, F.J. (2020) CaXyn30B from the solventogenic bacterium *Clostridium acetobutylicum* is a glucuronic acid-dependent endoxylanase. BMC Research Notes. 13(1), 1–6.

da Costa, A.C., Cavalheiro, G.F., de Queiroz Vieira, E.R., Gandra, J.R., de Tonissi e Buschinelli de Goes, R.H., da Paz, M.F., et al. (2019) Catalytic properties of xylanases produced by Trichoderma piluliferum and Trichoderma viride and

their application as additives in bovine feeding. Biocatalysis and Agricultural Biotechnology. 19, 101161.

Devi, A., Bajar, S., Kour, H., Kothari, R., Pant, D., Singh, A. (2022) Lignocellulosic biomass valorization for bioethanol production: a circular bioeconomy approach. Bioenergy Research. 15(4), 1820–1841.

Drula, E., Garron, M.L., Dogan, S., Lombard, V., Henrissat, B., Terrapon, N. (2022) The carbohydrate-active enzyme database: functions and literature. Nucleic Acids Research. 50(D1), D571–D577.

European Commission. (2018) A sustainable bioeconomy for Europe: strengthening the connection between economy, society and the environment.

Fu, T.T., Wang, L., Li, W.J., Chen, Y. (2023) Overexpression and characterization of Endo-1,4-β-xylanase from Fibrobacter succinogenes in *Pichia pastoris*. Applied Biochemistry and Microbiology. 59(6), 900–908.

Gavande, P.V., Goyal, A., Fontes, C.M. (2023) Carbohydrates and carbohydrate-active enzymes (CAZyme): An overview. In: Glycoside Hydrolases. 1–23.

Henrissat, B. (1991) A classification of glycosyl hydrolases based on amino acid sequence similarities. Biochemical Journal. 280(2), 309–316.

Henshaw, J.L., Bolam, D.N., Pires, V.M., Czjzek, M., Henrissat, B., Ferreira, L.M., Fontes, C.M. and Gilbert, H.J (2004). The family 6 carbohydrate binding module CmCBM6-2 contains two ligand-binding sites with distinct specificities. Journal of Biological Chemistry, 279(20), pp.21552-21559.

Hurlbert, J.C., Preston III, J.F. (2001) Functional characterization of a novel xylanase from a corn strain of *Erwinia chrysanthemi*. Journal of Bacteriology. 183(6), 2093–2100.

IPCC. (2021) Climate Change 2021: The Physical Science Basis. Contribution of Working Group I to the Sixth Assessment Report.

Izquierdo, J.A., Goodwin, L., Davenport, K.W., Teshima, H., Bruce, D., Detter, C., Lynd, L.R. (2012) Complete genome sequence of *Clostridium clariflavum* DSM 19732. Standards in Genomic Sciences. 6(1), 104–115.

Izquierdo, J.A., Sizova, M.V., Lynd, L.R. (2010) Diversity of bacteria and glycosyl hydrolase family 48 genes in cellulolytic consortia enriched from thermophilic biocompost. Applied and Environmental Microbiology. 76(11), 3545–3553.

Katapodis, P., Kavarnou, A., Kintzios, S., Pistola, E., Kekos, D., Macris, B.J., Christakopoulos, P. (2002) Production of acidic xylo-oligosaccharides by a family 10 endoxylanase from *Thermoascus aurantiacus* and use as plant growth regulators. Biotechnology Letters. 24, 1413–1416.

Kim, S.R., Park, Y.C., Jin, Y.S., Seo, J.H. (2019) Strain engineering of *Saccharomyces cerevisiae* for enhanced xylose metabolism. Biotechnology Advances. 37(6), 107449.

Kumar, A., Choudhury, B., Goyal, A. (2025) Advancement in Pretreatment Technologies for Mixed Lignocellulosic Biomass. In: Lignocellulosic Biomass and Enzymes: Fundamentals, Emerging Technologies and Applications. Springer Nature Singapore, 33–54.

Kumar, R., Singh, S., Singh, O.V. (2008) Bioconversion of lignocellulosic biomass: biochemical and molecular perspectives. Journal of Industrial Microbiology & Biotechnology. 36, 995–1007.

Linares-Pasten, A., Aronsson, J., Nordberg Karlsson, E. (2018) Structural considerations on the use of endo-xylanases for the production of prebiotic xylo-oligosaccharides from biomass. Current Protein and Peptide Science. 19(1), 48–67.

Liu, X., Liu, T., Zhang, Y., Xin, F., Mi, S., Wen, B., Gu, T., Shi, X., Wang, F., Sun, L.A.O. (2018) Structural insights into the thermophilic adaption mechanism of endo-1,4-β-xylanase from *Caldicellulosiruptor owensensis*. Journal of Agricultural and Food Chemistry. 66.

Long, L., Lin, Q., Wang, J., Ding, S. (2024) Microbial α-L-arabinofuranosidases: Diversity, properties, and biotechnological applications. World Journal of Microbiology and Biotechnology. 40(3), 84.

Maehara, T., Yagi, H., Sato, T., Ohnishi-Kameyama, M., Fujimoto, Z., Kamino, K., Kaneko, S. (2018) GH30 glucuronoxylan-specific xylanase from *Streptomyces turgidiscabies* C56. Applied and Environmental Microbiology. 84(4), e01850–17.

Malgas, S., Mafa, M.S., Mkabayi, L., Pletschke, B.I. (2019) A mini review of xylanolytic enzymes with regards to their synergistic interactions during hetero-xylan degradation. World Journal of Microbiology and Biotechnology. 35(12), 187.

Mankar, A.R., Pandey, A., Modak, A., Pant, K.K. (2021) Pretreatment of lignocellulosic biomass: A review on recent advances. Bioresource Technology. 334, 125235.

Nakamichi, Y., Fouquet, T., Ito, S., Watanabe, M., Matsushika, A., Inoue, H. (2019) Structural and functional characterization of a bifunctional GH30-7 xylanase B from the filamentous fungus *Talaromyces cellulolyticus*. Journal of Biological Chemistry. 294(11), 4065–4078.

Ndata, K., Nevondo, W., Cekuse, B., van Zyl, L.J., Trindade, M. (2021) Characterization of a highly xylose tolerant β-xylosidase isolated from high temperature horse manure compost. BMC Biotechnology. 21, 1–10.

Nordberg Karlsson, E., Schmitz, E., Linares-Pastén, J.A., Adlercreutz, P. (2018) Endoxylanases as tools for production of substituted xylooligosaccharides with prebiotic properties. Applied Microbiology and Biotechnology. 102, 9081–9088.

Puchart, V., Šuchová, K., Biely, P. (2021) Xylanases of glycoside hydrolase family 30–An overview. Biotechnology Advances. 47, 107704.

Qaseem, M.F., Shaheen, H., Wu, A.M. (2021) Cell wall hemicellulose for sustainable industrial utilization. Renewable and Sustainable Energy Reviews. 144, 110996.

Razeq, F.M. (2017) Discovery and biochemical characterization of new CAZYmes from PULs and metagenome sequences. PhD thesis, University of Toronto (Canada).

Rogowski, A., Briggs, J.A., Mortimer, J.C., Tryfona, T., Terrapon, N., Lowe, E.C., et al. (2015) Glycan complexity dictates microbial resource allocation in the large intestine. Nature Communications. 6(1), 7481.

Saini, J.K., Saini, R., Tewari, L. (2015) Lignocellulosic agriculture wastes as biomass feedstocks for second-generation bioethanol production: concepts and recent developments. 3 Biotech. 5, 337–353.

Santibáñez, L., Henríquez, C., Corro-Tejeda, R., Bernal, S., Armijo, B., Salazar, O. (2021) Xylo-oligosaccharides from lignocellulosic biomass: A comprehensive review. Carbohydrate Polymers. 251, 117118.

Saxena, A., Singh Chauhan, P. (2017) Role of various enzymes for deinking paper: a review. Critical Reviews in Biotechnology. 37(5), 598–612.

Shiratori, H., Sasaya, K., Ohiwa, H., Ikeno, H., Ayame, S., Kataoka, N., Ueda, K. (2009) *Clostridium clariflavum* sp. nov. and *Clostridium caenicola* sp. nov., moderately thermophilic, cellulose-/cellobiose-digesting bacteria isolated from methanogenic sludge. International Journal of Systematic and Evolutionary Microbiology. 59(7), 1764–1770.

Shrivastava, M., Maibam, P., Aishwarya, M., Goyal, A. (2023) Hemicellulases and auxiliary activities for biomass hydrolysis. In: Handbook of Biorefinery Research and Technology. Springer, 1–23.

Sizova, M.V., Izquierdo, J.A., Panikov, N.S., Lynd, L.R. (2011) Cellulose- and xylan-degrading thermophilic anaerobic bacteria from biocompost. Applied and Environmental Microbiology. 77(7), 2282–2291.

Sohail, M., Barzkar, N., Michaud, P., Jahromi, S.T., Babich, O., Sukhikh, S., Nahavandi, R. (2022) Cellulolytic and xylanolytic enzymes from yeasts: Properties and Industrial Applications. Molecules. 27(12), 3783.

St John, F.J., Dietrich, D., Crooks, C., Balogun, P., de Serrano, V., Pozharski, E., et al. (2018) A plasmid borne, functionally novel glycoside hydrolase family 30 subfamily 8 endoxylanase from solventogenic Clostridium. Biochemical Journal. 475(9), 1533–1551.

St John, F.J., González, J.M., Pozharski, E. (2010) Consolidation of glycosyl hydrolase family 30: a dual domain 4/7 hydrolase family consisting of two structurally distinct groups. FEBS Letters. 584(21), 4435–4441.

St John, F.J., Rice, J.D., Preston, J.F. (2006) Characterization of XynC from *Bacillus subtilis* subsp. subtilis strain 168 and analysis of its role in depolymerization of glucuronoxylan. Journal of Bacteriology. 188(24), 8617–8626.

Šuchová, K., Fehér, C., Ravn, J.L., Bedő, S., Biely, P., Geijer, C. (2022) Cellulose- and xylan-degrading yeasts: Enzymes, applications and biotechnological potential. Biotechnology Advances. 59, 107981.

Šuchová, K., Puchart, V., Biely, P. (2021) A novel bacterial GH30 xylobiohydrolase from *Hungateiclostridium clariflavum*. Applied Microbiology and Biotechnology. 105, 185–195.

Tomme, P., Boraston, A., Kormos, J.M., Warren, R.A.J., Kilburn, D.G. (2000) Affinity electrophoresis for the identification and characterization of soluble sugar binding by carbohydrate-binding modules. Enzyme and Microbial Technology. 27(7), 453–458.

Valenzuela, S.V., Diaz, P., Pastor, F.J. (2012) Modular glucuronoxylan-specific xylanase with a family CBM35 carbohydrate-binding module. Applied and Environmental Microbiology. 78(11), 3923–3931.

Valls, C., Pastor, F.J., Vidal, T., Roncero, M.B., Díaz, P., Martínez, J., Valenzuela, S.V. (2018) Antioxidant activity of xylooligosaccharides produced from glucuronoxylan by Xyn10A and Xyn30D xylanases and eucalyptus autohydrolysates. Carbohydrate Polymers. 194, 43–50.

Wasie, A.T., Tadesse, M.G., Wotango, A.S., Bachheti, R.K., Ahmed, I.N. (2024) Heterogeneous catalytic conversion of lignocellulose: towards green and renewable chemicals. Discover Applied Sciences. 6(2), 37.

Yang, M., Li, J., Wang, S., Zhao, F., Zhang, C., Zhang, C., Han, S. (2023) Status and trends of enzyme cocktails for efficient and ecological production in the pulp and paper industry. Journal of Cleaner Production. 418, 138196.

Yegin, S. (2023) Microbial xylanases in xylooligosaccharide production from lignocellulosic feedstocks. Biomass Conversion and Biorefinery. 13(5), 3619–3658.

Yousuf, A., Pirozzi, D., Sannino, F. (2020) Fundamentals of lignocellulosic biomass. In: Lignocellulosic biomass to liquid biofuels. Academic Press, 1–15.

Zerva, A., Pentari, C., Grisel, S., Berrin, J.G., Topakas, E. (2020) A new synergistic relationship between xylan-active LPMO and xylobiohydrolase to tackle recalcitrant xylan. Biotechnology for Biofuels. 13, 1–13.

Chapter 2

Cloning and expression of an endo-*β*-1,4-xylanase of family 30 Glycoside hydrolase (*Ac*Xyn30B_12) from *Acetivibrio clariflavus* DSM 19732

2.1 Introduction

Lignocellulosic biomass (LCB) is an abundant, renewable feedstock with considerable potential for the sustainable production of biofuels, biochemicals and biomaterials. Comprising mainly cellulose, hemicellulose and lignin, LCB serves as a viable alternative to fossil-derived raw materials (Saini *et al*., 2015; Qaseem *et al*., 2021). Among the different classes of hemicellulose, xylan is the predominant polysaccharide present in the secondary cell walls of most terrestrial plants (Devi *et al*., 2022). Efficient degradation of xylan is critical for unlocking its fermentable sugar content, thereby enabling its full valorization in biotechnological processes. This task is accomplished through the synergistic action of xylanolytic enzymes belonging to different CAZy families *viz.* glycoside hydrolases (GHs), carbohydrate esterases (CEs) and lytic polysaccharide monooxygenases (LPMOs), which together facilitate the deconstruction of complex heteroxylans (Biely *et al*., 2016; Malgas *et al*., 2019). Among these, xylanases play a central role by hydrolyzing the internal *β*-1,4-glycosidic linkages in the xylan backbone. Their action is vital for the saccharification of hemicellulose and supports various industrial applications such as biofuel generation, paper pulping and the production of value-added oligosaccharides. Within the CAZy database, among the

different glycoside hydrolases, the glycoside hydrolase family 30 (GH30) xylanases exhibit unique structural and catalytic characteristics (St John *et al*., 2010). The endo-xylanases from GH30 family can specifically target substituted xylans containing *α*-1,2-linked glucuronic acid or 4-*O*-methyl-D-glucuronic acid residues. These substrate specificities are conferred by conserved sequence motifs in their catalytic domains, allowing selective recognition and cleavage of decorated xylan chains (St John *et al*., 2010). Due to the distinctive properties like catalytic potential, thermostability and ability to act on complex and branched xylans, GH30 xylanases has emerged as a promising biocatalyst in several industrial applications. For example, in the pulp and paper industry, they are applied for chlorine-free bio-bleaching processes, in the food and feed sector, they enable the production of xylo-oligosaccharides (XOS) with prebiotic functions and in lignocellulosic biorefineries, they contribute to the enzymatic release of fermentable sugars for the production of ethanol, xylitol and butanol (Bharadwaj *et al*., 2019).

In the search for thermostable and efficient xylanases, extremophilic microorganisms have gained attention as valuable enzyme sources. *Acetivibrio clariflavus* DSM 19732 (earlier known as *Clostridium clariflavum* DSM 19732) is a thermophilic, chemo-organotrophic, anaerobic bacterium capable of degrading plant cell wall polysaccharides through a sophisticated enzyme complex known as the cellulosome (Izquierdo *et al*., 2012). This organism encodes an array of carbohydrate-active enzymes (CAZymes), including members of GH30, assembled into a multi-modular architecture to enhance substrate binding and hydrolysis. One such protein, *Ac*Xyn30B_12 (GenBank accession no. AEV69300.1 and gene locus Clocl_2746), is a GH30 endo-*β*-1,4-xylanase comprising a catalytic domain, carbohydrate-binding

module (CBM6) and a C-terminal type I dockerin domain, indicating its integration into the cellulosomal machinery. Despite its predicted functional role, *Ac*Xyn30B_12 remains biochemically uncharacterized. The present chapter describes cloning and expression of the full-length *Ac*Xyn30B_12 gene from *A. clariflavus* DSM 19732, setting the foundation for its subsequent purification and functional characterization for potential industrial applications.

In present study, the gene sequence of *Ac*Xyn30B_12 was retrieved from NCBI (https://www.ncbi.nlm.nih.gov/). The conserved structural domain for *Ac*Xyn30B_12 was determined using NCBI Conserved Domains Database (Lu *et al*., 2020; https://www.ncbi.nlm. nih.gov/Structure/cdd/wrpsb.cgi) and the molecular architecture was developed using DOG 2.0 software, version 1.0 (Ren *et al*., 2009). The full-length gene encoding *Ac*Xyn30B_12 contains a total of 673 amino acid residues with an N-terminal signal peptide (residues 1–27), followed by a catalytic module, Xyn30Bc (residues 29–440) a family 6 carbohydrate binding module, CBM6 (residues 471–592) and a C-terminal Type I dockerin domain, DocI (residues 606–671) and 2 amino acid residues at the C- terminal (residues 672–673). In this study, the full-length gene encoding the Xyn30Bc catalytic module, CBM6 and DocI without the signal peptide was cloned in the pET-28a(+) vector. The full-length gene encoding the protein, *Ac*Xyn30B_12 was expressed using

E. coli BL-21 (DE3) cells. Then the enzyme, *Ac*Xyn30B_12 was subjected to purification by using immobilized metal-ion affinity chromatography followed by size exclusion chromatography (SEC) column for biochemical, functional as well as structural characterization.

2.2 Materials and methods

2.2.1 Bacterial strains, chemicals, reagents and kits

The genomic DNA of *A. clariflavus* DSM 19732 was purchased from Deutsche Sammlung von Mikroorganismen und Zellkulturen (DSMZ), a German collection of microorganisms and cell culture. To carry out PCR amplification, Taq DNA polymerase and dNTPs was obtained from New England Biolabs, USA and oligonucleotides, forward and reverse primers were obtained from GCC Biotech, India. GenElute miniprep plasmid isolation kit, polyacrylamide gel electrophoresis components, ethidium bromide, Trizma base, DNAse-RNAse free water (pH 8.0), gel extraction kit, kanamycin and Bradford reagent were obtained from Sigma-Aldrich, USA. Both the restriction enzymes, *Nhe*I and *Xho*I were obtained from New England Biolabs, USA. The *Escherichia coli* cells, DH5α and BL21 (DE3) utilized for cloning and expressing the recombinant enzyme, *Ac*Xyn30B_12, respectively and the expression vector pET-28a(+) were obtained from Novagen (Madison, WI, USA). 10X ligase buffer and T_4 DNA ligase were purchased from Takara Bio Inc., Japan. The DNA ladder was procured from GeNei, India. Sodium hydroxide, ethylenediaminetetraacetic acid disodium salt (EDTA), glucose, sodium dodecyl sulphate (SDS), luria broth (LB) medium, protein staining dye Coomassie Brilliant Blue R-250 and pre-stained protein ladder were purchased from HiMedia Pvt. Ltd., India.

2.2.2 Amplification of gene encoding *Ac*Xyn30B_12 by PCR

The gene (1.9 kb) encoding *Ac*Xyn30B_12 (GenBank accession no. AEV69300.1 and gene locus ID. Clocl_2746) from the genomic DNA of *Acetivibrio clariflavus* DSM 19732 was amplified by PCR. The restriction sites, *Nhe*I and *Xho*I in forward and reverse primers, respectively are underlined and shown in Table 2.1. The PCR reaction

mixture of 60 µL and PCR cycles (denaturation, annealing and extension) for amplification are mentioned in Tables 2.2 and 2.3, respectively. The gene amplification by PCR was performed on a thermal cycler (Bio-Rad Laboratories India Pvt. Ltd., India). The PCR amplified product was run on 0.8% (w/v) agarose gel (as outlined below in Section 2.2.3) to check for the gene amplification.

Table 2.1. Oligonucleotide primer sequences used for amplification of gene encoding *Ac*Xyn30B_12.

Module	Primer name	Primer sequence
*Ac*Xyn30B_12	Forward	5′-TGGT**GCTAGC**AGCTATACAGCTTCTGTAGATGTC-3′
	Reverse	5′-ACCACC**CTCGAG**TTATTCCACAGGGAACTTACTAATCTG-3′

Underlined and bold part of the primer sequences present the restriction enzyme (NheI and XhoI) sites

Table 2.2. PCR mixture for amplification of gene encoding *Ac*Xyn30B_12 from *Acetivibrio clariflavus* DSM 19732.

PCR components	Volume (µL)	Final concentration
10X reaction buffer	6.0	1X
dNTPs mix (0.0025 M)	9.0	375 µM
Forward primer (15 µM)	1.8	0.45 µM
Reverse primer (15 µM)	1.8	0.45 µM
Sigma water (nuclease free), pH 8.0	39.3	--
Genomic DNA (86 ng/µL)	1.8	2.6 ng
Taq DNA polymerase (5 U/ µL)	0.3	0.025 U/µL
Total	60.0	--

Table 2.3. PCR cycles for amplification of gene encoding *Ac*Xyn30B_12 from *Acetivibrio clariflavus* DSM 19732.

Steps		Time (min)
1) Denaturation at 95°C		1 min
2) 30 cycles of	i) Denaturation at 95°C	30 s
	ii) Annealing at 57°C	1 min
	iii) Extension at 68°C	2 min
3) Final extension at 68°C		5 min

2.2.3 Agarose gel electrophoresis of PCR amplified products

The PCR amplified product was analysed by using agarose gel electrophoresis by using agarose gel of 0.8% (w/v). 10X Tris-acetate-EDTA (TAE) buffer stock was prepared using 0.4 M Tris-acetate and 0.01 M EDTA, pH 8.0 (according to Sambrook and Rusell 2001). The agarose gel, 0.8% (w/v) was prepared by mixing 0.4 g agarose in 0.05 L of TAE buffer (1X) followed by microwave heating until a transparent solution was formed. After the agarose gel solution cooled to 50°C, 5 µL of 5 mg/mL ethidium bromide solution was added to it and the solution was gently poured into a casting apparatus. The agarose gel was allowed to cool and solidify in around 30 min. For the agarose gel electrophoresis, the 1X TAE buffer used for agarose gel preparation was used as electrophoresis running buffer (Sambrook and Rusell 2001).

A stock of 5X DNA loading dye (final pH 8.0) was prepared by mixing the components as mentioned in Table 2.4. One volume of 5X DNA loading dye and four volumes of PCR amplified product was mixed to obtain a final concentration of 1X DNA loading dye before loading into the agarose gel. 10 µL of each of the sample-dye mixture were loaded in the gel and the gel was run at 50 volts for 1h. Band corresponding to the PCR product was visualized under UV illumination with the aid of a gel documentation system (Biorad XR, USA).

Table 2.4. Composition of 5X stock of DNA loading dye.

Components	**Final concentration (5X)**
Tris-HCl	0.05 M
Glycerol	25% (w/v)
EDTA	0.005 M
Bromophenol blue	0.2% (w/v)
Xylene cyanol	0.2% (w/v)

2.2.4 PCR amplified DNA extraction

The amplified gene product by PCR was extracted from the agarose gel (0.8%, w/v) by using a gel extraction kit (GenElute ^{TM} Gel extraction kit, Sigma-Aldrich, USA) and following the step-wise protocol provided by the manufacturer as discussed below:

1. A sterile and empty microcentrifuge tube (1.5 mL) was weighed and its mass was noted.
2. The PCR amplified product was resected from the agarose gel by utilizing a sterile and sharp scalpel. Then this excised gel part was transformed to the empty weighted micro-centrifuged tube. The tube was reweighed and the mass of resected gel was determined by subtracting the weight of the empty tube (noted in step1).
3. Three volumes of gel solubilization buffer were added to 1 volume of the excised gel (100 mg~ 0.3 mL).
4. The above gel mix was incubated at 50°C for a duration of 10 min (it was vortexed briefly every 2-3 min) until the gel had fully dissolved.
5. While the gel was solubilized, the GenElute binding column (DNA binding column) was prepared by placing it in a sterile 2 mL micro-centrifuge tube and adding 0.5 mL of column preparation solution in it. Then the column was centrifuged at 13,000*g*, 25°C for 1 min and the supernatant released in the collection tube was discarded.
6. 1 gel volume of 100% isopropanol was added to the gel mixture (step 4) and mixed properly until a homogenous solution was obtained.
7. 0.7 mL above mixture (step 6) was added to the prepared binding column (step 5) and centrifuged at 13,000*g*, 25°C for 1 min and the flow through was disposed. The same step was repeated until all the gel mixture was added to the binding column.

8. 0.7 mL of wash solution was gently poured to the binding column through which gel mixture was passed through as above (step 7) and centrifuged at 13,000*g*, 25°C for 1 min and the flow through collected was disposed.
9. The binding column was centrifuged again at 13,000*g*, 25°C for 1 min to remove any remaining trace of wash solution. Then, the binding column was placed on a fresh sterile micro-centrifuge tube (1.5 mL) for elution of PCR amplified DNA product.
10. 30 µL of DNAse free water (Sigma-Aldrich Pvt. Ltd. USA) was added to the binding column and incubated at 25°C for 5 min. The PCR amplified DNA was eluted by centrifugating at 13,000*g*, 25°C for 1 min and was stored in deep freezer at -20°C until further use.

2.2.5 Digestion of PCR amplified DNA by restriction enzymes

The above PCR amplified DNA was digested by using restriction enzymes *Nhe*I and *Xho*I following the set up as mentioned in Table 2.5. The digestion mixture was incubation at 37°C in a water bath (Grant, Sub Aqua dual plus) for 2h. The digested PCR amplified DNA was run on agarose gel (0.8%, w/v) and the desired gene fragment was extracted and purified by using the gel extraction kit as outlined in Section 2.2.4 and eluted using 30 µL of elution buffer.

Table 2.5. Digestion set up of PCR amplified DNA by Restriction Enzyme (RE).

Digestion reaction set up	**Volume (µL)**
10X reaction buffer	2.0
PCR amplified DNA (50 ng/µL)	10.0
*Nhe*I (10 U/µL)	1.0
*Xho*I (10 U/µL)	1.0
DNAse free water	6.0
Total	20.0

2.2.6 Description of pET-28a(+) expression vector

The pET-28a(+) vector is a widely used expression system in molecular biology, designed for efficient recombinant protein production in *Escherichia coli*. It belongs to the pET series of vectors, which are regulated by the T7 promoter, enabling high-level transcription when induced by T7 RNA polymerase. This T7 promoter system was originally developed by Studier and colleagues (Studier and Moffatt, 1986; Studier *et al*., 1990). This vector contains an N-terminal T7-Tag sequence and C-terminal His-tag. The His-tag facilitates easy purification of expressed proteins using affinity chromatography. Additionally, the presence of a kanamycin resistance gene ensures selective growth of transformed bacterial cells under antibiotic pressure. The multiple cloning site (MCS) within pET-28a(+) allows for the insertion of target genes through various restriction sites. The lac operon regulatory system, including the lacI repressor, controls expression, preventing basal transcription in the absence of an inducer (e.g., IPTG). Overall, the pET-28a(+) system provides a highly effective platform for expressing recombinant proteins with affinity purification tags, making it ideal for structural and functional studies. The location of His-tag, fi origin, T7 coding sequence, kanamycin coding gene and T7 terminator is displayed in the restriction map of pET-28a(+) vector as depicted in Fig. 2.1.

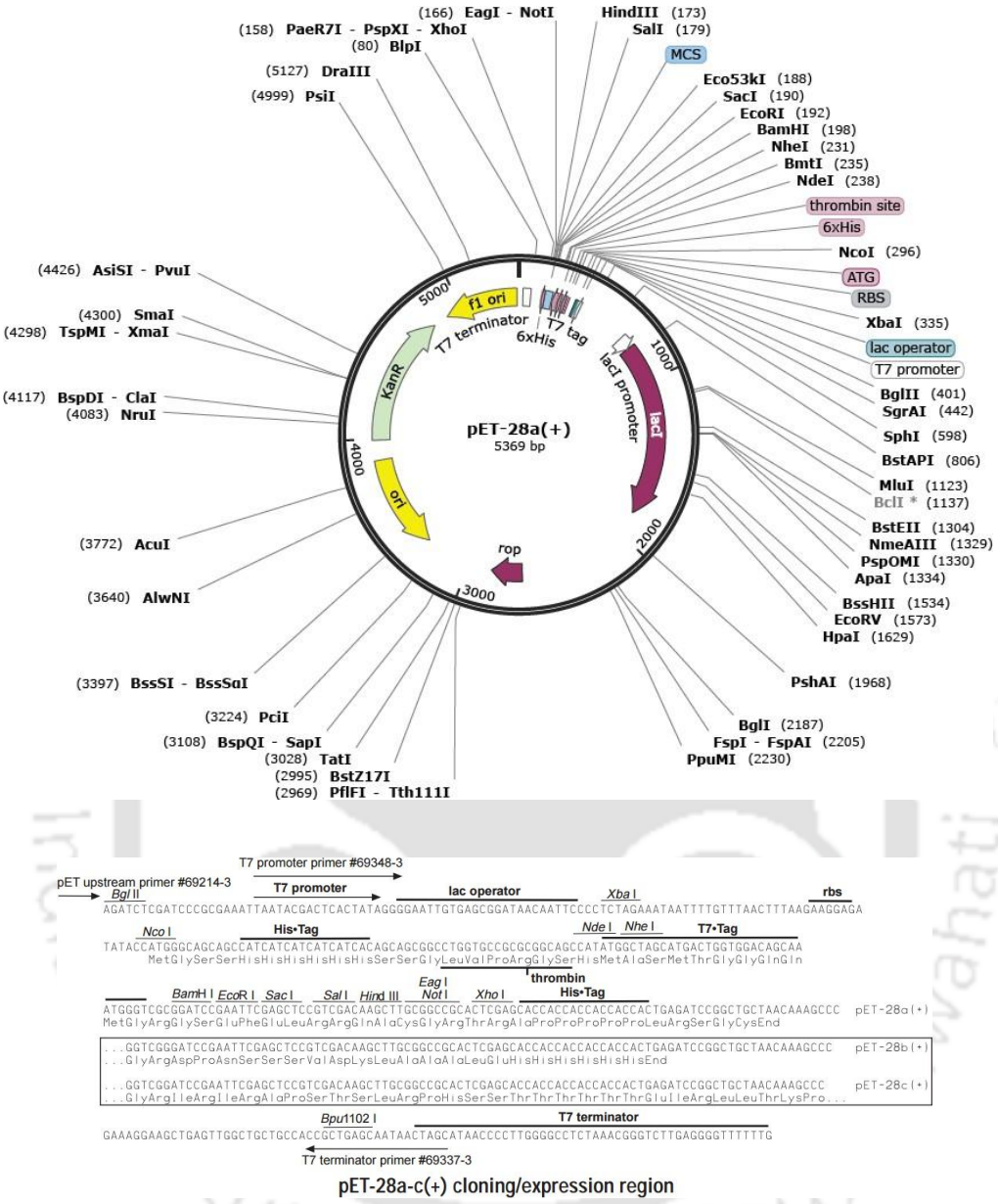

Fig. 2.1. A diagram illustrating the restriction map of the pET-28a(+) expression vector. Multiple cloning site (158-203 bp), restriction enzyme sites, C-terminal His_6-Tag coding sequence (140-157 bp), N-terminal His_6-Tag coding sequence (270-287), T7 promoter (370-386 bp), T7 terminator (26-72 bp), pBR322 origin (3286 bp), kanamycin marker (3995-4807 bp) and a f1 origin (4903-5358). *Nhe*I cuts at 231 and *Xho*I at 158.

2.2.7 Restriction digestion of pET-28a(+) expression vector

The pET-28a(+) expression vector (50 ng/µL) was digested by using restriction enzymes *Nhe*I and *Xho*I following the set up as mentioned in Table 2.6. The digestion mixture was incubation at 37°C in a water bath (Grant, Sub Aqua dual plus) for 2h. The *Nhe*I-*Xho*I digested pET-28a(+) vector was run on agarose gel (0.8%, w/v) and subsequently purified by following the protocol as described in Section 2.2.4 and eluted using in 30 µL elution buffer.

Table 2.6. Restriction Enzyme (RE) digestion set up of pET-28a(+).

RE reaction set up	**Volume (µL)**
Reaction buffer 10X (rCutSmart Buffer-NEB)	2.5
pET-28a(+) vector (50 ng/µL)	20.0
*Nhe*I (10 U/µL)	1.0
*Xho*I (10 U/µL)	1.0
DNAse free water	5.5
Total	30.0

2.2.8 Ligation of both *Nhe*I-*Xho*I digested PCR fragments into pET-28a(+) vector

The *Nhe*I-*Xho*I digested PCR amplified product (as mentioned in Section 2.2.5) was ligated to *Nhe*I-*Xho*I digested pET-28a(+) vector (as mentioned in Section 2.2.7) by using T4 DNA liagse. The molar ratio of insert (*Ac*Xyn30B_12) to vector was maintained at 3:1 and the amount of digested *Ac*Xyn30B_12 was determined using the formula given below (Engler and Richardson, 1982):

$$\frac{\text{ng of vector x kb size of insert}}{\text{kb size of vector}} \text{ x insert : vector molar ratio = ng of insert}$$

$$\frac{46 \text{ ng x } 1.9 \text{ kb}}{5.369 \text{ kb}} \text{ x } 3{:}\ 1 = 16.2 \text{ ng of insert (gene encoding } Ac\text{Xyn30B\_12)}$$

The set up for ligation of *Nhe*I-*Xho*I digested *Ac*Xyn30B_12 and pET-28a(+) vector was done as shown in Table 2.7.

Table 2.7. Ligation set up of PCR amplified insert and pET-28a(+) vector.

Ligation reaction set up	Volume (µL)
10X buffer (Standard Taq buffer)	1.2
pET-28a(+) vector (23 ng/µL)	2.0
Restriction digested PCR insert (5.8 ng/µL)	2.8
T4 DNA ligase (350 U/µL)	1.0
DNAse free water	5.0
Total	12.0

The ligation mixture was incubated for 16h at 16°C in a refrigerator.

2.2.9 Preparation of *E. coli* (DH5α) competent cells

The DH5α competent cells were prepared by following the steps given below:

Day 1

1. 0.05 mL of culture of *E. coli* (DH5α) from glycerol stock (22.5%) was inoculated into 5.0 mL Luria Bertani medium (Sambrook *et al*., 1989) and incubated at 37°C at180 rpm for 12h.
2. 0.1 M $CaCl_2$, 0.1 M $MgCl_2$ and 0.1 M $CaCl_2$ containing 15% (v/v) glycerol solutions were prepared and sterilized by filtration through a PVDF membrane (pore size 0.25 µm, 2.5 cm dia) using syringe filter under laminar airflow and stored at 4°C.

Day 2

3. 1.5 mL micro-centrifuge tubes, 50 mL centrifuge tubes, micro-tips and the above prepared solutions of 0.1 M $CaCl_2$, 0.1 M $MgCl_2$ and 0.1 M $CaCl_2$ containing 15% (v/v) glycerol were sterilized by autoclaving at 121°C and 5 psi for 20 min and were kept on ice bath and placed under laminar air flow hood.

4. From the overnight grown culture from above (Step 1), 1.0 mL was inoculated into 100 mL autoclaved Luria Bertani medium in a 250 mL conical flask. The culture was incubated at 37°C and 180 rpm until the absorbance at 600 nm (A_{600}) reached around 0.4-0.6.
5. 40 mL from 100 mL grown *E. coli* culture was transferred to 50 mL round bottom centrifuge tubes and centrifuged at 4,000*g* and 4°C for 10 min. Before placing the tubes in centrifuge machine, their weights were equally balanced.
6. Previous step (step 5) was repeated for making pellet from the remaining culture.
7. The supernatant was carefully discarded and the cell pellet was gently re-suspended by adding 4 mL of sterilized and ice chilled 0.1 M $MgCl_2$ followed by sterilized and ice chilled 0.1 M $CaCl_2$ solution and the final volume was adjusted upto 20 mL. The re-suspended cell solution was incubated on ice for duration of 10 min
8. The tubes containing the above mixture (step 7) were centrifuged at 4°C and 4,000*g* for 10 min.
9. The supernatant was removed and the cell pellet was again suspended in 3 mL sterile, ice-cold 0.1 M $CaCl_2$ solution and incubated on ice for 10 min. The cell suspension was then centrifuged again at 4°C and 4,000*g* for 10 min.
10. The supernatant was removed and cell pellet was now suspended in 1.5 mL of sterile, ice chilled 0.1 M $CaCl_2$ solution containing 15% (v/v) glycerol.
11. 0.1 mL of competent cells were aliquoted into each 1.5 mL micro-centrifuge tube and stored at -80°C for further utilization.

2.2.10 Preparation of Luria-Bertani (LB) medium

The Luria-Bertani (LB) medium is most commonly used medium for growth of recombinant *E. coli* cells. It was prepared by using the components according to Sambrook *et al*., 1989 as mentioned in Table 2.8. All the medium constituents were dissolved in 250 mL of deionized water and the pH was brought to 7.2 by using 2 N, NaOH. The final volume was adjusted up to 800 mL. 400 mL of LB medium was then transferred to 2 different 1.0 L conical flasks and autoclaved at 121°C, for 20 min at 15 psi. The autoclaved LB was cooled in 25°C and filter sterilized kanamycin (0.05mg/mL, final concentration) was added into it before inoculation.

Table 2.8. Composition of Luria-Bertani medium.

Component	Final concentration (%, w/v)
Tryptone	1.0
Yeast extract powder	0.5
Sodium chloride	1.0
pH	7.2

2.2.10.1 Preparation of LB-agar medium

The LB agar medium was prepared by solubilizing the medium components as mentioned in Table 2.8. In this LB medium, a final concentration of 2% (w/v) nutrient agar was added. The medium was sterilized by autoclaving at 121°C, for 20 min at 15 psi. The autoclaved medium was kept in a laminar air flow chamber and cooled down to 50-55°C. To the liquid medium filter sterilized kanamycin (0.05 mg/mL, final concentration) was added and immediately around 25 mL of medium was dispensed into each of the sterilized petri dishes. The LB Agar medium was left to solidify for 20 min, sealed with parafilm and stored in 4°C for further utilization.

2.2.11 Transformation of ligated DNA using *E. coli* (DH5α) competent cells

The recombinant plasmid DNA containing the gene encoding *Ac*Xyn30B_12 was transformed using *E. coli* (DH5α) competent cells. The following protocol was followed for transformation:

1. The micro-centrifuge tube (1.5 mL) containing 0.1 mL *E. coli* (DH5α) competent cells (as mentioned in Section 2.2.9) was taken out from -80°C and kept on ice for 5 min. The ligation mixture (as mentioned in Section 2.2.8) was given a short spin and 0.02 mL of the ligation mixture was gently mixed with 0.1 mL of *E. coli* (DH5α) competent cells.
2. The micro-centrifuge tube was tapped gently for around 4-5 times and incubated on ice for 30 min.
3. The cells were given a heat shock at 42°C for 40 s and then subsequently put back on to ice for 5 min.
4. 1.0 mL of autoclaved LB-medium was mixed with the *E. coli* (DH5α) cells and incubated at 37°C in a shaking incubator at 180 rpm for 1h.
5. The cells were pelleted by centrifugation at 3,000*g*, 25°C and 5 min.
6. 1.0 mL of the supernatant was gently removed and the cell pellet was resuspended in the remaining 0.1 mL of supernatant.
7. The cells were plated onto LB-agar medium containing 0.05 mg/mL kanamycin (as outlined in Section 2.2.10.1) and incubated at 37°C for 12h under static conditions.
8. The transformation efficiency was calculated by using the formula as given below

$$\text{Transformation efficiency} = \frac{\text{No. of colonies in LB agar plate x Dilution factor}}{\text{µg of insert DNA}} = \text{cfu/µg}$$

2.2.12 Isolation of recombinant plasmid DNA from transformed colonies

The colonies based on different morphology, were randomly picked up from the LB-agar plates containing *E. coli* (DH5α) cell (as outlined in Section 2.2.13) and inoculated in 10.0 mL autoclaved Luria Bertani medium containing 0.05 mg/mL of kanamycin. The inoculum was grown at 37°C, at 180 rpm for 12h in a shaking incubator. The plasmid DNA was isolated to check for positive clones by using the miniprep kit (Sigma-Aldrich, Co. LLC, USA) and following the step-wise manufacturer protocol as mentioned below:

1. The *E. coli* (DH5α) cells were taken in a fresh and sterile 2.0 mL micro-centrifuge and centrifuged at 13,000*g* and 25°C for 1 min.
2. The supernatant was discarded and the same process (step1) was repeated till entire 8.0 mL culture was harvested.
3. The resulting cell pellet was suspended in 0.2 mL resuspension solution (containing RNAse at final concentration of 0.3 mg/mL).
4. To the above mixture 0.2 mL of lysis solution was added and mixed by gently inverting the tube 4-6 times.
5. To the above mixture 0.35 mL of neutralization solution was added and mixed by gently inverting the tube 4-6 times.
6. The above mixture was centrifuged at 13,000*g*, 25°C for 10 min and a white cloudy pellet was obtained.
7. The binding column (GenElute miniprep binding column) was prepared by passing 0.5 mL column preparation solution and centrifugation at 13,000*g*, 25°C for 1 min.

8. The clear supernatant (obtained at step 6) was carefully transferred to the binding column (step 7) and centrifuged at 13,000*g* at 25°C for 1 min. The flow through accumulated in collection tube was discarded.
9. 0.75 mL of diluted wash buffer (ethanol added) was added to the binding buffer and centrifuged at 13,000*g* at 25°C for 1 min. The flow through accumulated in collection tube was disposed.
10. The empty binding column was again centrifuged at 13,000*g* at 25°C for 1 min for complete removal of any residual wash solution.
11. The binding column was transferred to a new and sterile 1.5 mL micro-centrifuge tube and 30 µL of elution solution was added to the column and incubated at 25°C for 5 min.
12. Plasmid DNA was then eluted by centrifugating the column at 13,000*g* at 25°C for 1 min.
13. The eluted plasmid was stored at -20°C for further utilization.

2.2.13 Screening of recombinant plasmids to identify positive clones through restriction digestion

The confirmation of pET-28a(+) plasmid containing the gene encoding for *Ac*Xyn30B_12 was done by restriction digestion. 15 µL of recombinant plasmid isolated (as mentioned in Section 2.2.12) was taken in a fresh and sterile 1.5 mL micro-centrifuge tube and digested using *Nhe*I and *Xho*I restriction enzymes. The reaction mixture was set up as mentioned in Table 2.9. The reaction mixture was incubation at 37°C in a water bath (Grant, Sub Aqua dual plus) for 1h. The *Nhe*I-*Xho*I digested product was analysed using 0.8% (w/v) agarose gel.

Table 2.9. Restriction Enzyme (RE) digestion set up of recombinant plasmid DNA.

RE reaction set up	**Volume (µL)**
Buffer 10X (rCutSmart Buffer-NEB)	1.2
Plasmid DNA (145 ng/µL)	5.0
*Nhe*I (10 U/µL)	1.0
*Xho*I (10 U/µL)	1.0
DNAse free water	3.8
Total	12.0

2.2.14 Preparation of *E. coli* BL-21 (DE3) competent cells

The *E. coli* BL-21 (DE3) competent cells were made by using the same procedure as outlined in Section 2.2.9. After addition of 0.1 M $CaCl_2$ solution containing 15% (v/v) glycerol to the competent cells, 0.1 mL aliquots were made in sterile 1.5 mL micro-centrifuge tubes and the tubes were stored at -80°C for further use.

2.2.15 Transformation of recombinant plasmids using *E. coli* BL-21 (DE3) cells for protein expression

The isolated recombinant plasmid DNA, 0.002 mL (as mentioned in Section 2.2.12), was transformed using 0.1 mL of *E. coli* BL-21 (DE3) competent cells (as mentioned in Section 2.2.15) for expression of *Ac*Xyn30B_12. The protocol followed for transformation was same as mentioned in Section 2.2.11. 0.1 mL of the transformed cells were spread on LB-agar medium plates containing 0.05 mg/mL kanamycin (as outlined in Section 2.2.10.1) and incubated at 37°C for 12h. The colonies based on different morphology were randomly picked from the LB-agar plates containing the grown *E. coli* BL-21 (DE3) cells and inoculated in 5 mL Luria Bertani medium containing 0.05 mg/mL (final concentration) kanamycin. The inoculum was incubated at 37°C, at 180 rpm for 12h in a shaking incubator for analysis of protein expression.

The *E. coli* BL-21 (DE3) cells harbouring the recombinant plasmid containing pET-28a(+) vector DNA and the gene encoding *Ac*Xyn30B_12 were grown in 10 mL of Luria Bertani medium containing 0.05 mg/mL kanamycin at 37°C and orbital shaking at 180 rpm, until it reached the intermediate exponential phase (OD_{550} nm=0.6). To express the recombinant enzyme *Ac*Xyn30B_12, isopropyl 1-thio-*β*-D-galactopyranoside at 1.0 mM final concentration was added to the above culture and further incubated for 16h, with orbital shaking at 180 rpm at 24°C. The induced cells were then collected by centrifuging the culture at 6000*g* at 4°C for 15 min. The cell pellets were resuspended in 0.04 mL distilled water and analysed for protein expression by SDS-PAGE using 12% (w/v) gel.

2.2.16 Analysis of recombinant protein expression by SDS-PAGE

The expression of recombinant protein, *Ac*Xyn30B_12, was examined by using Sodium dodecyl sulphate-Polyacrylamide gel electrophoresis (SDS-PAGE) using a 12% (w/v) gel. The Polyacrylamide gel was prepared by using the solutions as mentioned in Table 2.10. The SDS-PAGE was used by following the method of Laemmli, (1970) and Sambrook *et al*., (1989).

Table 2.10. Components used for resolving and stacking gels for SDS-PAGE.

Components	**Resolving gel, 12% (w/v), (µL)**	**Stacking gel, 4% (w/v), (µL)**
30% (w/v) Acrylamide solution*	4000	700
Distilled water	700	2800
10% (w/v) SDS	1000	500
50% (w/v) Glycerol	1000	--
1.5M Tris-HCl (pH 8.8)	3300	--
0.5M Tris-HCl (pH 6.8)	--	1000
10% (w/v) APS	100	50
TEMED	10	5

**30% (w/v) acrylamide solution was prepared fresh by mixing 0.8 g of bis-acrylamide and 29.2 g of acrylamide into 100 mL ultra-pure deionized water (Milli-Q water)*

The SDS-PAGE running buffer was prepared by using 1X Tris-Glycine buffer (pH 8.3), which was diluted from a 5X stock solution formulated using the components listed in Table 2.11.

Table 2.11. Components used for preparation of 5X Tris-Glycine running buffer.

Component	**Final concentration (5X)**
SDS	0.5% (w/v)
Tris-base	125 mM
Glycine	1250 mM
pH	8.3

The 5X sample loading buffer (pH 6.8) was prepared according to the composition given in Table 2.12. Protein samples were prepared by mixing 4 volumes of the protein solution with 1 volume of the 5X loading buffer to achieve a final 1X concentration of the buffer. This mixture was incubated in a boiling water bath at 100°C for 3 min. Subsequently, 20 µL of each sample was loaded into individual wells and

electrophoresis was performed at a constant current of 20 mA (equivalent to 2 mA per lane).

Table 2.12. Components used for preparation of 5X sample loading buffer.

Component	Final concentration (5X)
SDS	2.0% (w/v)
Tris-HCl	0.0625 M
Glycerol	20% (v/v)
Bromophenol blue	0.025% (w/v)
β-mercaptoethanol	5.0% (w/v)
pH	6.8

The protein staining solution was prepared by dissolving 250 mg of Coomassie Brilliant Blue R-250 dye in 50 mL of deionized water, followed by continuous stirring on a magnetic stirrer overnight to ensure complete dissolution. Subsequently, 40 mL of methanol and 10 mL of glacial acetic acid were added to this dye solution, to achieve a final solvent ratio of 5:4:1 (water: methanol: acetic acid) and a total volume of 100 mL. Protein bands were visualized by immersing the gel in this staining solution for 10 min under gentle shaking. The gels were destained by using 100 mL of destaining solution composed of methanol, glacial acetic acid and distilled water in the same ratio (5:1:4) and subjecting to gentle shaking until protein bands were clearly visible.

2.2.17 Determination of optimum IPTG concentration and temperature

The optimum concentration of IPTG for the expression of the recombinant protein *Ac*Xyn30B_12 using *E. coli* BL-21 (DE3) cells was determined by inducing the cells grown in 10 mL LB medium (supplemented with 0.05 mg/ml kanamycin) by 0.2 mM, 0.5 mM or1.0 mM IPTG concentration and incubated at optimum induction

temperature of 24°C for 16h. The expression level of *Ac*Xyn30B_12 was evaluated by incubating the cells grown in 10 mL LB medium (supplemented with 0.05 mg/ml kanamycin) at different temperatures, 16°C, 24°C and 37°C for 16h by using the optimum, final IPTG concentration of 1.0 mM. The expression levels of *Ac*Xyn30B_12 under each condition was analysed by SDS-PAGE using a 12% (w/v) gel.

2.3 Results and Discussion

2.3.1 Sequence analysis of *Ac*Xyn30B_12

The gene sequence of *Ac*Xyn30B_12 was retrieved from NCBI database. The conserved structural domain for *Ac*Xyn30B_12 was determined using NCBI Conserved Domains Database and the molecular architecture was developed using DOG 2.0 software (as shown in Fig 2.1). The full-length gene encoding *Ac*Xyn30B_12 contains a total of 673 amino acid residues with an N-terminal signal peptide (residues 1-27, in pink color), followed by a catalytic module, Xyn30Bc (residues 29-440, in cyan color) a family 6 carbohydrate binding module, CBM6 (residues 471-592, in green color) and a C-terminal Type I dockerin domain, DocI (residues 606-671, in purple color) and 2 amino acid residues at the C-terminal (residues 672-673, in silver color) as shown in Fig. 2.1. The N-terminal signal peptide and the GH30 catalytic module are separated by one amino acid residue (alanine, A28). There are two unknown modules containing the amino acid residues 441-470 (between Xyn30Bc and CBM6) and 593-605 (between CBM6 and DocI) shown in silver color (Fig. 2.1). The full-length gene encoding the Xyn30Bc catalytic module, CBM6 and DocI without the signal peptide was cloned in the pET-28a(+) vector. The full-length cloned gene expressing the mature protein, *Ac*Xyn30B_12 comprised 653 amino acids containing the pET-28a(+) vector sequence at N-terminal (residues 1-8) containing the His6 tag in yellow color followed by Xyn30Bc catalytic module (residues 9-412), CBM6 (residues 451-572), DocI (residues 587-651) and 2 amino acid residues at the C-terminal (residues 652-653) as shown in Fig. 2.1.

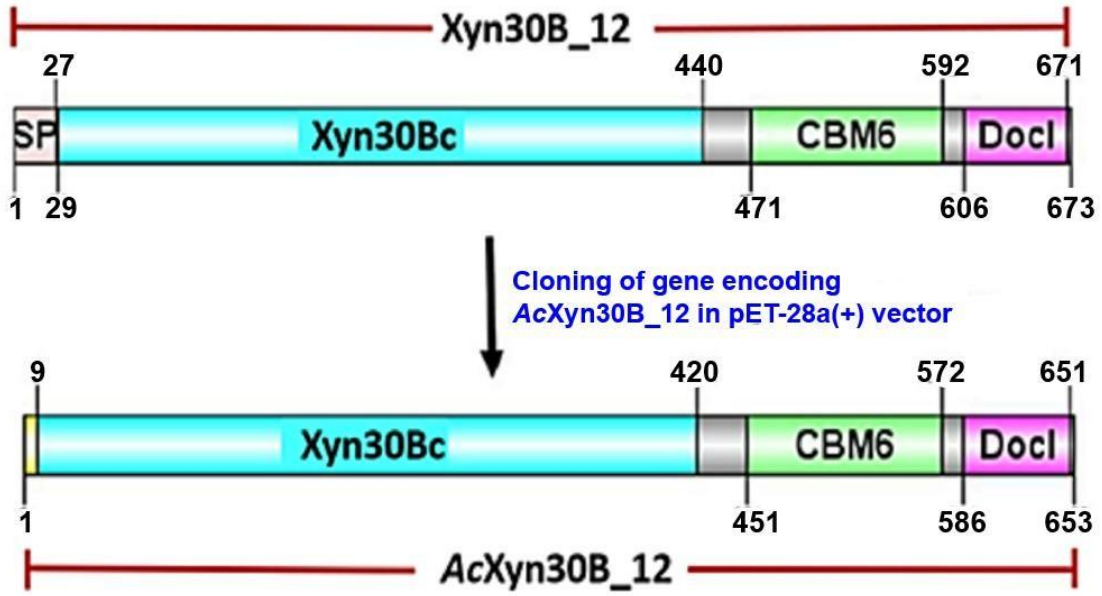

Fig. 2.1. Molecular architecture of *Ac*Xyn30B_12, developed by using DOG 2.0 software.

2.3.2 PCR amplification of *Ac*Xyn30B_12

The PCR amplified gene encoding the protein, *Ac*Xyn30B_12 (1900 bp) from the genomic DNA of the thermophilic organism, *Acetivibrio clariflavus* DSM 19732 (by following steps as mentioned in Section 2.2.2) was analysed using 1.0% w/v agarose gel as shown in Fig 2.2. The PCR amplified product displayed a band of size ~1.9 kb (Fig 2.2, Lane1). This band of amplified product was extracted and purified by following the procedure as outlined in Section 2.2.4.

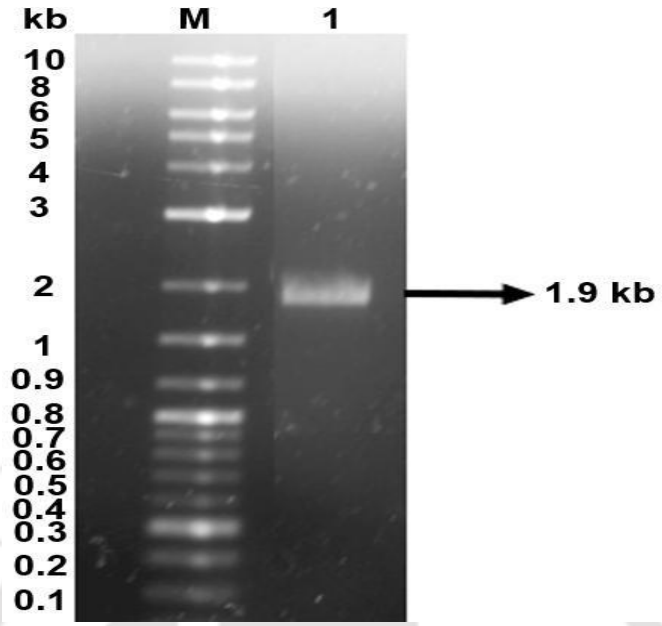

Fig. 2.2. Agarose gel electrophoresis (0.8%, w/v) showing, Lane M: DNA ladder (Genei, India) and Lane 1: PCR amplified product of gene encoding *Ac*Xyn30B_12.

2.3.3 Cloning of gene encoding *Ac*Xyn30B_12 into pET-28a(+) expression vector

The PCR amplified gene encoding *Ac*Xyn30B_12 and pET-28a(+) vector were double digested using restriction enzymes, *Nhe*I and *Xho*I (as mentioned in Section and respectively). Both the digested products were analysed using 0.8% (w/v) gel followed by extraction (as mentioned in Section 2.2.4). The extracted digested products were further subjected to ligation by following the procedure as outlined in Section 2.2.8. The above ligated product was transformed using *E. coli* DH5α competent cells. These cells were grown overnight on LB plates (supplemented with 0.05mg/mL kanamycin) at 37°C. The transformation efficiency of *E. coli* DH5 competent cells was found to be $1.5x10^5$ cfu/µg.

2.3.3.1. Isolation of recombinant DNA and screening of positive clones

The recombinant plasmid DNA from the grown colonies (as mentioned in Section 2.3.3) were isolated by utilizing the plasmid miniprep kit (Section 2.2.12). The isolated recombinant plasmid was further double digested using the restriction

enzymes, *Nhe*I-*Xho*I. Both the digested and undigested recombinant plasmid were analysed using 0.8% (w/v) to confirm positive clone (as shown in Fig. 2.3A, Lane1). The digested plasmid showed two bands, one with band equal to the size of pET-28a(+) vector (5.3 kb) and another with band equal to size of *Ac*Xyn30B_12 (1.9 kb). The undigested plasmid showed only one single band of 7.2 kb (as shown in Fig. 2.3B, Lane1).

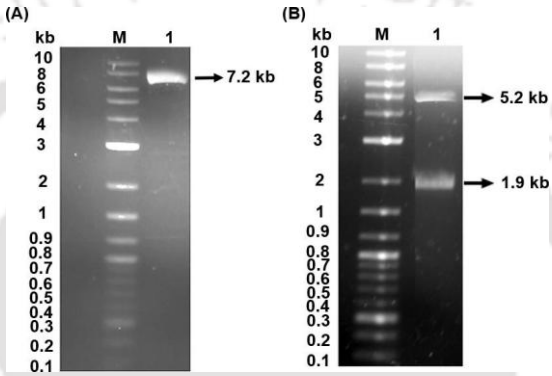

Fig. 2.3. Agarose gel electrophoresis (0.8%, w/v) showing **(A)** Lane M: DNA ladder (GeNei, India) and Lane 1: Undigested recombinant plasmid pET-28a(+). **(B)** Lane M: DNA ladder (GeNei, India) and Lane 1: *Nhe*I-*Xho*I digested fragments at 5.3 kb of vector pET-28a(+) and at 1.9 kb of gene encoding *Ac*Xyn30B_12 (insert).

The positive colonies were screened through sequencing (1st base Laboratories, Sanger sequencing services, Selangor, Malaysia) and no mutation was detected (as shown in Fig 2.4A and B). The absence of any mutation was verified by analyzing the sequence of the cloned gene encoding *Ac*Xyn30B_12 (obtained from sequencing) by aligning with the genomic sequence of *A. clariflavus* (CP003065.1) encoding the identical endo-xylanase by using Clustal Omega. By comparing the two sequence it was clearly observed that there is no mutation in the cloned gene (as shown in Fig. 2.4C).

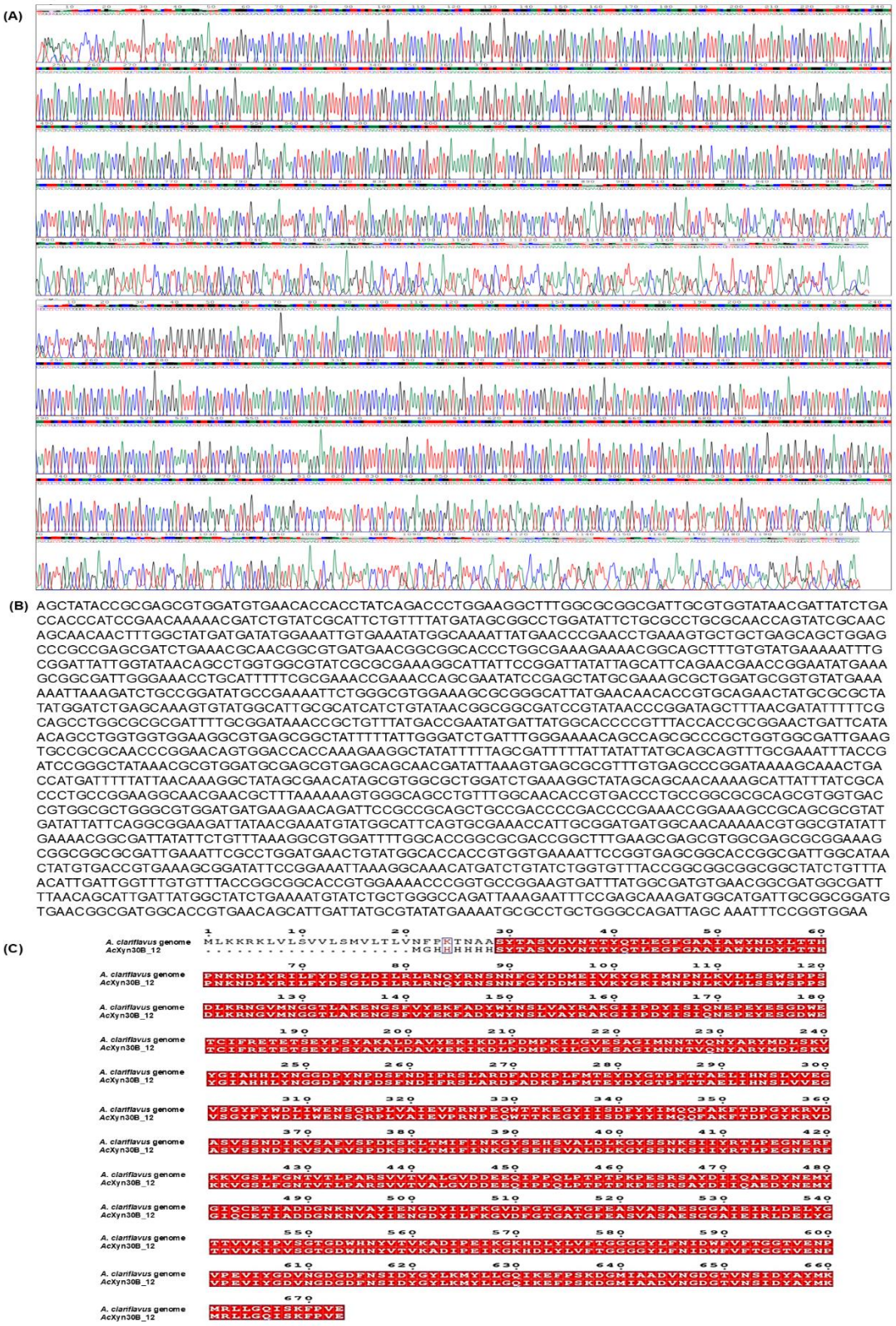

Fig. 2.4. DNA sequencing results of the gene encoding *Ac*Xyn30B_12 by using T7 promoter primers. **(A)** Electropherogram of DNA sequencing results for cloned gene encoding *Ac*Xyn30B_12 visualised by Chromas 2.6.6 software and **(B)** Sequence of *Ac*Xyn30B_12. **(C)** Multiple sequence alignment of cloned *Ac*Xyn30B_12 sequence with genome sequence of *A. clariflavus*.

2.3.4 Expression of recombinant protein *Ac*Xyn30B_12

The *E. coli* BL-21 (DE3) cells harbouring the recombinant plasmid were analysed for expression of protein *Ac*Xyn30B_12 after induction with 1.0 mM IPTG (as mentioned in Section 2.2.15) grown at 24°C. The expressed *Ac*Xyn30B_12 was analysed using SDS-PAGE in 12% (w/v) gel and a protein band at ~74 kDa (as shown in Fig 2.5) was found, which was in agreement with the theoretical molecular mass (75 kDa) by Protparam ExPASy server.

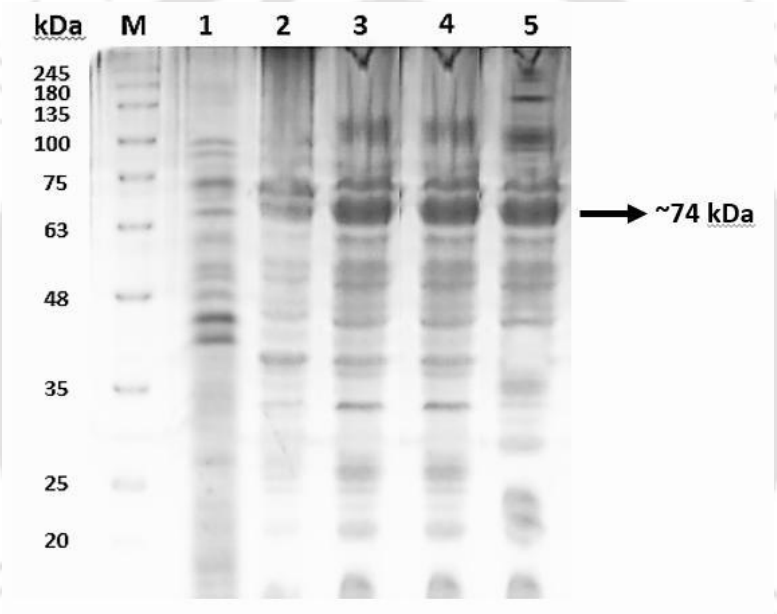

Fig. 2.5. Expression analysis of recombinant *Ac*Xyn30B_12 by SDS-PAGE using 12% (w/v) gel. Lanes M: Pre-stained protein ladder, 1: uninduced *E. coli* BL21 (DE3) cells, induced *E. coli* BL21 (DE3) cells (with 1.0 mM IPTG and grown at 24°C) from different colonies, 2: colony 1, 3: colony 2, 4: colony 3 and 5: colony 4.

2.3.5 Optimization of IPTG concentration for expression of *Ac*Xyn30B_12

The *E. coli* BL21 (DE3) cells containing the recombinant plasmid exhibited differential expression levels of *Ac*Xyn30B_12 upon induction with varying IPTG concentrations (0.2 mM, 0.5 mM and 1.0 mM) at the optimum incubation temperature of 24°C (Section 2.3.6) grown for 16h. The induction with 1.0 mM IPTG (Fig. 2.6, Lane

3) resulted in higher expression of *Ac*Xyn30B_12 as compared with 0.2 mM (Fig. 2.6, Lane 1) or 0.5 mM IPTG (Fig. 2.6, Lane 2). Therefore, 1.0 mM IPTG was determined to be the optimal concentration for recombinant protein expression and was used in all subsequent experiments.

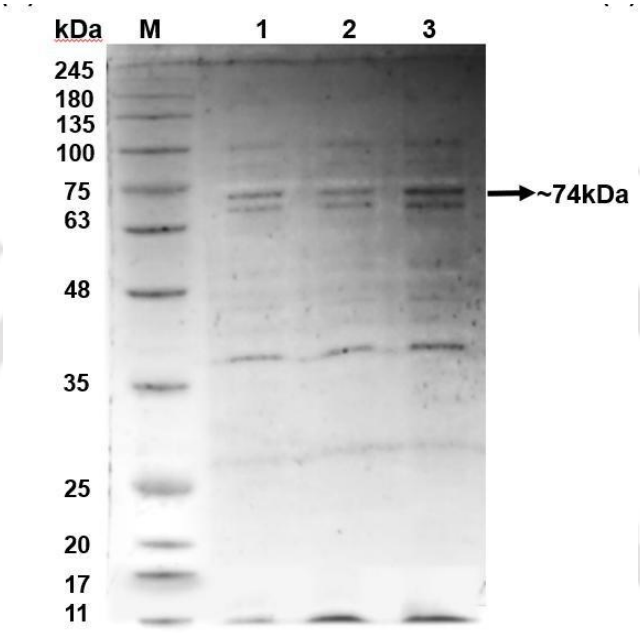

Fig. 2.6. Expression analysis of *Ac*Xyn30B_12 at different IPTG concentrations by SDS-PAGE using 12% (w/v) gel. Lanes M: Pre-stained protein ladder, induced *Ac*Xyn30B_12 by, 1: 0.2 mM IPTG, 2: 0.5 mM IPTG and 3: 1.0 mM IPTG.

2.3.6 Optimization of temperature for expression of *Ac*Xyn30B_12

The *E. coli* BL21 (DE3) cells harbouring the recombinant plasmid exhibited differential expression levels of *Ac*Xyn30B_12 at varying induction temperatures (16°C, 24°C and 37°C) using the optimal IPTG concentration of 1.0 mM (Section 2.3.5) grown for 16h. Induction at 24°C (Fig. 2.7, Lane 2) and 37°C (Fig. 2.7, Lane 3) resulted in comparable and higher expression levels as compared with induction at 16°C (Fig. 2.7, Lane 1). Based on these results, 24°C was selected as the optimal temperature for expression of *Ac*Xyn30B_12 and was used in all subsequent experiments.

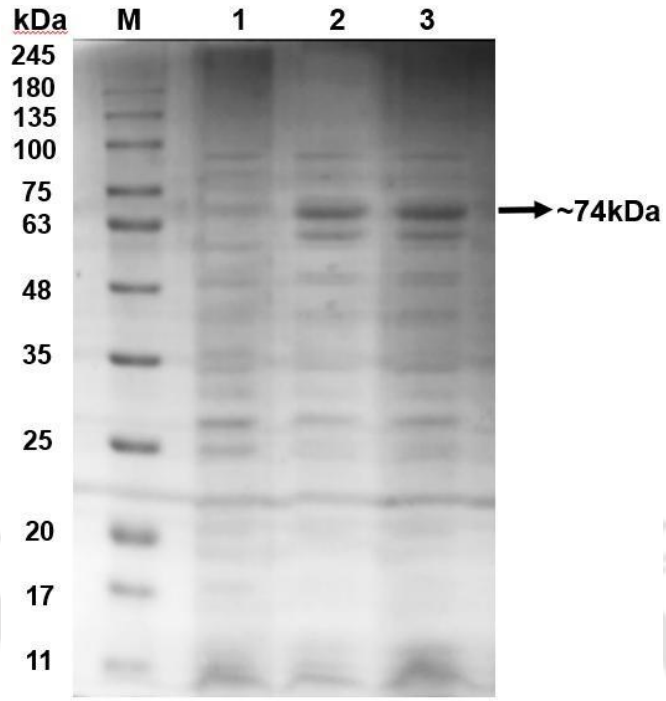

Fig. 2.7. Expression analysis of *Ac*Xyn30B_12 at different induction temperatures by SDS-PAGE using 12% (w/v) gel. Lanes M: Pre-stained protein ladder, expression of *Ac*Xyn30B_12 by 1.0 mM IPTG at temperatures, 1: 16°C, 2: 24°C and 3: 37°C.

2.4. Conclusion

The gene encoding *Ac*Xyn30B_12 enzyme, a member of glycoside hydrolase family 30 from *Acetivibrio clariflavus* DSM 19732 (GenBank accession no. AEV69300.1), was cloned, expressed and purified. Molecular architecture revealed that the full-length gene encoding *Ac*Xyn30B_12 contains a total of 673 amino acid residues and an N-terminal signal peptide, followed by a catalytic module, Xyn30Bc, CBM6 a C-terminal Type I dockerin domain, DocI. PCR amplification of the gene yielded a product approximately, 1.9kb in size. The amplified fragment was digested with restriction enzymes (*Nhe*I-*Xho*I) and ligated to the linearized pET-28a(+) expression vector. Upon transformation of ligated product using *E. coli* DH5α competent cells, positive clones harbouring the recombinant plasmid were verified *via* restriction digestion using enzymes, *Nhe*I and *Xho*I, which produced DNA bands of ~5.3 kb (vector) and ~1.9 kb (insert) as analysed by agarose gel electrophoresis analysis. The confirmed recombinant plasmid was subsequently introduced into *E. coli* BL21 (DE3) cells for protein expression. The recombinant *Ac*Xyn30B_12 protein was expressed showing a band corresponding to molecular size, ~74 kDa as confirmed by SDS-PAGE analysis, which was corroborated with its theoretically known molecular mass (75 kDa). The optimum concentration of IPTG for expression of *Ac*Xyn30B_12 obtained was 1.0 mM and the optimum induction temperature determined for protein expression was 24°C.

2.5. References

Bhardwaj, N., Kumar, B., & Verma, P. (2019). A detailed overview of xylanases: an emerging biomolecule for current and future prospective. Bioresources and Bioprocessing, 6(1), 1-36.

Biely, P., Singh, S., & Puchart, V. (2016). Towards enzymatic breakdown of complex plant xylan structures: state of the art. Biotechnology Advances, 34(7), 1260-1274.

Devi, A., Bajar, S., Kour, H., Kothari, R., Pant, D., & Singh, A. (2022). Lignocellulosic biomass valorization for bioethanol production: a circular bioeconomy approach. Bioenergy Research, 15(4), 1820-1841.

Engler, M.J., Richardson, D.C. (1982) DNA ligases. The Enzymes, (ed. Boyer P. D), Academic Press, San Diego, 15, 3-30.

J.A. Izquierdo, L. Goodwin, K.W. Davenport, H. Teshima, D. Bruce, C. Detter, R. Tapia, S. Han, M. Land, L. Hauser and C.D Jeffries (2012) Complete genome sequence of *Clostridium clariflavum* DSM 19732. Standards in Genomic Sciences. 6, 104–115.

Laemmli, U.K. (1970) Cleavage of structural proteins during the assembly of the head of bacteriophage T4. Nature, 227, 680-685.

L. Santibanez, C. Henríquez, R. Corro-Tejeda, S. Bernal, B. Armijo, O. Salazar. (2021). Xylooligosaccharides from lignocellulosic biomass: a comprehensive review. Carbohydrate Polymers. 251, 117118.

Malgas, S., Mafa, M. S., Mkabayi, L., & Pletschke, B. I. (2019). A mini review of xylanolytic enzymes with regards to their synergistic interactions during hetero-xylan degradation. World Journal of Microbiology and Biotechnology, 35(12), 187.

M.M. Bradford. (1976). A rapid and sensitive method for the quantitation of microgram quantities of protein utilizing the principle of protein-dye binding. Anal. Biochem. 72 (1–2), 248–254.

Qaseem, M. F., Shaheen, H., & Wu, A. M. (2021). Cell wall hemicellulose for sustainable industrial utilization. Renewable and Sustainable Energy Reviews, 144, 110996.

Ren, J., Wen, L., Gao, X., Jin, C., Xue, Y. and Yao, X (2009). DOG 1.0: illustrator of protein domain structures. Cell research, 19(2), pp.271-273.

S. Lu, J. Wang, F. Chitsaz, M.K. Derbyshire, R.C. Geer, N.R. Gonzales, M. Gwadz, D.I. Hurtwitz, G.H. Marchler, J.S. Song and N. Thanki (2020). CDD/ SPARCLE: the conserved domain database in 2020, Nucleic Acids Res. 48, 265–268.

Sambrook, J., Russel, D.W (2001) In (3rd ed.) Molecular Cloning. A Laboratory Manual, Vol. 1. Cold Spring Harbor Laboratory Press, Woodbury, New York.

Sambrook, J., Fritsch, E.F., Maniatis, T. (1989) In (2nd ed.) Molecular Cloning. A Laboratory Manual, Vol. 1. Plainview, Cold Spring Harbor Laboratory Press, Woodbury, New York.

Studier, F.W., Moffatt, B.A. (1986) Use of bacteriophage T7 RNA polymerase to direct high-level expression of cloned genes. Journal of Molecular Biology, 189, 113-130.

Studier, F.W., Rosenberg, A.H., Dunn, J.J., Dubendorff, JW. (1990) Use of T7 RNA polymerase to direct expression of cloned genes. Methods in Enzymology, 185, 60-89.

Šuchová, K., Fehér, C., Ravn, J. L., Bedő, S., Biely, P., & Geijer, C. (2022). Cellulose- and xylandegrading yeasts: Enzymes, applications and biotechnological potential. Biotechnology Advances, 59, 107981.

Chapter 3

Purification, biochemical and functional characterization of endo-*β*-1,4-xylanase (*Ac*Xyn30B_12) from *Acetivibrio clariflavus* DSM 19732

3.1. Introduction

Xylan, a predominant constituent of hemicellulose, is a heterogeneous polysaccharide composed of a *β*-1,4-linked xylose backbone with branching substitutions of α-L-arabinofuranosyl residues (substituted at carbon 2 and/or 3 by *α*-(1→2) or *α*-(1→3) linkage), α-D-glucuronic acid and its 4-*O*-methyl derivative (substituted at carbon 2 by *α*-(1→2) linkage) or acetyl groups (Collins *et al*., 2005). Xylan degradation plays an important role in the efficient utilization of lignocellulosic biomass (LCB) for various biotechnological applications. The enzyme, endo-*β*-1,4-xylanase catalyses the cleavage of internal *β*-1,4 linkages in the xylan main chain, leading to the release of xylo-oligosaccharides (XOS), which have potential applications such as prebiotics and bioactive compounds (Santibanez *et al*., 2021). Till date, in glycoside hydrolase family 30 (GH30) a total of 139 bacterial endo-xylanases have been biochemically, structurally and functionally characterized. A bacterial endo-xylanase Xyn30D of GH30 family from *Paenibacillus barcinonensis* showed highest activity of 30 U/mg against beechwood xylan at pH 6.5 and 60°C (Valenzuela *et al*., 2012).

Another endo-xylanase, *Cp*Xyn30A of GH30_8 family from *Clostridium papyrosolvens* showed activity of 17 U/mg against wheat arabinoxylan xylan under optimum conditions of pH 4.5 and 30°C (St. John *et al*., 2014). An endo-xylanase, *Ca*Xyn30A of GH30_8 family from *Clostridium acetobutylicum* displayed activity of 113 U/mg against wheat arabinoxylan at pH 6.0 and 50°C (St. John *et al*., 2018). A fungal endo-xylanase, *Tc*Xyn30C of GH30_7 family from *Talaromyces cellulolyticus* showed highest activity of 47 U/mg against wheat arabinoxylan at pH 4.0 and 55°C (Nakamichi *et al*., 2019).

Although endo-xylanases contribute significantly to xylan degradation, their action alone is not sufficient for complete xylan depolymerization. Synergistic activity between endo-xylanase and other xylan-degrading enzymes, such as xylobiohydrolases, enhances hydrolysis efficiency. Xylobiohydrolases act on the non-reducing ends of xylan chains to release xylobiose, working synergistically with endo-xylanases which cleave internal bonds in the xylan backbone. The GH30 family xylobiohydrolase *Ac*GH30A from *Acetivibrio clariflavus* exhibited its maximum residual activity (136 U/mg) toward 4-*O*-methyl glucuronoxylan at pH 7.0 and 80°C (Singh *et al*., 2024).

This present study focuses on the purification, biochemical and functional characterization of the endo-*β*-1,4-xylanase of family 30 Glycoside hydrolase (*Ac*Xyn30B_12) from *Acetivibrio clariflavus* DSM 19732. *Ac*Xyn30B_12 was purified using immobilised metal-ion affinity chromatography followed by size exclusion chromatography. The enzyme activity as well as substrate specificity of *Ac*Xyn30B_12 were determined against range of substrates. The different biochemical properties such as pH optimum, temperature optimum, pH stability, thermal stability, half-life ($t_{1/2}$) and melting temperature (T_m) of *Ac*Xyn30B_12 were investigated. The kinetic parameters

and effect of different metal ions and other chemical reagents on activity of endo-*β*-1,4-xylanase (*Ac*Xyn30B_12) were also analysed. The time dependent hydrolysed products of partially acetylated birchwood xylan (PABX) by *Ac*Xyn30B_12 was analysed using TLC, HPLC and MALDI-TOF-MS to determine both its endo- and exo-acting mode of cleavage. The synergistic interaction between endo-xylanase, *Ac*Xyn30B_12 and xylobiohydrolase, *Ac*GH30A was investigated against different xylan substrates. Additionally, TLC analysis of hydrolysis products and total reducing sugar quantification were performed for various pretreated biomasses hydrolysed by *Ac*Xyn30B_12.

3.2. Materials and Methods

3.2.1. Substrates and chemicals

The reagents used for estimation of reducing sugar on hydrolysis of various xylan substrates by *Ac*Xyn30B_12 by using method of Nelson [1944] and Somogyi [1945], *viz*. sodium bicarbonate, sodium sulphate anhydrous and ammonium molybdate were procured from Himedia Laboratories Pvt. Ltd., India. Sodium carbonate acquired from Merck, India. Sodium potassium tartarate and sulphuric acid were acquired from SRL India Pvt. Ltd and cupric sulphate acquired from Qualigens, Thermo Fisher Scientific, India. The substrates, *viz.* 4-*O*-methylglucuronoxylan, oat spelt xylan, curdlan and carboxy methyl cellulose sodium salt (CMC-Na) were procured from Sigma-Aldrich, USA. Partially acetylated birchwood xylan, beechwood xylan, wheat arabinoxylan (insoluble and low viscosity), rye arabinoxylan, larchwood xylan, rhamnogalacturonan (bean and potato pectic fibre), pecticgalactan (lupin), carob-galactomannan, galactan (potato), arabinogalactan, arabinan (sugarbeet) and 4-Nitrophenyl-β-D-xylopyranoside were purchased from Megazyme Ltd., Ireland. Xylan (M.w. 20–30kDa) and corn cob xylan were acquired from Carbosynth Ltd., UK. The sypro orange dye used for protein melting analysis was procured from Merck, Darmstadt, Germany. Salts of metal ions, *viz*. Ni^{+2}, Cu^{+2}, Co^{+2}, Ca^{+2}, Mg^{+2}, K^{+}, Na^{+} and Li^{+} and chemical reagents, *viz*. sodium dodecyl sulphate (SDS), ethylene diamine tetra acetic acid (EDTA), ethylene glycol-bis (β-aminoethyl ether)-N,N,N',N'-tetraacetic acid (EGTA), urea and guanidine hydrochloride (GnHCl) were acquired from Himedia Laboratories Pvt. Ltd., India. The standards used for TLC analysis *viz.* xylopentaose, xylotetraose, xylotriose, xylobiose and D-xylose were obtained from Megazyme Ltd., Ireland. The TLC silica gel plate was procured from Merck, Darmstadt, Germany. The

chemicals used for preparing TLC solvent, *viz*. chloroform was procured from Himedia Laboratories Pvt. Ltd., India and acetic acid glacial was procured from SRL, Pvt. Ltd., India. The chemicals required for TLC dye preparation, *viz*. diphenylamine, aniline and ethyl acetate were procured from Merck, India and phosphoric acid and hydrochloric acid were acquired from Finar LTD., India. For preparing matrix for MALDI-TOF-MS analysis, 2,5-dihydroxybenzoic acid (DHB) was acquired from Sigma-Aldrich, USA. The chemicals used for pretreatment of biomasses, *viz*. sodium hydroxide was acquired from Himedia Laboratories Pvt. Ltd., India and hydrogen peroxide was acquired from Finar LTD., India.

3.2.2. Purification of *Ac*Xyn30B_12

The *E. coli* BL-21 (DE3) cells were used for transformation of the recombinant plasmid containing pET-28a(+) vector DNA and the inserted gene encoding *Ac*Xyn30B_12. The *E. coli* BL21 cells were grown in 200 mL of Luria Bertani medium containing 0.05 mg/mL kanamycin at 37°C and orbital shaking at 180 rpm, until it reached the intermediate exponential phase (OD_{550} nm=0.6). To express the recombinant enzyme *Ac*Xyn30B_12, isopropyl-1-thio-*β*-D-galactopyranoside at 1 mM final concentration was added to the above culture and further incubated for 16h, with and orbital shaking at 180 rpm at 24°C. The induced cells were then collected by centrifuging the culture at 6000g at 4°C for 15 min. The cell pellet was resuspended in 5 mL of resuspension buffer (0.05 M sodium phosphate buffer, pH 7.5, 0.05 M imidazole, 0.3 M NaCl) and sonicated (Sonication cycle: 2 s of on and 8 s of off) for 30 min using a Sonics Vibra cell, USA. The sonicated cell suspension was subjected to centrifugation at 11,000*g* and 4°C for 1h. The supernatant obtained after centrifugation was filtered using a PVDF membrane (pore size 0.45 μm) using a syringe filter and with

the help of a peristaltic pump (GE Healthcare, P1) loaded onto a 1.0 mL HiTrap Chelating HP prepacked column (GE Healthcare, USA) charged with 100 mM Ni^{2+} ions for recombinant protein purification by immobilized metal-ion affinity chromatography (IMAC). The protein bound to the column was extensively washed with 25 mL of 0.05 M sodium phosphate buffer, pH 7.5 containing 0.05 M imidazole and 0.3 M NaCl. The bound protein, *Ac*Xyn30B_12 was eluted with 5 mL of elution buffer (0.05 M sodium phosphate buffer, pH 7.5, 0.3 M imidazole, 0.3 M NaCl), in 1.0 mL fractions. The enzyme eluted in different fractions was pooled and dialyzed against 3 L of dialysis buffer (0.05 M sodium phosphate buffer, pH 7.5) for removal of salt and imidazole. This dialysed enzyme sample was kept for SDS-PAGE analysis and protein concentration determination. The dialysed sample (4 mL) was loaded into a 120 mL XK (L x I.D. 60 cm × 16 mm) HiLoad 16/600 Superdex 75 pg prep grade prepacked size exclusion chromatography (SEC) column connected to Fast Protein Liquid Chromatography, FPLC system (AKTA prime plus, GE Healthcare, USA), for further purification. The column pressure (0.5 MPa) and flow rate (1 mL/min) were kept constant throughout the experiment. The enzyme was eluted by 0.05 M sodium phosphate buffer, pH 7.5 in 1.5 mL fractions. The purity of both the IMAC and SEC purified enzyme, was determined by sodium dodecyl sulphate-polyacrylamide gel electrophoresis (SDS-PAGE) analysis by using a 12% (w/v) gel. The gel was run at 2 mA per lane and stained with Coomassie Brilliant Blue R-250 (Neuhoff *et al*., 1988). The fractions containing only a single protein band at ~74 kDa were pooled and utilized for protein concentration determination and enzyme assays.

3.2.3. Protein estimation of purified *Ac*Xyn30B_12 using Bradford and UV method

The concentration of crude and purified *Ac*Xyn30B_12 was measured by Bradford's method (Bradford 1976). Before estimation of protein concentration, a standard plot of Bovine serum albumin (BSA) in the range 10-100 µg/mL was prepared. The protein estimation was done at 595 nm and the following formula was used:

$$\text{Concentration of protein (mg/mL)} = \frac{\Delta A_{595} \text{ x V x C}}{\text{v}}$$

Where,

ΔA_{595} = Change in absorbance of the protein sample

V = Volume of reaction mixture (mL)

C = 1 OD equivalent of Bovine serum albumin standard plot (mg/mL)

v = Volume of enzyme for the assay (mL)

Concentration of purified *Ac*Xyn30B_12 was also measured by UV method using a UV-Vis spectrophotometer (Thermo Fisher Scientific, USA). Molar extinction coefficient, Ɛ = 1,22,635 M^{-1} cm^{-1} of *Ac*Xyn30B_12 computed from the amino acid sequence by using Protparam ExPASy server (http://web.expasy.org/protparam/) was utilized for the estimation. The measurement of absorbance was conducted at 280 nm and the following formula was used for the calculation (Layne, 1957; Stoscheck, 1990):

$$\text{Concentration of protein (mg/mL)} = \frac{\text{Absorbance}_{280} \text{ x Molecular weight of protein (Da)}}{\text{Extinction coefiicient } (M^{-1}cm^{-1}) \text{ x Path length (1cm)}}$$

3.2.4. Enzyme activity assay for *Ac*Xyn30B_12

3.2.4.1. Estimation of reducing sugar

The enzyme activity was assayed in microcentrifuge tube using total reaction volume of 0.1 mL that contained final substrate concentration of 1.0% (w/v) in 0.09 mL of 0.05 M citrate phosphate buffer (pH 5.5) mixed with 0.01 mL of 0.05 mg/mL *Ac*Xyn30B_12 The reaction mixture was incubated at 70°C (optimum temperature) and for 4 min (optimum reaction time). For control, only substrate with without enzyme was

incubated under same conditions. All the assays were done in triplicates. The *Ac*Xyn30B_12 enzyme activity was calculated by measuring the released reducing sugar by protocols of Nelson [1944] and Somogyi [1945] using D- xylose as standard. For estimation of the reducing sugars following reagents were prepared:

Reagent A (Alkaline tartarate reagent)

Sodium carbonate anhydrous (Na_2CO_3)	3.75 g
Sodium potassium tartarate ($KNaC_4H_4O_6.4H_2O$)	3.75 g
Sodium bicarbonate ($NaHCO_3$)	3.0 g
Sodium sulphate anhydrous (Na_2SO_4)	30 g

All the above reagents were dissolve in 80 mL Milli-Q water and the final volume was adjusted to 150 mL. The solution was further filtered using a 0.45 µm membrane (Axiva Pvt., India) fitted in a filtration unit connected to a vacuum pump and subsequently stored at 25°C.

Reagent B (Copper reagent)

The copper reagent (reagent B) was prepared by dissolving 22.5 g of copper sulphate ($CuSO_4$) in 80 mL of water followed by the addition of two drops of concentrated sulphuric acid (H_2SO_4). The final volume was adjusted to 150 mL by Milli-Q water and then filtered through a 0.45 µm membrane (Axiva Pvt., India) fitted in a filtration unit connected to a vacuum pump and subsequently stored at 25°C.

Reagent C (Arsenomolybdate reagent)

The arsenomolybdate reagent (reagent C) was prepared in dark colour glass bottle. First of all 7.5 g of ammonium molybdate tetrahydrate [$(NH_4)_6Mo_7O_{24}.4H_2O$] was added to 135 mL of Milli-Q water taken in a 250 mL beaker and 6.3 mL of concentrated sulphuric acid (H_2SO_4) was added to it. In another, beaker 0.9 g of sodium

arsenate was added in 7.5 mL Milli-Q water and this solution was slowly added to ammonium molybdate solution. This solution (total volume ~150mL) was filtered using a 0.45 µm membrane (Axiva Pvt., India) fitted in a filtration unit connected to a vacuum pump and subsequently incubated in 37°C for 48h prior to use.

Reagent D

Reagent D was prepared by mixing Reagent A and reagent B in the ratio 25:1. For every enzyme assay fresh reagent D was prepared.

3.2.4.2. Determination of one OD equivalent from the standard plot of D-xylose

The standard plot of D-xylose was prepared at varying concentration in the range, 10-210 µg/mL. Each of the concentration (in 100 µL volume taken in 1.5 mL micro centrifuge tube) was prepared from a stock of 1 mg/mL (1 mL volume) of D-xylose dissolved in 50 mM sodium phosphate buffer, pH 7.5. For blank, 50 mM sodium phosphate buffer, pH 7.5 without D-xylose was used. To each of the concentration, 100 µL of reagent D (Section 3.2.3.1) was added and each tube was incubated in a boiling water bath at 100°C for 20 min. The tubes were cooled down at 25°C and 100 µL of reagent C (Section 3.2.3.1) was added. Then 700 µL of Milli-Q water was added to each tube to make final volume of 1 mL. An aliquot of 200 µL from each tube was loaded in 96-well plate (Tarsons Ltd., India) and the absorbance at 500 nm wavelength (A_{500}) was measured using a UV-Visible spectrophotometer (Thermo Fisher Scientific, USA). The standard plot of A_{500} vs D-xylose concentration (µg/mL) was generated and the one OD equivalent of D-xylose was calculated from it.

3.2.4.3. Calculation of enzyme activity of *Ac*Xyn30B_12

The enzyme activity (EA) of the enzyme, endo-*β*-1,4-xylanase (*Ac*Xyn30B_12) was expressed as U/mL and the specific activity as U/mg of protein. One unit (U) of

*Ac*Xyn30B_12 specific activity is defined as the µmole of xylose produced from xylan per minute per milligram of the enzyme (µmol/min/mg) under optimum conditions. The enzyme activity (EA) of *Ac*Xyn30B_12 was calculated using the equation given below:

$$EA(U/mL) = \frac{A_{500} \text{ x } C \text{ x } V}{M_{Wxyl} \text{ x } t \text{ x } v}$$

Where,

A_{500} = Change in absorbance of reaction sample at 500 nm

C = 1 OD equivalent from D-xylose standard plot

V = Total volume of reaction mixture (in mL)

t = Time of reaction (in min)

MW_{xyl} = Molecular mass of xylose (150 g/mol)

v = Volume of enzyme taken in reaction (in mL)

The specific activity (SA) of *Ac*Xyn30B_12 was calculated using the equation given below:

$$SA(U/mg) = \frac{EA\ (U/mL)}{\text{Concentration of protein } (mg/mL)}$$

3.2.4.4. Substrate specificity of *Ac*Xyn30B_12 against natural and synthetic substrates

The enzyme, endo-*β*-1,4-xylanase (*Ac*Xyn30B_12) was assayed against different commercial xylan substrates *viz.* partially acetylated birchwood xylan (PABX), corn cob xylan, xylan from Carbosynth (Mw. 20,000-30,000), oat spelt xylan, 4-*O*-methylglucuronoxylan, larchwood xylan, beechwood xylan, rye and wheat arabinoxylan (low viscosity and insoluble) and also against cellulose based and mannan based substrates to confirm its mode of action and substrate preference and efficiency. The enzyme activity of *Ac*Xyn30B_12 was also assayed against different in-house isolated xylan substrates *viz.* acacia saw dust xylan (Sharma, Khaire*et al*., 2020, Sharma, Morla

et al., 2020), neem saw dust xylan (Sharma, Khaire *et al*., 2020, Sharma, Morla *et al*., 2020), sugarcane top xylan (SCT), water hyacinth xylan and banana stem xylan (Khaire *et al*., 2021) and alkaline pretreated sugarcane top xylan, apSCT (Khaire *et al*., 2022). The enzyme activity was determined by taking the substrate at a final concentration of 1.0% (w/v) in 0.09 mL of 0.05 M citrate phosphate buffer (pH 5.5) and 0.01 mL of 0.05 mg/mL *Ac*Xyn30B_12 in a total reaction volume of 0.1 mL. The reaction mixture was incubated at 70°C, the optimum temperature and for 4 min, the optimum reaction time. The *Ac*Xyn30B_12 enzyme activity was calculated by measuring the released reducing sugar by protocols of Nelson [1944] and Somogyi [1945] using D-xylose as standard. *Ac*Xyn30B_12 was also assayed against the synthetic substrate the method reported earlier Thakur *et al*. (2020). For this assay, 4 mM of 4-Nitrophenyl-*β*-D-xylopyranoside in 0.48 mL of 0.05 M citrate phosphate buffer (pH 5.5) was hydrolysed using 0.02 mL of enzyme (50 µg/mL) in a total reaction volume of 0.5 mL, at 70°C for 20 min. The reaction was stopped by adding 0.5 mL of

0.5 M Na_2CO_3 solution and the produced *p*-nitrophenol (pNP) was estimated at 410 nm (A_{410}) by using a UV-Visible spectrophotometer (Thermo Fisher Scientific, USA). All the assays of *Ac*Xyn30B_12 were carried out in triplicate sets.

3.2.5. Biochemical characterization of *Ac*Xyn30B_12

3.2.5.1. Investigation of optimum pH and pH stability of *Ac*Xyn30B_12

Buffers with corresponding ranges of pH like, 0.05 M citrate phosphate buffer (pH 3 to 6.5), 0.05 M sodium phosphate buffer (pH 6 to 8), 0.05 M Tris-HCl (pH 7.5 to 9) and 0.05 M carbonate bicarbonate buffer (pH 9.5 to 10.5) were utilized to identify pH stability and optimum pH of the enzyme, endo-*β*-1,4-xylanase (*Ac*Xyn30B_12). For determination of optimum pH, the assay was performed in total reaction volume of 0.1mL consisting of 1.0% (w/v) PABX in 0.09 mL of 0.05 M each buffer individually

and 0.01 mL of *Ac*Xyn30B_12 (0.05 mg/mL) by incubating at 70°C for 4 min. For determining the pH stability, 50 µL of *Ac*Xyn30B_12 (0.05 mg/mL) was pre-incubated at different pH ranges mentioned above at 25°C for 2h. The assay was performed by taking an aliquot of 0.01 mL of incubated enzyme individually in 0.1 mL reaction mixture consisting of 1.0% (w/v) PABX in 0.09 mL of 0.05 M citrate phosphate buffer, pH 5.5 at 70°C for 4 min. The residual activity was determined as a percentage by setting the maximal specific activity at 100%.

3.2.5.2. Investigation of optimum temperature and thermostability of *Ac*Xyn30B_12

To determine the optimum temperature of the enzyme, endo-*β*-1,4-xylanase (*Ac*Xyn30B_12), the assay was performed in 0.1 mL reaction mixture, where 1.0% (w/v) PABX in 0.09 mL of 0.05 M citrate phosphate buffer (pH 5.5) was hydrolysed by 0.01 mL of *Ac*Xyn30B_12 (0.05 mg/mL) at different temperatures in the range, 20°C to 90°C for 4 min. For determining the thermal stability, 50 µL of *Ac*Xyn30B_12 (0.05 mg/mL) was incubated at various temperatures ranging from 4°C to 90°C for 2h. The assay was performed by taking an aliquot of 0.01 mL of incubated enzyme individually in 0.1 mL reaction mixture consisting of 1.0% (w/v) PABX in 0.09 mL of 0.05 M citrate phosphate buffer, pH 5.5 at 70°C for 4 min. The residual activity was determined as a percentage by setting the maximal specific activity at 100%. The half-life ($t_{1/2}$) of *Ac*Xyn30B_12 was analysed by following the protocol as reported by Nawaz *et al.* (2018). For the half-life analysis, 200 µL of 50 µg/mL *Ac*Xyn30B_12 was kept at different temperatures, 4°C and 25°C for a month and at 30°C, 40°C, 60°C and 70°C for 24h.

The equation used to calculate half-life ($t_{1/2}$) is given below:

$$t_{1/2} = \frac{0.693}{k}$$

Where,
k = Rate constant

$$k = \frac{2.303 \log(A_o/A_T)}{t}$$

Where,
A_o = Initial enzyme activity
A_T = Enzyme activity at a particular temperature at 24h
t = 24h

3.2.5.3. Thermal shift assay of *Ac*Xyn30B_12 by thermofluor dye

The thermal shift assay (TSA) also known as differential scanning fluorimetry (DSF) of endo-*β*-1,4-xylanase (*Ac*Xyn30B_12) was performed by thermofluor screen (Sypro orange dye) using Applied Biosystems software v.1.1 using RT-PCR (Agilent Technologies, Santa Clara, California, USA). For the assay, a mixture of total volume 25 µL was prepared that contained 4.3 µL *Ac*Xyn30B_12 (final concentration 1.6 µM), 12.5 µL, 0.1 M sodium phosphate buffer (pH 7.5) (final concentration 50 mM), 2.5 µL SYPRO orange dye (Steinberg *et al*., 1996) from 50X stock (final concentration 5X) and 5.7 µL distilled water following the method reported earlier (Boivin *et al*., 2013). The blank, 25 µL volume mixture contained the dye and buffer without *Ac*Xyn30B_12. After filling the 96 well microplate it was sealed with clear and transparent sealing tape and then heated from 25°C to 99.9°C with incremental steps of 1°C every minute. The SYPRO Orange fluorescence was measured at ($\lambda_{ex}/\lambda_{em}$) 470 nm/569 nm. The melting temperature (T_m) of *Ac*Xyn30B_12 was determined by the Boltzmann fit of the fluorescence curve by using Origin software (Lucet *et al*., 2014).

3.2.6. Determination of kinetic parameters of *Ac*Xyn30B_12

The reaction parameters like, maximum velocity (V_{max}), Michaelis-Menten constant (K_M), turnover number (k_{cat}) and catalytic efficiency (k_{cat}/K_M) for endo-β-1,4-xylanase (*Ac*Xyn30B_12), were determined by Michaelis-Menten equation and the Lineweaver–Burk plot (double-reciprocal plot). The evaluation of *Ac*Xyn30B_12 activity was conducted by using different substrates *viz.* PABX, corn cob xylan, xylan (Mw. 20-30 kDa), larchwood xylan, beechwood xylan and 4-*O*-methylglucuronoxylan, under optimum conditions. Each substrate at a concentration range of 0.02% (w/v) to 2.2% (w/v) in 0.09 mL of 0.05 M citrate phosphate buffer (pH 5.5) was incubated with 0.01 mL of *Ac*Xyn30B_12 (0.05 mg/mL) at 70°C for 4 min. The blank consisted of equivalent substrate concentration without the enzyme. The enzyme activity of *Ac*Xyn30B_12 was determined as described in Section 3.2.3.4.

3.2.7. Effect of metal-ions and chemical agents on the activity of *Ac*Xyn30B_12

The impact of various metal-ions and chemical agents at different concentrations on the activity of endo-β-1,4-xylanase (*Ac*Xyn30B_12) was analysed. 50 µL of *Ac*Xyn30B_12 (0.05 mg/mL) was incubated with various metal salts (2 mM and 5 mM; $NiSO_4$, $CuCl_2$, $CoCl_2$, $CaCl_2$, KCl, MgCl, NaCl, LiCl and $FeCl_2$) and other reagents (2 mM and 5 mM; SDS, EDTA, EGTA, GnHCl and Urea) individually, at 25°C for 20 min. For the assay, an aliquot of 0.01 mL of incubated enzyme was added to 1.0% (w/v) PABX in 0.09 mL of 0.05 M citrate phosphate buffer, pH 5.5 in 0.1 mL reaction mixture and incubated at 70°C for 4 min. For blank, substrate having the respective additives only without enzyme were analysed. The enzyme activity was calculated as mentioned in Section 3.2.3.4. The relative activity in the presence of each additive was calculated considering the reaction devoid of any additive as 100% under optimum conditions.

3.2.8. Investigating the mode of hydrolysis of *Ac*Xyn30B_12

3.2.8.1. TLC analysis of *Ac*Xyn30B_12 hydrolysed products of xylan substrates

The time dependent release of endo-*β*-1,4-xylanase (*Ac*Xyn30B_12) hydrolyzed products of PABX and corn cob xylan were investigated by using thin-layer chromatography (TLC). The reaction mixture (0.5 mL) consisting of 1.0% w/v (final concentration) PABX and corn cob xylan in 450 µL of 0.05 M citrate phosphate buffer (pH 5.5) and 50 µL of *Ac*Xyn30B_12 (50 µg/mL) was incubated for different time interval (5, 15, 30 min and 1, 3, 6 & 12h). The reaction was terminated by adding 3 volumes of 100% ethanol, followed by precipitation of undigested polysaccharides and centrifugation for 10 min at 13,000*g*. After transferring the supernatant containing the hydrolyzed products to a different microcentrifuge tube, it was dried by keeping at 70°C for 12h. Each sample, 0.6 µL of hydrolyzed product, the control sample only 1.0% (w/v) PABX and corn cob xylan in 0.05 M citrate phosphate buffer, pH 5.5) and the standard solutions (xylo-oligosaccharides, arabinose and galacturonic acid each visualizing solution containing 1 mL 37.5% HCl, 2 mL aniline, 10 mL 85% H_3PO_4, 100 mL ethyl acetate and 2 g diphenylamine reagent was used to stain the TLC plate (Verma *et al*., 2016). The TLC plate was dried at 70°C in a hot-air oven for 20 min. The reducing sugars manifested as dark brown patches on TLC plate. Another TLC experiment was set up to analyse the *Ac*Xyn30B_12 hydrolysed products of different xylan polysaccharides (PABX, corn cob, xylan Carbosynth, larchwood xylan, beechwood xylan, 4-*O*-methylglucurono xylan, low viscosity wheat arabinoxylan and rye arabinoxylan) and in-house xylan substrates (acacia saw dust xylan, neem saw dust xylan, SCT, banana stem xylan, apSCT and water hyacinth xylan) keeping the reaction conditions same as above but for an incubation period of only 12h. For PABX and corn

cob xylan, 100 µL of the hydrolysate at each time interval (5, 15, 30 min and 1, 3, 6 & 12h) was collected and analysed for estimating total reducing sugar (TRS) by using the method outlined in Section 3.2.3.4. To further confirm the enzymatic mode of action (endo- and exo-lytic), the hydrolysis of 1.1% (w/v) of each xylopentaose, xylotetraose, xylotriose and xylobiose in 0.09 mL of 0.05 M citrate phosphate buffer, pH 5.5 by 0.01 mL of *Ac*Xyn30B_12 (0.05 mg/mL) in 0.1 mL reaction mixture was performed at 50°C for 1h following the method reported earlier (Nath *et al*., 2019). The TLC analysis of the *Ac*Xyn30B_12 hydrolysed products of xylopentaose, xylotetraose, xylotriose and xylobiose was carried out similarly as mentioned above.

3.2.8.2. Analysis of *Ac*Xyn30B_12 hydrolysed products of PABX by HPLC

HPLC analysis of endo-*β*-1,4-xylanase (*Ac*Xyn30B_12) hydrolysed products of PABX was performed using Rezex™ RSO-Oligosaccharide Ag^+ 4 % column (Phenomenex, Inc., Torrance, CA, USA) on a Shimadzu HPLC system. The total reaction volume of 2 mL consisting of 1.0% (w/v) PABX in 1.8 mL of 0.05 M citrate phosphate buffer (pH 5.5) and 0.2 mL *Ac*Xyn30B_12 (0.05 mg/mL) was incubated at 50°C for different time periods (5 min, 15 min, 1h and 6h). For control, only 1.0% (w/v) PABX in 2 mL of 0.05 M citrate phosphate buffer (pH 5.5) without adding enzyme was used. The reaction was terminated by adding 3 volume of 100% ethanol, followed by precipitation of undigested polysaccharides and centrifugation for 10 min at 13,000*g*. After transferring the supernatant containing the hydrolyzed products to a different microcentrifuge tube, it was dried by keeping at 70°C for 12h. These dried samples were further resuspended in 0.5 mL degassed Milli-Q water and centrifuged at 13,000*g* for 10 min. From its supernatant, 20 µL of the hydrolysate was injected into the HPLC column. An isocratic mode of elution was used and the flow rate was 0.3mL/min for a total time of 5 min per hydrolysate sample. The eluent used for the HPLC analysis was

degassed Milli- Q water and the detection of oligosaccharides was carried out using a Refractive Index (RI) Detector. The chromatogram of each hydrolysate sample and xylo- oligosaccharides standard was analysed by utilizing Lab Solution software (Shimadzu, Japan) and then compared, to examine the presence of xylo-oligosaccharides.

3.2.8.3. Analysis of *Ac*Xyn30B_12 hydrolysed products of PABX by MALDI-TOF MS

Mass spectrometric analysis of endo-*β*-1,4-xylanase (*Ac*Xyn30B_12) hydrolysed products of PABX was performed using the time of flight (TOF) masss pectrometer Autoflexspeed (Bruker Daltonics, Bremen, Germany). The samples were prepared by following the method similar to HPLC (Section 3.2.8.2) for different reaction time periods: 5 min, 15 min, 1h and 6h. For matrix preparation, 10 mg/mL of 2,5-Dihydroxybenzoic acid (DHB) was mixed with a solvent containing 50:50 (v/v) water:acetonitrile and 0.1% (v/v) trifluoroacetic acid (Gavande *et al*., 2022). The sample and matrix were mixed in the ratio 1:1 and subjected to MALDI-TOF MS analysis. The following parameters were set for the analysis: accelerating voltage =4.9 x 2400 V, reflectron mode =positive, laser shot frequency =2000 Hz and time delay for pulse ion extraction =120 ns. The results were analyzed by generating m/z versus intensity (a.u) plots for each reaction sample and the peaks were compared with those of xylo-oligosaccharide standards.

3.2.9 Synergistic action of *Ac*Xyn30B_12 and xylobiohydrolase *Ac*GH30A on hydrolysis of xylan substrates

The synergistic effect of endo-*β*-1,4-xylanase, *Ac*Xyn30B_12 and a xylobiohydrolase, *Ac*GH30A from *A. clariflavus* (Singh *et al*., 2024) was investigated for hydrolysis of different xylan substrates *viz.* 4-*O*-methylglucuronoxylan, xylan from Carbosynth (Mw: 20,000–30,000) and beechwood xylan. The enzyme, *Ac*Xyn30B_12 was purified following the procedure mentioned in Section 3.2.2 and *Ac*GH30A was

purified by following the protocol reported by Singh *et al*. (2024). To compare the specific activity of individual enzymes and in combination, 1.0% (w/v) final substrate concentration in 90 µL 50 mM citrate phosphate buffer (pH 5.5), with 0.01 mL individual enzymes (0.7 µM of *Ac*Xyn30B_12 or 0.7 µM of *Ac*GH30A) and with 5 µL of each enzyme in equimolar concentration (0.7 µM of *Ac*Xyn30B_12 +0.7 µM *Ac*GH30A) in 0.1 mL total reaction mixture was incubated for 3 min at 70°C. The reducing sugar thus produced was quantified by protocol of Somogyi [1945] and used for calculation of the enzyme activity as described in section 3.2.4.3.

For TLC analysis of cleaved products and estimation of TRS, 0.36 mL of 1.0% (w/v) substrate in 50 mM citrate phosphate buffer, pH 5.5, was incubated with 40 µL individual enzymes (0.7 µM of *Ac*Xyn30B_12 or 0.7 µM of *Ac*GH30A) and with 20 µL of each enzyme in combination (0.7 µM of *Ac*Xyn30B_12 +0.7 µM *Ac*GH30A) in a total reaction mixture of 0.4 mL, for 1h at 50°C. From each reaction, 100 µL was utilized for TRS estimation and 300 µL was utilized for TLC analysis following the similar procedure as mentioned in Section 3.2.8.1.

The TLC analysis was also carried out to study the hydrolysed products released by the action of *Ac*GH30A on xylo-oligosaccharides. For this experiment, in total reaction volume of 0.1 mL, 0.09 mL of 1.0% (w/v) xylopentaose, xylotetraose, xylotriose or xylobiose in 0.05 mM sodium phosphate buffer (pH 7.0) separately was mixed with 0.01 mL of *Ac*GH30A (0.05 mg/mL) and incubated at 40°C for 1h as reported earlier (Singh *et al*., 2024). The chromatogram of the hydrolysed products of xylopentaose, xylotetraose, xylotriose and xylobiose was developed similarly as mentioned in Section 3.2.8.1.

3.2.10. Analysis of *Ac*Xyn30B_12 hydrolysed products of pretreated lignocellulosic biomass

The endo-*β*-1,4-xylanase, *Ac*Xyn30B_12 hydrolyzed products of three biomasses, *viz*. napier grass (*Pennisetum purpureum*) and kans grass (*Saccharum spontaneum*) available in IIT Guwahati campus and rice straw (*Oryza sativa*) from local fields of Barpeta district, Assam, India was analysed. Before the assay by *Ac*Xyn30B_12, each biomass was washed, grinded and sieved to < 1 mm size using wire mesh and then pretreated for optimal hemicellulose recovery and lignin removal. The biomass, napier grass at 7.5% (w/v) loading that was pretreated with 4.2% (v/v) alkaline hydrogen peroxide at 101.8°C for 147.6 min (Aishwarya *et al*., 2024), 20% (w/v) rice straw pretreated with 5% (v/v) NaOH at 90°C for 20 min (Suriyachai *et al*., 2013) and 5% (w/v) kans grass pretreated with 0.5 % (v/v) NaOH at 121°C for 30 min (Kataria *et al*., 2014) were used. The pretreated biomasses were filtered by cotton fabric cloth and the solid residue was washed with deionised water until pH 7.0 was obtained and then dried in a hot air oven at 80°C for 12h. Each pretreated biomass (2.0%, w/v) was suspended individually in 1.8 mL of 0.05 M citrate phosphate buffer (pH 5.5) and hydrolyzed with 0.2 mL *Ac*Xyn30B_12 (600 U/g, 0.05 mg/mL) at 50°C for 72h. For control, 2.0%, w/v of each pretreated biomass in 2 mL of 0.05 M citrate phosphate buffer (pH 5.5) without enzyme was used. At every 12h, 0.2 mL of hydrolysate was collected and 0.1 mL was used for TLC analysis and the remaining 0.1 mL was used for total reducing sugar (TRS) estimation (as described in Section 3.2.3.4).

3.3. Results and Discussion

3.3.1. Purification of recombinant *Ac*Xyn30B_12 and its concentration estimation

The protein, *Ac*Xyn30B_12 was purified by IMAC using 1 mL HiTrap™ prepacked column, which showed a prominent protein band of approximately, 75 kDa molecular size and an additional band at 65 kDa (Fig. 3.1A, lane-6). Its concentration was determined by Bradford method and UV spectroscopy, was 1.2 mg/mL for 4 mL protein eluted giving 4.8 mg protein purified from 200 mL culture. *Ac*Xyn30B_12 (purified by HiTrap Chelating HP prepacked column) was further purified by using SEC superdex 75 pg prep grade column and each fraction (1.5 mL) was collected and analysed by 12% (w/v) SDS-PAGE (data not shown). The fractions 1 to 3 (corresponding to peak 1, as shown in Fig. 3.1B) and fraction 4 (at the start of peak 2, as shown in Fig. 3.1B) showed no protein bands. Eluted fractions 5 to 8 (corresponding to peak 2, as shown in Fig. 3.1B) showed a single protein band of molecular size, ~74 kDa showing the removal of impure protein. These eluted fractions (5 to 8) were pooled for further assays. This pooled fraction of 6 mL gave a single protein band below 75 kDa (Fig. 3.1A, lane-7) and a protein concentration of 0.7 mg/mL. The theoretical molecular mass of *Ac*Xyn30B_12 determined by Protparam Expasy server utilizing the protein sequence that has a Histidine-6 tag incorporated at N-terminal in *Ac*Xyn30B_12-pET-28a(+) construct, yielded molecular mass of 73.5 kDa. Thus, the molecular mass of *Ac*Xyn30B_12, determined theoretically and analysed that by SDS-PAGE gel were in agreement with each other. There was no presence of *Ac*Xyn30B_12 protein in the sonicated cell pellet (Fig. 3.1A, lane-3), but it was present in the cell extract (Fig. 3.1A, lane-4) showing that *Ac*Xyn30B_12 expressed as a soluble protein. After the purification of *Ac*Xyn30B_12 by SEC, enzyme activity yield of 44% and fold purification of 52 was achieved (Table 3.1).

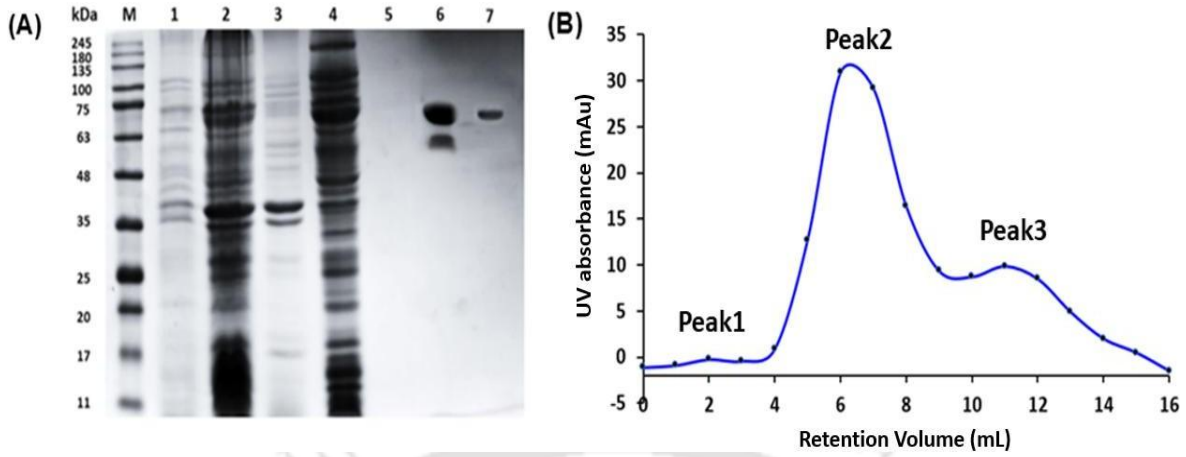

Fig. 3.1. **(A)** Purification analysis of recombinant *Ac*Xyn30B_12 by SDS-PAGE using 12% (w/v) gel. Lanes M: Pre-stained protein ladder, 1-uninduced *E. coli* BL21 (DE3) cells, 2-induced *E. coli* BL21 (DE3) cells, 3-sonicated cell pellet, 4-cell extract, 5-last column wash, 6-purified *Ac*Xyn30B_12 by affinity chromatography using HiTrap™ 1 mL column and 7-purified *Ac*Xyn30B_12 by SEC using Superdex-75 pg, **(B)** Purification of *Ac*Xyn30B_12 by SEC using Superdex-75 pg showing elution profile by UV absorbance (mAu, at 280 nm) vs Retention volume (mL) chromatogram.

Table 3.1. Purification of *Ac*Xyn30B_12.

Purification step	Volume (mL)	*Ac*Xyn30B_12			Protein (mg/mL)	SA (U/mg)	Fold Purification
		EA ($U.ml^{-1}$)	Total Units (U)	Overall % yield			
Crude lysate	15	68.1	1021.5	100	33	2.1	1
HiTrap™ (HP prepacked)	4	126	504	49.3	1.2	107.7	51
SEC (Superdex 75 pg)	6	75	450	44	0.7	109	52

EA=Enzyme activity, SA=Specific activity

Enzyme activity was determined against 1% (w/v) PABX under optimum conditions (pH 5.5, 70°C, 4 min)

3.3.2 Substrate specificity of *Ac*Xyn30B_12 against natural and synthetic substrates

The assay of *Ac*Xyn30B_12 carried out under optimum conditions of pH 5.5, temperature 70°C and reaction time 4 min showed the highest specific activity of 121.9 U/mg against PABX, which contains 24% acetyl group substitution. It also showed activity against corn cob xylan (118.8 U/mg), xylan (Mw. 20,000-30,000, 95.4 U/mg), larchwood xylan (79.2 U/mg) beechwood xylan (70.6 U/mg), 4-*O*-methylglucuronoxylan (70.2 U/mg), rye arabinoxylan (50.9 U/mg) and wheat

arabinoxylan (low viscosity, 47.5 U/mg) as shown in Table 3.2. These results confirmed the *β*-(1–4) xylanase activity of *Ac*Xyn30B_12. In the present study, the activity of *Ac*Xyn30B_12 (0.05 mg/mL, 0.68 μM) against 1.0% (w/v) 4-O methyl-glucuronoxylan (70.2 U/mg) in 0.05 M citrate phosphate, pH 5.5 at 70°C for 4 min was significantly higher (20-fold) than the activity (3.5 U/mg) of the same enzyme, 30.9 nM (2.2×10^{-3} mg/mL) *Ac*Xyn30B against 1.0% (w/v) 4-*O*-methylglucuronoxylan in 0.05 M sodium phosphate, pH 6.0 at 40°C as reported by Suchova *et al.* (2024). The observed differences in results can be attributed to the fact that, in our study the hydrolysis of xylan substrates by *Ac*Xyn30B_12 was performed under the optimum reaction conditions, including the enzyme concentration (0.05 mg/mL), substrate concentration (1.0%, w/v), pH (5.5, 0.05 M citrate phosphate), temperature (70°C) and the reaction time (4 min). *Ac*Xyn30B_12 demonstrated significantly higher activity against xylan polysaccharides substituted with either arabinose or glucuronic acid (Table 3.2). In rye arabinoxylan, the main chain is substituted with *α*-L-arabinofuranosyl residue at O-2 and/or O-3 by *α*-(1→2) or *α*-(1→3) linkage respectively, accounting for 38% of the substitution and the monosaccharide composition is arabinose: xylose =40:60. Also, in wheat arabinoxylan (low viscosity) and wheat arabinoxylan (insoluble) the main chain is substituted with 38% *α*-L-arabinofuranosyl residue however, the monosaccharide composition is arabinose: xylose =38:62 for wheat arabinoxylan (low viscosity) and arabinose: xylose: glucose: mannose: galactose =33.5:62:1.5:2:1 for wheat arabinoxylan (insoluble). Therefore, it can be concluded that in case of rye arabinoxylan, wheat arabinoxylan (low viscosity and insoluble) the *α*-L-arabinofuranosyl substitutions on xylan main chain might be inhibiting the activity of *Ac*Xyn30B_12 resulting in lower

enzyme activity as compared with the other xylan substrates with no side chain arabinose.

*Ac*Xyn30B_12 demonstrated a specific activity of 121.5 U/mg and 118.2 U/mg, respectively, against acacia sawdust xylan and neem saw dust xylan. It was earlier reported that, acacia sawdust xylan and neem saw dust xylan contain 15% (w/w) and 10.5% (w/w) glucuronic acid, respectively (Sharma *et al*., 2020, Sharma *et al*., 2020). Therefore, the presence of glucuronic acid substitution in xylan main chain of acacia saw dust xylan and neem saw dust xylan could be the reason for the higher activity of *Ac*Xyn30B_12 which increases the substrate recognition and enzyme specificity as reported earlier (Maehara *et al*., 2018). Similarly, it was reported earlier that, GH11 *endo*-xylanase XynA from *B. subtilis* 168 (St. John *et al*., 2006) has highest activity against methylglucuronoxylan substituted (MeGA) birchwood xylan and in MeGA substituted beechwood xylan hence confirming direct correlation between its enzyme activity and the degree of glucuronosyl moiety substitution on the xylan main chain. The activity of *Ac*Xyn30B_12 against SCT and apSCT was 98.7 U/mg and 87.3 U/mg, respectively. D-glucuronic acid and L-arabinose residues were found to be present in SCT at 16% (w/w) and 10% (w/w), respectively and in apSCT at 15% (w/w) and 11% (w/w), according to a report by Khaire *et al* (2021). Therefore, the presence of L-arabinose residues in SCT and apSCT could be the reason of low activity of *Ac*Xyn30B_12 as compared with those in acacia saw dust xylan and neem saw dust xylan. *Ac*Xyn30B_12 exhibited no activity against any of cellulosic-based and mannan-based substrates. Moreover, it did not show any activity against 4-Nitrophenyl-*β*-D-xylopyranoside, which confirmed the absence of xylosidase activity of the enzyme.

Table 3.2. Specific activity of *Ac*Xyn30B_12 against different natural and in-house isolated substrates.

Natural substrates (1%, w/v)	Specific **Activity (U/mg)**
Partially Acetylated Birchwood Xylan	121.9 ± 0.7
Corn Cob Xylan	111.8 ± 0.8
Xylan Carbosynth (MW-20-30 kDa)	95.4 ± 0.4
Larchwood Xylan	79.2 ± 0.7
Beechwood Xylan	70.6 ± 0.2
4-O-methylglucurono Xylan	70.2 ± 0.8
Rye Arabinoxylan	50.9 ± 0.8
Wheat Arabinoxylan (low viscosity)	47.5 ± 0.6
Oat spelt Xylan	44.3 ± 0.2
Wheat Arabinoxylan (Insoluble)	24.8 ± 0.7
Other substrates[a]	NAD
In-house isolated xylan substrates (1%, w/v)	Specific **Activity (U/mg)**
Acacia saw dust Xylan	121.5 ± 0.7
Neem saw dust Xylan	118.2 ± 1.5
Sugarcane top Xylan (SCT)	98.7 ± 3.3
Banana stem Xylan	88.7 ± 1.6
Alkaline pretreated sugarcane top Xylan (ApSCT)	87.3 ± 2.0
Neem Xylan	26.2 ± 0.8
Water hyacinth Xylan	20.1 ± 1.5

NAD= No activity detected

[a]*4-Nitrophenyl-β-D-xylopyranoside, Carboxy methyl cellulose (CMC), Galactan (potato), Arabinogalactan (larchwood and larchtree), Arabinan (Sugarbeet), Pecticgalactan (Lupin), Rhamnogalacturonan (Potato pectic fibre), Rhamnogalacturonan (Soyabean pectic fibre), Glucomannan (Konjac), Carob Galactomannan, β-D-Glucan (barley), Curdlan, Pullulan, Pustulan*

3.3.3. Biochemical characterization of *Ac*Xyn30B_12

3.3.3.1. Analysis of optimum pH and pH stability of *Ac*Xyn30B_12

The endo-*β*-1,4-xylanase, *Ac*Xyn30B_12 displayed an optimum pH of 5.5 using 0.05 M citrate phosphate buffer, where it showed highest specific activity, 122.1 U/mg with 1.0% (w/v) PABX (Fig. 3.2A). The pH profile showed that *Ac*Xyn30B_12 maintained >80% residual activity when assayed between pH 5.0 to 7.5, but rapidly lost

the activity above pH 7.5. The pH stability profile of *Ac*Xyn30B_12 when assayed at 70°C showed that it retains maximum stability in a wide pH range, 4.8–8.0 (Fig. 3.2B), where it retained 80% of residual activity when incubated for 2h. The pH stability profile of *Ac*Xyn30B_12 showed that the maximum specific activity of *Ac*Xyn30B_12 (taken as 100%) is at pH 7.5, 0.05 M sodium phosphate buffer (121.3 U/mg) followed by pH 5.0, 0.05 M citrate phosphate buffer (120.4 U/mg).

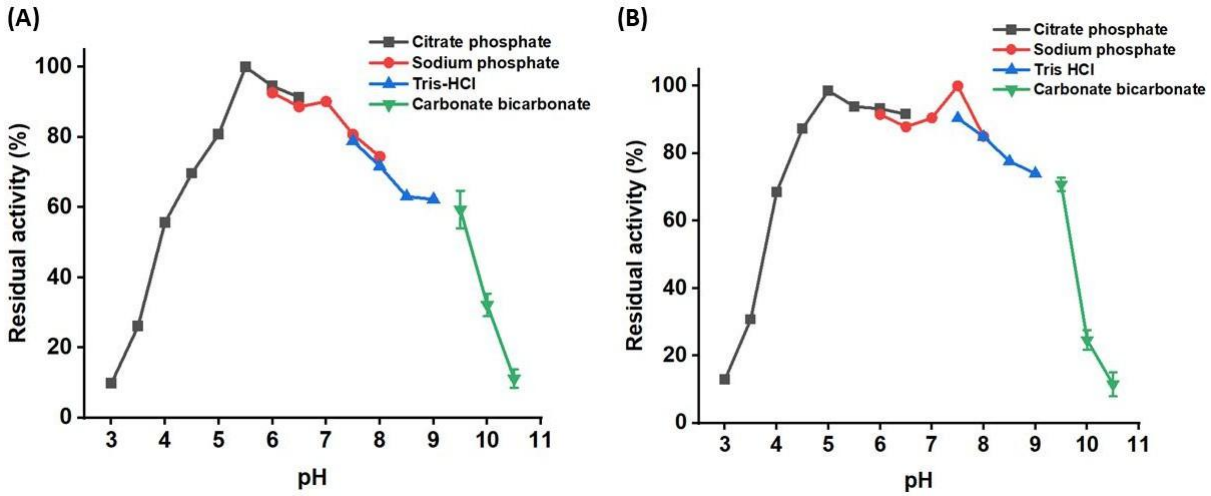

Fig. 3.2. (A) Optimum pH for *Ac*Xyn30B_12 activity and **(B)** pH stability of *Ac*Xyn30B_12.

3.3.3.2. Optimum temperature, thermal stability and melting temperature of *Ac*Xyn30B_12

The optimum temperature of endo-*β*-1,4-xylanase, *Ac*Xyn30B_12 was identified to be 70°C, where it showed maximum specific activity (taken as 100%) of 121.1 U/mg against 1.0% (w/v) PABX in 0.05 M citrate phosphate buffer, pH 5.5 (Fig. 3.3A). The investigation of thermostability of *Ac*Xyn30B_12 by incubating at a temperature range, 4°C-60°C, for 2h displayed >80 % residual activity (Fig. 3.3B). The maximum specific activity for *Ac*Xyn30B_12 was obtained at 4°C (121.4 U/mg). The half-life analysis of *Ac*Xyn30B_12 showed a $t_{1/2}$ of 7 days (~164h) at 30°C, 4 days (~105h) at 40°C, ~40h at 60°C and ~1.5h at 70°C (Fig. 3.3C). The enzyme,

*Ac*Xyn30B_12 retained 88% enzyme activity at 4°C and 75.3% enzyme activity at 25°C when incubated for 1 month. Thermal shift assay of *Ac*Xyn30B_12 was carried out using RT-PCR where on denaturation of protein, the SYPRO-orange dye binds to the hydrophobic patches and shows the changes in fluorescence intensity. The fluorescence intensity (a.u) *vs* temperature (°C) plot of *Ac*Xyn30B_12 showed highest fluorescence intensity at 83.3°C (Fig. 3.4D). The melting temperature (T_m) is the point at which 50% of a protein is in its folded (native) state and 50% in its unfolded (denatured) state. Tm of *Ac*Xyn30B_12 analysed by Boltzmann fitting of fluorescence *vs* temperature curve was found to be 69.4°C (Fig. 3.3D).

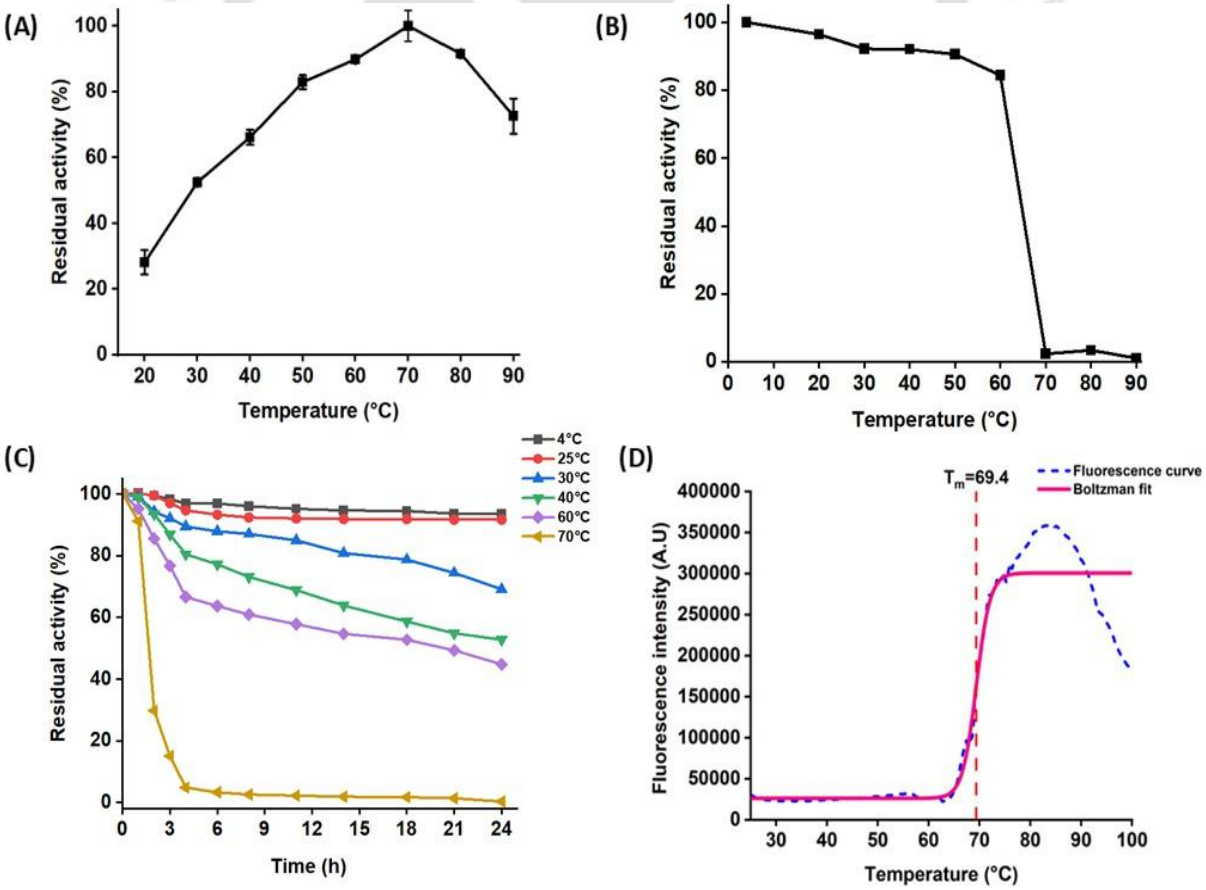

Fig. 3.3. (A) Optimum temperature for *Ac*Xyn30B_12 activity, **(B)** Thermal stability of *Ac*Xyn30B_12 and **(C)** Relative activity (%) vs incubation time (h) plot for *Ac*Xyn30B_12 at different temperatures. **(D)** Thermal shift assay of *Ac*Xyn30B_12.

3.3.4. Analysis of kinetic properties of *Ac*Xyn30B_12

The different kinetic parameters of endo-β-1,4-xylanase, *Ac*Xyn30B_12 were determined for PABX, corn cob xylan, xylan Carbosynth (Mw.20–30 kDa), larchwood xylan, beechwood xylan and 4-*O*-methylglucuronoxylan at optimum conditions of pH 5.5 and temperature 70°C. The Michaelis-Menten plot along-with the Lineweaver-Burk plot of *Ac*Xyn30B_12 against different xylan substrates are shown in Fig. 3.4. The maximum velocity of the reaction, V_{max} and the Michaelis-Menten constant, K_M for PABX were 133.3 U/mg and 0.9 mg/mL, respectively (Table 3.3) indicating the highest affinity for PABX among all substrates. *Ac*Xyn30B_12 gave turnover number (k_{cat}) of 9797.5 min^{-1} and the highest catalytic efficiency (k_{cat}/K_M) of 10,886.2 $min^{-1}mg^{-1}mL$ against PABX. In contrast, non-substituted linear xylans such as corn cob, larchwood, Carbosynth and beechwood exhibited lower k_{cat}/K_M values (7740.1, 2733.1, 4457.3 and 5831.0 min^{-1}. $mL.mg^{-1}$ respectively), likely due to their higher molecular weight, aggregation and reduced solubility, which limit enzyme accessibility despite good binding. In the present study, the catalytic efficiency (k_{cat}/K_M) of *Ac*Xyn30B_12 against 4-*O*-methylglucuronoxylan was 2129.0 min^{-1}. $mL.mg^{-1}$, however, as reported by Suchova *et al*., 2024 the k_{cat}/K_M of the same enzyme, *Ac*Xyn30B against 4-*O*-methylglucuronoxylan at pH 6.0 and 40°C was significantly lower, 4.1 s^{-1}.$mL.mg^{-1}$ (or 246 min^{-1}.$mL.mg^{-1}$) due to side chain substitutions of glucuronic acid. The lower value of k_{cat}/K_M reported by Suchova *et al*., 2024 could be due the difference in the source of the substrate as it was prepared by them in laboratory as mentioned, whereas in our case it was procured from Sigma Chem. Co. USA. Moreover, the optimized conditions for the enzyme assay in the present study were used. The kinetic parameters of *Ac*Xyn30B_12 with other xylan substrates are shown in Table 3.3.

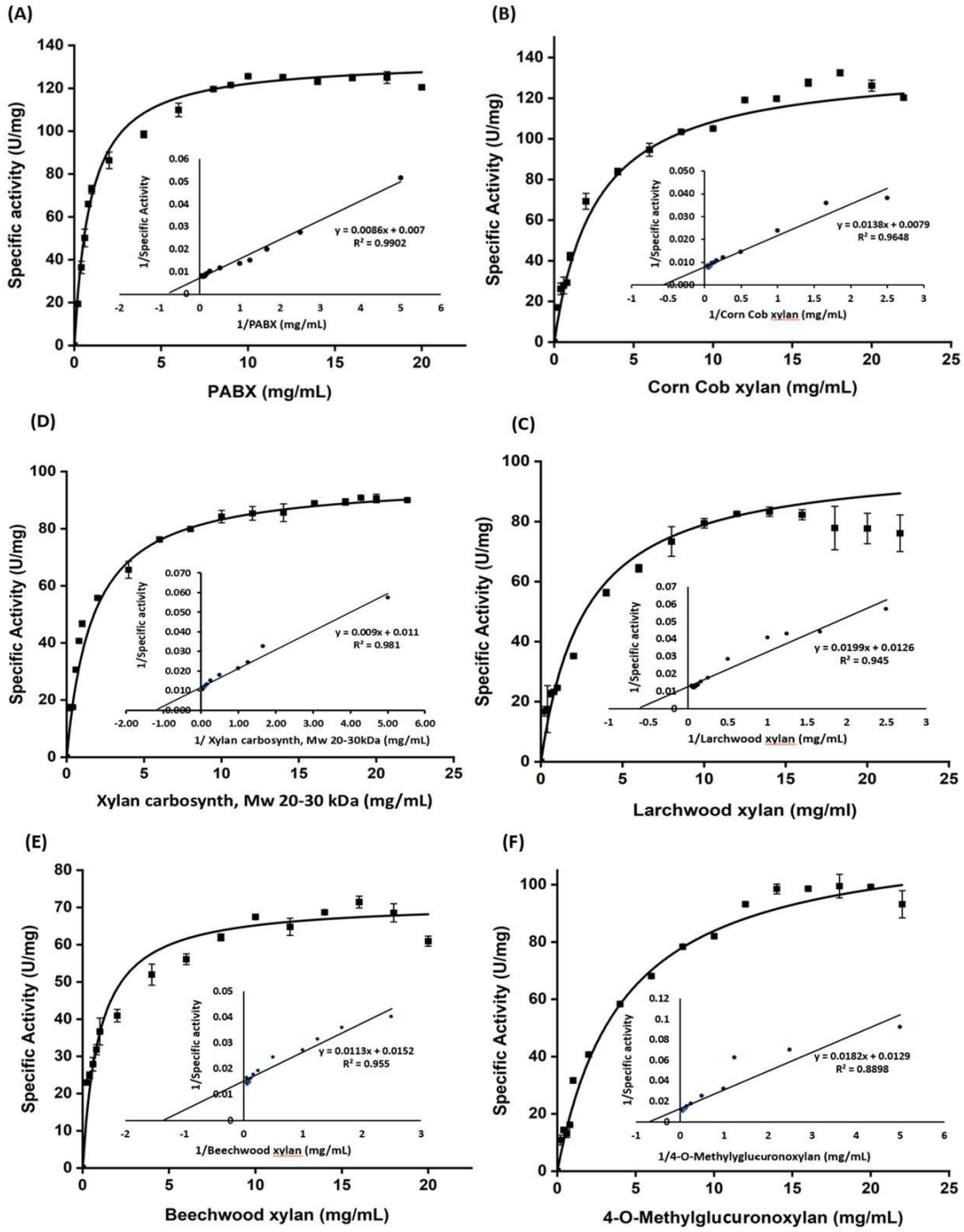

Fig. 3.4. Michaelis-Menten kinetics plots of *Ac*Xyn30B_12 against **(A)** PABX, **(B)** corn cob xylan, **(C)** xylan Carbosynth, **(D)** larchwood xylan, **(E)** beechwood xylan and **(F)** 4-O-methylglucurono xylan at optimum pH of 5.5, 0.05 M citrate-phosphate buffer, at 70°C and at 50 µg/mL enzyme. Lineweaver-Burk plot of *Ac*Xyn30B_12 against corresponding substrates is displayed in the inset of each diagram.

Table 3.3. Kinetic parameters of *Ac*Xyn30B_12 against natural xylan substrates.

Natural substrates	V_{max} (μmol.min^{-1}.mg^{-1})	K_M (mg.mL^{-1})	k_{cat} (min^{-1})	k_{cat}/K_M (min^{-1}.mL.mg^{-1})
Partially Acetylated Birchwood Xylan	133.3	0.9	9797.5	10886.2
Corn cob Xylan	136.9	1.3	10062.2	7740.1
4-O-methylglucuronoxylan	118.8	3.1	8731.8	2129.0
Larchwood Xylan	100.4	2.7	7379.4	2733.1
Xylan (Carbosynth, Mw.20-30 kDa)	97.03	1.6	7131.7	4457.3
Beechwood Xylan	71.4	0.9	5247.9	5831.0

3.3.5. Effect of metal-ions and chemical reagents on *Ac*Xyn30B_12 activity

The impact of various divalent and monovalent metal-ions (their respective salts) and chemical reagents on the activity of endo-*β*-1,4-xylanase, *Ac*Xyn30B_12 was investigated at 2 mM and 5 mM (Table 3.4). The residual activity of control (taken as 100%) was 121.4 U/mg. The *Ac*Xyn30B_12 activity was enhanced by 2 mM Ca^{2+} (10%) and Mg^{2+} (7.3%) while other divalent metal ions, Ni^{2+} (25%), Co^{2+} (13%) and Cu^{2+} (2.2%) at 2 mM inactivated the enzyme, *Ac*Xyn30B_12. In the presence of 5 mM monovalent cations such as Na^{+} (13%), Li^{+} (7.1%) and K^{+} (6.8%), a decrease in *Ac*Xyn30B_12 activity was observed. It was reported that an *endo*-xylanase Xln-1 from *Aspergillus niger* B03 shows the similar extents of decline in residual activity when exposed to Na^{+}, Li^{+} and K^{+} ions (Dobrev *et al*., 2009). *Ac*Xyn30B_12 showed 6.1% lower activity in the presence of 5 mM SDS and only 3% and 2% lower activity with 5 mM EDTA and EGTA, respectively. *Ac*Xyn30B_12 was inactivated in presence of 5 mM urea (15.5%) and by 2 mM guanidine hydrochloride (GnHCl) by 15%.

Table 3.4. Impact of chemical reagents and metal ions on *Ac*Xyn30B_12 activity.

Metal ion/ Additive	Relative activity (%)	
	2 mM	5 mM
Control	100	100
Ca^{2+}	109.6 ± 0.2	111.9 ± 0.6
Mg^{2+}	107.3 ± 1.0	95.6 ± 2.6
Cu^{2+}	97.8 ± 2.0	95.8 ± 4.5
Co^{2+}	87.2 ± 3.9	86.9 ± 2.8
Ni^{2+}	75.2 ± 1.3	65.3 ± 1.4
Li^{+}	104.5 ± 0.4	92.9 ± 3.7
Na^{+}	95.1 ± 4.3	87.1 ± 4.7
K^{+}	94.8 ± 1.1	93.2 ± 0.3
SDS	106.1 ± 1.6	93.9 ± 1.5
EGTA	105.2 ± 2.9	97.1 ± 1.9
EDTA	101.8 ± 2.2	98.0 ± 2.8
Urea	102.1 ± 7.3	84.5 ± 6.6
GnHCl	85.0 ± 2.6	108.8 ± 1.7

All assays were performed in triplicate sets and mean ± SD wasmentioned.

Relative activity of 120 U/mg for Control was taken as 100%.

3.3.6. Analysis of mode of hydrolysis of *Ac*Xyn30B_12

3.3.6.1. TLC analysis of *Ac*Xyn30B_12 hydrolysed products of xylan substrates

The TLC analysis of hydrolysed products of different xylan substrates by endo-*β*-1,4-xylanase, *Ac*Xyn30B_12 showed that, it can hydrolyse unsubstituted xylan as well as both arabinose substituted and glucuronic acid substituted xylan substrates. The thin layer chromatogram of hydrolysis of 1.0% (w/v) xylans (PABX, corn cob xylan, xylan Carbosynth, larchwood xylan, beechwood xylan, 4-*O*-methylglucurono xylan, low viscosity wheat arabinoxylan and rye arabinoxylan) by *Ac*Xyn30B_12 (50 µg/mL) in total reaction volume of 0.5 mL at 50°C, pH 5.5 for 12h showed the release of xylo-oligosaccharides *viz.* xylopentaose (X5), xylotetraose (X4), xylotriose (X3), xylobiose (X2) and xylose (X1) (Fig. 3.5A, lanes-1-6). However, as reported by Suchova *et al.*,

2024, the TLC analysis of hydrolysed products of 10 mg/mL 4-*O*-methylglucurono xylan (in 0.05 M sodium phosphate, pH 6.0) by the same enzyme, *Ac*Xyn30B (10 µg/mL) at 40°C displayed the release of X5, X4, X3 and X2 till 24h and no X1. This could be due to the low enzyme concentration used that was insufficient in achieving the saturation kinetics. In the present study, however, for rye arabinoxylan and wheat arabinoxylan, the TLC profile showed the presence of only X5, X4 and X3 (Fig. 3.5A, lanes-7-8) after 12h of hydrolysis. The TLC analysis of hydrolysed products of different in-house xylan substrates by *Ac*Xyn30B_12 displayed the presence of X5, X4, X3, X2 and X1 for all substrates (Fig. 3.5B, lanes-1-6) except for water hyacinth xylan, where only X5 and X4 could be seen (Fig. 3.5B, lane7). Based on the above results, it can be concluded that the in-house substrates *viz*., acacia sawdust xylan, neem sawdust xylan, SCT and apSCT containing relatively low levels of arabinose substitution (10% w/w) were efficiently hydrolyzed by *Ac*Xyn30B_12, resulting in the production of XOS ranging from xylopentaose to xylose. In contrast, rye arabinoxylan and wheat arabinoxylan (low viscosity) exhibit higher degrees of α-L-arabinofuranosyl substitution on the xylan backbone, accounting for approximately 38% substitution. Therefore, this extensive substitution due to steric hindrance interfered with the enzymatic activity of *Ac*Xyn30B_12, leading to limited hydrolysis of the polysaccharide and resulting in the release of only xylopentaose and xylotetraose.

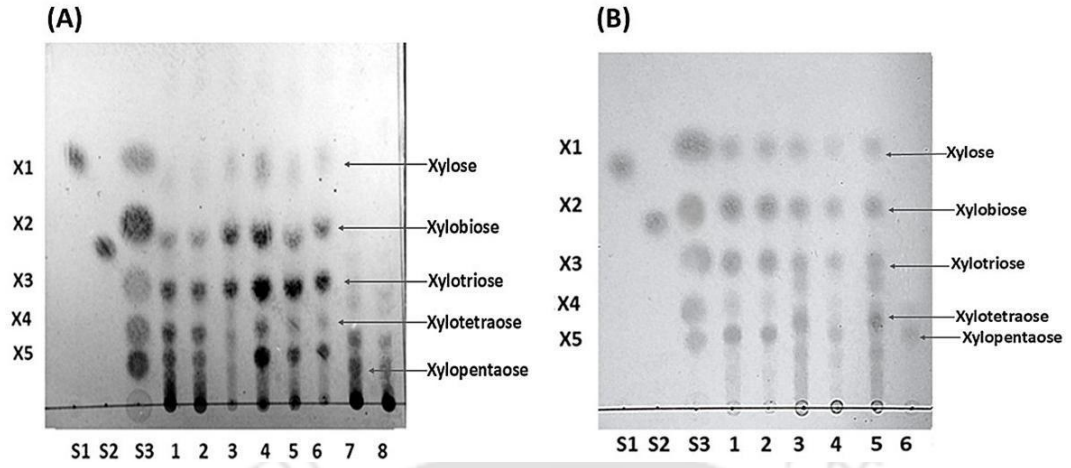

Fig. 3.5 TLC of **(A)** Hydrolysis of different xylan substrates (1.0%, w/v) by *Ac*Xyn30B_12 (50 µg/ml) at 50°C, pH 5.5 for 12h. Lanes, Standards S1: arabinose, S2: glucuronic acid and S3: X1-xylose, X2-xylobiose, X3-xylotriose, X4-xylotetraose, X5-xylopentaose; 1- PABX, 2-corn cob, 3-xylan Carbosynth, 4-larchwood xylan, 5-beechwood xylan, 6-4-O-methylglucurono xylan, 7-rye arabinoxylan and 8-wheat arabinoxylan (low viscosity), **(B)** Hydrolysis of different in-house xylan substrates (1.0 %, w/v) by *Ac*Xyn30B_12 (50 µg/ml) at 50°C, pH 5.5 for 12h. Lanes, Standards S1: arabinose, S2: glucuronic acid and S3: X1-xylose, X2-xylobiose, X3-xylotriose, X4-xylotetraose, X5-xylopentaose; 1-acacia saw dust xylan, 2-neem saw dust xylan, 3-SCT, 4-banana stem xylan, 5-apSCT, 6-water hyacinth xylan.

The mode of time-dependent hydrolysis of PABX by *Ac*Xyn30B_12 was also analysed. The control sample containing only PABX without enzyme showed no spot for any xylo-oligosaccharides showing that the PABX substrate remained intact and was not contaminated with pre-existing or broken XOS fragments (Fig. 3.6A, lane1). The time dependent analysis of the action of *Ac*Xyn30B_12 on PABX by TLC, at 5 min showed the release of only X5, X4 and X3 as shown in Fig. 3.6A, lane 2. Whereas, from 15 min onwards X2 was released besides X5, X4 and X3 (Fig. 3.6A, lanes-3-8). Moreover, after 1h hydrolysis xylose (X1) was also released along with the other xylo-oligosaccharides, X5-X2 (Fig. 3.6A, lanes-5-8). Hence, these results proved both, endo- and exo-acting modes of cleavage by *Ac*Xyn30B_12. Similar results were obtained for the time dependent hydrolysis of corn cob xylan by *Ac*Xyn30B_12 as shown in Fig.

3.6B. The quantification of TRS produced by PABX and corn cob xylan upon hydrolysis by *Ac*Xyn30B_12 at different time intervals is shown in Fig. 3.6a and 3.6b, respectively. The TRS production from PABX hydrolysis rapidly increased in the initial 15 min and subsequently reached saturation to 0.4 mg/mL at 3h (Fig. 3.6a). Similar results were obtained with corn cob xylan hydrolysis by *Ac*Xyn30B_12 and TRS saturation reached 0.36 mg/mL at 3h (Fig. 3.6b).

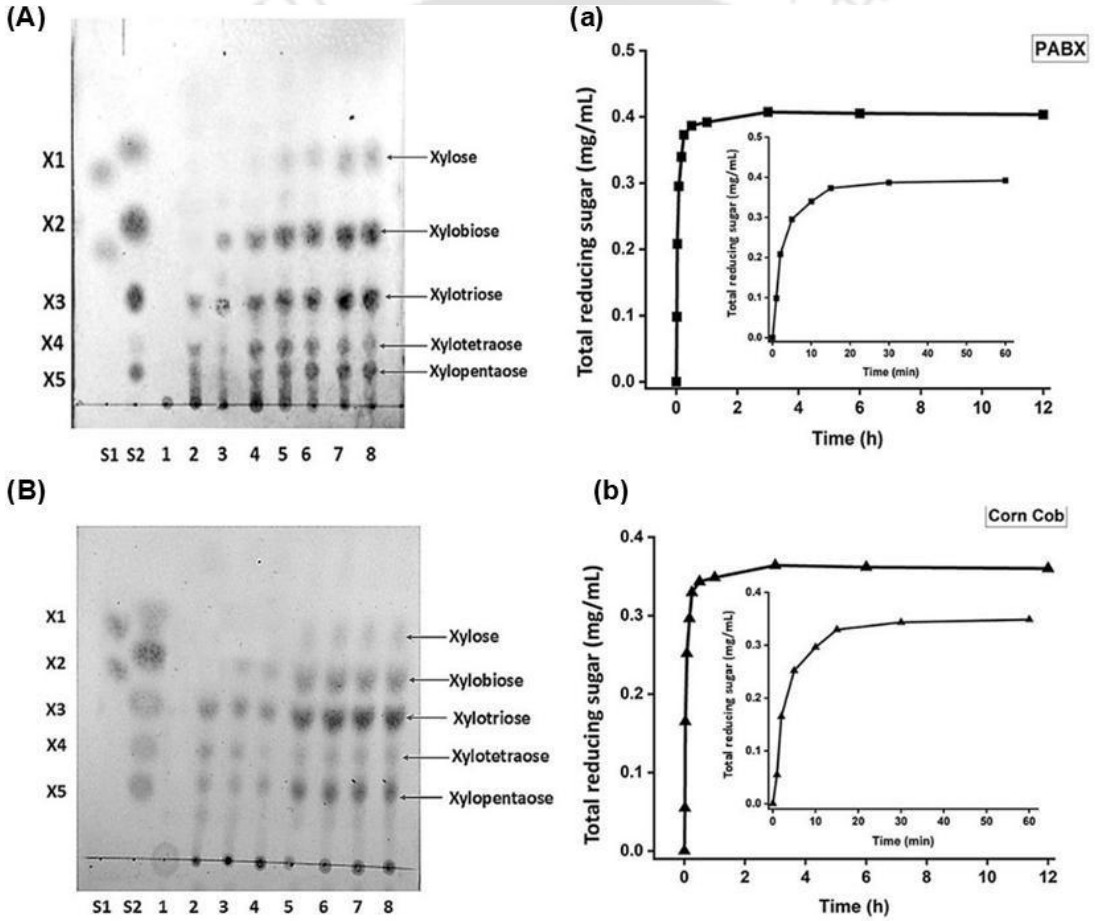

Fig. 3.6. Time dependent hydrolysis of **(A)** PABX and **(B)** Corn cob xylan (1.0%, w/v) at 50°C, pH 5.5 incubated with *Ac*Xyn30B_12 for 5 min to 12h. Lanes, Standards S1: arabinose (above) and glucuronic acid (below), S2: X1-xylose, X2-xylobiose, X3-xylotriose, X4-xylotetraose, X5-xylopentaose; 1-control, 2-5min, 3-15min, 4-30min, 5-1h, 6-3h, 7-6h, 8-12h and Plot of the total reducing sugar concentration (mg/mL) vs time (h) after hydrolysis of **(a)** PABX and **(b)** corn cob xylan.

3.3.6.2. TLC analysis of *Ac*Xyn30B_12 hydrolysed products of xylo-oligosaccharides

The TLC profile containing the hydrolysed products of xylo-oligosaccharides, X5, X4, X3 and X2 by *Ac*Xyn30B_12 for 1h is shown in Fig. 3.7. The hydrolysis of X5 showed the presence of X4, X3, X2 and X1 indicating that the cleavage of X5 by *Ac*Xyn30B_12 gives rise to the formation of X4 and X1 and also X3 and X2 confirming both *exo*- and *endo*-xylanase activity (Fig. 3.7, lane-1). The hydrolysis of X4 by *Ac*Xyn30B_12 showed the presence of X3, X2 and X1 indicating that the cleavage of X4 by *Ac*Xyn30B_12 is giving rise to the formation of X3 and X1 and also X2, again confirming both *exo*- and *endo*-xylanase activity (Fig. 3.7, lane-2). The hydrolysis of X3 by *Ac*Xyn30B_12 showed the presence of X2 and X1 further corroborating its *exo*-xylanase activity (Fig. 3.7, lane-3). However, *Ac*Xyn30B_12 did not hydrolyze X2 (Fig. 3.7, lane-4), confirming its specificity for longer than X2 xylo-oligosaccharides. Similar results on hydrolysis of X6, X5, X4, X3 and X2 (each 0.6 mg/mL in 0.05 M sodium phosphate, pH 6) by *Ac*Xyn30B_12 (0.01 mg/mL) at 40°C for 24h were obtained by Suchova *et al.*, 2024, indicating both endo- and exo-acting mode of hydrolysis mechanism of the enzyme.

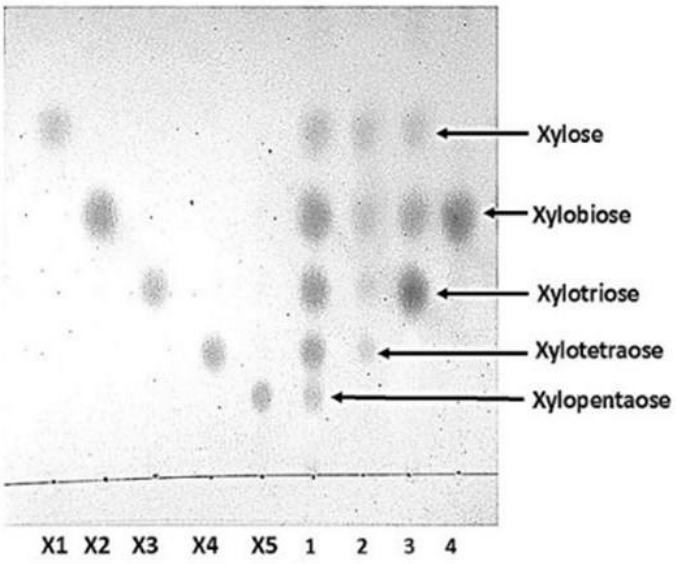

Fig. 3.7. *Ac*Xyn30B_12 hydrolysed products of 1.1% (w/v) xylopentaose, xylotetraose and xylotriose at 50°C, pH 5.5 for 1h. Lanes, X1-xylose, X2-xylobiose, X3-xylotriose, X4-xylotetraose, X5-xylopentaose; hydrolysed products of 1-xylopentaose, 2-xylotetraose, 3-xylotriose and 4-xylobiose.

3.3.6.3. HPLC analysis of *Ac*Xyn30B_12 hydrolysed products of PABX

The HPLC profiles of endo-β-1,4-xylanase, *Ac*Xyn30B_12 hydrolysed products of PABX at different time intervals and standard xylo-oligosaccharides (X5, X4, X3, X2 and X1) are depicted in Fig. 3.8 (A, B, C, D & E). The retention time of xylo-oligosaccharides produced by PABX hydrolysis (Fig. 3.8 B, C, D & E) corroborated with the retention time of standard xylo-oligosaccharides (Fig. 3.8 A). The HPLC chromatogram, indicated the existence of both X5 (*RT* = 22.6 min) and X4 (*RT* = 27.4 min) at 5 min hydrolysis time (Fig. 3.8 B). However, no peak for X3 was seen after 5 min as observed in TLC (Section 3.3.6.1). As shown in Fig. 3.8 C, at 15 min hydrolysis time, X5 produced at 5 min was hydrolysed to X3 (*RT* =32.6 min) and X2 (*RT* =36.2 min) showing endo mode of action. However, X5 was also hydrolysed to X4 (*RT* =27.4 min) and X1 (*RT* =42.9 min) after 1h (Fig. 3.8 D) showing its exo mode of action. As shown in Fig. 3.8 D, X4 produced at 5 min hydrolysis was hydrolysed to X2 (*RT* =36.2

min) after 1h showing endo mode of hydrolysis. Also, X4 was hydrolysed to X3 (*RT* =32.6 min) and X1 (*RT* =42.9 min) after 6h (Fig. 3.8 E). All these results corroborated with the hydrolysis pattern reported in the TLC analysis (Section 3.3.6.1). The HPLC and TLC results confirmed the *endo*-cleaving activity of *Ac*Xyn30B_12 for 1h and after that it acts in both endo- and exo-modes of hydrolysis.

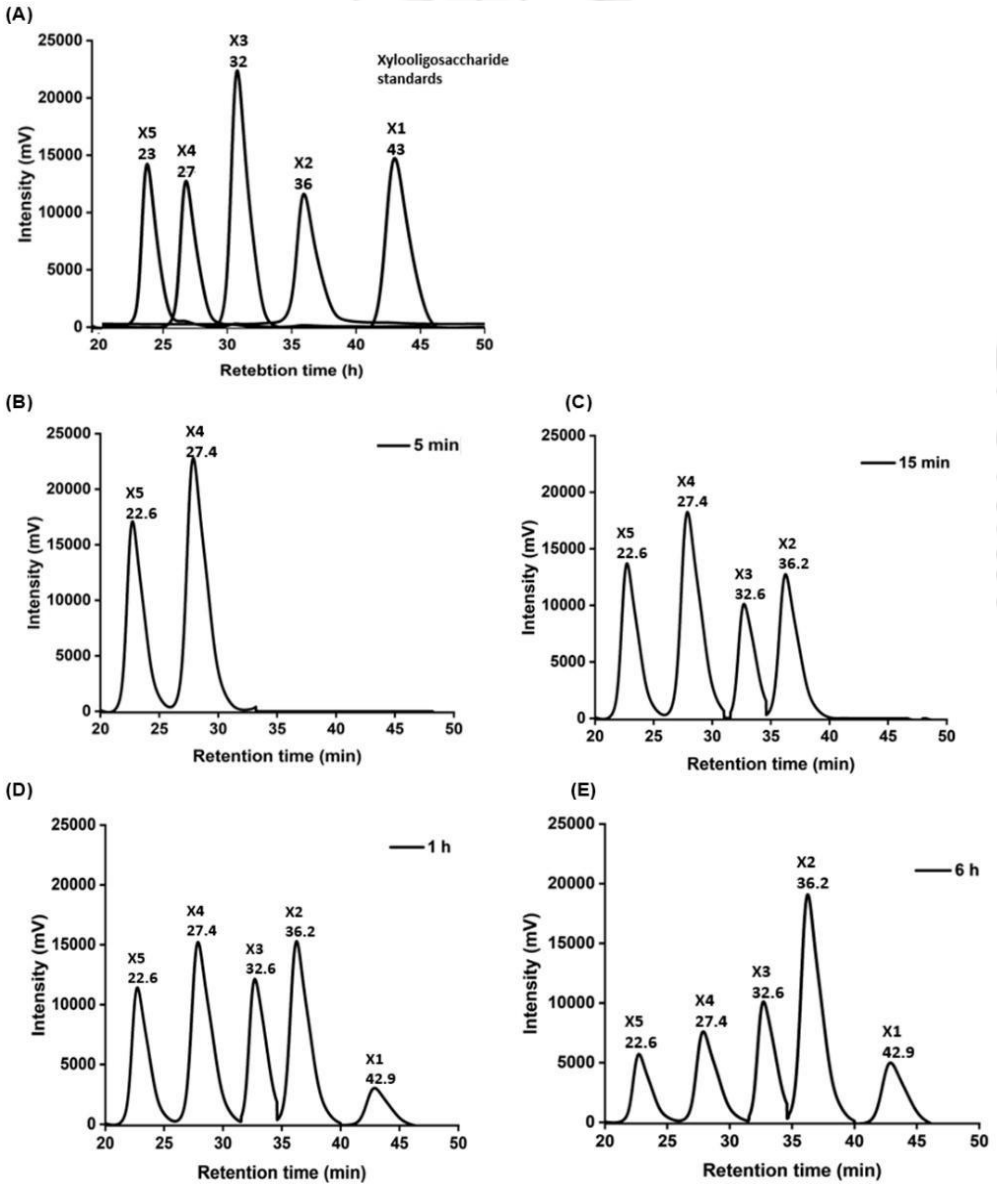

Fig. 3.8. HPLC analysis of **(A)** Xylo-oligosaccharide standards used: X1-xylose, X2-xylobiose, X3-xylotriose, X4-xylotetraose, X5-xylopentaose. *Ac*Xyn30B_12 hydrolysed products of PABX at **(B)** 5 min, **(C)** 15 min, **(D)** 1h and **(E)** 6h.

3.3.6.4. MALDI analysis of *Ac*Xyn30B_12 hydrolysed products of PABX

MALDI-TOF MS analysis of PABX hydrolyzed products of *Ac*Xyn30B_12 at 5 min, 15 min, 1h and 6h reaction time is displayed in Fig. 3.9 (A, B, C and D). The mass-to-charge ratio (*m*/*z*) for each xylo- oligosaccharide and xylose was detected as $[M+Na]^+$ after positive-ion mode ionization. The DHB matrix is represented by the peak at 198.5 *m/z* ratio Fig. 3.9 (A, B, C and D). The MALDI-TOF MS spectrum analysis showed that after 5 min hydrolysis, X5 (*m/z* ratio =701.1), X4 (*m/z* ratio =569.5) and X3 (*m/z* ratio=437.3) were present (Fig. 3.9A) showing endo mode of action. X5 (*m/z* ratio =701.1) produced after 5 min hydrolysis, was hydrolysed to X3 (*m/z* ratio =437.3) and X2 (*m/z* ratio =304.9) after 15 min (Fig. 3.9B). However, after 1h, X5 was hydrolysed to X4 (*m/z* ratio =569.5) and X1 (*m/z* ratio =173.7) as shown in Fig. 3.9C displaying its exo mode of action. X4 produced after 5 min hydrolysis, was hydrolysed to X2 after 1h (Fig. 3.9C) showing its continued endo cleaving activity. Moreover, X4 was also hydrolysed to X3 (*m/z* ratio =437.3) and X1 (*m/z* ratio =173.7) after 6h (Fig. 3.9D) showing its exolytic activity. Hence the MALDI-TOF MS results of time dependent hydrolysis of PABX corroborated with those reported for the TLC (Section 3.3.6.1) and HPLC analyses (Section 3.3.6.3). Therefore, all these results confirmed the *endo*-cleaving activity up to 1h and both endo- and exo- cleaving activity of *Ac*Xyn30B_12 after 1h. The xylo- oligosaccharide peaks obtained in the present study were nearly in line with the previously reported *m*/*z* ratio (Brasseur *et al*., 2014, Suchova *et al*., 2021). Similar findings were reported by Wang *et al*., 2015, where 80 U of purified xylanase enzyme, Xyn-lxy from Hu sheep rumen fluid hydrolyzed 1.0% (w/v) birchwood xylan at 50°C into shorter-length xylo-oligosaccharides (X3, X2) and X1 after 5 min of incubation. Following the 5 min hydrolysis, the concentrations of X1 and X2 increased as the reaction progressed and reached the stationary phase at 4h (Wang *et*

al., 2015). Also, the purified recombinant enzyme, *β*-1,4-xylanase (rXylU) from *Streptomyces mexicanus* HY-14 showed release of X5 to X1 while hydrolysing 10 mg birchwood xylan (in 50 mM sodium phosphate buffer, pH 5.5) when incubated for 12h at 30°C (Kim *et al*., 2014).

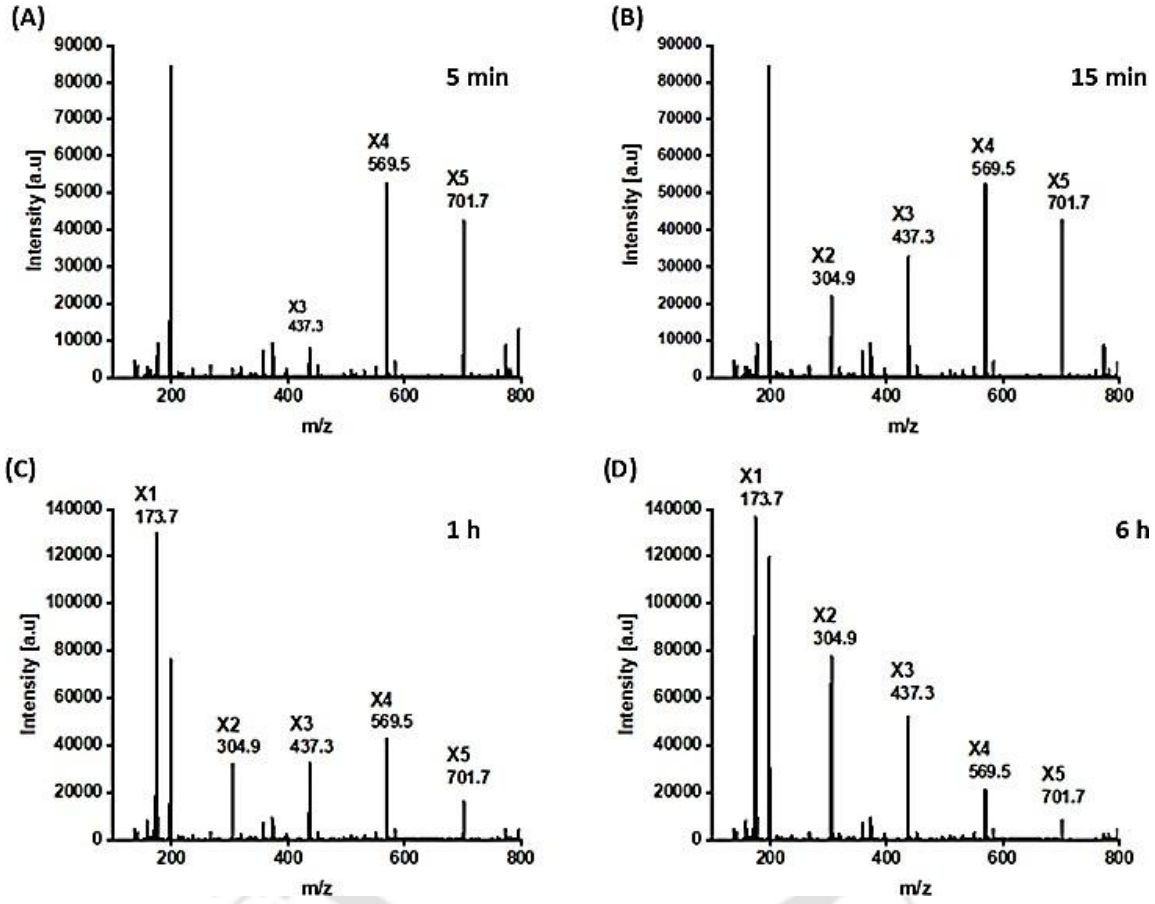

Fig. 3.9. MALDI-TOF mass spectrum of the products generated by *Ac*Xyn30B_12 cleavage of PABX at **(A)** 5min, **(B)** 15min, **(C)** 1h and **(D)** 6h reaction time at optimum conditions. Here X5- xylopentaose, X4-xylotetraose, X3-xylotriose, X2-xylobiose and X-xylose Putative xylo-oligosaccharides and their calculated masses are given above each detected mass signal.

3.3.6.5. Proposed hydrolysis mechanism of *Ac*Xyn30B

The hydrolytic mechanism of endo-*β*-1,4-xylanase, *Ac*Xyn30B_12 based on TLC, HPLC and MALDI-TOF MS results is proposed in Fig. 3.10. It shows that, initially in first 5 min, *Ac*Xyn30B_12 releases X5, X4 and X3 from polysaccharide PABX. *Ac*Xyn30B_12 further hydrolyses this released X5, to X3 and X2 at 15 min and later at 1h also to X4 and X1. *Ac*Xyn30B_12 also hydrolysed X4 to X2 at 1h and later at 6h to X3 and X1 confirming endo- and exo-mode of hydrolysis (as depicted in Fig. 3.10).

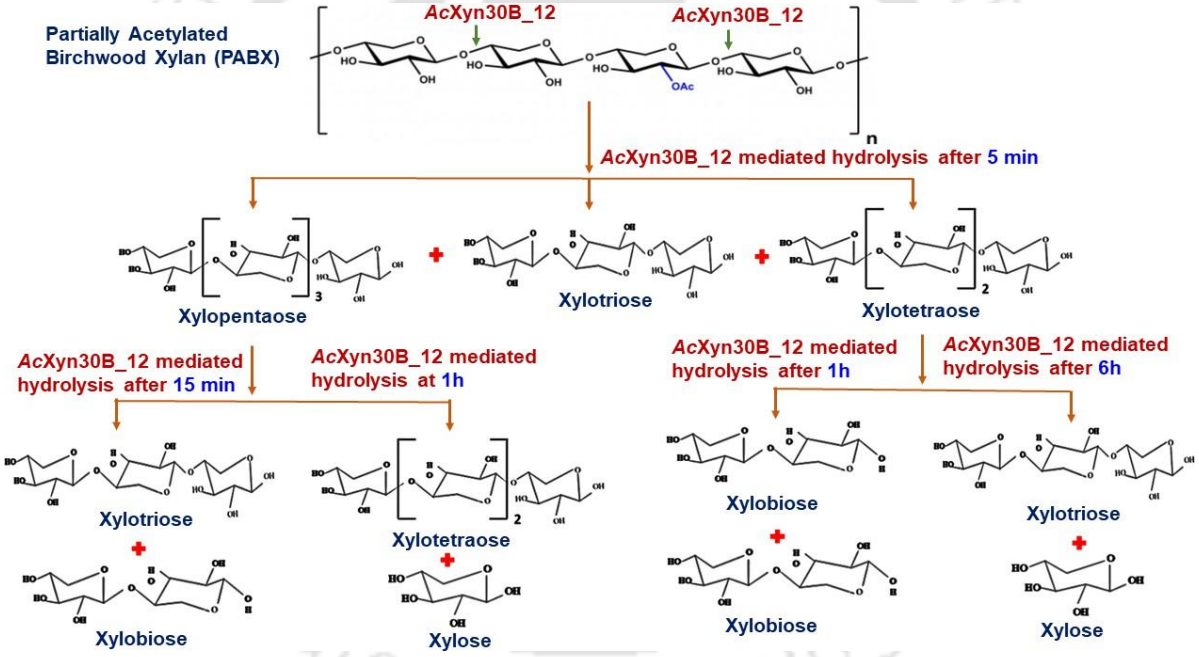

Fig. 3.10. Proposed hydrolysis mechanism of *Ac*Xyn30B_12 based on results of enzyme hydrolysis of PABX by TLC, HPLC and MALDI-TOF MS analyses.

3.3.7. Synergistic action of endo-*β*-1,4-xylanase, *Ac*Xyn30B_12 and xylobiohydrolase, *Ac*GH30A on hydrolysis of xylan substrates

3.3.7.1. Analysis of specific activity of *Ac*Xyn30B_12 or *Ac*GH30A and in combination

The role of endo-*β*-1,4-xylanase, *Ac*Xyn30B_12 in synergistic studies was investigated by combining with a xylobiohydrolase, *Ac*GH30A from *A. clariflavus*. The specific activity of the individual enzymes *Ac*Xyn30B_12 and *Ac*GH30A, as well as their combination in equimolar concentration (*Ac*Xyn30B_12 +*Ac*GH30A), were assessed on the hydrolysis of various xylan substrates (1.0% w/v, in 0.05 M citrate phosphate, pH 5.5) at 70°C for 3 min (Table 3.5). The activity of enzyme *Ac*Xyn30B_12 against all xylan substrates was increased by the presence of xylobiohydrolase, *Ac*GH30A, when analysed in the combination of the two. The combined enzymatic activity against 4-*O*-methylglucuronoxylan was 115.2 U/mg, showing a 40% increase as compared with the activity of *Ac*Xyn30B_12 alone (82 U/mg). Additionally, the specific activity against beechwood xylan was 96.9 U/mg, reflecting a 12% increase as compared with the activity of *Ac*Xyn30B_12 alone (86.6 U/mg).

The TRS produced from the hydrolysis of various xylan substrates (1.0% w/v, in 0.05 M citrate phosphate, pH 5.5) by both enzymes together (*Ac*Xyn30B_12 +*Ac*GH30A) gave much higher values as compared with the individual enzymes *Ac*Xyn30B_12 or *Ac*GH30A at 50°C for 1h (Table 3.5). The TRS released from the hydrolysis of xylan from Carbosynth by the combined action of *Ac*Xyn30B_12 and *Ac*GH30A (0.48 mg/mL) was 2.3-fold higher than TRS released by *Ac*Xyn30B_12 alone (0.21 mg/mL). Similarly, the TRS released from the hydrolysis of beechwood xylan by the enzyme combination (0.47 mg/mL) was 2.1-fold higher than *Ac*Xyn30B_12 alone (0.22 mg/mL). All these results demonstrated the synergistic effect of *Ac*Xyn30B_12 and *Ac*GH30A in hydrolysing different xylan substrates.

Table 3.5. Hydrolysis of xylan substrates by *Ac*Xyn30B_12 or *Ac*GH30A and in combination.

	***Enzyme specific activity* (U/mg)**		
Xylan (1.0%, w/v)	***Ac*Xyn30B_12 (0.7 µM)**	***Ac*GH30A (0.7 µM)**	***Ac*Xyn30B_12 (0.7 µM) +*Ac*GH30A (0.7 µM)**
4-O-methylglucurono Xylan	82.0 ± 0.2	122.0 ± 0.2	115.2 ± 0.9
Partially Acetylated Birchwood Xylan	105.5 ± 0.4	NA	108.6 ± 0.2
Xylan Carbosynth (MW, 20-30 kDa)	96.8 ± 0.2	109.9 ± 0.1	102.2 ± 0.5
Acacia saw dust Xylan (in house)	96.3 ± 0.3	102.4 ± 0.4	101.9 ± 0.3
Beechwood Xylan	86.6 ± 0.1	88.2 ± 0.1	96.9 ± 0.3
Larchwood Xylan	84.6 ± 0.4	99.6 ± 0.5	87.3 ± 0.2
Rye arabino Xylan	80.5 ± 0.0	74.3 ± 0.0	87.0 ± 0.0
Oat spelt Xylan	76.7 ± 0.2	84.6 ± 0.5	85.1 ± 0.2
Wheat arabino Xylan	74.9 ± 0.1	69.7 ± 0.0	79.3 ± 0.1
***Total reducing sugar, TRS* (mg/mL)**			
4-*O*-methylglucurono Xylan	0.35	0.30	0.56
Xylan Carbosynth (MW- 20-30 kDa)	0.21	0.15	0.48
Beechwood Xylan	0.22	0.11	0.47

3.3.7.2. TLC analysis of hydrolysed products of xylan substrates by *Ac*Xyn30B_12 or *Ac*GH30A and in combination

The TLC analysis of the hydrolysed products of xylan Carbosynth, beechwood xylan and 4-*O*-methyl-D-glucurono xylan by *Ac*Xyn30B_12 showed that it releases X5 to X1 (also mentioned in Section 3.3.6.1) and *Ac*GH30A releases only X2 as also reported earlier (Singh *et al*., 2024), whereas the combined action of *Ac*Xyn30B_12 +*Ac*GH30A showed the presence of only X2 and X1, confirming the disappearance of X5 to X4 and X3 (Fig. 3.11A, lanes-3, 6 and 9). This result confirmed that the xylo-oligosaccharides (X5-X3) produced by *Ac*Xyn30B_12 alone were further digested by xylobiohydrolase, *Ac*GH30A.

The hydrolysis of X5 by xylo-biohydrolase, *Ac*GH30A showed the presence of X3 and X2 (Fig. 3.11B, lane-1). The hydrolysis of X4 by *Ac*GH30A showed the presence of only X2 (Fig. 3.11B, lane-2). However, *Ac*GH30A did not hydrolyse X3 and X2 as unhydrolyzed X3 and X2, respectively, were observed (Fig. 3.11B lanes 3 and 4). As already seen in Section 3.3.6.2, *Ac*Xyn30B_12 was found to hydrolyze X5 into X4, X3, X2 and X1; X4 into X2 as well as into X3 and X1 and X3 into X2 and X1. All these results clearly indicate that X5 will be utilized by both enzymes *Ac*Xyn30B_12 and *Ac*GH30A to give X3 and X2 which is challenging to precisely determine which enzyme is responsible for releasing these products. Similarly, X4 is also utilized by both the enzymes to give X2 again making it difficult to elucidate which enzyme of the two resulted it. Moreover, as *Ac*GH30A did not hydrolyse X3, further indicated that it requires at least two xylose residues at the non-reducing end of xylan chain for its cleaving action. In contrast, *Ac*Xyn30B_12 could cleave X3 to X2 and X1. However, both the enzymes did not cleave X2 thereby necessitating the requirement of xylosidase for its breakdown.

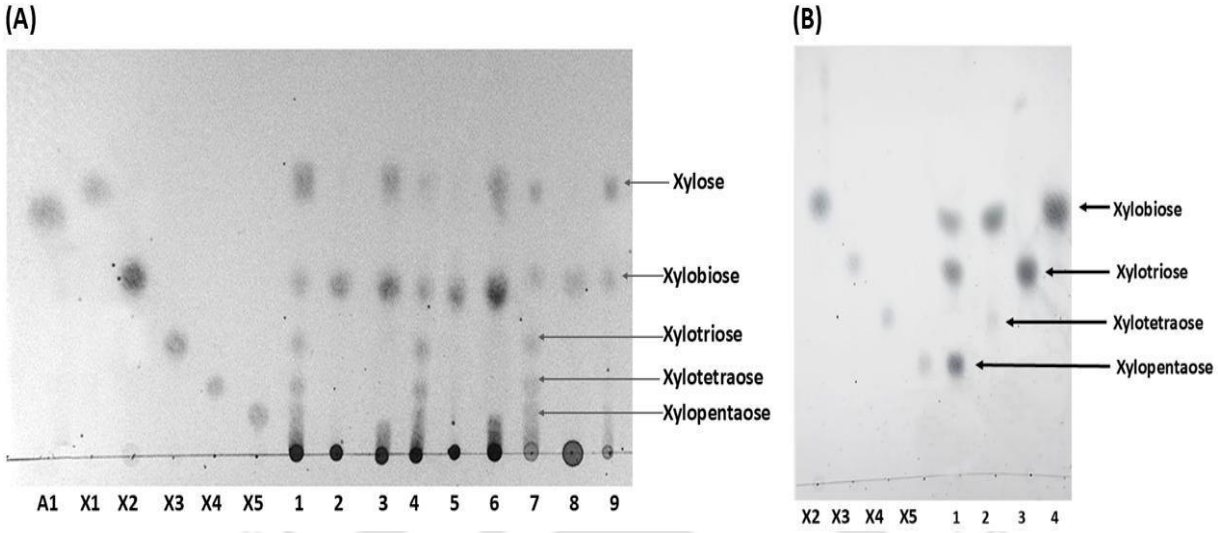

Fig. 3.11. TLC analysis of **(A)** Synergistic effect in hydrolysis of different xylan substrates (1.0%, w/v, 0.05 M citrate phosphate buffer, pH 5.5) by *Ac*Xyn30B_12 and *Ac*GH30A (each 0.7 µM) at 50°C for 1h. Standards: A1-arabinose, X1-xylose, X2-xylobiose, X3-xylotriose, X4-xylotetraose, X5-xylopentaose. Lanes: 1-xylan Carbosynth+*Ac*Xyn30B_12, 2-xylan Carbosynth+*Ac*GH30A, 3-xylan Carbosynth+*Ac*Xyn30B_12+*Ac*GH30A, 4-beechwood xylan+*Ac*Xyn30B_12, 5-beechwood xylan+*Ac*GH30A, 6-beechwood xylan+*Ac*Xyn30B_12+*Ac*GH30A, 7-4-O-methylglucurono xylan+*Ac*Xyn30B_12, 8-4-O-methylglucuronoxylan+*Ac*GH30A,9-4-O-methylglucurono xylan+*Ac*Xyn30B_12+*Ac*GH30A and **(B)** Xylobiohydrolase, *Ac*GH30A hydrolysed products of 1% (w/v) xylopentaose, xylotetraose, xylotriose or xylobiose at 40°C, pH 7.0 for 1h. Lanes, X2-xylobiose, X3-xylotriose, X4-xylotetraose, X5-xylopentaose; hydrolysed products of 1-xylopentaose, 2- xylotetraose, 3- xylotriose, 4-xylobiose.

3.3.7.2.1. Analysis of *Ac*Xyn30B_12 hydrolyzed products of pretreated lignocellulosic biomass

The biomass pretreatment prior to hydrolysis by *Ac*Xyn30B_12 was carried out as described in Section 3.2.10 and is schematically presented in Fig. 3.12. The raw biomasses (biomass before pretreatment) *viz*. napier grass, rice straw and kans grass are depicted in Fig. 3.12A, B and C, respectively. Their corresponding pretreated and dried forms, which were subsequently used for hydrolysis by *Ac*Xyn30B_12, are shown in Fig. 3.12a, b and c.

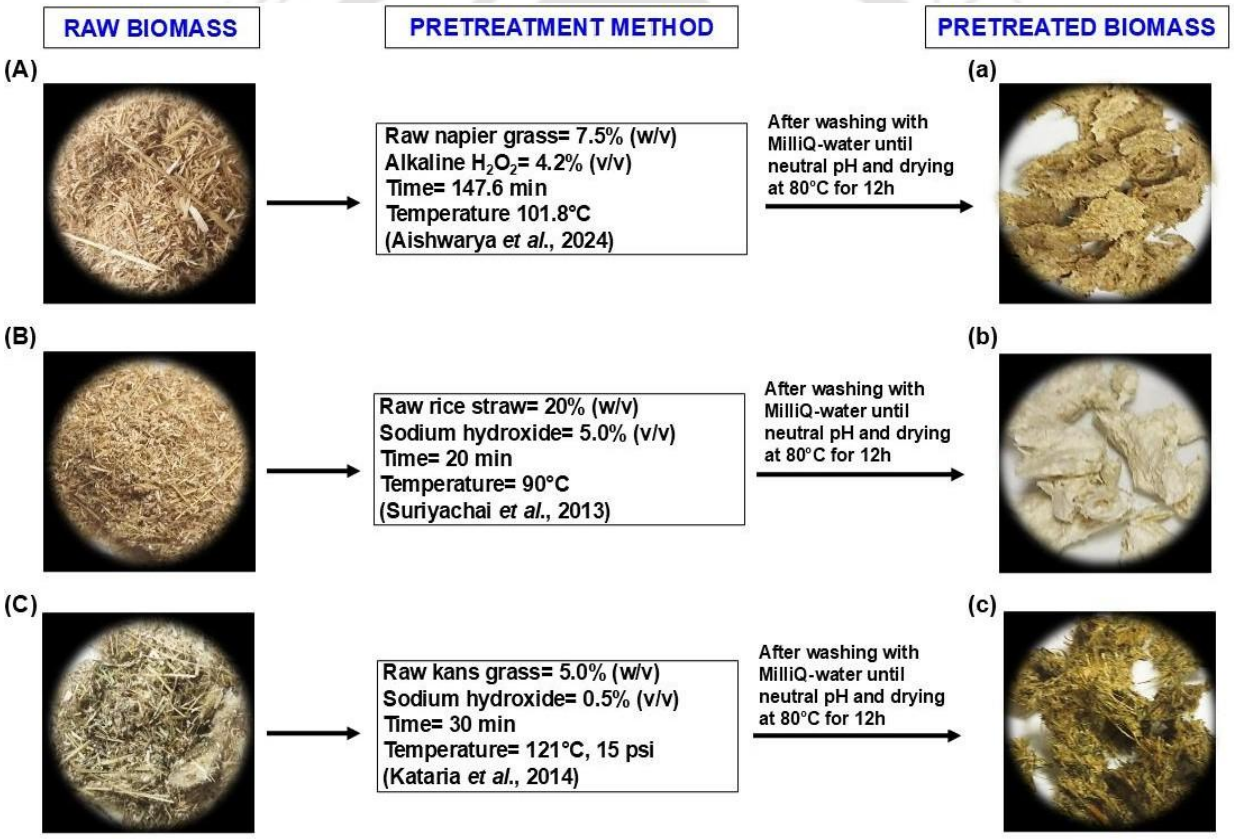

Fig. 3.12. Schematic diagram of pretreatment of the three biomasses. **(A)** Napier grass **(B)** Rice straw and **(C)** Kans grass are the raw biomasses before pretreatment. **(a)** Napier grass **(b)** Rice straw and **(c)** Kans grass are the pretreated biomasses.

The hydrolyzed products of 2.0% (w/v) pretreated Kans grass, Rice straw or Napier grass in 0.05 M citrate phosphate, pH 5.5 by endo-β-1,4-xylanase, *Ac*Xyn30B_12 (600 U/g, 0.05 mg/mL) at 50°C from 12h-72h showed the presence of

X5-X2 and X1 (Fig. 3.13A, B & C, lanes-1-4). This proved that the enzyme, *Ac*Xyn30B_12 can independently and efficiently degrade the xylan polysaccharides of different pretreated biomass into various degrees of xylo-oligosaccharides and xylose. The highest TRS released on hydrolysis of 2.0% (w/v) kans grass, napier grass and rice straw by *Ac*Xyn30B_12 were 22.5 ±0.1 mg/g, 19.0 ±0.1 mg/g and 17.5 ±0.2 mg/g, respectively, at 72h (Fig. 3.13a, b & c). The TRS profile for *Ac*Xyn30B_12 hydrolyzed biomasses showed saturation after 60h of reaction (Fig. 3.13a, b & c). The TRS yield of pretreated Rice straw (17.5 mg/g) on hydrolysis by *Ac*Xyn30B_12 was 1.4-fold high than the TRS yield (12.7 mg/g) of 1.0% (w/v) pretreated (NaOH combined with sonication) finger millet straw in 50 mM sodium phosphate buffer, pH 7.5 on hydrolysis by an endo-*β*-1,4-xylanase, *Ct*Xyn11A (100 U/g) from *Clostridium thermocellum* in 1.0 mL reaction volume, at 65°C for 1h (Jamaldheen *et al*., 2019). The TRS yield of pretreated kans grass (22.5 mg/g) on hydrolysis by *Ac*Xyn30B_12 was 1.5-fold high than the TRS yield (15.3 mg/g) of 1.0% (w/v) pretreated sugarcane bagasse in 50 mM sodium phosphate buffer, pH 7.5 on hydrolysis by an endo-*β*-1,4-xylanase, *Ct*Xyn11A (100 U/g) from *Clostridium thermocellum* in 1.0 mL reaction volume, at 65°C for 3h (Thakur *et al*., 2021). This shows the ability of *Ac*Xyn30B_12 to have a significant efficiency of hydrolysis of hemicellulose components of pretreated biomass.

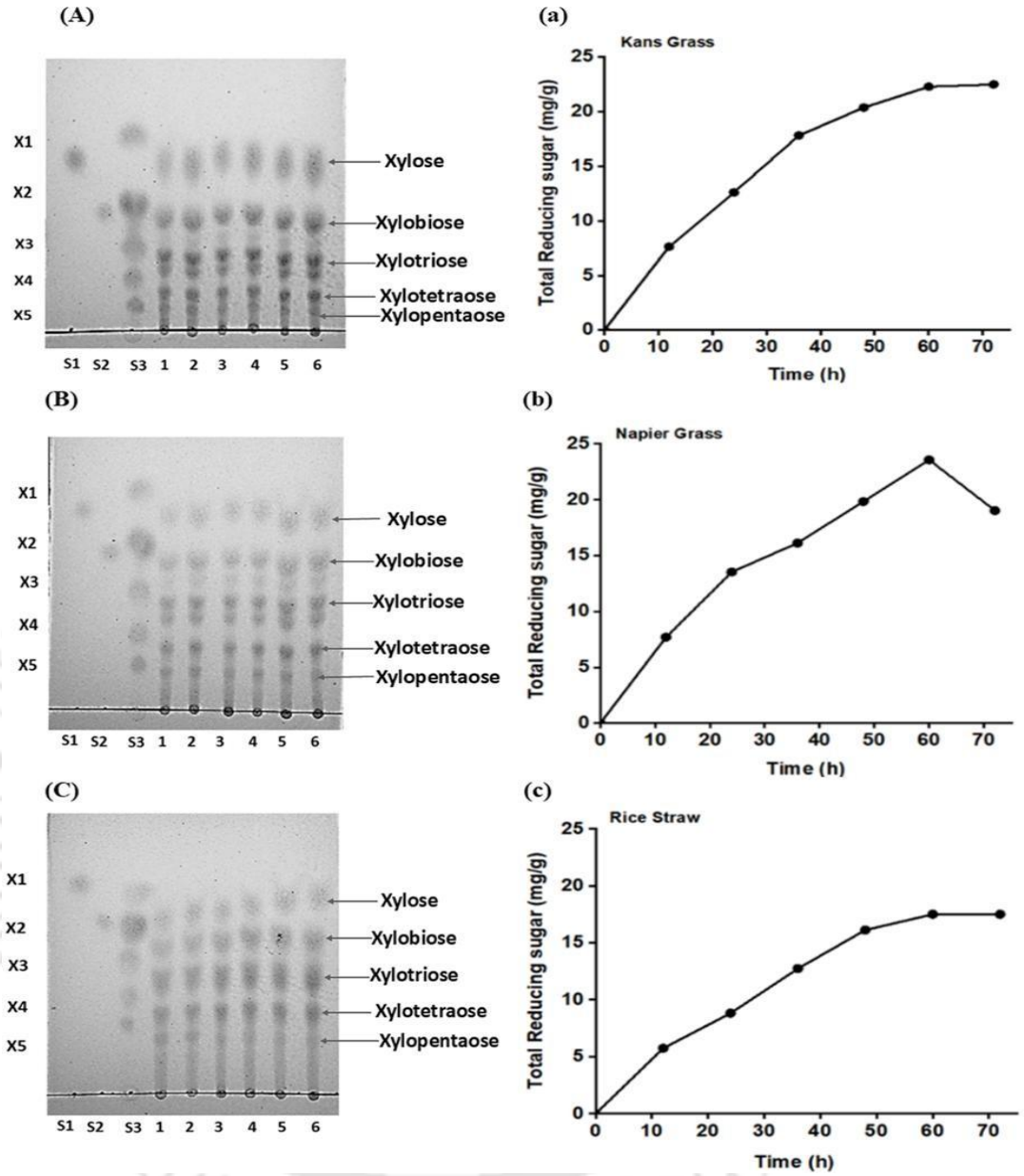

Fig. 3.13. Thin layer chromatography analysis of hydrolysis of pretreated 2% (w/v) **(A)** Kans grass, **(B)** Napier grass and **(C)** Rice straw by *Ac*Xyn30B_12 (50 µg/mL) at 50°C and 0.05 M citrate phosphate buffer, pH 5.5 for 72h. Lanes, Standards S1: arabinose, S2: glucuronic acid and S3: X1-xylose, X2-xylobiose, X3- xylotriose, X4-xylotetraose, X5-xylopentaose. Lanes,1-12h, 2-24h, 3-36h, 4-48h, 5-60h and 6-72h. Plot of total reducing sugar (TRS) concentration (mg/g) vs time (h) after hydrolysis of pretreated 2% (w/v) **(a)** Kans grass, **(b)** Napier grass and **(c)** Rice straw by *Ac*Xyn30B_12 (50 µg/mL) at 50°C and 0.05 M citrate phosphate buffer, pH 5.5 for 72h.

3.4. Conclusion

An endo-*β*-1,4-xylanase, *Ac*Xyn30B_12 from *Acetivibrio clariflavus* DSM 19732 was purified, which displayed a molecular size of ~74 kDa. It displayed maximum activity at pH 5.5 and 70°C. *Ac*Xyn30B_12 exhibited broad substrate specificity, with the highest catalytic efficiency against partially acetylated birchwood xylan (PABX), yielding a V_{max} of 133.3 U/mg and a K_M of 0.9 mg/mL. *Ac*Xyn30B_12 activity was enhanced by Ca^{2+} (10%) and Mg^{2+} (7.3%) ions. The enzyme also showed notable thermostability and pH tolerance, maintaining activity up to 60°C and within a pH range of 4.5-8.0. Time-course hydrolysis experiments revealed the ability of *Ac*Xyn30B_12 to release a variety of xylo-oligosaccharides (from xylopentaose to xylobiose) and xylose from PABX, confirming both its *endo* and *exo*-acting mechanisms. Additionally, *Ac*Xyn30B_12 effectively degraded lignocellulosic biomass, releasing significant amounts of xylo-oligosaccharides and xylose from complex substrates. In contrast, *Ac*GH30A, previously characterized as an *exo*-xylobiohydrolase, removes xylobiose from non-reducing ends of xylan and xylo-oligosaccharides. This study also demonstrated the synergistic action of *Ac*GH30A and *Ac*Xyn30B_12 in complex carbohydrate hydrolysis, with *Ac*Xyn30B_12 generating the non-reducing ends that serve as substrates for *Ac*GH30A. This enzyme synergy underscores the potential industrial applications of these enzymes in high-temperature processes, including prebiotic production, bioethanol generation and the paper and pulp industries.

3.5. References

Aishwarya, A., Maibam, P.D., Goyal, A. (2024) Statistical optimization of thermo-chemical pretreatment of elephant grass for efficient delignification and enzymatic saccharification. Biomass Conversion and Biorefinery, 1, 1–12.

Brasseur, C., Bauwens, J., Tarayre, C., Mattéotti, C., Thonart, P., Destain, J., Francis, F., Haubruge, E., Portetelle, D., Vandenbol, M., Focant, J.F. (2014) MALDI-TOF MS analysis of cellodextrins and xylo-oligosaccharides produced by hindgut homogenates of *Reticulitermes santonensis*. Molecules, 19, 4578–4594.

Bradford, M. (1976) A rapid and sensitive method for quantification of microgram quantities of protein utilizing the principle of protein-dye binding. Analytical Biochemistry, 72, 248-254.

Boivin, S., Kozak, S., Meijers, R. (2013) Optimization of protein purification and characterization using Thermofluor screens. Protein Expression and Purification, 91, 192–206.

Collins, T., Gerday, C., Feller, G. (2005) Xylanases, xylanase families and extremophilic xylanases. FEMS Microbiology Reviews, 29, 3–23.

Dobrev, G., Zhekova, B., Delcheva, G., Koleva, L., Tziporkov, N., Pishtiyski, I. (2009) Purification and characterization of endo-xylanase Xln-1 from *Aspergillus niger* B03. World Journal of Microbiology and Biotechnology, 25, 2095–2102.

Gavande, P.V., Nath, P., Kumar, K., Ahmed, N., Fontes, C.M., Goyal, A. (2022) Highly efficient, processive and multifunctional recombinant endoglucanase RfGH5_4 from *Ruminococcus flavefaciens* FD-1 v3 for recycling lignocellulosic plant biomasses. International Journal of Biological Macromolecules, 209, 801–813.

Jamaldheen, S.B., Thakur, A., Moholkar, V.S., Goyal, A. (2019) Enzymatic hydrolysis of hemicellulose from pretreated Finger millet (Eleusine coracana) straw by recombinant endo-1,4-β-xylanase and exo-1,4-β-xylosidase. International Journal of Biological Macromolecules, 135, 1098–1106.

Kataria, R., Ghosh, S. (2014) NaOH pretreatment and enzymatic hydrolysis of *Saccharum spontaneum* for reducing sugars production. Energy Sources Part A Recovery Utilization and Environmental Effects, 36, 1028–1035.

Khaire, K.C., Sharma, K., Thakur, A., Moholkar, V.S., Goyal, A. (2021) Extraction and characterization of xylan from sugarcane tops as a potential commercial substrate. Journal of Bioscience and Bioengineering, 131, 647–654.

Khaire, K.C., Moholkar, V.S., Goyal, A. (2022) A biorefinery approach for sequential extraction of commercial grade xylan and alkali lignin from alkali pretreated sugarcane tops hydrolysate. Industrial Crops and Products, 187, 115545.

Kim, D.Y., Shin, D.H., Jung, S., Lee, J.S., Cho, H.Y., Bae, K.S., Park, H.Y. (2014) Biocatalytic properties and substrate-binding ability of a modular GH10 β-1,4-

xylanase from an insect-symbiotic bacterium, Streptomyces mexicanus HY-14. Journal of Microbiology, 52, 863–870.

Layne, E. (1957) Spectrophotometric and turbidimetric methods for measuring proteins. Methods in Enzymology, 3, 447-455.

Lucet, I.S., Hildebrand, J.M., Czabotar, P.E., Zhang, J.G., Nicola, N.A., Silke, J., Babon, J.J., Murphy, J.M. (2014) Determination of pseudokinase-ligand interaction by a fluorescence-based thermal shift assay. Bio-protocol, 4.

Maehara, T., Yagi, H., Sato, T., Ohnishi-Kameyama, M., Fujimoto, Z., Kamino, K., Kaneko, S. (2018) GH30 glucuronoxylan-specific xylanase from *Streptomyces turgidiscabies* C56. Applied and Environmental Microbiology, 84.

Nakamichi, Y., Fujii, T., Fouquet, T., Matsushika, A., Inoue, H. (2019) GH30-7 endoxylanase C from the filamentous fungus *Talaromyces cellulolyticus*. Applied and Environmental Microbiology, 85(22), e01442-19.

Nath, P., Dhillon, A., Kumar, K., Sharma, K., Jamaldheen, S.B., Moholkar, V.S., Goyal, A. (2019) Development of bi-functional chimeric enzyme (CtGH1-L1-CtGH5-F194A) from endoglucanase (CtGH5) mutant F194A and β-1,4-glucosidase (CtGH1) from *Clostridium thermocellum* with enhanced activity and structural integrity. Bioresource Technology, 282, 494–501.

Nawaz, M.H., Ferreira, J.C., Nedyalkova, L., Zhu, H., Carrasco-López, C., Kirmizialtin, S., Rabeh, W.M. (2018) The catalytic inactivation of the N-half of human hexokinase 2 and structural and biochemical characterization of its mitochondrial conformation. Bioscience Reports, 38.

Nelson, N. (1944) A photometric adaptation of the Somogyi method for the determination of glucose. Journal of Biological Chemistry, 3, 375–380.

Neuhoff, V., Arold, N., Taube, D., Ehrhardt, W. (1988) Improved staining of proteins in polyacrylamide gels including isoelectric focusing gels with clear background at nanogram sensitivity using Coomassie Brilliant Blue G-250 and R-250. Electrophoresis, 9, 255–262.

Santibanez, L., Henríquez, C., Corro-Tejeda, R., Bernal, S., Armijo, B., Salazar, O. (2021) Xylo-oligosaccharides from lignocellulosic biomass: a comprehensive review. Carbohydrate Polymers, 251, 117118.

Sharma, K., Morla, S., Khaire, K.C., Thakur, A., Moholkar, V.S., Kumar, S., Goyal, A. (2020) Extraction, characterization of xylan from *Azadirachta indica* (neem) sawdust and production of antiproliferative xylooligosaccharides. International Journal of Biological Macromolecules, 163, 1897–1907.

Sharma, K., Khaire, K.C., Thakur, A., Moholkar, V.S., Goyal, A. (2020) Acacia xylan as a substitute for commercially available xylan and its application in the production of xylooligosaccharides. ACS Omega, 5, 13729–13738.

Singh, Y.R., Thakur, A., Fontes, C.M., Goyal, A. (2024) A novel thermophilic recombinant obligate xylobiohydrolase (AcGH30A) from *Acetivibrio clariflavus* orchestrates the deconstruction of xylan polysaccharides. Carbohydrate Polymers, 340, 122295.

Somogyi, M. (1945) A new reagent for the determination of sugars. Journal of Biological Chemistry, 160, 61–68.

Steinberg, T.H., Jones, L.J., Haugland, R.P., Singer, V.L. (1996) SYPRO orange and SYPRO red protein gel stains: one-step fluorescent staining of denaturing gels for detection of nanogram levels of protein. Analytical Biochemistry, 239, 223–237.

St. John, F.J., Rice, J.D., Preston, J.F. (2006) Characterization of XynC from *Bacillus subtilis* subsp. subtilis strain 168 and analysis of its role in depolymerization of glucuronoxylan. Journal of Bacteriology, 188, 8617–8626.

St. John, F.J., Dietrich, D., Crooks, C., Pozharski, E., Gonz´alez, J.M., Bales, E., Smith, K., Hurlbert, J.C. (2014) A novel member of glycoside hydrolase family 30 subfamily 8 with altered substrate specificity. Acta Crystallographica Section D Biological Crystallography, 70, 2950–2958.

St. John, F.J., Dietrich, D., Crooks, C., Balogun, P., de Serrano, V., Pozharski, E., Hurlbert, J. (2018) A plasmid-borne, functionally novel glycoside hydrolase family 30 subfamily 8 endo-xylanase from solventogenic Clostridium. Biochemical Journal, 475, 1533–1551.

Stoscheck, C.M. (1990) Quantification of protein. Methods in Enzymology, 182, 50-69.

Suchova, K., Puchart, V. (2024) Characterization of a novel GH30 non-specific endoxylanase AcXyn30B from *Acetivibrio clariflavus*. Applied Microbiology and Biotechnology, 108, 312.

Suchova, K., Puchart, V., Spodsberg, N., Krogh, M.M., Biely, P. (2021) Catalytic diversity of GH30 xylanases. Molecules, 26(15), 4528.

Suriyachai, N., Weerasaia, K., Laosiripojana, N., Champreda, V., Unrean, P. (2013) Optimized simultaneous saccharification and co-fermentation of rice straw for ethanol production by *Saccharomyces cerevisiae* and *Scheffersomyces stipitis* co-culture using design of experiments. Bioresource Technology, 142, 171–178.

Thakur, A., Sharma, K., Jamaldheen, S.B., Goyal, A. (2020) Molecular characterization, regioselective and synergistic action of first recombinant Type III α-L-arabinofuranosidase of family 43 glycoside hydrolase (PsGH43_12) from *Pseudopedobacter saltans*. Molecular Biotechnology, 62, 443–455.

Thakur, A., Sharma, K., Khaire, K.C., Moholkar, V.S., Pathak, P., Bhardwaj, N.K., Goyal, A. (2021) Two-step saccharification of the xylan portion of sugarcane waste by recombinant xylanolytic enzymes for enhanced xylose production. ACS Omega, 6, 11772–11782.

Valenzuela, S.V., Diaz, P., Pastor, F.J. (2012) Modular glucuronoxylan-specific xylanase with a family CBM35 carbohydrate-binding module. Applied and Environmental Microbiology, 78(11), 3923–3931.

Verma, A.K., Goyal, A. (2016) A novel member of family 30 glycoside hydrolase subfamily 8 glucuronoxylan endo-β-1,4-xylanase (CtXynGH30) from

Clostridium thermocellum orchestrates catalysis on arabinose-decorated xylans. Journal of Molecular Catalysis B: Enzymatic, 129, 6–14.

Wang, Q., Luo, Y., He, B., Jiang, L.S., Liu, J.X., Wang, J.K. (2015) Characterization of a novel xylanase gene from rumen content of Hu sheep. Applied Biochemistry and Biotechnology, 177, 1424–1436.

Yogalakshmi, K.N., Sivashanmugam, P., Kavitha, S., Kannah, Y., Varjani, S., Kumar, S., Kumar, G. (2022) Lignocellulosic biomass-based pyrolysis: a comprehensive review. Chemosphere, 286, 131824.

Chapter 4

Structure and functional insights into an endo-*β*-1,4-xylanase (*Ac*Xyn30B_12) from thermophilic *Acetivibrio clariflavus* DSM 19732

4.1. Introduction

Hemicellulose, a major structural polysaccharide in lignocellulosic biomass, accounts for approximately 20-35% of plant cell walls and is characterized by its branched, amorphous nature (Saini *et al*., 2015). Among hemicellulose polysaccharides, xylan is the most abundant, composed of a *β*-1,4-linked D-xylopyranose backbone that may be substituted with side groups such as arabinofuranosyl, acetyl, glucuronosyl and feruloyl residues. These substitutions vary depending on the plant source and influence the solubility, recalcitrance and enzymatic accessibility of the xylan structure. Complete depolymerization of xylan requires the concerted action of several enzymes, including endo-*β*-1,4-xylanases, *β*-xylosidases, *α*-glucuronidases and acetyl xylan esterases. Among all the xylanolytic enzymes present in GH30 family, endo-*β*-1,4-xylanase (EC 3.2.1.8), marks an important role as it is involved in direct cleavage of *β*(1-4) glycosidic bonds in xylan chains liberating xylo-oligosaccharides (XOS) (Santibáñez *et al*., 2021). GH30 endo-*β*-1,4-xylanases are skilled at detecting the side chains of glucuronic acid in order to recognize the xylan primary backbone (Šuchová *et al*., 2018). As single- domain enzymes, GH30 endo-*β*-1,4-xylanases have a typical $(\beta/\alpha)_8$ barrel catalytic domain fused to a side *β*-structure of 9 strands that is necessary for catalytic activity

(Moreira *et al*., 2016). For hydrolysis of xylan substrates, mechanism followed by GH30 endo xylanases is retaining mechanism of hydrolysis.

Till date, few endo-xylanases from GH30 family have been structurally characterized. The endo-*β*-1,4-xylanase *Ec*Xyn30A from *Erwinia chrysanthemi* was the first 3D structure solved (Puchart *et al*., 2021). The $(\beta/\alpha)_8$- barrel motif in the catalytic domain (residues 46 to 315) features a binding cleft with the C-terminal of the *β*-barrel. The two catalytic amino acid residues Glu165 and Glu253 found were having a distance of 4.22 Å between them (Larson *et al*., 2003). The modelled structure of glucuronoxylan-xylanohydrolase, C*t*XynGH30 showed the main catalytic core consists of a $(\beta/\alpha)_8$ barrel fold with a *β*-strand rich region also known as 'side *β*-structure' (Verma *et al*., 2014). Structural superimposition of C*t*XynGH30 reflected Glu136 and Glu225 as a catalytic acid/base and catalytic nucleophile respectively (Verma *et al*., 2014). Xylanase, *Rf*GH30 from *Ruminococcus flavefaciens* on homology modelling revealed $(\beta/\alpha)_8$ TIM barrel like topology accompanied by a 'side *β*-structure' (Singh *et al*., 2023). The two catalytic residues found in *Rf*GH30 were Glu200 and Glu302 with a distance of 5.6 Å (Singh *et al*., 2023).

Acetivibrio clariflavus DSM 19732, is a thermophilic anaerobe, chemo-organotrophic, curved and rod-shaped bacterium (Artzi *et al*., 2014). A xylan specific and a thermostable endo-*β*-1,4-xylanase belonging to family 30 glycoside hydrolase (GH30) was identified in its genome. The gene encoding *Ac*Xyn30B_12 (GenBank accession no. AEV69300.1) was cloned, expressed and biochemically characterized showing high thermostability and stability across a wide pH range as reported in Chapter 2 and 3. In this study, the molecular arrangement, stability as well as the conformational behaviour of the protein, *Ac*Xyn30B_12 in solution form were determined. The

molecular dynamic (MD) simulation and homology modelling were used for characterization of the structure, conformational flexibility and stability of *Ac*Xyn30B_12. Small angle X-ray scattering and dynamic light scattering investigations were carried out for elucidation of the conformation and molecular organization of *Ac*Xyn30B_12 structure in solution state.

4.2. Materials and methods

4.2.1. Amino acid sequence analysis of *Ac*Xyn30B_12

The amino acid sequence of endo-*β*-1,4-xylanase from family GH30 (*Ac*Xyn30B_12) from *Acetivibrio clariflavus* DSM 19732 with GenBank accession no. AEV69300.1 and UniParc ID: UP000005435 was redeemed from NCBI database (http://www.ncbi.nlm.nih.gov). The calculated molecular mass, the isoelectric point (pI) and the molar extinction coefficient of *Ac*Xyn30B_12 were calculated from ExPASY-ProtParam server (https://web.expasy.org/cgi-bin/protparam/protparam) (Gasteiger *et al*., 2005). To search for homologous sequences of *Ac*Xyn30B_12, its amino acid sequence was submitted to the PDB-BLAST tool(https://blast.ncbi.nlm.nih.gov/Blast.cgi) (Boratyn *et al*., 2013). Following the PDB-BLAST analysis, multiple sequence alignment (MSA) of these homologous sequences were carried out by utilizing Clustal Omega (https://www.ebi.ac.uk/Tools/msa/clustalo/) (Sievers *et al*., 2014) and then visualized by using ESPript 3.0 (https://espript.ibcp.fr/ESPript/cgi-bin/ESPript.cgi) (Gouet *et al*., 1999). The different metal ion binding sites in *Ac*Xyn30B_12 was identified and analysed by submitting the amino acid sequence of *Ac*Xyn30B_12 into the Metal Ion-Binding site prediction and modeling server (MIB2) server (https://combio.life.nctu.edu.tw/MIB2/).

4.2.2. Expression and purification of *Ac*Xyn30B_12

The gene (1.9 kb) encoding the full-length *Ac*Xyn30B_12 containing (excluding the signal peptide) was cloned, expressed and purified as reported in Chapter 2 and Chapter 3.

4.2.3. Secondary structure elements analysis of *Ac*Xyn30B_12

Using the circular dichroism (CD) approach, the secondary structural study of *Ac*Xyn30B_12 was analysed. Before analysis, the purified *Ac*Xyn30B_12 enzyme was centrifuged at 13,000 g for 15 min at 4°C and was subsequently passed through a syringe filter that filtered the protein using a membrane of pore size 0.25 µm from Pall Corporation, USA. The CD analysis was performed by using a JASCO J-815 spectropolarimeter (Japan, JASCO Corporation) installed with a Peltier temperature controller set to 25°C. The enzyme, *Ac*Xyn30B_12 (0.68 µM or 0.05 mg/mL) in 0.05 M sodium phosphate buffer, pH 7.5 was loaded in a quartz cuvette and then with scans conducted at 50 nm/min scanning rate, in far UV range (190-250 nm) using the same buffer as baseline was analysed. An average of 5 scans were taken with a 1 nm bandwidth. The data obtained were interpreted in terms of molar ellipticity difference (Δε, deciliter mol^{-1} cm^{-1}), as described earlier (Ahmed *et al*., 2021). To estimate the content (%) of α-helix as well as β-sheets in *Ac*Xyn30B_12, the Δε values for the specified adjacent wavelengths were submitted to the K2D3 server (http://cbdm-01.zdv.uni-mainz.de/~andrade/k2d3/) (Louis-Jeune *et al*., 2012) and BeStSel server (https://bestsel.elte.hu/index.php) (Micsonai *et al*., 2022).

The secondary structure of *Ac*Xyn30B_12 was also analyzed computationally by putting the amino acid sequence into various web servers, *viz.* PSIPRED (http://bioinf.cs.ucl.ac.uk/psipred/), PDBSum (https://www.ebi.ac.uk/thornton-srv/databases/pdbsum/), 2Struc (http://2struc.cryst.bbk.ac.uk) and SOPMA (https://npsa-pbil.ibcp.fr/cgi-bin/npsa_automat.pl?page=/NPSA/npsa_sopma.html). The default settings in the servers were used for the secondary structure analyses. To further validate the results, the theoretical prediction results were compared with the CD data.

4.2.4. Homology modelling and validation of *Ac*Xyn30B_12 structure

The 3D structure prediction of *Ac*Xyn30B_12, was carried out by several web servers, including PHYRE2 (http://www.sbg.bio.ic.ac.uk/phyre2), Robetta (http://robetta.bakerlab.org), SWISSMODEL(https://swissmodel.expasy.org/), AlphaFold2(https://colab.research.google.com/github/sokrypton/ColabFold/blob/main/AlphaFold2.ipynb) and I-TASSER (https://zhanggroup.org/I-TASSER/). The default settings in the servers were used for the 3D structure analyses. The models obtained from these servers were further improved using the YASARA energy minimization tool (http://www.yasara.org/minimizationserver.htm). Structure validation of the predicted *Ac*Xyn30B_12 3D models, both before and after energy minimization, was conducted by using the SAVES v6.0 server (https://saves.mbi.ucla.edu/). This validation included assessments of compatibility and stereochemical properties by using ERRAT (Colovos *et al*., 1993), VERIFY-3D (Bowie *et al*., 1991; Lüthy *et al*., 1992) and PROCHECK (Pontius *et al*., 1996). The results from these validations were compared and the best model for *Ac*Xyn30B_12 was selected based on the following criteria: a high-quality factor (above 90%), a high percentage of residues with a 3D-1D score $\geq$ 0.2 (above 90%) and above 90% of residues in the favored regions of the Ramachandran plot. Additionally, the Protein Structure Analysis (ProSA) (Wiederstein *et al*., 2007) web server (https://prosa.services.came.sbg.ac.at/prosa.php) was used to estimate Z-score variations of the final modeled structure of *Ac*Xyn30B_12 comparing it within PDB database. The energy-minimized structure of the finalized model was analysed using the PyMOL v3.0 software. The topology outline for the *Ac*Xyn30B_12 structure was also generated by using the PDBSum web server to further validate the compatibility of 3D modelled structure of *Ac*Xyn30B_12. The modelled structure of *Ac*Xyn30B_12 was

further superimposed with the PDB structure of its homologous protein, XynA (PDB ID: 5CXP) from *Clostridium acetobutylicum* ATCC 824 by PyMOL v3.0 software.

4.2.5. Molecular dynamic simulation of *Ac*Xyn30B_12

Molecular dynamic **(**MD) simulation of modelled structure of *Ac*Xyn30B_12 was conducted on super computer (PARAM-KAMRUPA, a 838 Teraflops capacity hybrid HPC in IIT Guwahati, Assam, India). The atoms of *Ac*Xyn30B_12 were defined with the Charmm36 force field and the most recent algorithm from GROMACS v5.1.4 software was employed for coordination (Sharma *et al.*, 2021). The centre location of the *Ac*Xyn30B_12 modelled structure was placed in a cubic box of volume 541.03 nm^3 that was solvated with 5,8642 water molecules. The addition of 31 Na^+ ions neutralized and balanced the system as a whole. Energy minimization with a force of 1000 kJ mol^{-1} nm^{-1} and 50,000 iteration steps was applied to this solvated structure followed by two phase equilibrations to bring the solvated and neutralized system to equilibrium. The first phase of equilibration was conducted under isothermal-isochoric circumstances for 500 ns using an NVT aggregate (N: constant number of particles, V: constant volume and T: constant temperature). The second stage of equilibration was performed in an NPT aggregate (N: constant number of particles, P: constant pressure and T: constant temperature) in isothermal-isobaric circumstances for 500 ns (Hess *et al.*, 2008). The MD run was executed for 100 ns with an interval time of 10 ps. The structural properties and stability of the simulated protein, *Ac*Xyn30B_12 was then determined using various factors like, radius of gyration (R_g), root mean square fluctuation (RMSF), root mean square deviation (RMSD, calculated by least square fitting method, intramolecular hydrogen-bonds and solvent accessible surface area (SASA), *via* commands *gmx gyrate*, *gmx rmsf*, *gmx rms*, *gmx hbonds* and

gmx sasa, respectively. Every dataset was converted to a graphical presentation with the aid of OriginPro software.

4.2.6. Active-site analysis of *Ac*Xyn30B_12

After predicting the modelled structure of *Ac*Xyn30B_12, its active-site was examined for accessible ligand-binding pockets. The analysis also included homologous proteins of *Ac*Xyn30B_12, endo-xylanase XynA from *Clostridium acetobutylicum* ATCC 824 (PDB ID: 5CXP). For the identification of plausible pockets, the PDB format files containing 3D structures of *Ac*Xyn30B_12 and XynA from *Clostridium acetobutylicum*, were submitted to the Computed Atlas of Surface Topography of proteins (CASTp) server (http://sts.bioe.uic.edu/castp/index.html?3igg). Both the volume as well as area of the accessible ligand-binding pockets on the surface of *Ac*Xyn30B_12 and XynA from *Clostridium acetobutylicum* were determined by using a default probe radius of 1.4 Å.

4.2.7. Ligand binding analysis of *Ac*Xyn30B_12 using molecular docking approach

Molecular docking approach was used to study the ligand binding analysis of *Ac*Xyn30B_12. AutoDockTools-1.5.7, connected to the MGLTools 1.5.6 (http://mgltools. scripps.edu/), was used to investigate the interaction of ligands *viz.* xylo-oligosaccharides (xylopentaose, xylotetraose, xylotriose, xylobiose and xylose) with the active-site of the modelled *Ac*Xyn30B_12 structure. The canonical structure of all xylo-oligosaccharides was obtained in 3D SDF format from the Pubchem (https://pubchem.ncbi.nlm.nih.gov/) web service and then translated to PDB format using the Open Babel GUI 3.1.1 program. The specific molecular docking was conducted targeting the amino acid residues in the CASTp server predicted the active-

site pocket in *Ac*Xyn30B_12 (Section 4.2.6). The active-site of *Ac*Xyn30B_12 was positioned within a grid box, with a 0.37 Å spacing between grid points and values of 63 Å (X dimension), 61 Å (Y dimension) and 79 Å (Z dimension). Using the Lamarckian genetic algorithm (LGA), protein-ligand docking was carried out with total 50 runs. After analysing all 50 runs, the protein-ligand conformation having the lowest binding energy (ΔG) value was chosen in PDBQT format and transformed into PDB format using Open Babel software. Using the Ligplot software (Wallace *et al*., 1995), a 2D interaction plot was created to explore the interactions (hydrophobic and polar) between xylo-oligosaccharides and *Ac*Xyn30B_12.

4.2.8. MD simulation analysis of *Ac*Xyn30B_12-xylotriose complex

The MD simulation was utilized to ascertain the interaction between *Ac*Xyn30B_12 and xylotriose. GROMACS v5.1.4 software was used to simulate the *Ac*Xyn30B_12-xylotriose complex with the lowest ΔG value obtained through molecular docking analysis (Section 4.2.7). Charmm36 force field was employed to compute protein forces and the SwissParam site (www.swissparam.ch) (Bugnon *et al*., 2023) was used to build the topology of the xylotriose ligand. The *Ac*Xyn30B_12-xylotriose complex that was produced was solvated using 58642 solvent (water) molecules in a cubic box. To neutralize the system and achieve equilibrium, 31 Na^+ ions was introduced. For 500 ns and 2fs iterations two phases of equilibration were carried out with NVT and NPT conditions sequentially. For this solvated and equilibrated system MD run was performed for 100 ns and at intervals of 10 ps trajectories were recorded. For the simulated system, R_g, RMSD, RMSF, SASA and H-bonds were analysed by using similar commands as discussed in Section 4.2.5 and further equated

with the parameters of the simulated protein model. For each dataset, a graphical representation was created using the OriginPro software.

4.2.9. Small angle X-ray scattering (SAXS) analysis of *Ac*Xyn30B_12

The SAXS analysis of *Ac*Xyn30B_12 was conducted at concentrations of 3 mg/mL as well as 5 mg/mL by utilizing a SAXSpace system (Anton Paar GmbH, Graz, Austria), to investigate molecular geometry and structural dynamics of *Ac*Xyn30B_12 in solution form. The methodology was followed as previously reported by Ahmed *et al*., 2021. Scattering profiles were obtained for *Ac*Xyn30B_12 and its matching buffer (0.05 M sodium phosphate, pH 7.5) for monitoring beam stability and accessing radiation damage, at a wavelength of 1.54 Å. The SAXS profile of *Ac*Xyn30B_12 at 3 mg/mL and 5 mg/mL was obtained by subtracting the buffer profile using SAXS analysis software. The software and tools incorporated in ATSAS v2.8.4 suite (Franke *et al*., 2017) was used for data processing, normalization and averaging.

Through the indirect Fourier transformation using GNOM software (Svergun *et al*., 1992) and the Guinier approximation (Guinier *et al*., 1955; Konarev *et al*., 2003), radius of gyration (R_g) for both globular shape and rod shape were analysed. GNOM software was also used to compute the maximum particle dimension (D_{max}) as well as the distance distribution function plot P(R). At both the concentrations, the persistence length was computed utilizing the following formula: $[\sqrt{12}\{(R_g^2)-(R_c^2)\}]$ as reported by Odijk *et al*., 1977. The Kratky plot was used to assess the folding and compactness of *Ac*Xyn30B_12. The molecular weight (M_w) was estimated using the SAXSMoW server (Fisher *et al*., 2010). Using DAMMIF (Svergun *et al*., 2001), 20 separate dummy atom models (DAMs) were created. These were then averaged using DAMAVER (Volkov *et al*., 2003) and refined using DAMMIN (Svergun *et al*., 1999). The

pyDockSAXS webserver (https://life.bsc.es/pid/pydocksaxs) developed by Jiménez-García *et al*., (2015) was utilized to conduct the protein-protein docking against the scattering profile in order to fit the DAM envelope with dimeric *Ac*Xyn30B_12. Utilizing the SUPCOMB program (Kozin *et al*., 2001), only the top 10 models were assessed to choose the best model. Using the CRYSOL program, the SAXS experiment data were fitted to the modelled structure (Svergun *et al*., 1995). PyMOL v3.0 was used to visualize the DAM envelopes and OriginPro software was used to construct the figures.

4.2.10. Hydrodynamic diameter and zeta-potential analysis of *Ac*Xyn30B_12 using Dynamic light scattering

Dynamic Light Scattering (DLS) analysis of *Ac*Xyn30B_12 in aqueous solution was conducted using Particle Analyzer (Litesizer 500, Anton Paar, Graz, Austria), to investigate the hydrodynamic diameter (D_h) and polydispersity index. Before the analysis, with the help of a concentrator (Centricon, cut off 30 kDa, Amicon Ultra, Millipore) purified *Ac*Xyn30B_12 (1.5 mg/mL) was concentrated up to 3 mg/mL and 5 mg/mL by centrifuging at 4000g and 4°C for 10 min. For removing any aggregated protein, *Ac*Xyn30B_12 at all three concentrations (1, 3 and 5 mg/mL) was centrifuged at 13000g and 4°C 15 min. A syringe filter was used to filter each sample individually using a membrane of pore size 0.25 μm (Pall Corporation, USA) and then the samples were evaluated via light scattering analysis. This analysis was observed at an average backscatter angle of 6 runs per response (Lorber *et al*., 2012). A temperature controller supported by Peltier helped to keep the system temperature at 25°C. The enzyme, *Ac*Xyn30B_12 0.4 mL, at 3.0 as well as 5.0 mg/mL were placed individually inside the cuvette (Anton Paar Omega electrode) for zeta potential (ζ) (Salgin *et al*., 2012)

investigation. The surface charge of *Ac*Xyn30B_12 was measured and processed for a total of 100 runs. Also, the average zeta potential was recorded for each experiment.

4.3. Results and Discussion

4.3.1. Amino acid sequence analysis of *Ac*Xyn30B_12

Using the ExPASY-ProtParam website, the molecular mass, isoelectric point (PI) and molar mass extinction coefficient of *Ac*Xyn30B_12 were determined to be 73.5 kDa, 4.79 and 122635 M^{-1} cm^{-1}, respectively. The amino acid sequence of *Ac*Xyn30B_12 was analyzed using PDB-BLAST to identify homologous sequences and those establishing the evolutionary relationships and functional relevance with *Ac*Xyn30B_12, are summarized in Table 4.1. The PDB-BLAST results showed that the PDB structure of XynA (PDB ID: 5CXP) from *Clostridium acetobutylicum* ATCC 824 has the highest sequence identity (27.81%) with *Ac*Xyn30B_12. This was followed by XynC (PDB ID: 3GTN) from *Bacillus subtilis* 168 (26.58%), XynA (PDB ID: 1NOF) from *Dickeya chrysanthemi* (26.56%), endo-xylanase (PDB ID: 4FMV) from *Ruminiclostridium papyrosolvens* DSM 2782 (26.49%) and endoxylanase (PDB ID: 2WNW) from *Salmonella enterica* subsp. *enterica serovar Typhimurium* str. LT2 (25.51%).

Table 4.1. BLASTp analysis of *Ac*Xyn30B_12 amino acid sequence against the PDB database.

Protein name	Organism	Max Score	Query Cover (%)	*E* - value	Identity (%)	Accession length	Accession ID
Xylanase A	*Clostridium acetobutylicum* ATCC 824	95.1	86%	6e-21	27.81%	390	5CXP
Xylanase C	*Bacillus subtilis* 168	62.8	86%	3e-10	26.58%	401	3GTN
Xylanase A	*Dickeya chrysanthemi*	82.0	89%	1e-16	26.56%	383	1NOF
Endoxylanase	*Ruminiclostridium papyrosolvens* DSM 2782	95.1	92%	6e-21	26.49%	396	4FMV
Endoxylanase	*Salmonella enterica subsp. enterica serovar Typhimurium str. LT2*	82.0	68%	2e-16	25.51%	447	2WNW
Chain A, CBM6	*Acetivibrio thermocellus*	58.5	96%	8e-09	24.19%	409	4UQA
Chain A, CBM 6	*Acetivibrio thermocellus*	57.0	96%	2e-08	24.19%	409	4CKQ

The multiple sequence alignment (MSA) analysis of *Ac*Xyn30B_12 with its homologous proteins using Clustal Omega revealed the distribution of secondary structural elements (α-helices and β-sheets), within the *Ac*Xyn30B_12 sequence (Fig. 4.1). The MSA highlighted the conservation patterns of amino acid residues i.e. fully conserved residues (by white letters on a red background), semi-conserved residues (by red letters on a white background) and non-conserved residues (by black letters on a white background) within *Ac*Xyn30B_12 sequence (Fig. 4.1). Furthermore, the dark blue, light blue and white lines at the bottom of the MSA represent high solvent accessible, intermediate solvent accessible and least solvent accessible (or buried areas) regions, respectively (Fig. 4.1). Aditionally, the MSA showed 2 catalytic residues, Glu151 (acid/base) and Glu259 (nucleophile) marked by green stars as shown in Fig. 4.1. These two catalytic residues were found to be conserved and lie in least solvent accessible region i.e they are present in core of the protein. However, in the study reported by Šuchová *et al*., 2024, the same protein labelled as *Ac*Xyn30B contained the signal peptide (20 amino acid long) along with the catalytic, CBM6 and Dockerin type I module, which on alignment with the sequences of selected representatives of GH30 subfamilies, gave the different catalytic residue numbers, *viz.* Glu171 (acid/base) and Glu279 (nucleophile), because of extra signal peptide sequence which was not present in our study.

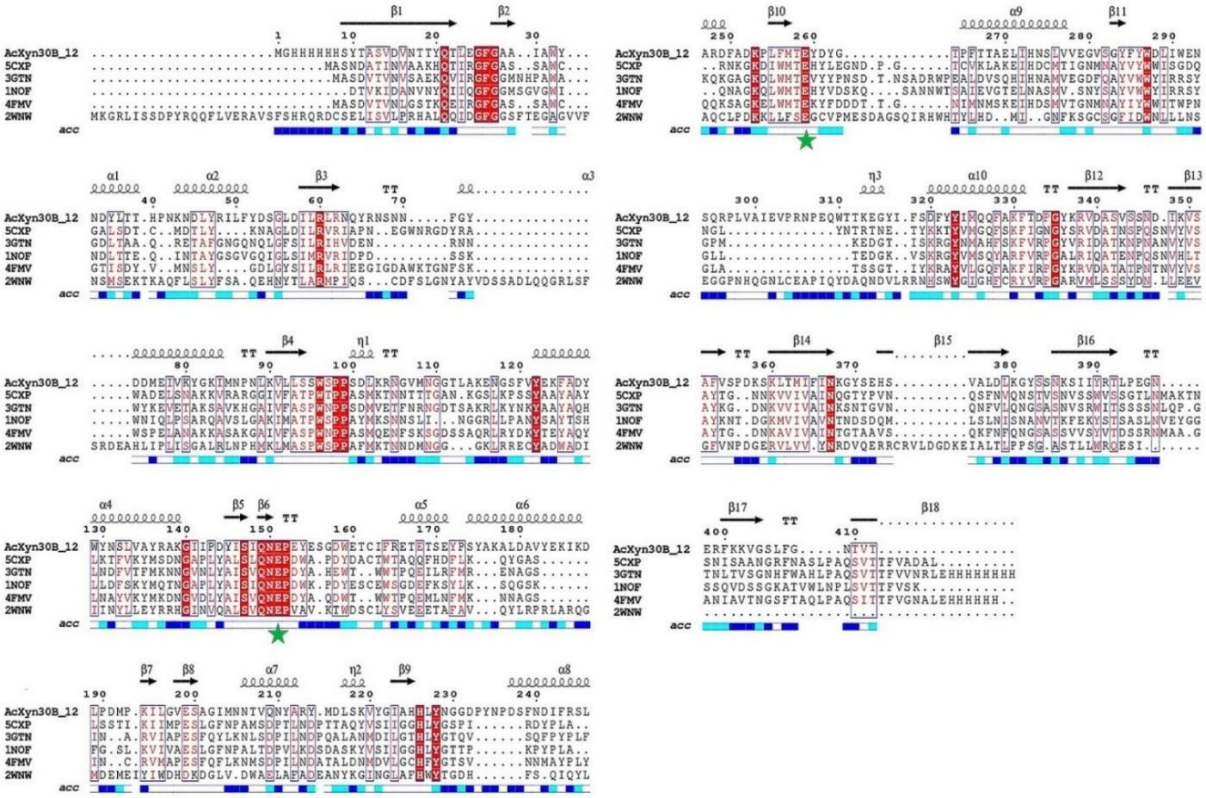

Fig. 4.1. Multiple sequence alignment of *Ac*Xyn30B_12 with homologos by using Clustal Omega. Conserved amino acids are highlighted with white letters on a red background, semi-conserved amino acids appear as red letters on a white background and non-conserved amino acids are represented by black letters on a white background. The residues Glu 151 and Glu 259 are the catalytic residues of *Ac*Xyn30B_12 (marked with green star). The highly solvent accessible areas are represented by dark blue lines and intermediate solvent accessible areas by light blue lines.

Metal ion binding site prediction using the MIB2 server revealed a substantial number of residues within both the catalytic module and the CBM6 domain of *Ac*Xyn30B_12 exhibiting high binding scores for Ca^{2+} and Mg^{2+} ions as shown in Fig. 4.2. Glu151 was predicted to bind Ca^{2+} not in isolation, but in coordination with neighbouring residues such as Asp152 and Leu153, indicating a cooperative binding environment that likely confers greater rigidity and stability to the local structure (Fig. 4.2). Similarly, Glu259 was also predicted to coordinate Ca^{2+} in concert with

surrounding residues (Thr258, Glu259 and Asp261) suggesting the formation of a tightly bound metal-binding pocket that is critical for maintaining catalytic efficiency. The catalytic residues Glu151 and Glu259 displayed binding scores of 1.3 and 2.08 for Ca^{2+} and 2.05 and 1.5 for Mg^{2+}, respectively. These results suggest that metal ion coordination, particularly with Ca^{2+} and Mg^{2+}, enhanced the structural and functional integrity of the enzyme, potentially contributing to increased catalytic activity. This observation is consistent with the experimental findings discussed in Chapter 3, Section 3.3.4.

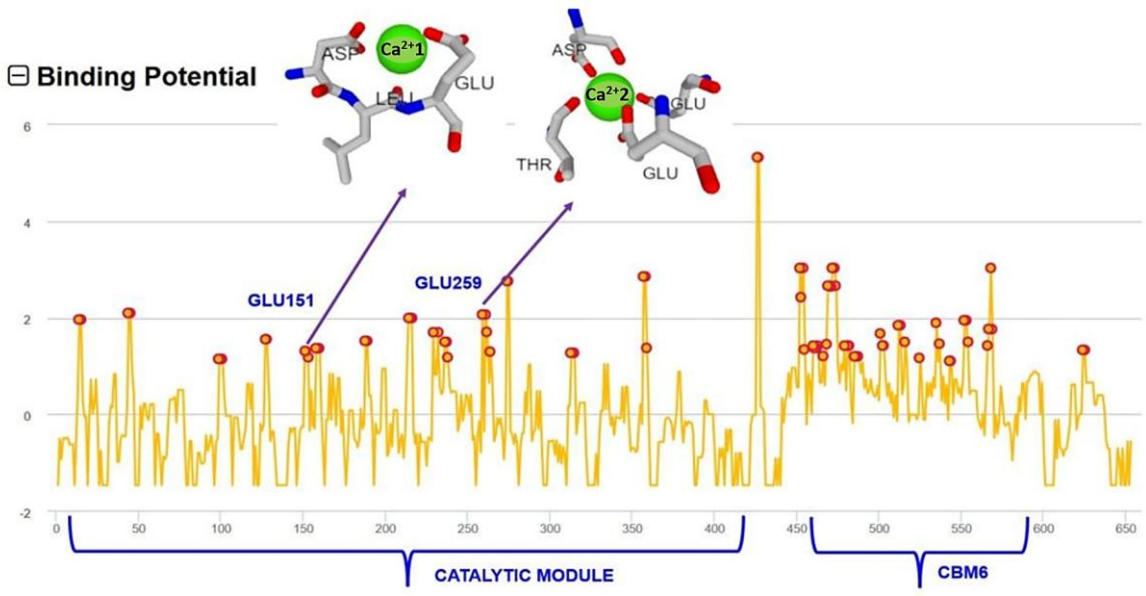

Fig. 4.2. Ca^{2+} ion binding-site prediction using Metal-Ion binding site prediction and modelling server (MIB2).

4.3.2. Secondary structure analysis of *Ac*Xyn30B_12

The *Ac*Xyn30B_12 amino acid sequence was found to have 24.0% α-helices and 26.5% β-strands, according to the PSIPRED (Fig. 4.3A) and 23.4% α-helices and 28.3% β-strands according to SOPMA as also mentioned in Table 4.2. Fig. 4.3A displays the distribution of secondary structural elements α-helices (by pink line), β-sheets (by yellow line) and random coils (by black line) within *Ac*Xyn30B_12 sequence. The CD

spectrum profile of purified *Ac*Xyn30B_12 displays the plot of wavelength vs mean residue ellipticity, MRE (Fig. 4.3B). The CD spectrum data of *Ac*Xyn30B_12 analysed by BestSel server revealed 26.2% α-helices and 28.1% β-strands, whereas the analysis by K2D3 server also showed similar content of 24.3% α-helices and 27.7% β-strands (Table 4.2). All the prophesied secondary structure elements analysed by prediction tools as well as CD spectrum analyses closely agreed with one another.

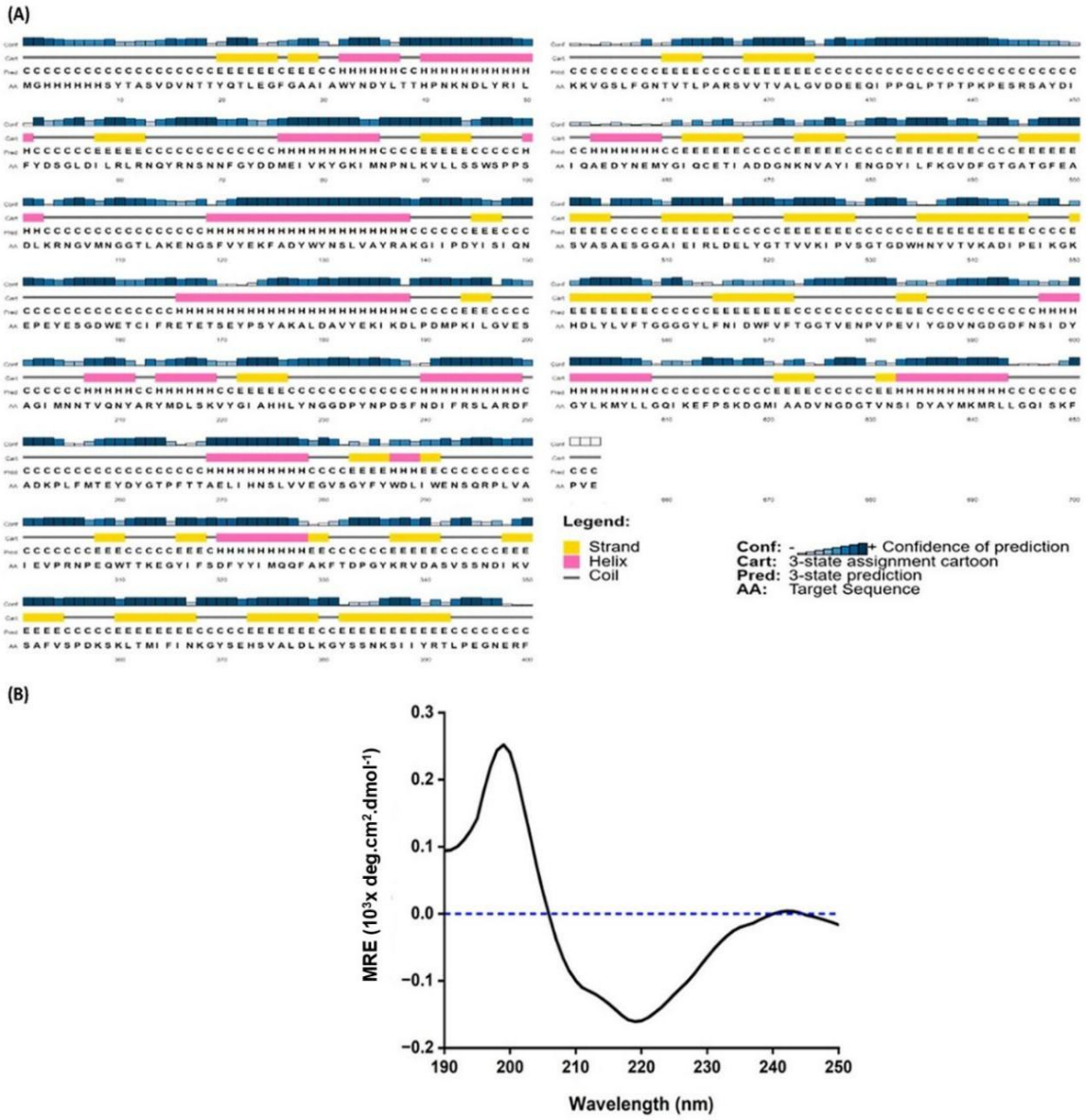

Fig. 4.3. Secondary structure investigation of *Ac*Xyn30B_12 **(A)** PSIPRED server indicating beta strands (yellow line), alpha helix (pink line) and random coils (black lines) and **(B)** CD spectrum.

Table 4.2. Secondary structure inspection of *Ac*Xyn30B_12.

Server/Tool	*α*-helix (%)	*β*-strands (%)	Random coil (%)
PSIPRED	24.0	26.5	49.5
SOPMA	23.4	28.3	48.2
PDBSum	22.8	30.2	47.0
2Struc	22.5	30.2	47.3
CD (BeStSel server)	26.2	28.1	47.4
CD (K2D3 server)	24.3	27.7	47.9

4.3.3. Homology modelling and validation of *Ac*Xyn30B_12 structure

The SAVES v6.0 webserver's validation variables were used to compare the three-dimensional modelled structures of the *Ac*Xyn30B_12 protein before and after energy minimization (using the YASARA tool). The structure from Alphafold2 was regarded as the final model for *Ac*Xyn30B_12 based on the comparative analysis (based on the criteria specified in Section 4.2.4). The energy minimized 3D structure of *Ac*Xyn30B_12 from Alphafold2 has an overall model quality of 92.8%, according to ERRAT (Fig. 4.4A), indicating that it is of acceptable quality. 91.4% amino acid residues in the modelled structure *Ac*Xyn30B_12 are predicted by VERIFY3D (Fig. 4.4B) exhibiting 3D-1D score of ≥ 0.2, which indicates fitness of the structure. The PROCHECK server verified the validity of the modelled structure *Ac*Xyn30B_12. The Ramachandran Plot (Fig. 4.4C) revealed total of 653 amino residues. It showed, 88.6% (499) of amino acid residues in the most- favored region, 11% (62) in the additionally allowed region, 0.2% (1) in the generously allowed region and only 0.2% (Asp516) in the disallowed region. This finding showed that the modelled *Ac*Xyn30B_12 structure followed phi (φ) as well as psi (ψ) angles within the Ramachandran plot. However, with 8.71 Z-score, the ProSA results also

confirmed the *Ac*Xyn30B_12 modelled structure's correctness and compatibility (Fig. 4.4D). According to ProSA assessment of the local model quality of *Ac*Xyn30B_12, all residues exhibited non-positive value, meaning that no portion of the modelled structure is incorrect (Fig. 4.4E).

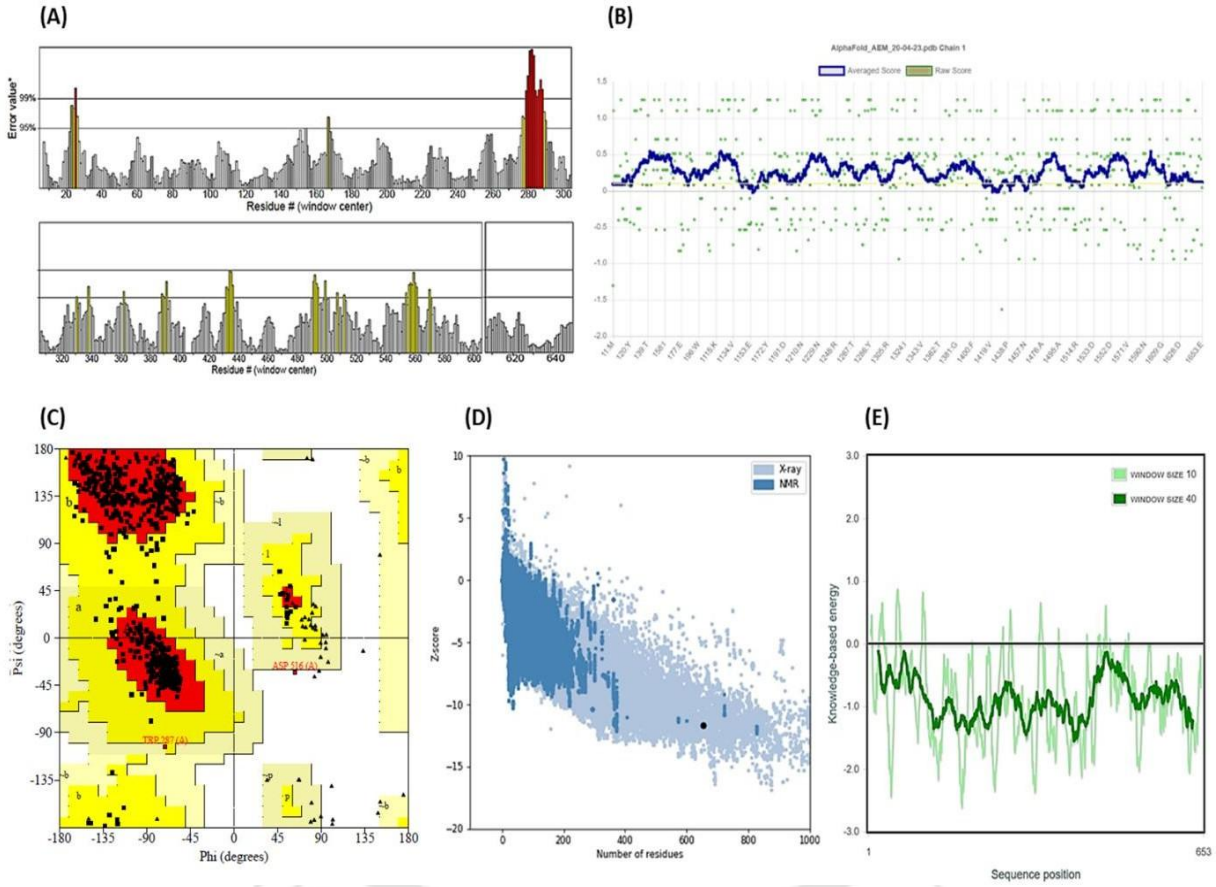

Fig. 4.4. Quality assessment of Alphafold2 energy minimized modelled structure of *Ac*Xyn30B_12 by SAVES server. **(A)** ERRAT plot, on the residue window 2 lines (indicating confidence level for rejecting regions that surpass the specified error value) are drawn against error value axis. Red, yellow and gray lines represent regions that surpass the error value, moderate error and below error threshold respectively. **(B)** VERIFY3D plot, blue line denotes mean 3D-1D score for amino acids and green dots denote raw scores. **(C)** Ramachandran Plot investigation (PROCHECK server), representing different colour-coded regions: most favored in red, additionally allowed in yellow, generously allowed in whitish and disallowed region in white area. Glycine residues denoted by triangular shape, proline residues by black square and both non-glycine and non-proline residues by red square and **(D)** ProSA graphical representation, illustrating the overall model quality and Z-score. **(E)** The energy departure from the energy distribution produced from random configurations is measured by the ProSA local model quality plot.

The cartoon depiction of the Alphafold2 modelled *Ac*Xyn30B_12 structure was examined by using PyMOL 3.0 (Fig. 4.5A). The conserved modules of *Ac*Xyn30B_12, analyzed by the NCBI-CDD database as depicted in Fig. 4.5A are, the catalytic module (in blue colour), the carbohydrate binding module family 6 (CBM6) (in green colour) and dockerin type I (DocI) (in brown colour). The catalytic module consists of 8 β-strands enclosed by 8 α-helices forming a $(\beta/\alpha)_8$ barrel structure. Moreover, 9 β-strands were also found at the side of $(\beta/\alpha)_8$ barrel fold which is called as 'side-β structure' char of this family. The presence of $(\beta/\alpha)_8$ barrel fold accompanied by the side-β structure in *Ac*Xyn30B_12 is the characteristic feature of GH30 family enzymes as reported earlier (Moreiara *et al*., 2016). The CBM6 and dockerin are composed of only β-strands and α-helices, respectively. PyMOL v3.0 software was used to superpose the modelled structure *Ac*Xyn30B_12 (shown in green colour) with its homologous proteins, XynA (PDB ID: 5CXP) from *Clostridium acetobutylicum* ATCC 824 (St. John *et al*., 2018) and XynC (PDB ID: 3GTN) from *Bacillus subtilis* 168 (St. John *et al*., 2011) as shown in Fig. 4.5B. The superposition gave a Root Mean Square Deviation (RMSD) value of 1.63 Å and match align score of 672.3. The spatial alignment and conservation of the catalytically significant active-site residues of *Ac*Xyn30B_12 (Glu 151 and Glu 259 shown in magenta colour) with that of XynA (Glu 141 and Glu 230 shown in red colour) and XynC (Glu 140 and Glu 229 shown in cyan colour) can be observed through this superposition (Fig. 4.5C). According to a previous study by Wang *et al*., (1994) on the experimental mechanisms for hydrolysis, it was determined that, for the inverting mechanism, the mean distance between the two -COOH groups should fall within of 8.5 Å to 12.5 Å, while for the retaining mechanism, it should be 5.5 Å. The in-silico technique assessed the distance of 5.0 Å between the -COOH groups of Glu151 and

Glu259 for *Ac*Xyn30B_12, indicating a retention type of hydrolytic mechanism (Fig. 4.5C).

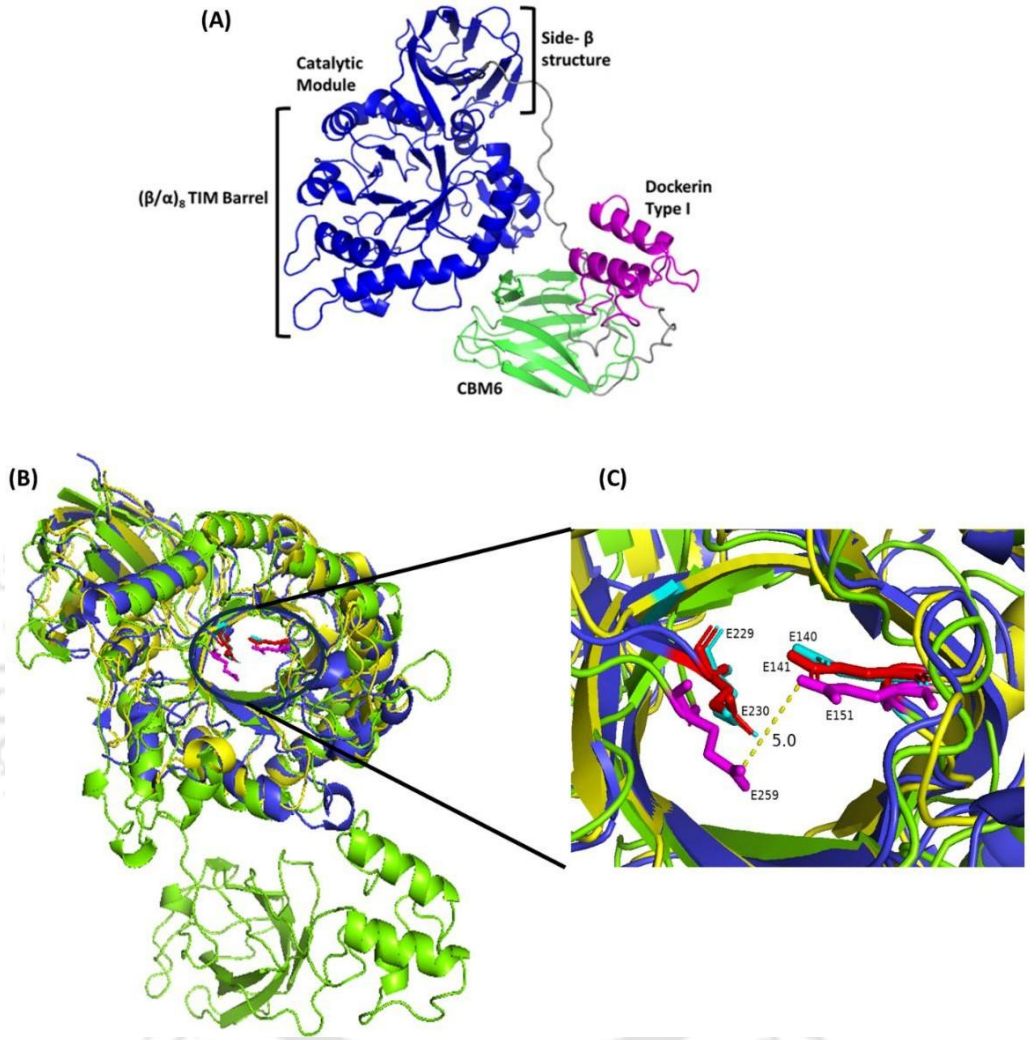

Fig. 4.5. **(A)** Cartoon view of 3D modelled structure of *Ac*Xyn30B_12. **(B)** Superposition of modelled structure of *Ac*Xyn30B_12 structure (green) with its homologous proteins XynA (PDB ID: 5CXP) from *Clostridium acetobutylicum* ATCC 824 (blue) and XynC (PDB ID: 3GTN) from *Bacillus subtilis* 168 (yellow). **(C)** Superposition of Glu151 and Glu259 catalytic residues; in magenta and distance of 5.0 Å) of *Ac*Xyn30B_12 with catalytic residues (Glu141 and Glu230; red) of XynA from *Clostridium acetobutylicum* ATCC 824.

According to the topological profile inferred by the PDBSum server, a total of 19 α-helices and 36 β-strands were found in the full length *Ac*Xyn30B_12 predicted structure (Fig. 4.6). Out of all, 8 β-strands contribute to the formation of $(\beta/\alpha)_8$ barrel

fold structure. Through its topological diagram, the PDBsum server also provides information regarding residue numbering involved in producing β-strands and α-helices.

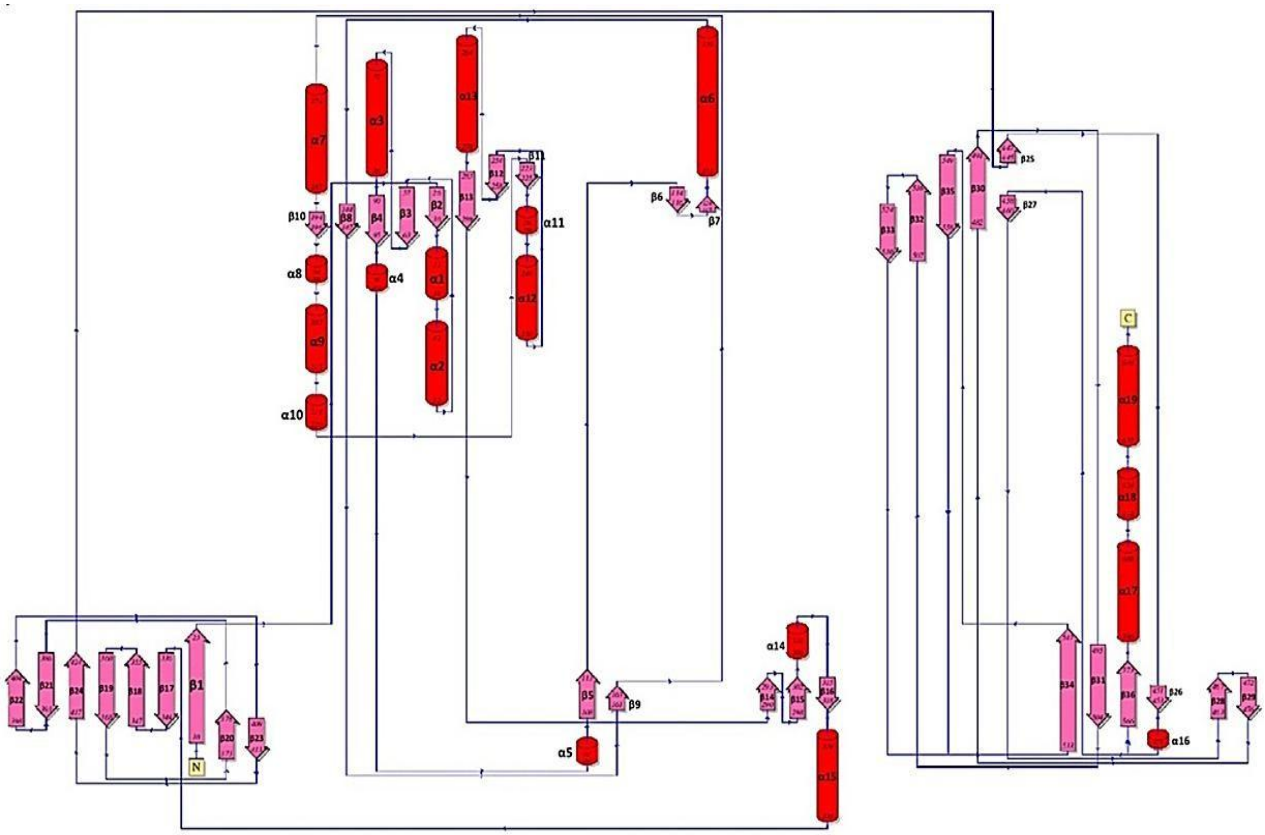

Fig. 4.6. Topology diagram of *Ac*Xyn30B_12 modelled structure by PDBSum server which denotes secondary structures, alpha-helix (by red cylindrical shapes) and beta-strands (by pink arrows) along with their respective amino acid sequence range.

4.3.4. Molecular dynamic simulation of *Ac*Xyn30B_12

The 3D modelled structure of *Ac*Xyn30B_12 was put through a 100 ns MD simulation for observing the structural dynamics, compactness and stability. The observed RMSD vs. time graph first displayed variations between 0.5 and 1.2 nm from 0 to 32 ns. After 32 ns, the structure displayed stability with RMSD values between 1.2 and 1.3 nm up to 100 ns giving an average RMSD of 1.2 nm (Fig. 4.7A). The RMSF value of *Ac*Xyn30B_12 was employed to ascertain the stability of the structure (atoms

displacement from their original shape). High variations were seen within residues implicated in loops, including L1 (103-121 aa), L2 (148-165 aa), L5 (286-312 aa) and L-10 (609-618 aa) (Fig. 4.7B, highlighted in red). The catalytic residue Glu259, with an RMSF value of 0.3, demonstrated limited flexibility, whereas the catalytic residue Glu151 in L2 was shown to be flexible (Fig. 4.7B, green). The R_g varied mid 1 and 9 ns, then stabilized after 9 ns, falling within a narrow range of 3.98–3.75 nm and with a mean R_g of 3.9 nm denoting remarkable compactness (Fig. 4.7C). The SASA plot (Fig. 4.7D) demonstrated the stability over the course of the 100 ns run with an average value of 332.8 nm^2 suggesting that catalytically significant residues were accessible to the substrate and that no deformation was occurring. Up to 100 ns, the *Ac*Xyn30B_12 main chain had an average of 423 intramolecular H-bonds (Fig. 4.7E). The structural stability of the protein was significantly influenced by these hydrogen bonds. After superposing the *Ac*Xyn30B_12 modelled structure on top of the simulated structure, the RMSD value was 0.33 nm. Hence, it was concluded that the simulated structure was stable, compact and appropriate for further investigation.

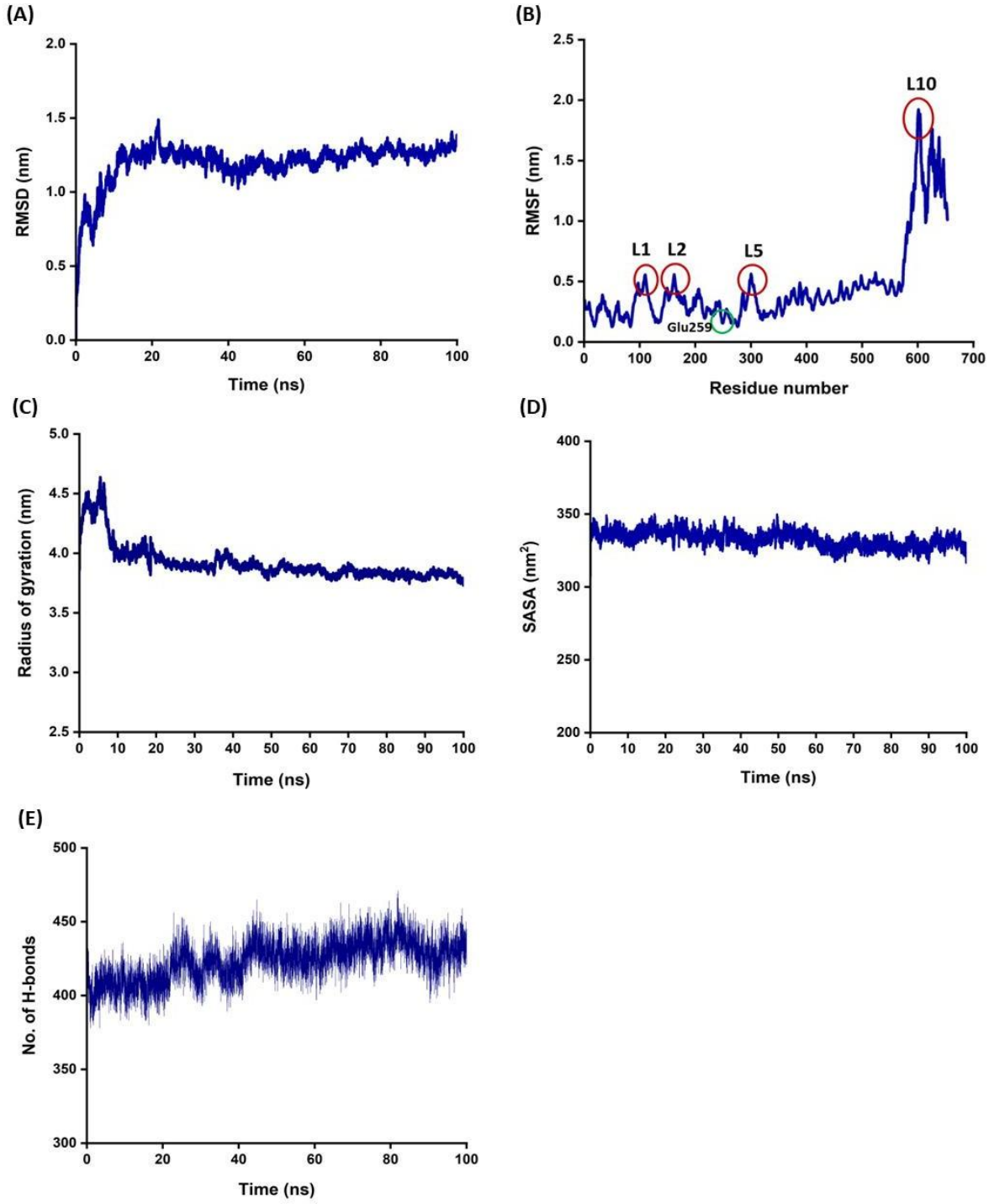

Fig. 4.7. Different graphs of molecular dynamic simulation of *Ac*Xyn30B_12 modelled structure **(A)** Root mean square deviation, **(B)** Root mean square fluctuation, where L1, L2, L5 and L10 represent loops sequentially numbered according to the PDB topology file generated by the PDBsum server, **(C)** Radius of gyration, **(D)** Solvent accessible surface area and **(E)** Intra-molecular hydrogen bonds.

4.3.5. Active-site examination of *Ac*Xyn30B_12 by using CASTp server

After measuring the volume and area of the *Ac*Xyn30B_12 active-site pocket by using the CASTp server, the characteristics of the active-pocket site were compared with those of its homolog, endo-xylanase XynA from *Clostridium acetobutylicum* ATCC 824. The active-site of *Ac*Xyn30B_12 had a solvent accessible surface area of 156.5 $Å^2$ and volume of 215 $Å^3$ (shown in red colour in Fig. 4.8A). The conserved residues Trp96, Asn150 and Tyr228, non-conserved residues Tyr154, Trp159, Glu160, Thr161, Ala201 and Tyr262, as well as catalytic residues Glu151 and Glu259 were found in this active-site pocket. Similarly, for XynA from *Clostridium acetobutylicum* ATCC 824, the predicted active-site area and volume were 84.8 $Å^2$ and 101.3 $Å^3$, respectively (shown in red colour in Fig. 4.8B). The comparison of the active-site of *Ac*Xyn30B_12 with that of its homologue, endo-xylanase, XynA disclosed that the active-site of *Ac*Xyn30B_12 is deeper than XynA.

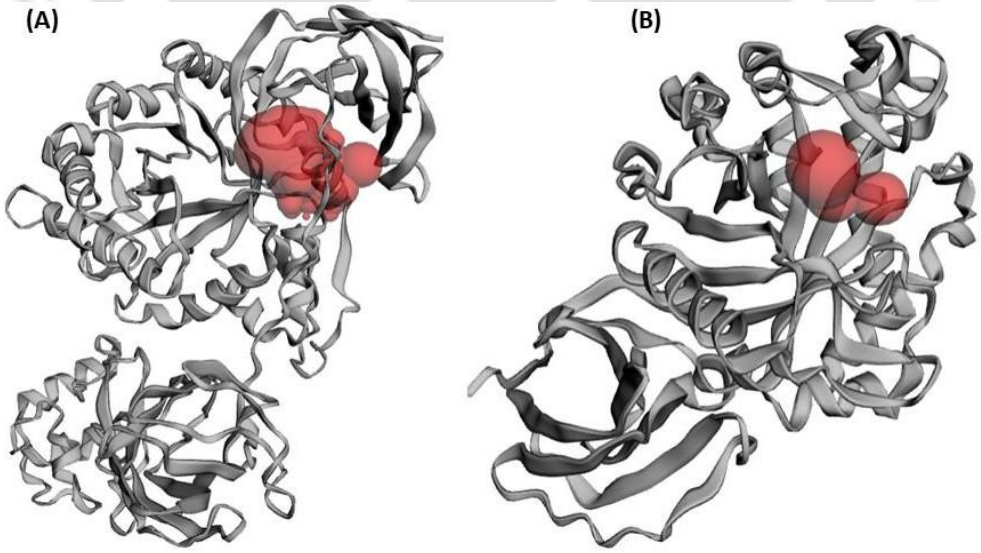

Fig. 4.8. Active-site investigation of **(A)** *Ac*Xyn30B_12 and **(B)** endo-xylanase XynA (PDB ID: 5CXP) from *Clostridium acetobutylicum* ATCC 824 by using CASTp web-server.

4.3.6. Analysis of ligand binding by *Ac*Xyn30B_12 using molecular docking

The molecular docking by AutoDockTools-1.5.7 software was carried out to investigate the interactions of the active-site amino acid residues of *Ac*Xyn30B_12 with xylose, xylo-oligosaccharides (xylobiose, xylotriose, xylotetraose, xylopentaose). *Ac*Xyn30B_12 exhibited binding with xylose, xylobiose, xylotriose, xylotetraose and xylopentaose with binding free energy (ΔG) of -8.9, -9.6, -11.2, -9.1 and -8.6 kcal/mol, respectively (Table 4.3). Hence this displayed the maximum affinity of *Ac*Xyn30B_12 for xylotriose (-11.2 kcal/mol). The catalytic residue, Glu151 was observed to participate in polar interactions with xylotriose and xylotetraose (Table 4.3). The amino acids in the catalytic cleft of *Ac*Xyn30B_12 involved in interactions (both polar and non-polar) with xylopentaose, xylotetraose, xylotriose, xylobiose and xylose is shown in Table 4.3.

Table 4.3. Molecular docking analysis of *Ac*Xyn30B_12 with different xylo-oligosaccharides.

Ligand	Binding free energy (ΔG) (kcal/mol)	Residues involved in polar interactions	Residues involved in non-polar interactions
Xylose	-8.9	Ala29, Tyr33, Asp288, Leu289, Ile290	Ile30, Leu37
Xylobiose	-9.6	Glu151, Tyr228, Asp261, Arg296	Tyr260, Tyr262, Gly263, Trp287, Pro297
Xylotriose	-11.2	Asp261, Gly263, Asp288, Arg296	Glu151, Tyr228, Tyr260, Tyr262, Tyr286, Trp287, Gln295, Pro297, Leu298
Xylotetraose	-9.1	Glu151, Ser156, Asn229, Asp261, Arg296	Tyr154, Trp159, Tyr228, Tyr262, Trp287
Xylopentaose	-8.6	Ser156, Asp158	Trp32, Tyr154, Glu155, Trp159, Trp287, Trp291

The alignment of xylose, xylotriose and xylopentaose inside the catalytic cleft of the modelled *Ac*Xyn30B_12 with polar (in orange colour) and non-polar (in green colour) interactions was envisioned using Pymol v3.0 software as shown in Fig. 4.9 (A, B and C). The 3D interaction of ligand and amino acid residues of *Ac*Xyn30B_12 with polar interactions using Pymol v3.0 software is shown in Fig. 4.9(D, E and F). The 2D interaction analysis using Ligplot software of docked *Ac*Xyn30B_12 and different xylo-oligosaccharide is shown in Fig. 4.9 (G, H and I). The 2D diagrams display the binding environment within the active-site of *Ac*Xyn30B_12, showing the residues participating in both polar and non-polar interactions with ligand molecules differentiating the nature of these interactions. The 2D interaction analysis of docked *Ac*Xyn30B_12-xylotriose complex showed that the residues; Asp216, Gly263, Asp288 and Arg296 make polar interactions, while Tyr 228, Tyr260, Tyr262, Tyr286, Trp287, Gln295, Pro297 and Leu298 make non-polar interactions with xylotriose (Fig. 4.9H).

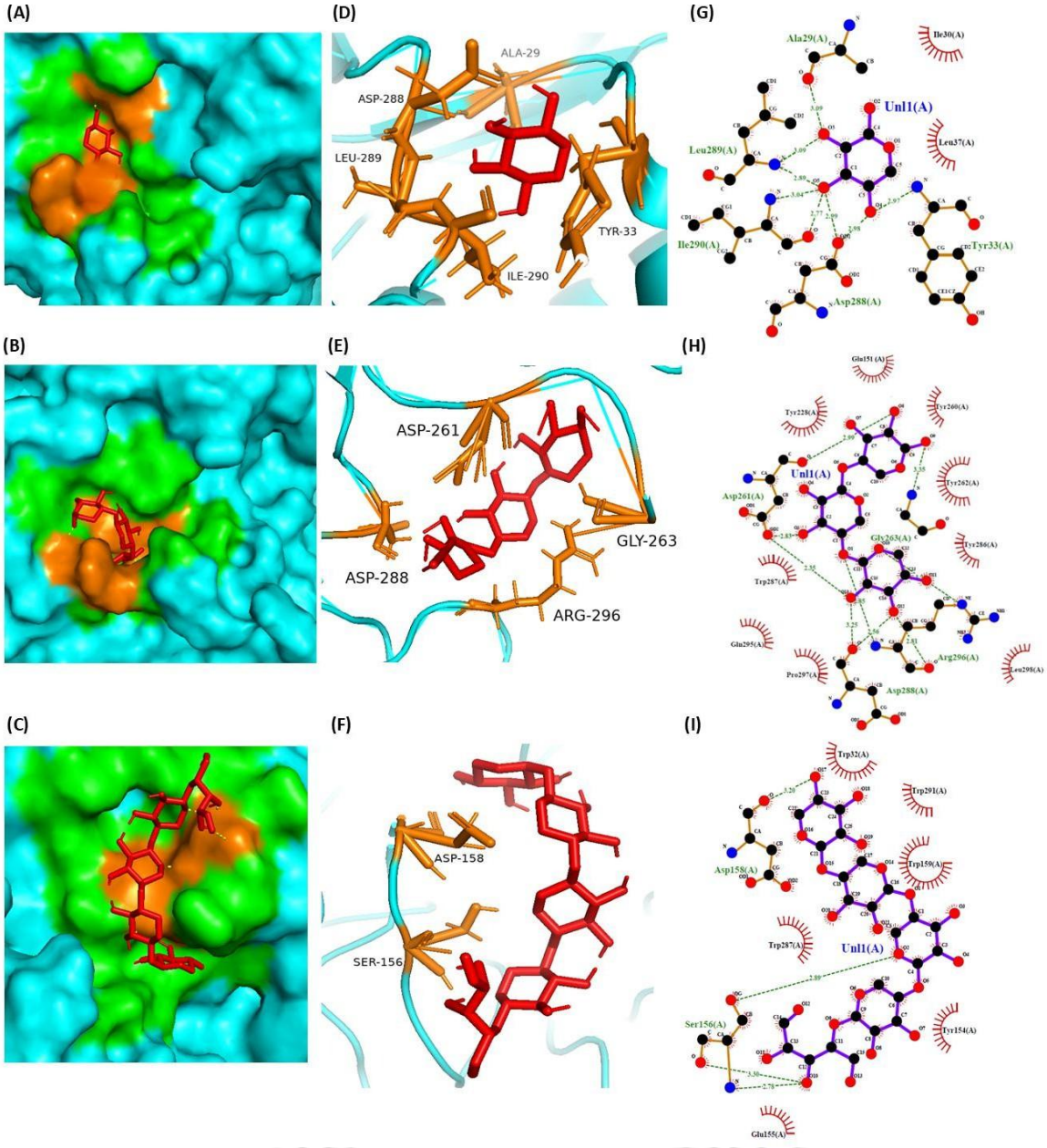

Fig. 4.9. Molecular docking of *Ac*Xyn30B_12 with xylo-oligosaccharides. **(A, B and C)** Surface view of *Ac*Xyn30B_12 (cyan) showing the fitting of xylose, xylotriose and xylopentaose (red) respectively in the catalytic cleft (amino acids with polar interactions are shown in orange and with non-polar interactions are shown in green). **(D, E and F)** 3D schematic representation of docked xylose, xylotriose and xylopentaose (red) respectively with the amino acid residues (orange) of the active-site with polar interactions only. **(G, H and I)** 2D schematic representation by using Ligplot software. Showing interaction of xylose, xylotriose and xylopentaose respectively with the amino acids at active-site of *Ac*Xyn30B_12 plotted (dashed lines represent hydrogen bonds and the amino acid are depicted in an arc with spokes, indicating non-polar interactions with the xylo-oligosaccahrides).

The binding analysis of xylotriose with *Ac*Xyn30B_12 revealed the presence of subsite, where the negative numeral designation (-1) corresponds to the non-reducing end of the bound xylotriose (Fig. 4.10A). While, the reducing end is represented by positive numeral subsites (+1 and +2). The amino acid residues Asp288 and Arg296 are placed at -1 subsite and play a crucial role in binding xylotriose at its non-reducing end within *Ac*Xyn30B_12 (Fig. 4.10B). Additionally, Asp261 is associated with the +1 subsite, while Gly263 associated with the +2 subsite (Fig. 4.10B).

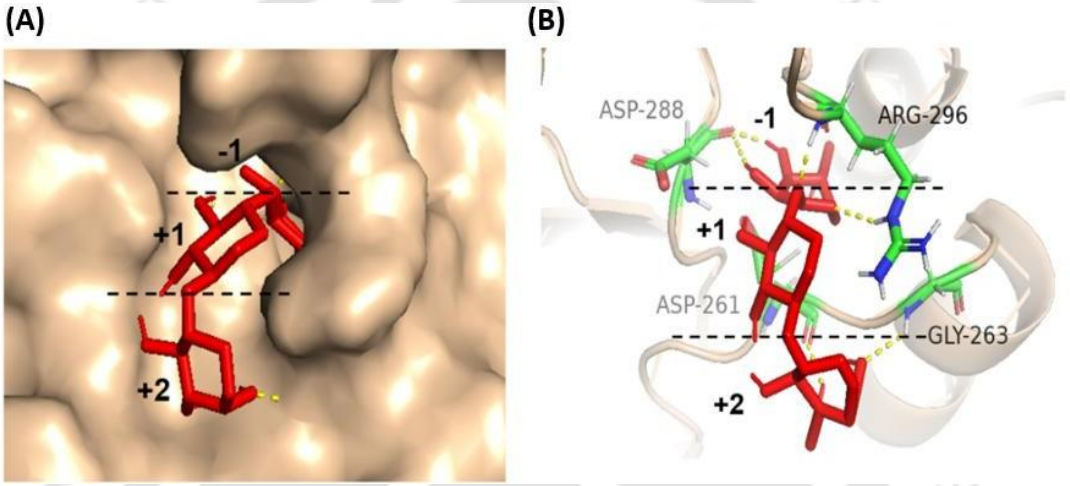

Fig. 4.10. Subsite analysis of *Ac*Xyn30B_12 with xylotriose. **(A)** Xylotriose as red ball and stick model and *Ac*Xyn30B_12 in sand colour with the subsites and **(B)** amino acid residues of *Ac*Xyn30B_12 involved in hydrogen bonding with xylotriose ligand.

4.3.7. MD simulation analysis of *Ac*Xyn30B_12-xylotriose complex

The *Ac*Xyn30B_12-xylotriose docked complex was submitted for MD simulation (100 ns) in order to establish its global compactness and stability. Comparisons were made between the acquired dynamics datasets and the datasets of unbound *Ac*Xyn30B_12 simulated structure. Beyond 16 ns, the average RMSD of the complex reduced to 0.9 nm indicating that it is relatively more stable and compact than the unbound *Ac*Xyn30B_12 (Fig. 4.11A). This implied that the existence of ligand in

*Ac*Xyn30B_12 active-site cleft, reduced slightly the RMSD value. The catalytic residues, Glu151 and Glu259 showed decrease in their RMSF values from 0.37 nm to 0.23 nm and from 0.24 to 0.12 nm, respectively. This suggests that upon ligand binding the catalytic residues were more rigid when attached to the ligand. Furthermore, as shown in Fig. 4.11B, the loop regions in the ligand bound *Ac*Xyn30B_12 structure exhibit reduced variability, indicating reduction in flexibility within the *Ac*Xyn30B_12-xylotriose complex. The R_g of the *Ac*Xyn30B_12-xylotriose complex fluctuated initially mid 1ns and 7 ns, then stabilized after 7 ns within a narrow range of 3.75–3.64 nm, finally giving an average R_g of 3.6 nm, approximately 0.3 nm less than the unbound simulated *Ac*Xyn30B_12 structure (Fig. 4.11C). This demonstrated that how the ligand interaction increases the compactness of the *Ac*Xyn30B_12 structure. The SASA effectively dropped by 17 nm^2 from the SASA of the unbound *Ac*Xyn30B_12 simulated structure (Fig. 4.11D) and stayed near to 316 nm^2 throughout the MD run until 100 ns. This suggested that there is a decrease in the available surface area upon ligand binding in catalytic cleft of *Ac*Xyn30B_12. The *Ac*Xyn30B_12-xylotriose docked complex generated an average of 463 intramolecular hydrogen bonds which was around 39 more than unbound *Ac*Xyn30B_12, showing that the ligand was strongly bound to its catalytic cleft of the enzyme (Fig. 4.11E).

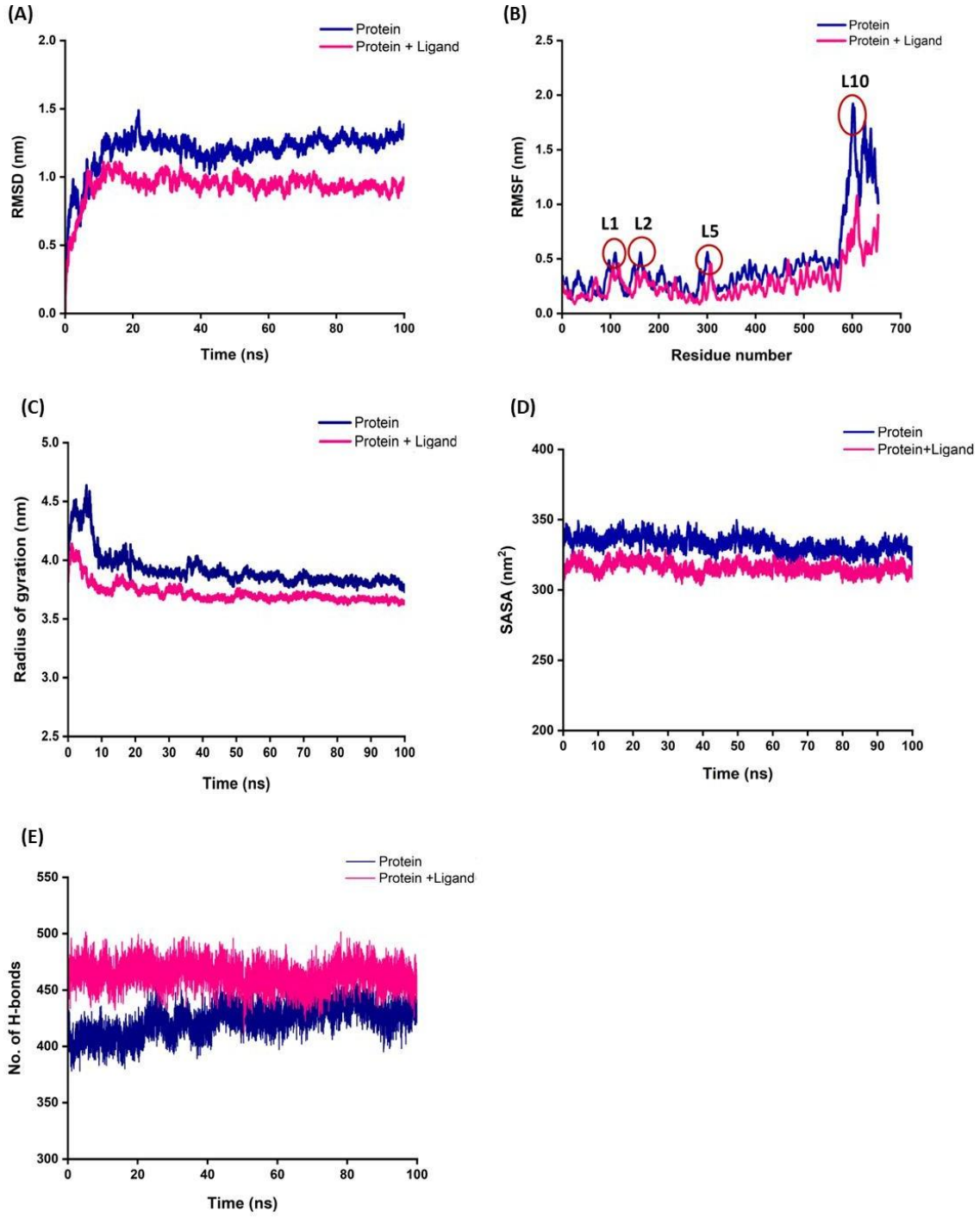

Fig. 4.11. Graphs showing comparative study between molecular dynamic simulation of docked complex *Ac*Xyn30B_12-xylotriose (pink) and unbound *Ac*Xyn30B_12 structure (blue); **(A)** Root mean square deviation, **(B)** Root mean square fluctuation, where L1, L2, L5 and L10 represent loops sequentially numbered according to the PDB topology file generated by the PDBsum server **(C)** Radius of gyration, **(D)** Solvent accessible surface area and **(E)** Intra-molecular hydrogen bonds.

4.3.8. Solution structure analysis of *Ac*Xyn30B_12 by SAXS analysis

The solution structure of *Ac*Xyn30B_12 at 3 mg/mL and 5 mg/mL was analysed by Small Angle X-ray Scattering analysis (SAXS) and the data obtained were examined by utilising ATSAS v2.8.4 suite. Polydispersity at both concentrations and aggregation at 5 mg/mL are displayed in the intensity vs. scattering plot (Fig. 4.12A). Fig. 4.12B displays the Guinier plot and R_g values for *Ac*Xyn30B_12 computed using the Guinier approximation is shown in Table 4.4. The R_g values for globular and rod shapes were, 4.01 and 2.7 nm at 3 mg/mL and 5.13 nm and 3.9 nm at 5 mg/mL (Table 4.4). According to SAXSMoW, the molecular weight of *Ac*Xyn30B_12 was 73.3 kDa and 144.4 kDa at 3 mg/mL and 5 mg/mL, respectively. This demonstrated that the molecular weight of *Ac*Xyn30B_12, at 5 mg/mL, was nearly twice of its theoretical molecular mass, suggesting that the protein is in dimeric state. This conformational flexibility indicates that the enzyme undergoes concentration-dependent structural changes, which may influence substrate binding and catalysis as reported earlier (Koch *et al*., 2013). The persistent length was 30.3 nm and 40.7 nm at 3 mg/mL and 5 mg/mL, respectively (Table 4.4). Through the Indirect Fourier Transformation (IFT) of the scattering profiles at 3 mg/mL as well as 5 mg/mL, a symmetric bell-shaped curve for 3 mg/mL and an asymmetric bell-shaped curve for 5 mg/mL were derived from the P(R) plot as shown in Fig. 4.12C. The R_g values obtained by the Guinier plot (Table 4.4) were supported by the R_g by P(R) which were 4.0 and 5.2 nm at 3 mg/mL and 5 mg/mL, respectively. The maximum particle dimension (D_{max}) of *Ac*Xyn30B_12 was 13.3 nm and 17.9 nm at 3 mg/mL and 5 mg/mL, respectively (Table 4.4). Therefore, the three-fold higher D_{max} value than R_g value at both concentrations indicated that *Ac*Xyn30B_12 has an extended structure contrary to a folded globular form. In the Kratky plot (at low Q regio) the

*Ac*Xyn30B_12 structure at 3 as well as 5 mg/mL displayed symmetric bell-shaped curves (Fig. 4.12D) that suggested the compactness, fully folded conformation and minimal flexibility of *Ac*Xyn30B_12 structure in the solution state.

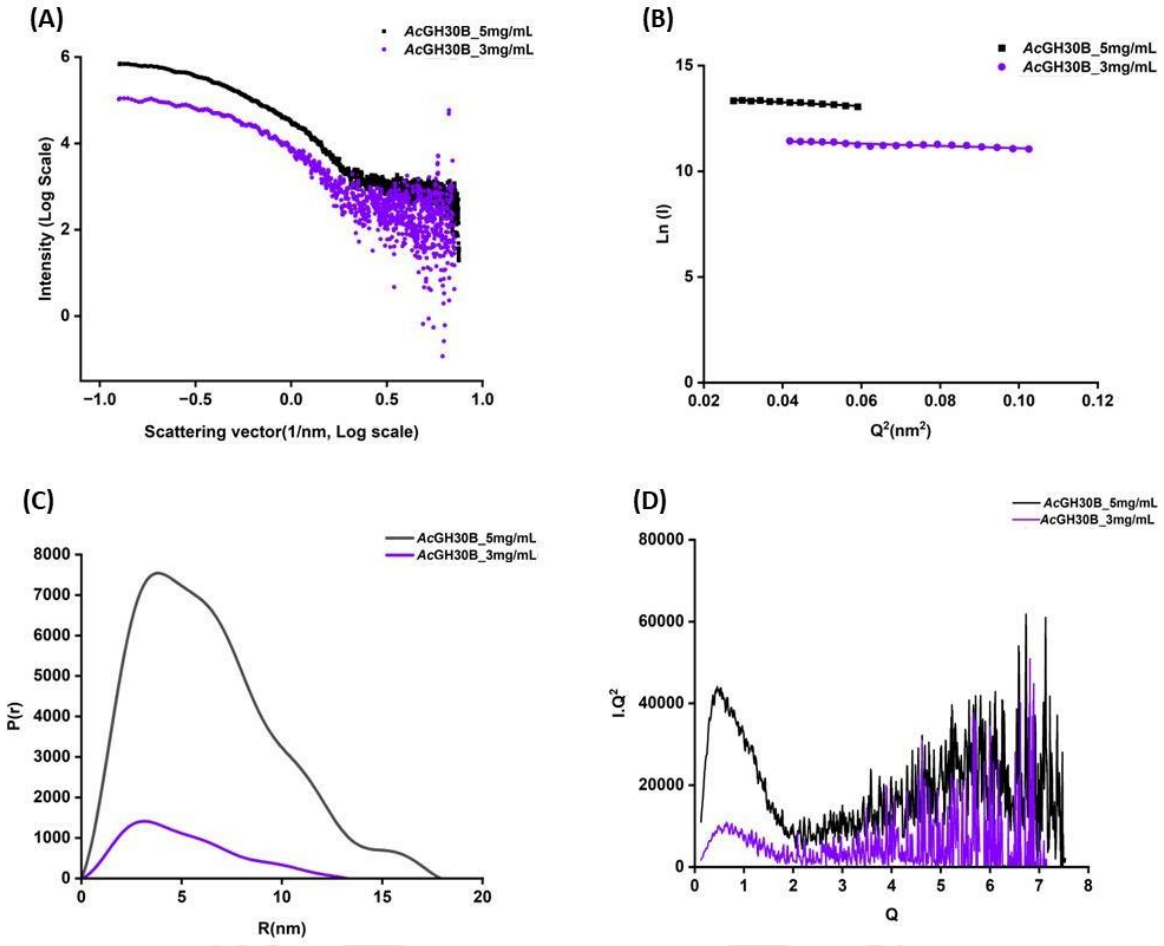

Fig. 4.12. SAXS analysis of *Ac*Xyn30B_12 at 3 mg/mL and 5 mg/mL concentrations. **(A)** SAXS profiles at 3 mg/mL and 5 mg/mL, **(B)** Guinier plot **(C)** P(R) plot as a function of R and **(D)** Kratky plot.

Table 4.4. Collection of SAXS data and derived parameters of *Ac*Xyn30B_12.

Data Collection parameters	***Ac*Xyn30B_12**	
Instrument	SAXS-Anton Paar	
Wavelength (Å)	1.54	
Q range (nm^{-1})	0.12-7.53	
Exposure time (min)	30 x 2	
Temperature (°C)	10	
Protein Concentration (mg/mL)	**3 mg/mL**	**5 mg/mL**
Structural parameters		
Q range (nm^{-1}) used for Rg analysis	0.20-0.32	0.16-0.24
I(0) au from Guinier	112057.0 ± 4770.0	820492.0 ± 26439.7
R_g (nm) from Guinier	4.01	5.13
I(0) au from P(R)	109300.0	793000.0
R_g (nm) from P(R)	4.02	5.17
D_{max} (nm)	13.3	17.9
Porod volume estimate (nm^3)	118.5	223.4
Persistent length (nm)	30.3	40.7
Molecular mass determination		
Theoritical molecular mass (kDa)	73.5	
Mw from SAXSMoW (kDa)	73.3	144.4
Modeling parameters		
Q range (nm^{-1}) used for structure modeling	0.20-0.38	0.16-0.29
Resolution (nm)	3.79	4.66
X^2 (Chi^2)	0.012	0.73
Normalized spatial discrepancy (NSD)	1.09	0.73
Software employed		
Data processing	Primus	
P(R) function calculation	GNOM	
Ab initio modeling	DAMMIF	
Validation and averaging	DAMAVER	
Structure superposition	SUPCOMB	
3D graphical representation	PyMOL	

Using the DAMMIF tool, 20 dummy atom models were created. DAMAVER and DAMMIN then refined the models. Additionally, the average of the 20 separate models normalized spatial discrepancy (NSD) values was calculated. For the ab initio model at 3 mg/mL (Fig. 4.13A), the normalized spatial discrepancy (NSD) value was 1.1 which indicates a good alignment between the model and DAM envelope. Also, this structure displayed nearly the monomeric form of DAM envelope. When the simulated modelled structure of *Ac*Xyn30B_12 was superimposed on this monomeric dummy atom model it imitated the structure of a chicken thigh bone (Fig. 4.13B). The normalized spatial discrepancy (NSD) value for ab initio model at 5 mg/mL was 0.7 which indicates a good alignment between the model and DAM envelope. This structure displayed nearly the dimeric form of DAM envelope (Fig. 4.13C). The protein-protein docking of simulated *Ac*Xyn30B_12 model as ligand and SAXS profile as receptor was carried out and using SUPCOMB program the best model generated was superposed with the DAM envelope attained at 5 mg/mL (Fig. 4.13D). At both protein concentrations, the DAM envelopes had an extended shape (Fig. 4.13A, Fig. 4.13C). A CRYSOL fitting between the simulated modelled structure and the experimental SAXS data at 3 mg/mL and 5 mg/mL yielded an X^2 value of 0.012 and 0.73 respectively (Fig. 4.13E). This low X^2 values at both the concentrations indicates good fit between the experimental data and modelled structure.

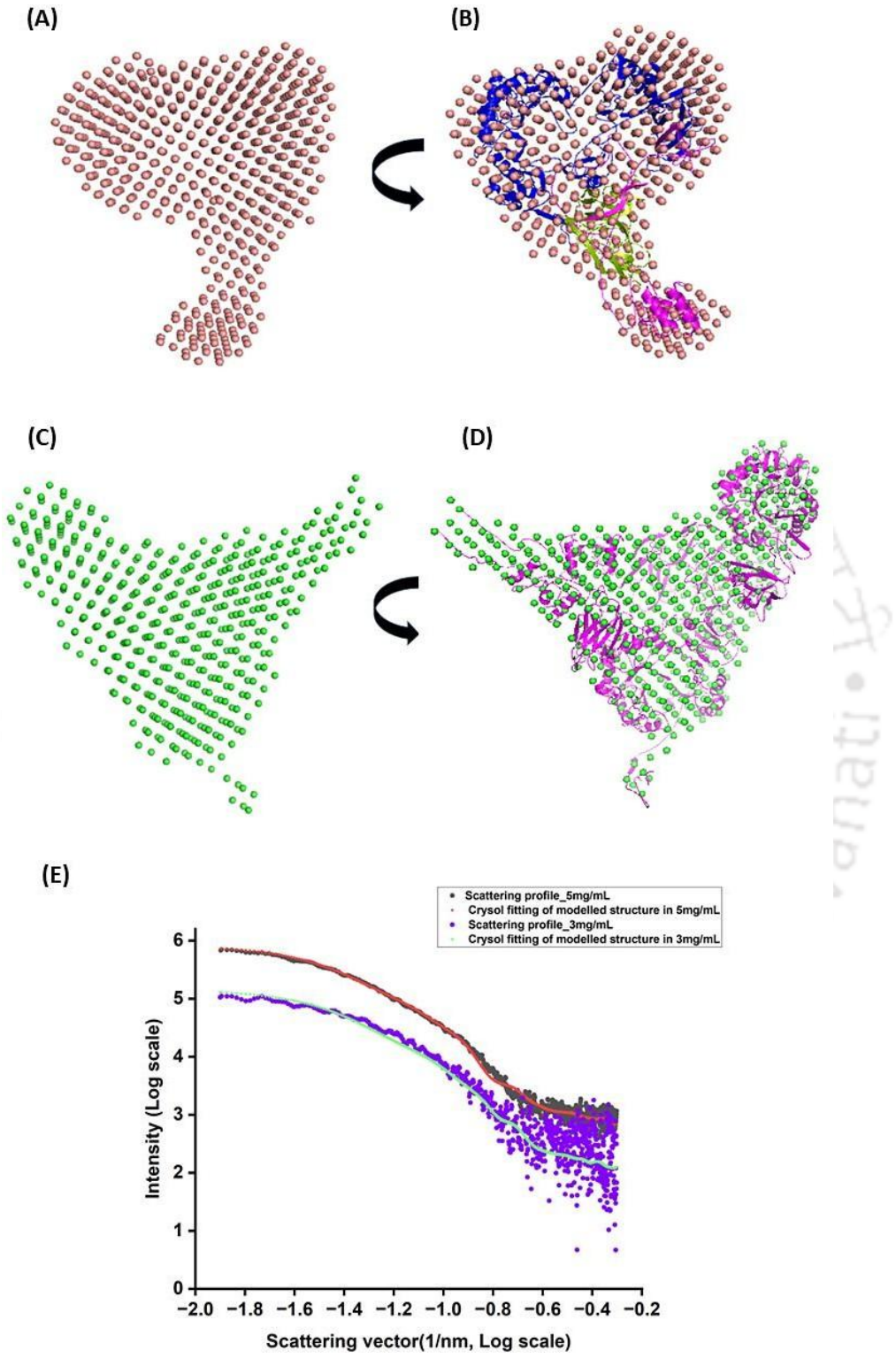

Fig. 4.13. *Ab initio* model **(A)** at 3 mg/mL, **(B)** superposed with *Ac*Xyn30B_12 modelled structure (monomer), **(C)** at 5 mg/mL, **(D)** superposed with *Ac*Xyn30B_12 (dimer) attained by pyDockSAXS and **(E)** Crysol fitting using SAXS datasets and modelled structures for both concentrations.

4.3.9. Hydrodynamic diameter and zeta-potential analysis of *Ac*Xyn30B_12 by using Dynamic light scattering

The hydrodynamic diameters (D_h) of *Ac*Xyn30B_12 measured at protein concentrations 1, 3 and 5 mg/mL by dynamic light scattering (DLS) gave values of 8.4 nm, 9.0 nm and 10.6 nm, respectively (Fig. 4.14A). The hydrodynamic radii (R_h) measured at the same concentrations were 4.2 nm, 4.5 nm and 5.3 nm, respectively. The observed increase in R_h at higher protein concentrations indicated that *Ac*Xyn30B_12 undergoes oligomerization in solution. These R_h values corroborated with the radius of gyration (R_g) values obtained from SAXS analysis (Section 4.3.8). Fig. 4.14 (A) shows the decrease in intensity at 3 mg/mL and 5 mg/mL which suggested aggregation due to particle interactions at these higher concentrations. The Polydispersity Index (PI) value at 5 mg/mL was 24.4%, which is higher than the standard threshold of 20% (Panalytical *et al*., 2019), indicating that *Ac*Xyn30B_12 exhibits significant polydispersity in solution.

Zeta potential analysis of *Ac*Xyn30B_12 showed a net negative surface charge of -10.5 ± 1.6 mV at 3 mg/mL (Fig. 4.14B) and -4.0 ± 1.0 mV at 5 mg/mL (Fig. 4.14C), confirming the protein's solubility and stability in an aqueous environment. The reduction in zeta potential by 5.5 mV from 3 mg/mL to 5 mg/mL suggests a decrease in overall surface charge, likely due to surface charge shielding and increased electrostatic interactions between *Ac*Xyn30B_12 monomers, leading to oligomerization and aggregation at higher concentrations.

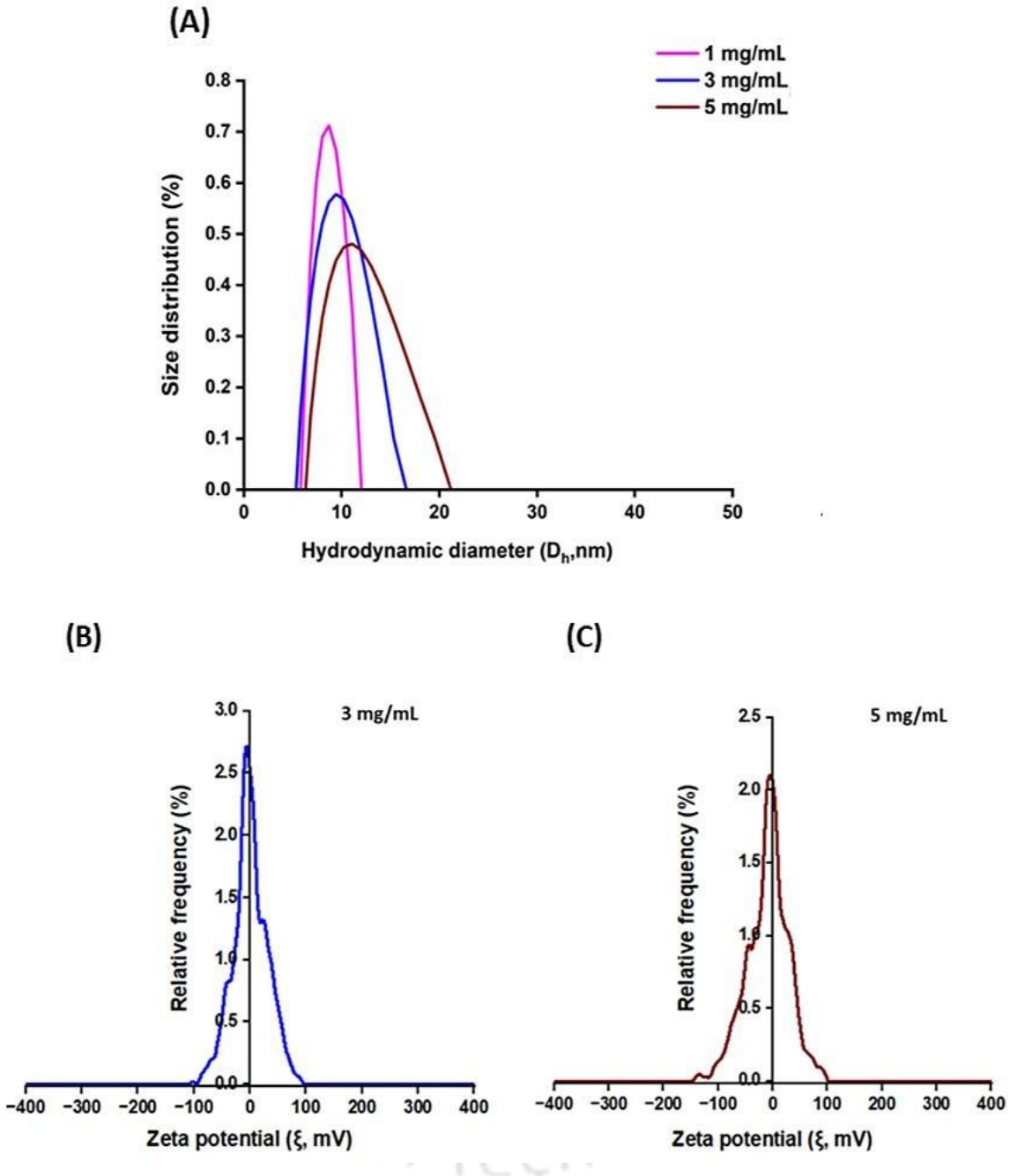

Fig. 4.14. DLS analysis of *Ac*Xyn30B_12. **(A)** D_h of *Ac*Xyn30B_12 at 1, 3 and 5 mg/mL. Surface charge analysis of *Ac*Xyn30B_12 at, **(B)** 3 and **(C)** 5 mg/mL in 0.05 M sodium phosphate buffer, pH 7.5.

4.4. Conclusion

The sequence analysis of the cloned gene encoding *Ac*Xyn30B_12 along with pET-28a(+) vector sequence including N-terminal His6 tag revealed a total of 653 amino acids giving its molecular weight, 73.5 kDa and the isoelectric point of 4.79. BLASTp analysis of *Ac*Xyn30B_12 with its homologous proteins showed highest sequence identity (27.81%) of *Ac*Xyn30B_12 with XynA (PDB ID: 5CXP) from *Clostridium acetobutylicum* ATCC 824. Glu151 and Glu259 were the catalytic residues that were found to be conserved on multiple sequence alignment and superimposition with its homologous protein sequences. The distance between these catalytic residues was found to be 5.5 Å which revealed the retaining-type mechanism of hydrolysis followed by *Ac*Xyn30B_12. Circular dichroism analysis of *Ac*Xyn30B_12 showed 26.2% α-helices and 28.1% β-strands, corroborating with predictions from PSIPRED and SOPMA servers. 3D modelled structure of *Ac*Xyn30B_12 by Alphafold2 was the best showing 99.8% of amino acid residues in favorable region and only 0.2% in disallowed region of Ramachandran plot. ProSA results also validated the *Ac*Xyn30B_12 modelled structure's correctness and compatibility with Z-score of 8.71. The 3D model structure of *Ac*Xyn30B_12 showed the presence of $(\beta/\alpha)_8$ barrel and an associated a 'side-β structure', which is a characteristic feature of glycoside hydrolase family 30 (GH30) proteins. This structural arrangement aligns with known features of GH30 enzymes, supporting its classification within this family. The active-site of *Ac*Xyn30B_12 predicted by CastP server showed a solvent accessible surface area of 156.5 $Å^2$ and volume of 215 $Å^3$. Molecular docking revealed the highest affinity of amino acids of catalytic cleft of *Ac*Xyn30B_12 with xylotriose (-11.2 kcal/mol) followed by xylobiose (-9.6 kcal/mol), xylotetraose (-9.1 kcal/mol), xylose (-8.9

kcal/mol) and xylopentaose (-8.6 kcal/mol). MD simulation analyses of both unbound *Ac*Xyn30B_12 and docked *Ac*Xyn30B_12-xylotriose complex, revealed that the docked complex had low RMSD value, lower fluctuation and lower flexibility at loop region (by RMSF value), lower surface area accessible on ligand binding (by SASA value) and higher compactness (by R_g value) as compared with unbound *Ac*Xyn30B_12. These results suggest that xylotriose binding induces structural stabilization in *Ac*Xyn30B_12, enhancing its rigidity and reducing flexibility, particularly in catalytically relevant regions. The R_g value of 3.9 nm found by MD simulation for unbound *Ac*Xyn30B_12 was similar with the results of SAXS and DLS. Small angle X-ray scattering (SAXS) analysis of *Ac*Xyn30B_12 confirmed the polydisperse and elongated structure of *Ac*Xyn30B_12 at 3 mg/mL and 5 mg/mL concentrations. Dummy atom model analysis of *Ac*Xyn30B_12 revealed monomeric form at 3 mg/mL and dimeric form at 5 mg/mL. Dynamic light scattering (DLS) analysis of *Ac*Xyn30B_12 confirmed the polydisperse nature at all concentrations (1, 3 and 5 mg/mL). The DLS study showed R_h values of 4.2 nm, 4.5 nm and 5.3 nm at 1, 3 and 5 mg/mL, respectively, matching the R_g results from SAXS analysis. A lower zeta potential of -4.0 mV at 5 mg/mL compared to -10.5 mV at 3 mg/mL indicated protein aggregation and dimerization at higher concentration which makes the enzyme valuable for production of different value-added products like prebiotics and biofuel.

4.5. References

Artzi, L., Dassa, B., Borovok, I., Shamshoum, M., Lamed, R., & Bayer, E. A. (2014) Cellulosomics of the cellulolytic thermophile *Clostridium clariflavum*. Biotechnology. Biofuels. 7, 1-14.

Ahmed, J., Kumar, K., Sharma, K., Fontes, C. M., & Goyal, A. (2021) Computational and SAXS-based structure insights of pectin acetyl esterase (Ct Pae12B) of family 12 carbohydrate esterase from *Clostridium thermocellum* ATCC 27405. Journal of Biomolecular Structure and Dynamics 40(18), 8437-8454.

Boratyn, G. M., Camacho, C., Cooper, P. S., Coulouris, G., Fong, A., Ma, N., et al. (2013) BLAST: a more efficient report with usability improvements. Nucleic Acids Research. 41, 29-33.

Bowie, J. U., Lüthy, R., & Eisenberg, D. (1991) A method to identify protein sequences that fold into a known three-dimensional structure. Science. 253(5016), 164-170.

Bugnon, M., Goullieux, M., Röhrig, U. F., Perez, M. A., Daina, A., Michielin, O., et al. (2023) SwissParam 2023: a modern web-based tool for efficient small molecule parametrization. Journal of Chemical Information and Modeling 63(21), 6469-6475.

Colovos, C., & Yeates, T. O. (1993) Verification of protein structures: patterns of nonbonded atomic interactions. Protein Science. 2(9), 1511-1519.

Fischer, H., Neto, M. D., Napolitano, H. B., Polikarpov, I., & Craievich, A. F. (2010) Determination of the molecular weight of proteins in solution from a single small-angle X-ray scattering measurement on a relative scale. Journal of Applied Crystallography 43(1), 101–109.

Franke, D., Petoukhov, M. V., Konarev, P. V., Panjkovich, A., Tuukkanen, A., Mertens, H. D. T., et al. (2017) ATSAS 2.8: a comprehensive data analysis suite for small-angle scattering from macromolecular solutions. Journal of Applied Crystallography 50(4), 1212-1225.

Gasteiger, E., Hoogland, C., Gattiker, A., Duvaud, S. E., Wilkins, M. R., Appel, R. D., & Bairoch, A. (2005) Protein identification and analysis tools on the ExPASy server. Humana Press. 571-607.

Gouet, P., Courcelle, E., Stuart, D. I., & Metoz, F. (1999) ESPript: analysis of multiple sequence alignments in PostScript. Bioinformatics. 15(4), 305-308.

Guinier, G., Fournet, G., & Yudowitch, K. L. (1955) Small-angle Scattering of X-rays. Wiley, New York.

Hess, B., Kutzner, C., Van Der Spoel, D., & Lindahl, E. (2008) GROMACS 4: algorithms for highly efficient, load-balanced, and scalable molecular simulation. Journal of Chemical Theory and Computation 4, 435-447.

Jiménez-García, C., Pons, D. I., Svergun, P., Bernadó, J., & Fernández-Recio, J. (2015) py-DockSAXS: protein–protein complex structure by SAXS and computational docking. Nucleic Acids Research. 43, 356-361.

Koch, C., Tria, G., Fielding, A. J., Brodhun, F., Valerius, O., Feussner, K., Braus, G. H., Svergun, D. I., Bennati, M., & Feussner, I. (2013) A structural model of PpoA derived from SAXS-analysis—Implications for substrate conversion. Biochimica et Biophysica Acta (BBA) - Molecular and Cell Biology of Lipids 1831, 1449-1457.

Kozin, M. B., & Svergun, D. I. (2001) Automated matching of high- and low-resolution structural models. Journal of Applied Crystallography 34, 33-41.

Larson, S. B., Day, J., Barba de la Rosa, A. P., Keen, N. T., & McPherson, A. (2003) First crystallographic structure of a xylanase from glycoside hydrolase family 5: implications for catalysis. Biochemistry. 42, 8411-8422.

Lorber, F., Fischer, M., Bailly, H., Roy, D., & Kern, D. (2012) Protein analysis by dynamic light scattering: methods and techniques for students. Biochemistry and Molecular Biology Education 40, 372-382.

Louis-Jeune, C., Andrade-Navarro, M. A., & Perez-Iratxeta, C. (2012) Prediction of protein secondary structure from circular dichroism using theoretically derived spectra. Proteins. 80, 374-381.

Lüthy, R., Bowie, J. U., & Eisenberg, D. (1992) Assessment of protein models with three-dimensional profiles. Nature. 356, 83-85.

Mankar, A. R., Pandey, A., Modak, A., & Pant, K. K. (2021) Pretreatment of lignocellulosic biomass: A review on recent advances. Bioresource Technology. 334, 125235.

Micsonai, A., Moussong, E., Wien, F., Boros, E., Vadászi, H., Murvai, N., Lee, Y. H., Molnár, T., Réfrégiers, M., Goto, Y., & Tantos, A. (2022) BeStSel: webserver for secondary structure and fold prediction for protein CD spectroscopy. Nucleic Acids Research. 50, 90-98.

Moreira, L. R. S., & Filho, E. X. F. (2016) Insights into the mechanism of enzymatic hydrolysis of xylan. Applied Microbiology and Biotechnology100, 5205-5214.

Konarev, P. V., Volkov, V. V., Sokolova, A. V., Koch, M. H. J., & Svergun, D. I. (2003) PRIMUS: a Windows PC-based system for small-angle scattering data analysis. Journal of Applied Crystallography 36, 1277-1282.

Odijk, T. (1977) Polyelectrolytes near the Rod Limit. Journal of Polymer Science Part B: Polymer Physics.15, 477–483.

Pontius, J., Richelle, J., & Wodak, S. J. (1996) Deviations from standard atomic volumes as a quality measure for protein crystal structures. Journal of Molecular Biology. 264, 121-136.

Puchart, V., Šuchová, K., & Biely, P. (2021) Xylanases of glycoside hydrolase family 30–An overview. Biotechnology Advances. 47, 107704.

Saini, J.K., Saini, R., & Tewari, L. (2015) Lignocellulosic agriculture wastes as biomass feedstocks for second-generation bioethanol production: concepts and recent developments. 3 Biotech. 5, 337-353

Salgın, S., Salgın, U., & Bahadır, S. (2012) Zeta potentials and isoelectric points of biomolecules: the effects of ion types and ionic strengths. International Journal of Electrochemical Science 7, 12404-12414.

Santibáñez, L., Henríquez, C., Corro-Tejeda, R., Bernal, S., Armijo, B., & Salazar, O. (2021) Xylooligosaccharides from lignocellulosic biomass: A comprehensive review. Carbohydrate. Polymers. 251, 117118.

Sharma, K., Fontes, C., Najmudin, S., & Goyal, A. (2021) Small angle X-ray scattering based structure, modeling and molecular dynamics analyses of family 43 glycoside hydrolase alpha-l-arabinofuranosidase from *Clostridium thermocellum*. Journal of Biomolecular Structure and Dynamics. 39, 209-218.

Sievers, F., & Higgins, D.G. (2014) Clustal Omega, accurate alignment of very large numbers of sequences. Methods. 105-116.

Singh, S., Ahmed, J., Gavande, P.V., Fontes, C.M., & Goyal, A. (2023) Structural and functional insights into the glycoside hydrolase family 30 xylanase of the rumen bacterium *Ruminococcus flavefaciens*. Journal of Molecular Structure. 1272, 134155.

Sohail, M., Barzkar, N., Michaud, P., Tamadoni Jahromi, S., Babich, O., Sukhikh, S., Das, R., & Nahavandi, R. (2022) Cellulolytic and xylanolytic enzymes from yeasts: Properties and industrial applications. Molecules. 27, 3783.

St John, F.J., Dietrich, D., Crooks, C., Balogun, P., de Serrano, V., Pozharski, E., Smith, J.K., Bales, E., & Hurlbert, J. (2018) A plasmid borne, functionally novel glycoside hydrolase family 30 subfamily 8 endoxylanase from solventogenic Clostridium. Biochemical Journal 475, 1533-1551.

St John, F.J., Hurlbert, J.C., Rice, J.D., Preston, J.F., & Pozharski, E. (2011) Ligand bound structures of a glycosyl hydrolase family 30 glucuronoxylan xylanohydrolase. Journal of Molecular Biology 407, 92-109.

Šuchová, K., Fathallah, W., & Puchart, V. (2024) Characterization of a novel GH30 non-specific endoxylanase AcXyn30B from *Acetivibrio clariflavus*. Applied Microbiology and Biotechnology 108, 312.

Šuchová, K., Kozmon, S., Puchart, V., Malovíková, A., Hoff, T., Krogh, K.B.M., & Biely, P. (2018) Glucuronoxylan recognition by GH 30 xylanases: a study with enzyme and substrate variants. Archives of Biochemistry and Biophysics 643, 42-49.

Svergun, D. I., Petoukhov, M. V., & Koch, M. H. (2001) Determination of domain structure of proteins from X-ray solution scattering. Biophysical Journal 80(6), 2946–2953.

Svergun, D. I. (1999) Restoring low resolution structure of biological macromolecules from solution scattering using simulated annealing. Biophysical Journal 76(6), 2879–2886.

Svergun, C., Barberato, M.H.J., & Koch, M. (1995) CRYSOL–a program to evaluate X-ray solution scattering of biological macromolecules from atomic coordinates. Journal of Applied Crystallography 28, 768–773.

Svergun, D. I. (1992) Determination of the regularization parameter in indirect-transform methods using perceptual criteria. Journal of Applied Crystallography 25(4), 495–503.

Tvaroška, I. (2004) Molecular modeling insights into the catalytic mechanism of the retaining galactosyltransferase LgtC. Carbohydrate Research339, 1007-1014.

Verma, A.K., & Goyal, A. (2014) In silico structural characterization and molecular docking studies of first glucuronoxylan-xylanohydrolase (Xyn30A) from family 30 glycosyl hydrolase (GH30) from *Clostridium thermocellum*. Molecular Biology 48, 278-286.

Volkov, V.V., & Svergun, D.I. (2003) Uniqueness of ab initio shape determination in small-angle scattering. Journal of Applied Crystallography 36, 860–864.

Wallace, A.C., Laskowski, R.A., & Thornton, J.M. (1995) LIGPLOT: a program to generate schematic diagrams of protein-ligand interactions. Protein Engineering, Design and Selection 8, 127-134.

Wang, Q., Graham, R.W., Trimbur, D., Warren, R.A.J., & Withers, S.G. (1994) Changing enzymic reaction mechanisms by mutagenesis: conversion of a retaining glucosidase to an inverting enzyme. Journal of the American Chemical Society. 116, 11594–11595.

Wiederstein, M., & Sippl, M.J. (2007) ProSA-web: interactive web service for the recognition of errors in three-dimensional structures of proteins. Nucleic Acids Research. 35, 407-410.

Chapter 5

Efficient and eco-friendly enzymatic deinking of waste papers using endo-*β*-1,4-xylanase (*Ac*Xyn30B_12) from *Acetivibrio clariflavus* DSM 19732

5.1. Introduction

The global pulp and paper industry is facing increasing pressure to adopt environmentally sustainable practices in response to resource scarcity, rising production costs and environmental regulations. Traditional recycling of printed papers especially newspapers and office paper utilize chemical-intensive deinking methods (Desai and Iyer, 2016). These chemical treatments, including the use of sodium hydroxide, surfactants and hydrogen peroxide, although effective in ink removal, often result in environmental pollution and degraded fiber quality (Saxena and Chauhan, 2017). As a result, the development of enzyme-based deinking strategies has gained attention as a promising alternative to conventional methods.

Enzymatic deinking offers a cleaner (releasing less toxic effluent) and more fiber-preserving approach (targeted hydrolysis of cellulose, hemicellulose and lignin) by utilizing hydrolytic enzymes such as cellulases, xylanases, pectinases and laccases to disrupt the ink-fiber bonds. Among these enzymes, xylanases have shown particular promise due to their ability to specifically degrade hemicellulose (xylan), which is abundantly present in lignocellulosic paper fibers (Yang *et al.*, 2023). Unlike cellulases that may weaken the mechanical strength of recycled paper by hydrolyzing cellulose,

xylanases selectively target non-cellulosic components, thus facilitating ink removal without compromising pulp integrity (Desai and Iyer, 2016). Xylanases that function efficiently at mildly acidic pH (5.0-6.0) are particularly well-suited to the native pH conditions of many waste paper types, thereby offering enhanced compatibility with practical recycling environments (Dutt *et al*., 2012). The deinking efficiency achieved by different xylanases is evaluated through various parameters such as brightness, effective residual ink concentration (ERIC), whiteness, fiber strength and many more. Among these parameters, ERIC is one of the widely used quantitative indicators that reflects the amount of residual ink is remaining on the paper surface after deinking treatment. For instance, the application of 15 U/g purified bacterial xylanase from *Bacillus halodurans* FNP 135 for the deinking of 5.0% (w/v) old newspaper at 65°C for 3h resulted in a 45% deinking efficiency, as determined by the ERIC method (Virk *et al*., 2013). Similarly, the deinking of 10% (w/v) old paper at 100°C for 30 min by 50 U/g purified fungal endo-xylanase from *Aspergillus niger* DX-23, led to a 79% deinking efficiency, as determined by the ERIC method (Desai *et al*., 2016). These findings highlight the potential of xylanase as effective bio-based agent in the enzymatic deinking of waste paper, especially under conditions that align with industrial recycling processes.

In this study, the endo-*β*-1,4-xylanase (*Ac*Xyn30B_12) from *Acetivibrio clariflavus* DSM 19732 was investigated for its effectiveness in the eco-friendly deinking of newspaper waste (NEPW) and notebook paper waste (NOPW). The different deinking conditions (enzyme dosage, time and temperature) were optimized using response surface methodology (RSM) and their effect on pulp properties was comprehensively assessed through various analytical techniques, including FTIR,

XRD, FESEM, brightness and Cobb tests. The total reducing sugars (TRS) present in the effluent were also analyzed to evaluate the extent of hemicellulose hydrolysis and residual sugar released during the deinking process. To evaluate the environmental sustainability of the process, the effluent generated during deinking was analyzed for total dissolved solid (TDS) and total suspended solid (TSS) levels. Moreover, comparative evaluation was performed using the crude enzyme, purified *Ac*Xyn30B_12 and chemical treatment (NaOH) to determine their relative effectiveness in the deinking process, along with an assessment of their environmental impact to identify sustainable and eco-friendly alternative to conventional chemical methods.

5.2. Materials and methods

5.2.1. Chemicals and reagents

The 5 different types of waste papers (each at least six months old) *viz*., *Assam Tribune* newspaper waste (NEPW), unruled *Classmate* notebook paper waste (NOPW) with blue ballpoint pen ink, *Amazon* packing cardboard paper waste (CaPW), A4-sized *HP LaserJet* printed paper waste (LPW) and magazine paper waste (MPW) were selected and collected from IIT Guwahati campus. The reagents used for the standard TAPPI protocols *viz*., sodium chlorite, disodium phosphate and citric acid were procured from HiMedia, Laboratories Pvt. Ltd., India. Acetic acid from SRL Pvt. Ltd., India and acetone from Actylis, India were purchased. For the standard NREL protocol, sulfuric acid was obtained from Actylis, India, while sodium hydroxide was procured from Sigma-Aldrich, USA.

5.2.2. Collection and composition analysis of different waste papers

The five different types of waste papers *viz*., NEPW, NOPW, CaPW, LPW and MPW were cut into uniform sizes (15 cm x 15 cm, l x b), ensuring ~100% ink coverage on both sides. Subsequently, the papers were shredded into smaller pieces using a domestic mixer grinder. The prepared samples were stored at 25°C until further use. The hemicellulose and cellulose contents of each waste paper type were determined by using the standard Technical Association of the Pulp and Paper Industry (TAPPI) protocol (Weinstock *et al*., 1995). The lignin content was estimated following the National Renewable Energy Laboratory (NREL) protocol (Sluiter *et al*., 2008). For deinking, the waste paper with higher hemicellulose content and lowest lignin content were selected for enzymatic deinking with the crude enzyme and purified endo-xylanase, *Ac*Xyn30B_12 (produced as described in Chapter 3, Section 3.3.1).

5.2.3. Statistical optimization of efficient deinking of NEPW and NOPW by *Ac*Xyn30B_12 using response surface methodology

5.2.3.1. Experimental design and variable selection for response surface methodology

The deinking conditions *viz*., enzyme dosage (U/g), temperature (°C) and incubation time (min), were optimized by using a response surface methodology (RSM) based on Box-Behnken experimental design (Box and Behnken, 1960). The deinking efficiency (%) was set as response in the model. A total of 17 randomized experimental runs, including 5 unique combinations and 3 center point replicates, were generated using Design Expert version 9 software (Stat-Ease Inc., Minneapolis, USA). The ranges of the 3 independent variables used in the design are presented in Table 5.1.

Table 5.1. Independent variables and their levels used in Box-Behnken design.

Independent variables	Units	Levels	
		-1	**+1**
Enzyme dosage (For purified *Ac*Xyn30B_12)	U/g	10	100
Temperature	°C	40	70
Time	min	30	90

5.2.3.2. Deinking procedure using purified *Ac*Xyn30B_12 and evaluation of deinking efficiency

Prior to the deinking experiment the endo-xylanase enzyme, *Ac*Xyn30B_12 was purified by following the protocol as described in Chapter 3, Section 3.3.1. For each experimental run, a 10 mL reaction mixture was prepared with a pulp consistency

of 5.0% (w/v) by dispersing NEPW and NOPW separately in 50 mM citrate-phosphate buffer (pH 5.5). The buffer 50 mM citrate-phosphate (pH 5.5) was selected as the reaction buffer for deinking as it represented the optimal pH for *Ac*Xyn30B activity, as determined in Chapter 3, Section 3.3.2.1. Deinking was performed under varying conditions of enzyme dosage, temperature and incubation time, as specified by the Box-Behnken design, with orbital shaking at 150 rpm in a shaking incubator. Upon completion of each run, the reaction mixtures were heat-inactivated by incubation at 100°C for 5 min. The resulting pulp was thoroughly washed using 200 mL of Milli-Q water in a 25 mL sintered glass funnel connected to a vacuum pump, ensuring the removal of residual ink particles. The washed pulp was then pressed by using a 15-ton hydraulic press (Perkin Elmer, USA) to form circular and uniform paper sheets each with diameter of 3 cm and thickness ~1.0 mm. These sheets were dried at 50°C (in hot air oven) for 6h and stored at 25°C for further analysis. The reflectance of each deinked sheet was measured at 950 nm (Jordan and Popson 1994) with a resolution of 4.0 cm^{-1} using ATR-FTIR spectrophotometer (Spectrum Two, Perkin Elmer, USA). To ensure reproducibility, each RSM-suggested experimental run was carried out in duplicate.

The deinking efficiency (for each run) was assessed by calculating the Effective Residual Ink Content (ERIC), using the Kubelka Munk equation (Dzimbeg-Malcic *et al*., 2011) as given below:

$$ERIC = \frac{k}{k_{ink}} \times 10^6 \text{ ppm}$$

Where,

ERIC = Effective residual ink content

k = Kubelka-Munk coefficient

$k_{ink} = 10^3$ m^2/kg

The Kubelka-Munk coefficient was calculated by using the following formula (Malcic *et al*., 2011):

$$k = s \frac{(1 - R)^2}{2R}$$

Where,

k = Kubelka-Munk coefficient

s = specific scattering coefficient (default value =50 m^2/kg)

R = reflectance at 950 nm

The deinking efficiency using ERIC values of untreated (paper in buffer without enzyme) and treated NEPW and NOPW was calculated by using the following formula (Li *et al*., 2011):

$$\text{Deinking efficiency (\%)} = \frac{ERIC_{\text{Treated sample}} - ERIC_{\text{Untreated sample}}}{ERIC_{\text{Untreated sample}}}$$

5.2.4. Comparative analysis of deinking of NEPW and NOPW by crude enzyme, purified *Ac*Xyn30B_12 and NaOH under optimized conditions

The deinking efficiency of crude enzyme and purified *Ac*Xyn30B_12, as well as NaOH, was evaluated by treating NEPW and NOPW under optimized conditions of 70°C for 90 min, as determined in Section 5.2.3. Each reaction was carried out in a total volume of 10 mL with a pulp consistency of 5.0% (w/v), prepared by suspending the waste papers individually in 50 mM citrate-phosphate buffer (pH 5.5) and incubated at 150 rpm in a shaking incubator (as mentioned in Section 5.2.3.2). The enzyme dosage for both crude enzyme and purified *Ac*Xyn30B_12 were applied at their respective optimized levels *viz*., 46.4 U/g of paper for NEPW and 58.6 U/g of paper for NOPW (as determined in Section 5.3.2). NaOH was selected for the comparative study because it

is one of the most prominent deinking agents used in industrial processes (Bajpai *et al*., 2015). Hence, it was included under present optimized conditions to evaluate its efficiency relative to the enzymatic treatment. The NaOH concentration of 0.6% (w/v) was chosen, in accordance with the INGEDE Method 11 (International Association of the Deinking Industry). Upon completion of the reaction, the mixtures were heat-inactivated by incubating at 100°C for 5 min. The resulting pulp was thoroughly washed using 200 mL of Milli-Q water in a 25 mL sintered glass funnel connected to a vacuum pump, ensuring the removal of residual ink particles. Subsequently, the washed pulp was pressed and uniform circular sheets were prepared by following the procedure as described in Section 5.2.3. The reactions were performed in duplicate.

5.2.5. Crystallinity index (*CrI*) analysis of deinked NEPW and NOPW using X-ray diffraction

The crystallinity index (*CrI*) of untreated (paper dissolved in buffer but without enzyme) and crude enzyme, purified *Ac*Xyn30B_12 and NaOH treated NEPW and NOPW samples was determine by X-ray diffraction (XRD) analysis. Prior to XRD analysis, deinking treatments were performed with crude enzyme (46.4 U/g for NEPW and 58.6 U/g for NOPW), purified *Ac*Xyn30B_12 (46.4 U/g for NEPW and 58.6 U/g for NOPW) and NaOH (0.6% w/v), in a total reaction volume of 10 mL with 5.0% (w/v) pulp consistency in 50 mM citrate-phosphate buffer (pH 5.5) at 150 rpm, at 70°C for 90 min (as mentioned in Section 5.2.3.2). Pulp washing and hand-sheet preparation were carried out as described in Section 5.2.3.2. The dried hand-sheets were cut into small fragments (~1.0 mm in length) and 1.0 g of each sample was analyzed for *CrI* using an X-ray diffractometer (D8 Advance, Bruker, Germany). Scanning was performed over a 2θ range of 10° to 80° with a step size of 0.05° (Virk *et al*., 2013).

The crystallinity index of each sample was calculated using the Segal equation (Segal *et al*., 1959), as given below:

$$CrI = \frac{I_{002} - I_{am} \times 100\%}{I_{002}}$$

Where,

I_{002} = peak intensity of (0 0 2) lattice plane (2Θ =22.6)

I_{am} = peak intensity of amorphous phase (2Θ =19.0)

The apparent crystalline size (*ACS*) was evaluated to assess the impact of deinking treatments on the structural crystallinity of cellulose fibers in the deinked paper (Virk *et al*., 2013). It was calculated by using the following Scherrer equation (Heinze and Liebert 2001):

$$ACS = 0.89\,\lambda\beta Cos\boldsymbol{\theta}$$

Where,

λ = wavelength of incident X-ray (1.5 Å)

Θ = Bragg angle corresponding to I_{002} plane

β = half height width of the peak angle of I_{002} reflection

5.2.6. Functional group analysis of deinked NEPW and NOPW using ATR-Fourier Transform Infrared (FTIR) spectroscopy

The ATR-FTIR analysis of untreated (paper dissolved in buffer but without enzyme) and crude enzyme, purified *Ac*Xyn30B_12 and NaOH treated NEPW and NOPW samples was performed to investigate the alterations in functional groups after pretreatment, thereby analysing the associated structural modifications. Prior to ATR-FTIR analysis, deinking treatments of waste papers were performed with crude enzyme (46.4 U/g for NEPW and 58.6 U/g for NOPW), purified *Ac*Xyn30B_12 (46.4 U/g for NEPW and 58.6 U/g for NOPW) and NaOH (0.6% w/v), in a total reaction

volume of 10 mL with 5.0% (w/v) pulp consistency in 50 mM citrate-phosphate buffer (pH 5.5) at 150 rpm, at 70°C for 90 min (as mentioned in Section 5.2.3.2). Pulp washing and hand-sheet preparation were carried out as described in Section 5.2.3.2. The dried hand-sheets were analyzed by using an ATR-FTIR spectrophotometer (Spectrum Two, Perkin Elmer, USA) over a wavenumber range of 4000-400 cm^{-1}, with a resolution of 4.0 cm^{-1} and a total number of 3 scans per sample.

5.2.7. Morphological analysis of deinked NEPW and NOPW using field emission scanning electron microscopy (FESEM)

To study and compare the morphological changes, the untreated (paper dissolved in buffer but without enzyme), crude enzyme, purified *Ac*Xyn30B_12 and NaOH treated NEPW and NOPW samples were analysed by FESEM. Prior to the morphological analysis, deinking treatments were performed with crude enzyme (46.4 U/g for NEPW and 58.6 U/g for NOPW), purified *Ac*Xyn30B_12 (46.4 U/g for NEPW and 58.6 U/g for NOPW) and NaOH (0.6% w/v), in a total reaction volume of 10 mL with 5.0% (w/v) pulp consistency in 50 mM citrate-phosphate buffer (pH 5.5) at 150 rpm, at 70°C for 90 min (as mentioned in Section 5.2.3.2). Pulp washing and hand-sheet preparation were carried out as described in Section 5.2.3.2. The dried hand-sheets were cut into small pieces (~1.0 mm) mounted on carbon tape, coated with a thin layer of gold and then examined by for FESEM under varying magnifications using accelerating voltage of 2 kV (Zeiss, Sigma, Germany).

5.2.8. Evaluation of optical properties of deinked NEPW and NOPW via brightness measurement

The improvement in the optical property i.e. brightness (%) of the deinked NEPW and NOPW was also measured using the standard TAPPI T452 OM-87 protocol (Weinstock *et al*., 1995). Prior to the brightness measurement, deinking treatments were performed with crude enzyme (46.4 U/g for NEPW and 58.6 U/g for NOPW), purified *Ac*Xyn30B_12 (46.4 U/g for NEPW and 58.6 U/g for NOPW) and NaOH (0.6% w/v), in a total reaction volume of 10 mL with 5.0% (w/v) pulp consistency in 50 mM citrate-phosphate buffer (pH 5.5) at 150 rpm, at 70°C for 90 min (as mentioned in Section 5.2.3.2). Pulp washing and hand-sheet preparation were carried out by following the methods as described in Section 5.2.3.2. The dried hand-sheets were cut into circular samples of 1.5 cm diameter and placed in a sample holder cell. Reflectance of each hand-sheet was measured at 457 nm using directional reflectance spectroscopy (DRS) mode on a Perkin Elmer Lambda 500 Reflectometer, following the protocol as reported by Lee *et al*. (2013).

5.2.9. Analysis of water absorptivity of deinked NEPW and NOPW by Cobb test

Water absorptivity is a critical parameter that influences the suitability of recycled paper for applications such as writing, printing and packaging. It provides insight into the porosity and surface properties of the deinked paper. Evaluating water absorption behavior helps in determining whether further treatments (such as sizing) are required before the pulp can be effectively reused in papermaking (Hubbe *et al*., 2009). Prior to this analysis, deinking treatments were performed with crude enzyme (46.4 U/g for NEPW and 58.6 U/g for NOPW), purified *Ac*Xyn30B_12 (46.4 U/g for NEPW and 58.6 U/g for NOPW) and NaOH (0.6% w/v), in a total reaction volume of

10 mL with 5.0% (w/v) pulp consistency in 50 mM citrate-phosphate buffer (pH 5.5) at 150 rpm, at 70°C for 90 min (as described in Section 5.2.3.2). Pulp washing and hand-sheet preparation were carried out as described in Section 5.2.3.2. The absorptivity of each deinked paper was measured using the standard TAPPI T441 om-09 method (Weinstock *et al*., 1995). Each deinked paper sample was immersed in 50 mL of Milli-Q water for 1h (Manandhar *et al*., 2022) and the weight of the soaked paper samples was recorded at specific time intervals to assess water absorption. The cobb value was calculated using the following formula (Soz, 2021):

$$Z = \frac{(X - Y)\ x\ 1000}{Area\ of\ paper\ (m^2)}$$

Where,

Z = cobb value (g/ m^2)

X= weight of paper before soaking in water (g)

Y= weight of paper after soaking in water at each time interval (g)

5.2.10. Analysis of effluent generated during deinking of NEPW and NOPW

5.2.10.1. Total reducing sugar estimation in effluents produced from deinking of NEPW and NOPW

The total reducing sugar (TRS) released after the deinking of NEPW and NOPW by crude enzyme, purified *Ac*Xyn30B_12 and NaOH was measured to evaluate the extent of hemicellulose hydrolysis resulting from enzymatic or chemical treatment. For TRS estimation, 5.0% (w/v) of each paper type (NEPW and NOPW) was suspended individually in 50 mM citrate-phosphate buffer (pH 5.5) in a total reaction volume of 10 mL. The samples were treated with crude enzyme (46.4 U/g for NEPW and 58.6 U/g for NOPW), purified *Ac*Xyn30B_12 (46.4 U/g for NEPW and 58.6 U/g for NOPW) and NaOH (0.6% w/v) at 70°C for 90 min at 150 rpm in a shaking

incubator (as mentioned in Section 5.2.3.2). After the end of reaction, each reaction mixture was centrifuged at 13,000*g* at 25°C for 5 min. From the supernatant obtained, 100 µL of the effluent was collected and TRS was estimated using the method of Nelson [1944] and Somogyi [1945], as described in Chapter 3. All the assays were performed in duplicate.

5.2.10.2. Analysis of total suspended solids and total dissolved solids in effluents from deinking of NEPW and NOPW

Total suspended solids (TSS) include solid particles that are not dissolved in water, such as ink particles, fiber fines or sludge, while total dissolved solids (TDS) include all inorganic and organic substances dissolved in water (e.g., salts, minerals, ions). Prior to TSS and TDS estimation, 5.0% (w/v) of each paper type (NEPW and NOPW) was suspended individually in 50 mM citrate-phosphate buffer (pH 5.5) in a total reaction volume of 10 mL. The samples were treated with crude enzyme (46.4 U/g for NEPW and 58.6 U/g for NOPW), purified *Ac*Xyn30B_12 (46.4 U/g for NEPW and 58.6 U/g for NOPW) and NaOH (0.6% w/v) at 70°C for 90 min at 150 rpm in a shaking incubator (as mentioned in Section 5.2.3.2). After the end of reaction, each reaction mixture was centrifuged at 13,000*g* at 25°C for 5 min. From the supernatant obtained, 4 mL of the effluent was collected for TDS and TSS analysis. The analysis of TDS and TSS was carried out by following the standard protocol described by APHA (1998). For TSS determination, 2 mL of each effluent sample was filtered through pre-weighed 0.45 µm PVDF membrane using syringe filter. The membrane filters were then dried at 100°C for 4h and cooled until a constant weight was obtained. For TDS analysis, 2 mL of the above filtrate (filtered effluent) was transferred into pre-weighed 15 mL quartz crucible, dried at 100°C for 4h and cooled until a constant

weight was obtained. The weight of both dried membrane filter and dried crucible was measured. The differences in weights of membrane filters and crucibles, before and after drying were used to calculate the concentrations of TSS (mg/L) and TDS (mg/L), respectively. Both the assays were performed in duplicate. The TDS was calculated by using the following formula (Wahab *et al*., 2018):

$$\text{TSS (mg/L)} = \frac{\text{Weigh of membrane filter after filtering} - \text{Initial weigh of membrane filter}}{\text{Volume of sample (L)}}$$

The TSS was calculated using the following formula:

$$\text{TDS (mg/L)} = \frac{\text{Final weigh of crucible} - \text{Initial weigh of crucible}}{\text{Volume of sample (L)}}$$

5.3. Results and Discussion

5.3.1. Composition analysis of different waste papers

The hemicellulose and cellulose compositions of 5 different types of waste papers *viz*., *Assam Tribune* newspaper waste (NEPW), unruled *Classmate* notebook paper waste (NOPW) with blue ballpoint pen ink, *Amazon* packing cardboard paper waste (CaPW), A4-sized *HP LaserJet* printed paper waste (LPW) and magazine paper waste (MPW) were determined by using the standard TAPPI protocol. The composition analysis of the waste papers revealed that the highest hemicellulose content of 34.6% (w/v) in NEPW, followed by 18.6% (w/v) in NOPW and lowest hemicellulose content of 10.4% (w/v) in MPW was observed. The details of hemicellulose and cellulose content for all the tested waste paper types are presented in Table 5.2. Additionally, the lignin and ash contents of NEPW, NOPW, CaPW, MPW and LPW were determined by the standard NREL protocol. Among these, NEPW exhibited the lowest lignin content of 1.1% (w/v), followed by NOPW (2.6%, w/v), whereas CaPW showed the highest lignin content of 8.5%, w/v (Table 5.2). Moreover, the hemicellulose, cellulose and lignin contents of NEPW and NOPW were found to be close with the values previously reported by Estrella *et al*. (2017) and Chen *et al.* (2012), respectively. Based on the relatively high hemicellulose and low lignin contents, NEPW and NOPW were selected for further enzymatic deinking process by using the endo-xylanase enzyme, *Ac*Xyn30B_12.

Table 5.2. Composition analysis of different waste papers.

Waste paper samples	Cellulose % (w/w)	Hemicellulose % (w/w)	Lignin % (w/w)	Ash % (w/w)
Newspaper (NEPW)	59.9	34.6	1.1	2.3
Notebook paper (NOPW)	64.5	18.6	2.6	12.7
Cardboard paper (CaPW)	53.4	16.5	8.5	20.3
HP Laser print paper (LPW)	67.9	13.9	6.1	4.7
Magazine paper (MPW)	47.5	10.4	5.2	19.0

5.3.2. Statistical optimization of efficient deinking of NEPW and NOPW by *Ac*Xyn30B_12 using response surface methodology (RSM)

The deinking process of newspaper waste (NEPW) and notebook paper waste (NOPW) was statistically optimized using a Box-Behnken experimental design under the response surface methodology (RSM) framework. Each experimental run was conducted in a 10 mL reaction volume, maintaining a pulp consistency of 5.0% (w/v) in 50 mM citrate-phosphate buffer (pH 5.5) and incubated at rotation of 150 rpm in a shaking incubator. The variables tested included temperature (°C), enzyme dosage (U/g) and incubation time (min). The reaction setup, along with the procedures for paper washing and drying, pulp washing and hydraulic press paper-sheet formation, are illustrated in Fig. 5.1.

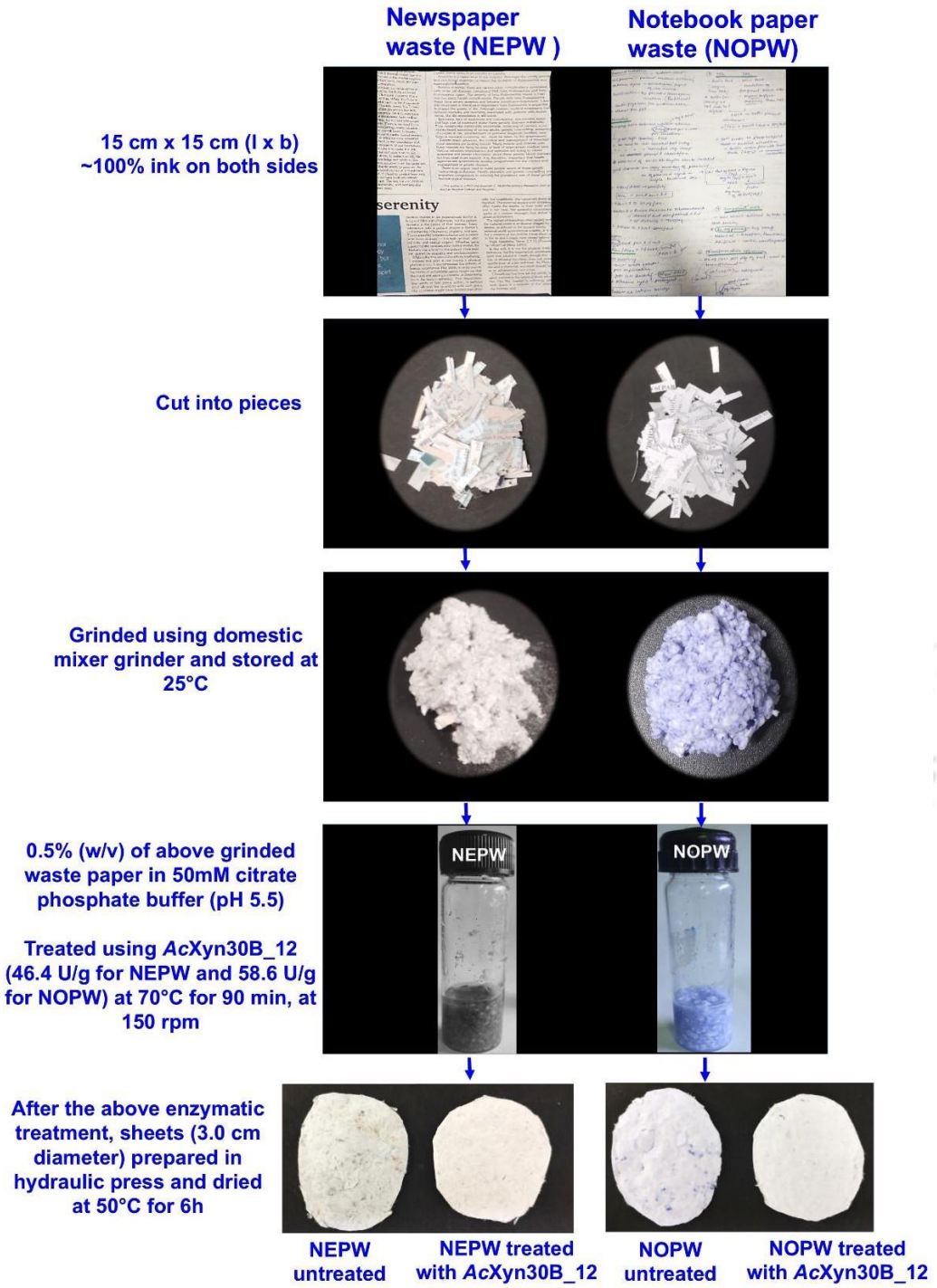

Fig. 5.1. Schematic presentation of the sequential procedure for preparation of paper samples, *Ac*Xyn30B_12 mediated NEPW and NOPW treatment, pulp washing and laboratory hand sheet formation.

The RSM model for NEPW demonstrated that, at a constant incubation time, the deinking efficiency improved with simultaneous increase in both temperature and enzyme dosage (Fig. 5.2A). Similarly, at a constant temperature, with simultaneous increase in both incubation time and enzyme dosage led to the enhanced deinking efficiency, however, increasing only one of the two factors did not yield a significant improvement (Fig. 5.2B). When enzyme dosage was held constant, the deinking efficiency increased with increase in both temperature and time, but elevating temperature alone without extending the reaction time did not improve the deinking efficiency (Fig. 5.2C). The ANOVA results for NEPW indicated that the quadratic model provided a statistically significant fit to the data, as evidenced by p-value of 0.0012. The coefficient of determination (R^2), which ranges from 0 to 1, reflects the extent to which the variability in the response can be attributed to changes in the model variables and their interactions. In this study, a R^2 value of 0.95 was obtained, suggesting that the quadratic model fits the experimental data reasonably well. The second-order equation in terms of the factors (enzyme dosage, temperature and time) given by the RSM model is as follows:

$$Deinking\ efficiency = 59.50 + 11.98*A + 0.91*B + 7.15*C + 2.86*A*B + 18.16*A*C + 24.54*B*C - 6.10*A^2 + 7.47*B^2 - 13.05*C^2$$

Where,

A=enzyme dosage (U/g), B =temperature (°C) and C =incubation time (min)

Using the point prediction tool in Design Expert software, the deinking efficiency for NEPW was estimated to be 80.0% under the conditions of enzyme dosage 46.4 U/g pulp, temperature 70°C and a reaction time 90 min. This predicted

value closely matched with the experimentally observed deinking efficiency of 81.3%, indicating the reliability and validity of the predicted model value.

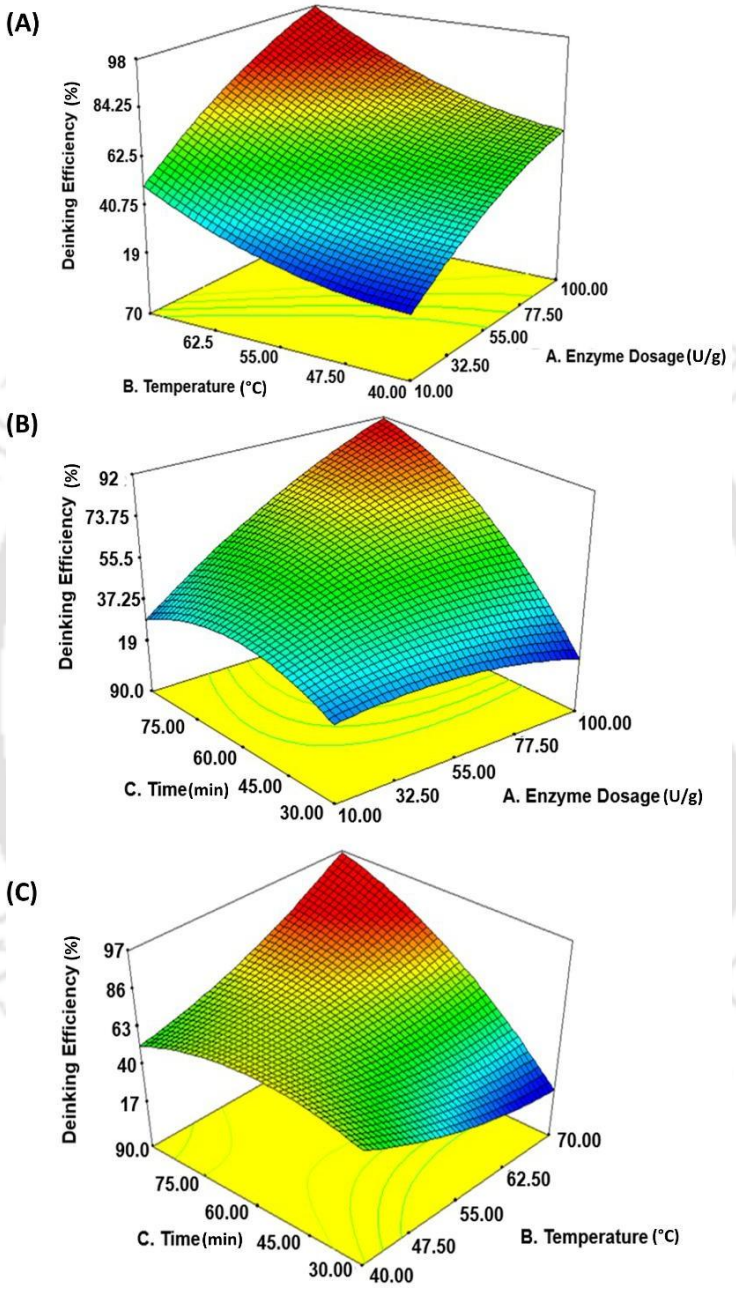

Fig 5.2. Response surface curves showing effect of **(A)** temperature (°C) and enzyme dosage (U/g) at constant time (min), **(B)** time (min) and enzyme dosage (U/g) at constant temperature (°C) and **(C)** time (min) and temperature (°C) at constant enzyme dosage (U/g) on deinking of NEPW by *Ac*Xyn30B_12.

The RSM model for NOPW demonstrated that at constant time, an increase in enzyme dosage at a specific temperature enhanced deinking efficiency, with maximum efficiency achieved when both enzyme dosage and temperature were high (Fig. 5.3A). When temperature was kept constant, deinking efficiency increased with both longer incubation time and higher enzyme dosage (Fig. 5.3B). However, when enzyme dosage was kept constant, the highest deinking efficiency was observed at a moderate temperature range and with moderate to high incubation time, suggesting a more complex interaction between the variables in NOPW deinking as compared with that of NEPW (Fig. 5.3C). The ANOVA results for NOPW indicated that the quadratic model provided a statistically significant fit to the data, as confirmed by p-value of 0.0035. The R^2 value of 0.93 was obtained, suggesting that the quadratic model fits reasonably well. The second-order equation in terms of the factors (enzyme dosage, temperature and time) given by the RSM model is as follows:

$$Deinking\ efficiency = 64.21 + 19.28*A - 16.22*B + 10.92*C + 11.46*A*B + 3.05*A*C + 22.20*B*C + 8.41*A^2 - 5.84*B^2 + 2.68*C^2$$

Where,

A=enzyme dosage (U/g), B =temperature (°C) and C =incubation time (min)

Using the point prediction tool in Design Expert software, the deinking efficiency for NOPW was estimated to be 80.4% under the conditions of enzyme dosage 58.6 U/g pulp, temperature 70°C and a reaction time 90 min. This predicted value fairly matched with the experimentally determined deinking efficiency of 77.2%, indicating the reliability and validity of the predicted model value.

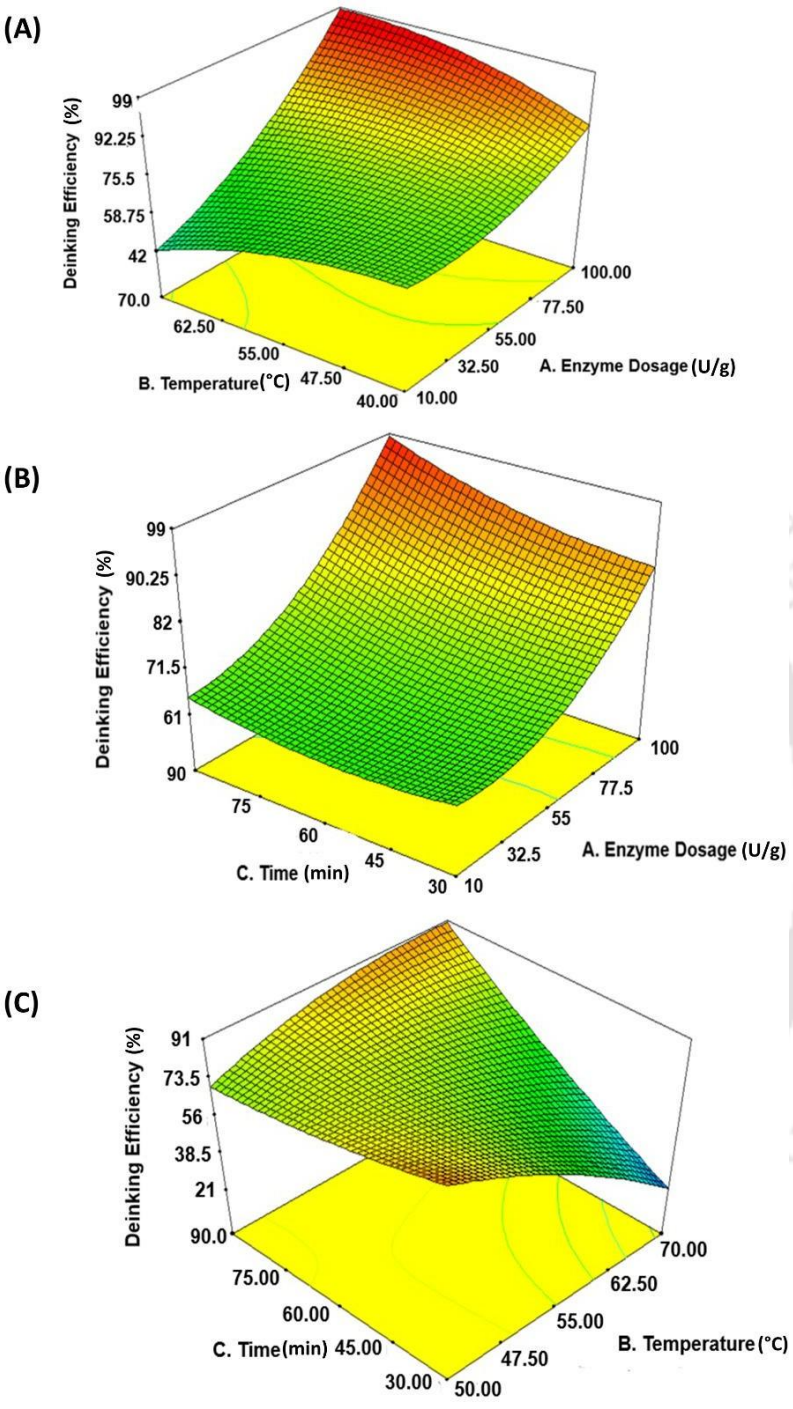

Fig 5.3. Response surface curves showing effect of **(A)** temperature (°C) and enzyme dosage (U/g) at constant time (min), **(B)** time (min) and enzyme dosage (U/g) at constant temperature (°C) and **(C)** time (min) and temperature (°C) at constant enzyme dosage (U/g) on deinking of NOPW by *Ac*Xyn30B_12.

A comparative analysis, highlighting the deinking efficiencies of *Ac*Xyn30B_12 (present study) and other reported xylanases under their respective optimized conditions across different types of waste papers is presented in Table 5.3. The deinking efficiency of 81% for NEPW and 77% for NOPW of *Ac*Xyn30B_12 was significantly higher than that of endo-xylanase from *Bacillus halodurans* FNP 135 (15 U/g), which gave 48% deinking efficiency (analyzed using ERIC) when treated 5.0% (w/v) old newspaper at 65°C and pH 9.0 for 3h (Virk *et al*., 2013). The deinking efficiency of *Ac*Xyn30B_12 was also higher than that reported by Chutani *et al.* (2015), where a fungal endo-xylanase (100 U/g) from *Aspergillus oryzae* MDU-4 resulted much lower deinking efficiency of 35% (analyzed using ERIC) on treatment of 5.0 % (w/v) newspaper in 100 mM citrate phosphate buffer, pH 6.0 at 40°C for 3h. However, the deinking efficiency of *Ac*Xyn30B_12 was lower than that reported for endo-xylanase from *Bacillus halodurans* TSEV1, which gave high deinking efficiency of 150% when treated 5.0 % (w/v) A4 printed paper dissolved in100 mM glycine-NaOH, pH 9.0 (Kumar *et al*., 2013). This notably high value may be attributed to the considerably higher enzyme loading (1200 U/g) and an extended incubation time of 38h. Although, a comparable deinking efficiency with that of *Ac*Xyn30B_12 (81% for NEPW and 77% for NOPW) was reported for endo-xylanases (74.3%) from *Bacillus subtilis* (Sango *et al*., 2020), endo-xylanases (75.3%) from *Bacillus halodurans* (Gupta *et al*., 2015) and endo-xylanase (78.8%) from *Aspergillus niger* DX-23 (Desai et al., 2016) as mentioned in Table 5.3.

Table 5.3. Comparison of deinking efficiency of various xylanases on different waste papers.

Enzyme/Organism	Waste paper type	Deinking conditions	Deinking parameter	Deinking efficiency (%)	References
Endo-xylanase from *Aspergillus oryzae* MDU-4	Newspaper	100U/g, 40°C, 3h, 5.0% (w/v), 100 mM Citrate phosphate, pH 6.0	ERIC	35%	Chutani et al., 2015
Endo-xylanase from *Bacillus halodurans* FNP 135	ONP (old newspaper)	15 U/g, 65°C, 3h, pH 9.0, 5.0% (w/v) paper	ERIC	47.9%	Virk et al., 2013
Endo-xylanase from *Bacillus subtilis*	Printed paper	0.6 U/g, 60 min	ERIC	74.3%	Sango et al., 2020
Endo-xylanase from *Bacillus licheniformis*	A4 printed paper	20 U/g, 60°C, 1h	Diazo dye	88%	Malhotra et al., 2023
Endo-xylanase from *Beauveria bassiana* SAN01	Printed paper	1200 U/g, 40.2°C, 17.7 h, 8.0% (w/v) paper, 50 mM sodium acetate, pH 6.0, 5 mL reaction mixture	Diazo dye	106.7%	Amobonye et al., 2021
Endo-xylanase from *Aspergillus niger* DX-23	Old newspaper	50 U/g, 100°C, 30 min, 60 mL reaction mixture 10% (w/v) paper, 100 mM sodium citrate, pH 5.5	Brightness	78.8%	Desai et al., 2016
Endo-xylanase from *Bacillus halodurans*	Old news paper	15 U/g, 70°C, 80 rpm, 3h, 5.0% (w/v) paper 0.1 M, Tris-Cl, pH 9.0	Whiteness	75.3%	Gupta et al., 2015
Endo-xylanase from *Bacillus halodurans* TSEV1	A4 printed paper	1200 U/g, 70°C, 38h, 5.0% (w/v), 100mM glycine-NaOH, pH 9.0, 2 mL reaction mixture	Diazo dye	150%	Kumar et al., 2013
Endo-xylanase (*Ac*Xyn30B_12) from *Acetivibrio clariflavus* DSM 19732	Newspaper (NEPW) and Notebook paper (NOPW)	48 U/g (NEPW), 50 U/g (NOPW), 70°C, 90 min, 150 rpm, 5.0% (w/v) paper, 50 mM Citrate phosphate, pH 5.5	ERIC	81% for NEPW and 77% for NOPW	Present study

5.3.3. Deinking of NEPW and NOPW at large scale using *Ac*Xyn30B_12 under optimized conditions

The deinking efficiency of *Ac*Xyn30B_12 using NEPW and NOPW was further evaluated at larger reaction volumes of 20 mL and 50 mL under the same optimized conditions as mentioned in Section 5.3.2. The enzyme, *Ac*Xyn30B_12 was applied at a constant loading (46.4 U/g for NEPW and 58.6 U/g for NOPW) and reactions were carried out under optimum conditions of 70°C with agitation at 150 rpm for 90 min. Paper pulp consistency was maintained at 0.5% (w/v) in 50 mM citrate-phosphate buffer, pH 5.5 (as mentioned in Section 5.2.3). The deinking efficiency achieved for NEPW was 79.0%, corresponding to a reduction in ERIC from 6300.0 ppm (untreated) to 1323.0 ppm (treated) at 20 mL scale. NEPW showed a deinking efficiency of 78.7%, with ERIC decreasing from 7100.0 ppm (untreated) to 1511.0 ppm (treated) at the 50 mL scale. These values were comparable to those obtained for NEPW exhibiting a deinking efficiency of 81.3% with ERIC reducing from 2838.4 ppm (untreated) to 532.3 ppm (after treatment) at the 10 mL scale. Similarly, for NOPW, the deinking efficiency was 72.1%, with ERIC reduced from 7550.0 ppm (untreated) to 2109.4 ppm (treated) at 20 mL scale, while it was 71.3%, with ERIC decreasing from 8000.0 ppm (untreated) to 2294.6 ppm (treated) at 50 mL scale. These results were in close agreement where NOPW showed a deinking efficiency of 77.2% and ERIC declined from 6746.1 ppm (treated) to 1537.8 ppm (untreated) at the 10 mL scale (Table 5.4). These results demonstrated that *Ac*Xyn30B_12 maintains its deinking efficiency even at higher reaction volumes, indicating its potential scalability and applicability for higher scale deinking processes. Furthermore, biomass recovery during large-scale deinking reactions using

*Ac*Xyn30B_12 was consistent across different volumes. For NEPW, a biomass recovery of 77% was observed at both 20 mL and 50 mL, while for NOPW, the recovery remained steady at 76% at both volumes.

Table 5.4. Comparison of deinking efficiency (%) and biomass recovery (%) of NOPW and NEPW by *Ac*Xyn30B_12 at large scale.

Deinked samples in different reaction volumes	ERIC (ppm)		Biomass recovery (%)	Deinking efficiency (%)
	After enzyme treatment	Paper in solution but without enzyme (control)	After enzyme treatment	After enzyme treatment
NEPW				
10 mL	532.3 ± 0.6	2838.4 ± 0.1	78 ± 0.4	81.3 ± 0.6
20 mL	1323.0 ± 0.1	6300.0 ± 0.1	77 ± 0.2	79.0 ± 0.1
50 mL	1511.0 ± 0.2	7100.0 ± 0.7	77 ± 0.2	78.7 ± 0.2
NOPW				
10 mL	1537.8 ± 0.9	6746.1 ± 0.8	76 ± 0.7	77.2± 0.9
20 mL	2109.4 ± 0.4	7550.3 ± 0.1	76 ± 0.4	72.1 ± 0.4
50 mL	2294.6 ± 0.5	8000.0 ± 0.1	76 ± 0.9	71.3 ± 0.5

Each treatment was carried out using 46.4 U/g (for NEPW) and 58.6 U/g (for NOPW) AcXyn30B_12 under optimized conditions (70°C, 90 min, 150 rpm) and in duplicate.

5.3.4. Comparative analysis of deinking efficiency of deinked NEPW and NOPW using crude enzyme, purified *Ac*Xyn30B_12 and NaOH

The deinking efficiency of crude enzyme and purified *Ac*Xyn30B_12 (both at 46.4 U/g and 58.6 U/g for NEPW and NOPW respectively, as optimized in Section 5.3.2), as well as 0.6% (w/v) NaOH, was evaluated by treating NEPW and NOPW in a total volume of 10 mL with a pulp consistency of 5.0% (w/v) in 50 mM citrate-phosphate buffer (pH 5.5) under optimized conditions of 70°C and 90 min and at 150 rpm in a shaking incubator (Section 5.3.2). The ERIC values (ppm) and corresponding deinking efficiencies following each treatment are summarized in Table 5.5. Among all the treatments, NaOH exhibited the highest deinking efficiency for NEPW and NOPW, achieving 87.3% and 87.7%, respectively, which corresponded to the lowest

ERIC values of 368.9 ppm (NaOH treated NEPW) and 809.5 ppm (NaOH treated NOPW) as shown in Table 5.5). In comparison, treatment with purified *Ac*Xyn30B_12 enzyme resulted in slightly lower, yet comparable, deinking efficiencies of 81.3% for NEPW and 77.2% for NOPW, with corresponding ERIC values of 532.3 ppm (*Ac*Xyn30B_12 treated NEPW) and 1537.8 ppm (*Ac*Xyn30B_12 treated NOPW). The superior performance of NaOH can be attributed to its strong alkaline nature, which promotes effective swelling and fiber loosening, as well as enhanced solubilization and dispersion of ink particles. However, the deinking efficiency of *Ac*Xyn30B_12 was found to be relatively close to that of NaOH, indicating the promising potential of the enzyme as an environment-friendly alternative for waste paper deinking, especially when considering its eco-toxicological advantages over chemical treatments. Additionally, the crude enzyme showed deinking efficiencies of 43.4% for NEPW and 52.4% for NOPW, corresponding to higher ERIC values of 1606.0 ppm (crude enzyme treated NEPW) and 3211.2 ppm (crude enzyme treated NOPW) demonstrating that even the unpurified form of the enzyme exhibited at least 50% of the deinking efficiency given by the purified AcXyn30B_12 enzyme.

Although deinking efficiency was higher in the case of NaOH treatment, the harsh chemical treatment led to excessive hydrolysis of cellulose fibers, resulting in lower biomass recovery of 68% for NEPW and 72% for NOPW. In contrast, treatment with purified *Ac*Xyn30B_12 resulted in significantly higher biomass recovery, with values of 78% for NEPW and 76% for NOPW, as presented in Table 5.5.

Table 5.5. Comparison of waste paper deinking efficiency (%) by crude enzyme, purified *Ac*Xyn30B_12 and NaOH.

Deinked sample	ERIC (ppm)	Biomass recovery (%)	Deinking efficiency (%)
NEPW			
Untreated	2838.4 ± 1.2	--	--
Crude treated	1606.0 ± 0.8	64 ± 0.3	43.4 ± 0.8
NaOH treated	368.9 ± 0.5	68 ± 0.2	87.3 ± 0.5
Purified *Ac*Xyn30B_12 treated	532.3 ± 0.6	78 ± 0.4	81.3 ± 0.6
NOPW			
Untreated	6746.1 ± 0.8	--	--
Crude treated	3211.2 ± 1.2	66 ± 0.8	52.4 ± 1.2
NaOH treated	809.5 ± 0.8	72 ± 0.2	87.7 ± 0.8
Purified *Ac*Xyn30B_12 treated	1537.8 ± 0.9	76 ± 0.7	77.2 ± 0.9

Each treatment was carried out in 10 mL reaction volume under optimized conditions (70°C, 90 min, 150 rpm) and in duplicate.

5.3.5. Crystallinity index analysis of untreated and deinked NEPW and NOPW using X-ray diffractometer

The Crystallinity index (*CrI*) and average crystallite size (ACS) of the deinked NEPW and NOPW were examined to study the structural changes. For NEPW, treatment with crude enzyme marginally increased the *CrI* to 54.2% (3.9% increase), followed by NaOH treatment resulting even higher *CrI* of 54.9% showing 5.5% increase (Table 5.6). Notably, the treatment of NEPW with purified *Ac*Xyn30B_12 significantly enhanced the *CrI* to 58.8%, giving a 12.9% increase exhibiting the highest among all treatments (Table 5.6). A similar trend was observed in ACS, where *Ac*Xyn30B_12 treatment increased the average crystallite size from 15.3% in untreated NEPW to 17.7 giving an 16% increase as shown in Table 5.6.

In the case of NOPW, crude enzyme treatment led to a substantial *CrI* increase to 60.3% (35.4%), while NaOH further improved it to 63.2% (41.9%) as compared with untreated NOPW (44.5%). The *Ac*Xyn30B_12 treatment of NOPW resulted in

achieved the highest *CrI* of 63.4%, reflecting a 42.3% increase over the untreated control (Table 5.6). The ACS of NOPW also improved significantly with *Ac*Xyn30B_12 treatment, reaching 22.8% giving 23.0% increase (Table 5.6). These results underscore the superior performance of *Ac*Xyn30B_12 enzyme in effectively removed ink and hemicellulose part and reorganizing and purifying cellulose fibers in both newspaper and notebook paper waste.

Table 5.6. Comparison of *CrI* and ACS of deinked NEPW and NOPW by *Ac*Xyn30B_12 and NaOH.

Deinked sample	*CrI*	Increase in *CrI* (%)	ACS	Increase in ACS (%)
NEPW				
Untreated	52.1	--	15.3	--
Crude treated	54.2	3.9	16.5	7.8
NaOH treated	54.9	5.5	17.1	11.7
Purified *Ac*Xyn30B_12 treated	58.8	12.9	17.7	15.6
NOPW				
Untreated	44.5	--	17.6	--
Crude enzyme treated	60.3	35.4	18.2	2.9
NaOH treated	63.2	41.9	21.3	21.0
Purified *Ac*Xyn30B_12 treated	63.4	42.3	22.8	23.0

The X-ray diffractograms of untreated and treated NEPW and NOPW samples, are shown in Fig. 5.4A and Fig. 5.4B, respectively. The sharp diffraction peak observed at 2Θ =22.6° corresponds to the (002) lattice plane of crystalline cellulose and the broad peak at 2Θ =19.0° corresponds to the amorphous region. In addition to this, the diffractograms (Fig. 5.4A and B) exhibit characteristic peaks corresponding to inorganic fillers *viz*., kaolinite (2Θ =25.0°), magnesium silicate (2Θ =28.6°) and

calcite (2Θ =29.4°) commonly employed in paper manufacturing (Manandhar *et al.*, 2020).

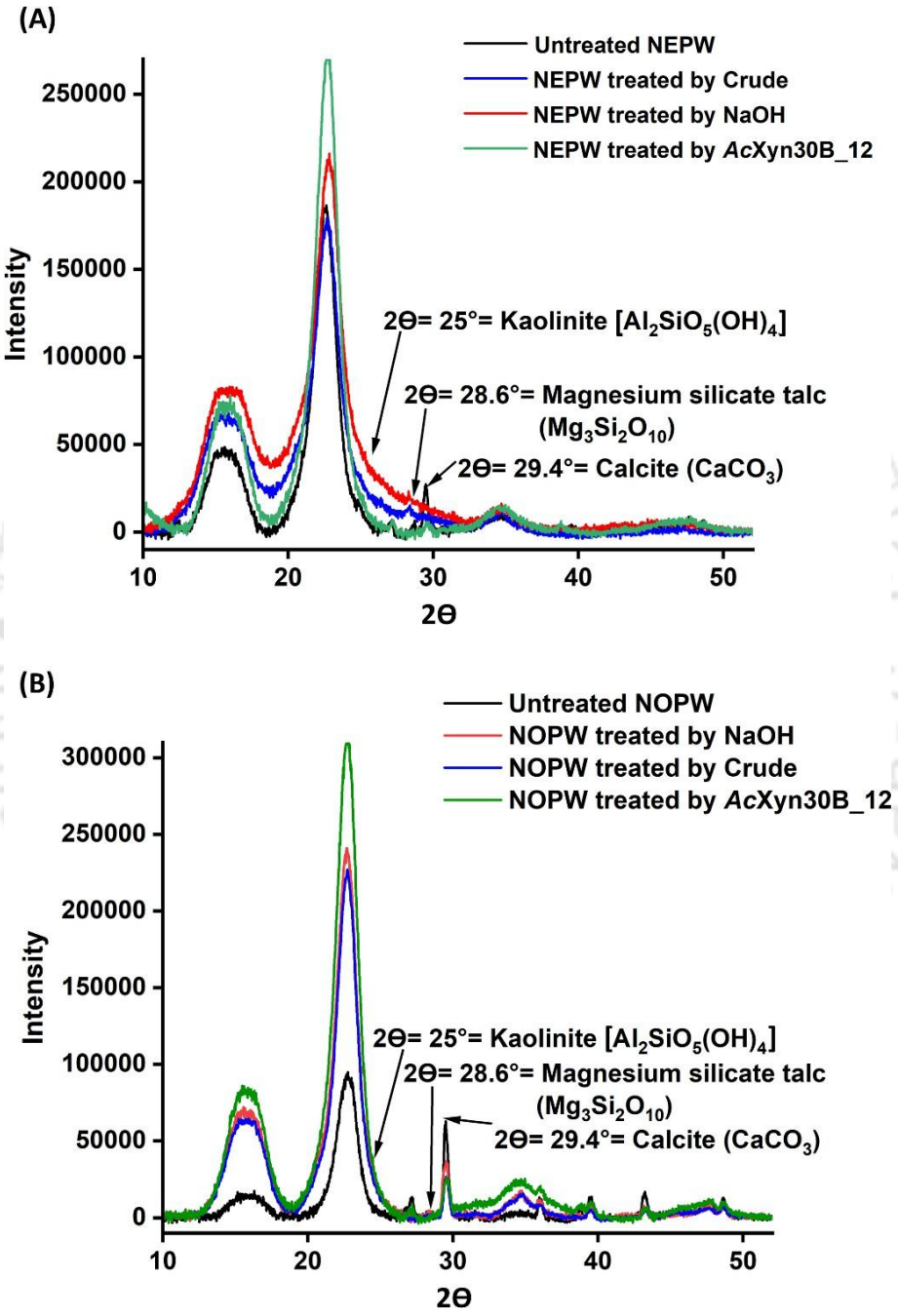

Fig. 5.4. X-ray diffractogram of untreated and crude enzyme, purified *Ac*Xyn3B_12 and NaOH treated deinked waste papers **(A)** newspaper waste (NEPW) and **(B)** notebook paper waste (NOPW).

5.3.6. Functional group analysis of untreated and deinked NEPW and NOPW using ATR-Fourier Transform Infrared (FTIR) spectroscopy

The Attenuated Total Reflectance-Fourier Transform Infrared (ATR-FTIR) spectroscopy was employed to investigate the structural changes in deinked NEPW and NOPW. The functional groups and their peak frequencies corresponding to laser ink components, as reported by Lee *et al*. (2014) and those present in blue ballpen ink, as reported by Zaharullil *et al*. (2012), are summarized in Table 5.7.

Table 5.7. FTIR band assignments of various functional groups detected in ink and hemicellulose components of NEPW and NOPW.

Bands (cm^{-1})	**Assignment**
NEPW	
3025-3060	-C-H stretching of aromatic group in laser ink
2995-2918	-CH_2 and CH_3 stretching in laser ink
1729-1452	-C=O of laser toner
1315	-OH stretching in hemicellulose
1075-1000	-CO stretching in hemicellulose
810	-CH stretching in hemicellulose
NOPW	
3000-3600	-CH_2OH groups in blue ink
2800-2900	-CH_2 and CH_3 stretching in blue ink
1315	-OH stretching in hemicellulose
1075-1000	-CO stretching in hemicellulose
810	-CH stretching in hemicellulose

The ATR-FTIR spectra for NEPW and NOPW are presented in Fig. 5.5A and 5.5B, respectively. For NEPW, the C-H stretching vibrations corresponding to aromatic groups in the laser ink appeared in the range of 3025-3060 cm^{-1}, indicating the presence of toner-derived aromatic structures (Fig. 5.5A). Additionally, symmetric and asymmetric stretching vibrations of $-CH_2$ and $-CH_3$ groups, corresponding to organic components in laser ink, were observed between 2995-2918 cm^{-1} (Fig. 5.5A). A distinct band in the range 1729-1452 cm^{-1} was assigned to the stretching vibrations of carbonyl (C=O) groups present in the laser toner formulation (Fig. 5.5A). Peaks specific to hemicellulose components of the NEPW fiber were evident at 1315, 1075-1000 and 810 cm^{-1}, corresponding to -OH stretching, C-O stretching and C-H stretching vibrations, respectively (Fig. 5.5A). A notable decrease in peak intensity was observed in the region corresponding to $-CH_2$ and CH_3 stretching in laser ink (2995-2918 cm^{-1}) in treated NEPW when compared with the untreated NEPW indicating removal of laser ink after treatment (Fig. 5.5A). Moreover, significant decrease in peak intensity at -OH stretching vibrations of hemicellulose (1315 cm^{-1}) in *Ac*Xyn30B_12 treated NEPW compared to crude enzyme and NaOH treated NEPW indicated the specific and efficient hydrolysis of hemicellulose region of NEPW by *Ac*Xyn30B_12.

In the case of NOPW, the FTIR spectrum showed broad absorption between 3000-3600 cm^{-1}, which can be attributed to $-CH_2OH$, indicative of the hydroxyl groups in blue ink (Fig. 5.5B). Stretching vibrations of $-CH_2$ and $-CH_3$ groups, from ink and residual additives, were observed in the range of 2800-2900 cm^{-1} (Fig. 5.5B). Similar to NEPW, the hemicellulose region was confirmed by peaks at 1315 cm^{-1} for -OH stretching, 1075–1000 cm^{-1} for C-O stretching and 810 cm^{-1} for C-H stretching (Fig.

5.5B). A notable decrease in peak intensity was observed in the region corresponding to -CH_2 and CH_3 stretching in laser ink (2900-2800 cm^{-1}) and -OH stretching vibrations of hemicellulose (1315 cm^{-1}) in treated NOPW when compared with untreated NOPW indicating removal of ink and hydrolysis of hemicellulose region after treatment (Fig. 5.5B). Among various treatments, purified *Ac*Xyn30B_12 treated NEPW and NOPW samples exhibited the most significant peak intensity decrease in these regions (2900-2800 cm^{-1} and 1315 cm^{-1}), followed by NaOH-treated and crude enzyme-treated samples. These spectral changes suggested that *Ac*Xyn30B_12 treatment led to more effective disruption or removal of toner ink components, due to the targeted hydrolysis of hemicellulosic components in the fiber-ink matrix. In contrast, NaOH treatment, although effective to a certain extent, likely achieved ink removal through non-specific chemical degradation.

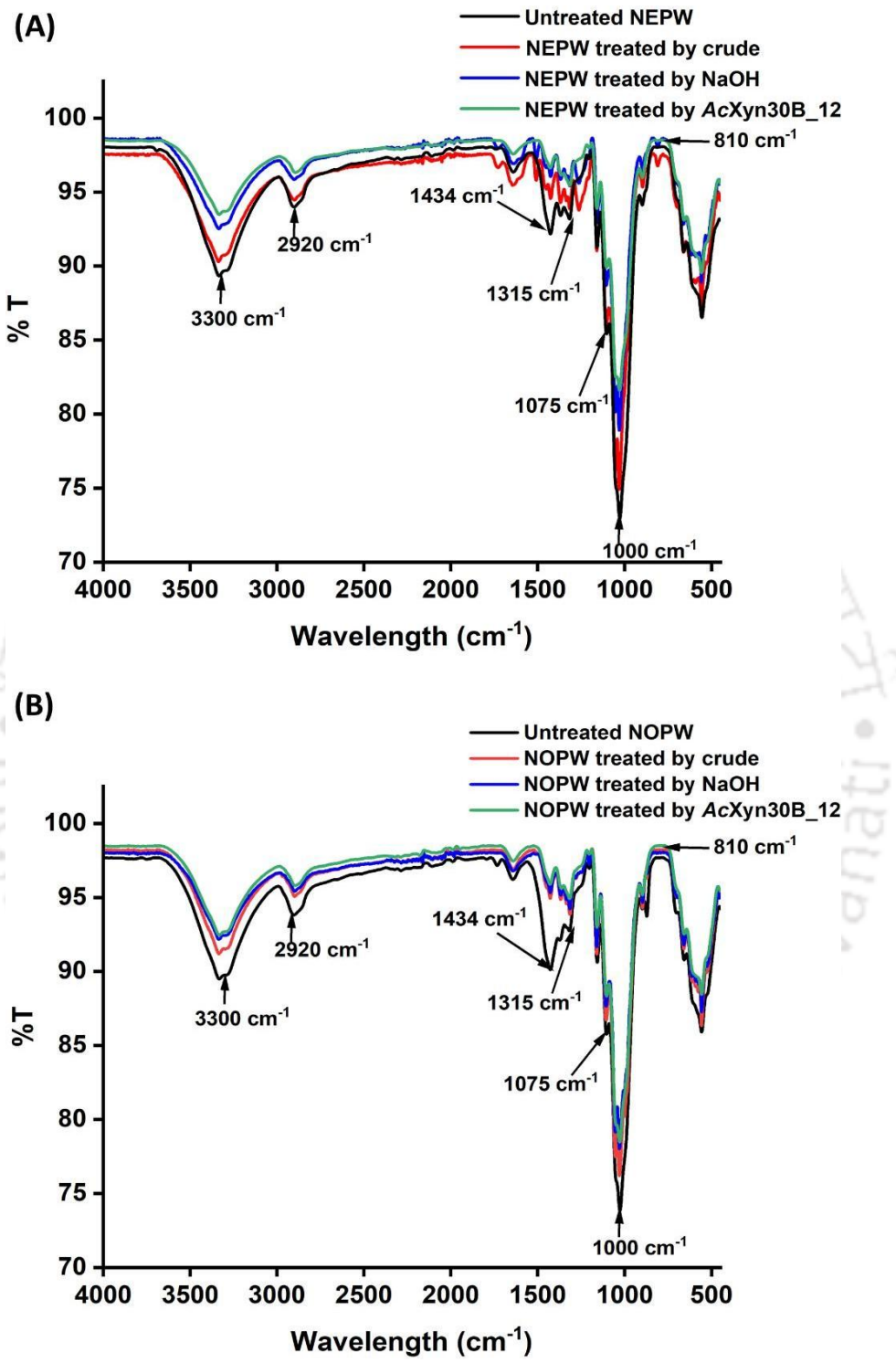

Fig. 5.5. ATR-FTIR spectra of crude enzyme, purified *Ac*Xyn3B_12 and NaOH treated deinked waste papers **(A)** newspaper waste (NEPW) and **(B)** notebook paper waste (NOPW).

5.3.7. Morphological analysis of untreated and deinked NEPW and NOPW using field emission scanning electron microscopy

Field Emission Scanning Electron Microscopy (FESEM) was employed to examine the surface morphology of untreated and deinked NEPW and NOPW samples. The untreated NEPW displayed a compact and dense structure and the fiber surface appeared rough and coated (Fig. 5.6A). The crude enzyme treated NEPW exhibited a comparable level of broken and damaged fibers as observed in the untreated sample, suggesting limited fiber disruption (Fig. 5.6B). In contrast, treatment with NaOH (Fig. 5.6C) and *Ac*Xyn30B_12 (Fig. 5.6D) resulted in significantly more broken and fragmented fibers, with both treatments showing almost similar degrees of differentiated fiber. This suggested that *Ac*Xyn30B_12 imparted a strong hydrolytic effect on the hemicellulosic components of the fiber matrix, leading to increased fiber disruption similar to that caused by the chemical treatment by NaOH.

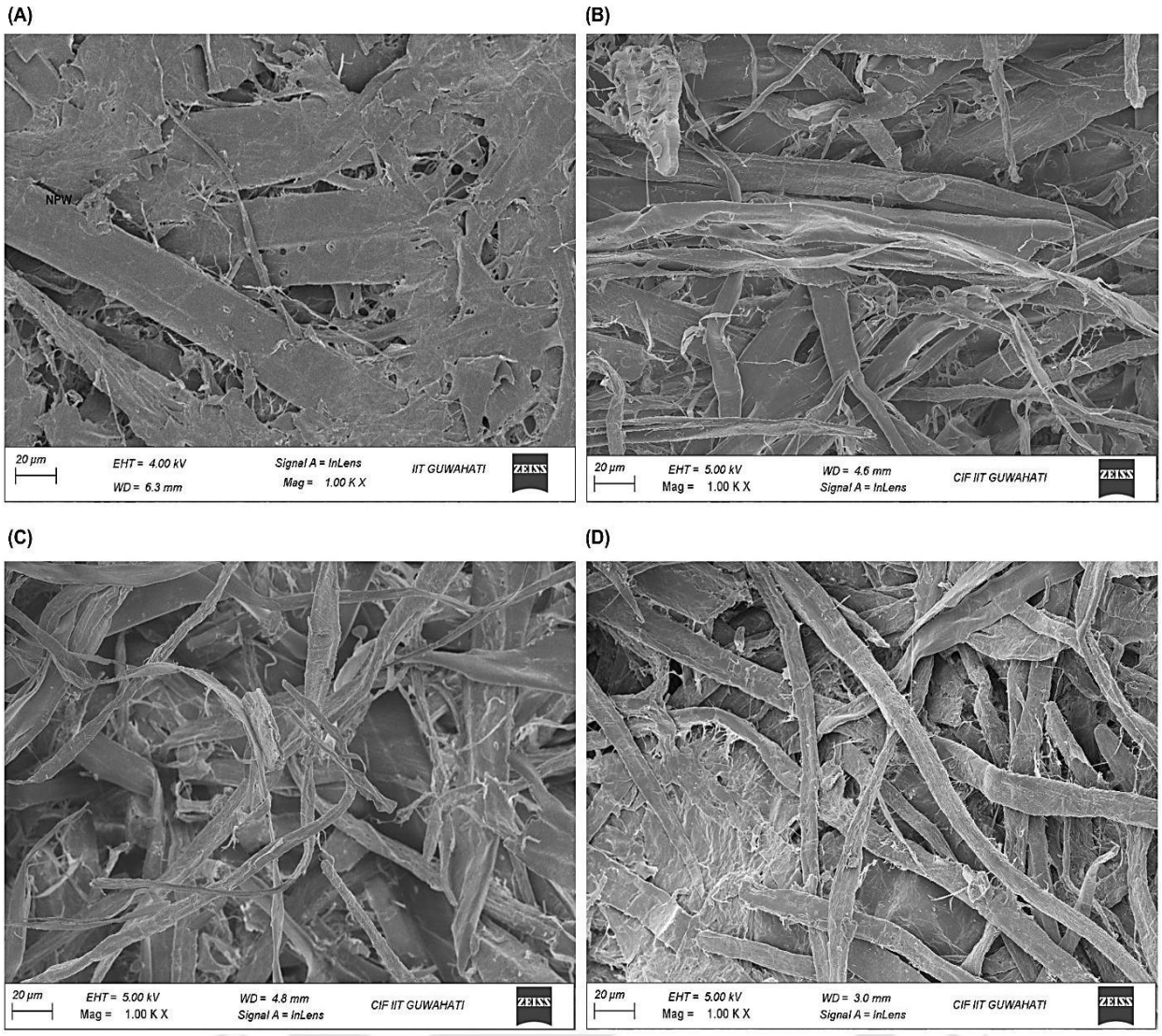

Fig. 5.6. FESEM micrographs of **(A)** untreated NEPW and deinked NEPW by **(B)** crude enzyme, **(C)** NaOH and **(D)** purified *Ac*Xyn3B_12.

The FESEM results for both untreated and treated NOPW samples by, crude enzyme, purified *Ac*Xyn30B_12 and NaOH are shown in Fig 5.7 (A-D) which showed similar results like NEPW. The untreated NOPW displayed a compact and dense structure and the fiber surface appeared rough and coated (Fig. 5.7A). The crude enzyme treated NOPW exhibited a comparable level of broken and damaged fibers suggesting limited fiber disruption (Fig. 5.7B). The NOPW treated with NaOH (Fig.

5.7C) and *Ac*Xyn30B_12 (Fig. 5.7D) resulted in significantly more broken and fragmented fibers, with both treatments showing almost similar degrees of differentiated fiber. Similarly, like NEPW, these results also suggested *Ac*Xyn30B_12 imparted a strong hydrolytic effect on the hemicellulose components of the fiber matrix, leading to fiber disruption similar to that caused by the chemical treatment by NaOH.

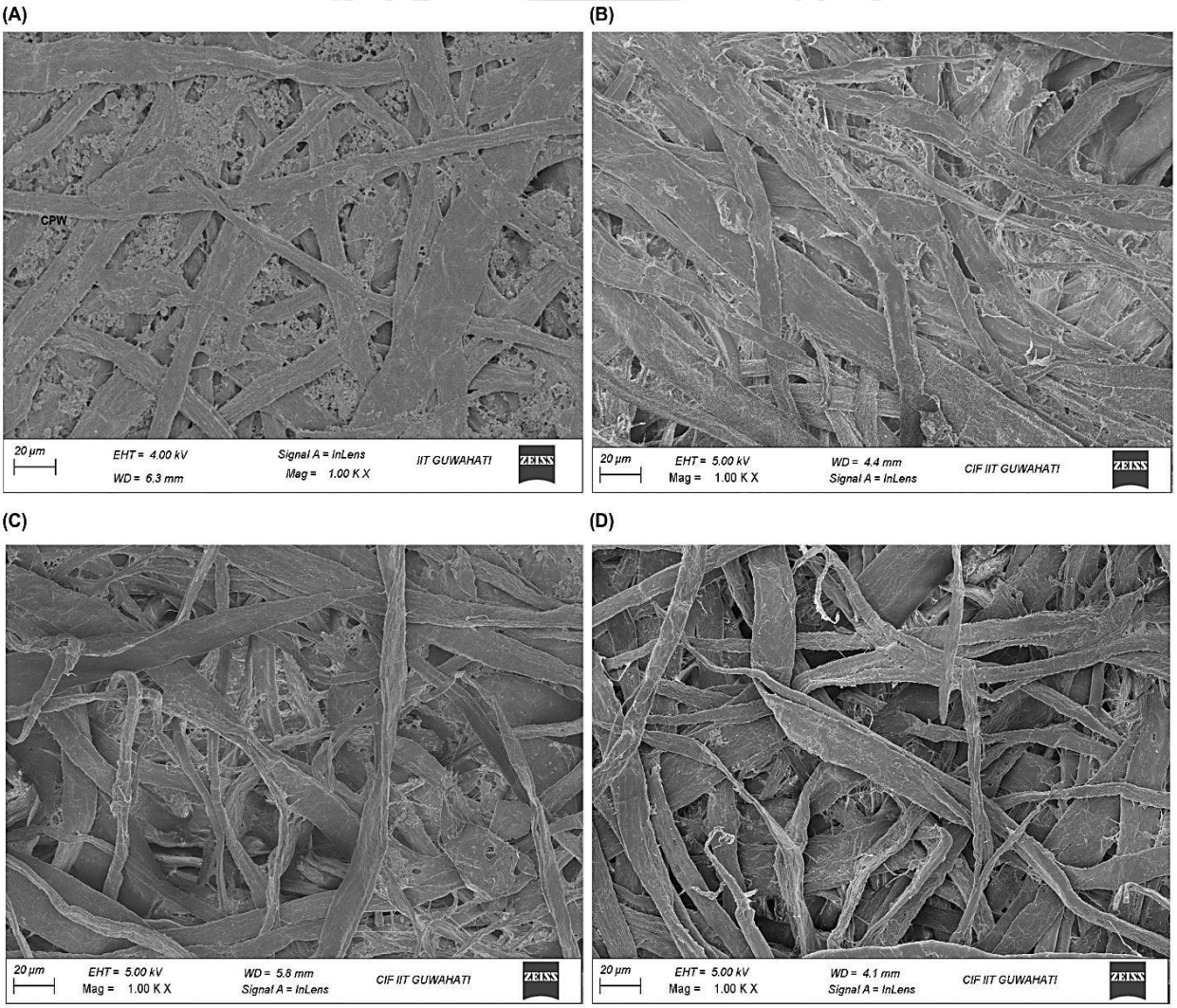

Fig. 5.7. FESEM micrographs of **(A)** untreated NOPW and deinked NOPW by **(B)** crude enzyme, **(C)** NaOH and **(D)** purified *Ac*Xyn3B_12.

5.3.8. Evaluation of optical properties of untreated and deinked NEPW and NOPW via brightness measurement

The brightness of deinked NEPW and NOPW samples was assessed to evaluate the effectiveness of different treatments, including crude enzyme, NaOH, and the purified *Ac*Xyn30B_12. For NEPW, the crude enzyme treatment slightly increased the brightness to 69.6%, reflecting a 3.9% enhancement, while NaOH treatment showed a marginal improvement with a brightness of 67.9% (1.3% increase), as presented in Table 5.7. In contrast, the treatment of NEPW with *Ac*Xyn30B_12 significantly enhanced the brightness to 75.3%, corresponding to a 12.4% increase, as compared to 67% for untreated NEPW (Table 5.8). A similar trend was observed for NOPW, where crude enzyme treatment increased the brightness to 41.5% (9.2% increase) and NaOH treatment showed a modest rise to 39.2% (3.2% increase) as compared with 38% for untreated NOPW (Table 5.8). The enzyme, *Ac*Xyn30B_12 treated NOPW displayed a substantial improvement in brightness, reaching 48.0%, which corresponded to a 26.3% increase (Table 5.8). These results clearly indicated that *Ac*Xyn30B_12 is more effective in enhancing the optical properties of both NEPW and NOPW, due to its specific and efficient action on hemicellulosic components and ink detachment, thereby contributing to improved deinking performance.

Table 5.8. Comparison of brightness (%) of deinked NEPW and NOPW by *Ac*Xyn30B_12 and NaOH.

Deinked sample	Brightness (%)	Increase in brightness (%)
NEPW		
Untreated	67.0	--
NaOH treated	67.9	1.3
Crude enzyme treated	69.6	3.9
Purified *Ac*Xyn30B_12 treated	75.3	12.4
NOPW		
Untreated	38.0	--
NaOH treated	39.2	3.2
Crude enzyme treated	41.5	9.2
Purified *Ac*Xyn30B_12 treated	48.0	26.3

5.3.9. Analysis of water absorptivity in deinked NEPW and NOPW by Cobb test

The water absorptivity of untreated and deinked NEPW and NOPW samples was assessed over a time interval of 0 to 60 min using the Cobb method. Cobb value (g/m^2) indicates the capacity of the paper to absorb water and serves as an important parameter for evaluating the reusability of recycled paper in printing and writing applications. The untreated NEPW showed a gradual increase of Cobb value from 0 to 5.9 g/m^2, while untreated NOPW showed an increased only up to 2.6 g/m^2 from 0 to 60 min (Fig. 5.8A). The low absorptivity confirms poor water absorption due to residual hydrophobic components such as ink, sizing agents and fillers. Moreover, it indicates that the untreated waste papers retain surface coatings that inhibit moisture penetration, rendering them less suitable for reprocessing without the prior treatment. The crude *Ac*Xyn30B_12 treated NEPW showed Cobb value rapidly rising from 3.5 g/m^2 at 5 min to 28.0 g/m^2 at 60 min (Fig. 5.8A), demonstrating enhanced fibre exposure due to enzymatic removal of matrix-bound ink and hemicellulose. Similarly,

NOPW treated with crude enzyme showed a steady increase, reaching 17.7 g/m² at 60 min (Fig. 5.8B), indicating that the enzyme likely acted non-specifically to cleave hemicellulosic linkages, increasing water retention. In NEPW treated by *Ac*Xyn30B_12, water absorptivity increased from 18.1 g/m² at 5 min to 28.1 g/m² at 60 min (Fig. 5.8A), closely approaching the levels obtained with crude enzyme. Similarly, NOPW treated with *Ac*Xyn30B_12 displayed a sharp initial increase of 13.1 g/m² at 5 min and then stabilizing at 14.9 g/m² by 60 min (Fig. 5.8B). While the cobb value slightly lower than the crude enzyme treatment in later phases, the faster initial uptake suggests that purified *Ac*Xyn30B_12 acts rapidly and specifically on xylan-rich regions of the fiber surface, enhancing hydrophilicity early in the treatment. The NEPW sample treated by NaOH showed a sharp rise from 24.6 g/m² at 5 min to 35.6 g/m² at 60 min (Fig. 5.8A), while NOPW reached 24.6 g/m² in 60 min (Fig. 5.8B). Hence, the NaOH-treated samples showed the highest Cobb values with both the paper types, reflecting aggressive chemical delamination and ink removal but at the same time compromising the cellulosic strength leading to increase in water absorption. In contrast, *Ac*Xyn30B_12 facilitates significant water absorptivity with reduced structural damage making it highly suitable for paper recycling applications like deinking.

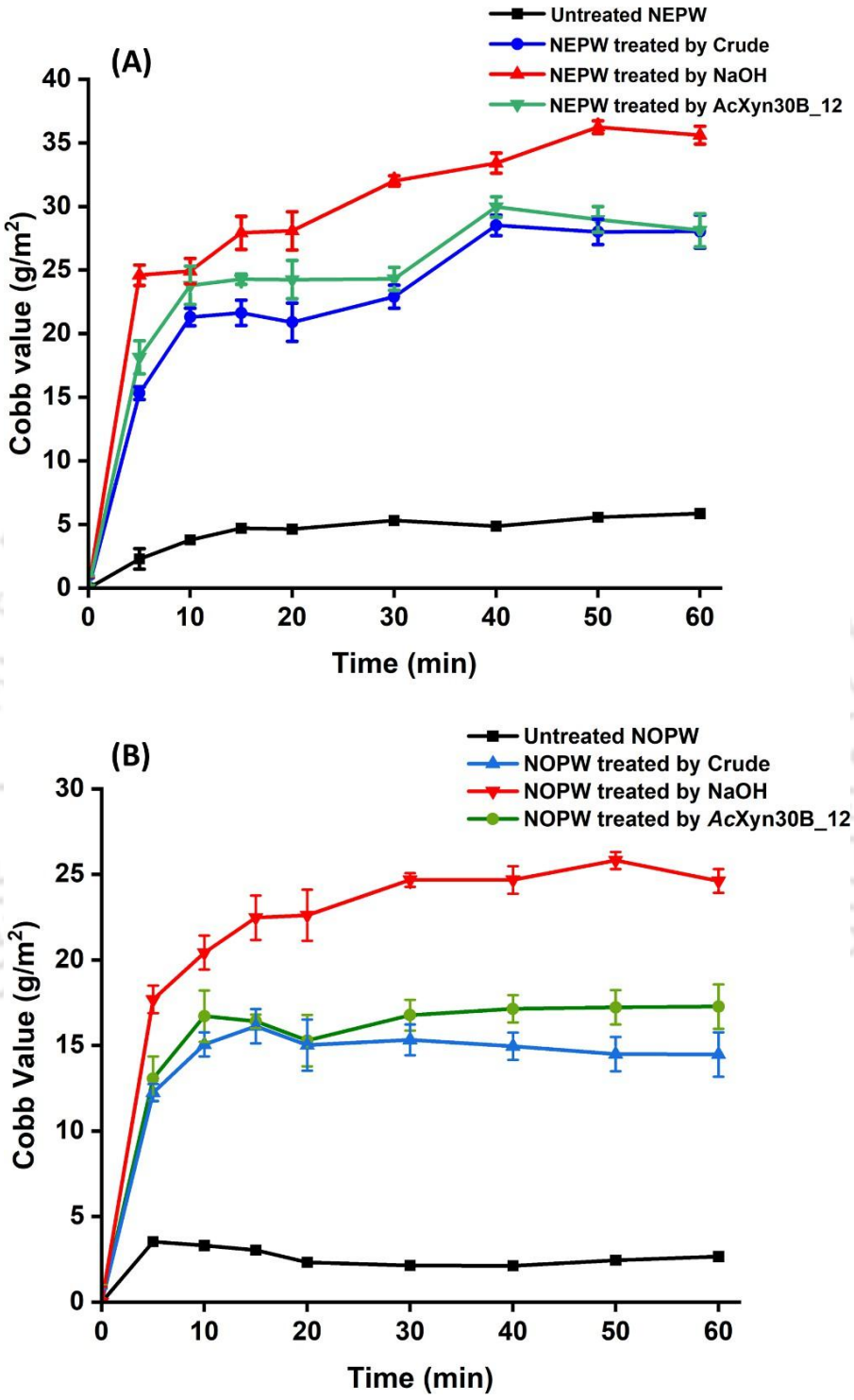

Fig. 5.8. Cobb value (g/m^2) of untreated, crude enzyme, NaOH and purified *Ac*Xyn3B_12 treated deinked **(A)** NEPW and **(B)** NOPW with time (min).

5.3.10. Analysis of effluent generated during deinking of NEPW and NOPW

5.3.10.1. Total reducing sugar estimation in effluents from deinking of NEPW and NOPW

The total reducing sugar (TRS) released from treated NEPW and NOPW samples was measured to evaluate the extent of hemicellulose (xylan) hydrolysis during deinking. For NEPW, the treatment with crude enzyme showed increase in the TRS concentration to 1.5 mg/g in effluent, indicating partial hydrolysis of xylan components (Table 5.9). NaOH treatment released only 0.3 mg/g of TRS, suggesting limited polysaccharide breakdown under alkaline conditions (Table 5.9). Notably, the treatment with purified *Ac*Xyn30B_12 showed higher release of 1.8 mg/g TRS (Table 5.9), representing the highest among all treatments and reflecting its superior xylan degrading efficiency. A similar trend was observed for NOPW, where crude enzyme treatment yielded 1.4 mg/g of TRS (Table 5.9). In contrast, *Ac*Xyn30B_12 treatment resulted in a substantial higher TRS to 2.3 mg/g in the effluent (Table 5.9), again indicating higher hemicellulose degradation and effective deinking.

Table 5.9. Comparison of TRS in effluents of deinked NEPW and NOPW by *Ac*Xyn30B_12 and NaOH.

Deinked sample	TRS (mg/mL)	TRS (mg/g)
NEPW		
NaOH treated	0.02 ± 0.08	0.3 ± 0.08
Crude treated	0.07 ± 0.06	1.5 ± 0.6
Purified *Ac*Xyn30B_12 treated	0.09 ± 0.01	1.8 ± 1.0
NOPW		
NaOH treated	0.01 ± 0.02	0.2 ± 0.02
Crude treated	0.06 ± 0.03	1.4 ± 0.3
Purified *Ac*Xyn30B_12 treated	0.1 ± 0.04	2.3 ± 0.4

5.3.10.2. Analysis of TDS and TSS in effluents from deinking of NEPW and NOPW

The Total suspended solids (TSS) and Total dissolved solids (TDS) were evaluated to assess the quality of effluents generated from deinking of NEPW and NOPW using different treatments. For NEPW, the untreated sample exhibited a TSS of 1.0 mg/L and TDS of 5.5 mg/L. Its treatment with the crude enzyme increased TSS and TDS to 2.0 mg/L and 7.5 mg/L, respectively. NaOH treatment led to a higher increase, in TSS (4.5 mg/L) and TDS (13 mg/L) as shown in Table 5.10. In contrast, treatment with purified *Ac*Xyn30B_12 resulted in moderate TSS (3.0 mg/L) and a TDS of 10 mg/L (Table 5.10). For NOPW, untreated samples had a very low TSS of 0.1 mg/L and TDS of 4.0 mg/L. The crude enzyme treatment raised these values to 1.0 mg/L (TSS) and 8.0 mg/L (TDS), whereas NaOH treated NOPW showed the highest TSS and TDS at 5.5 mg/L and 10.5 mg/L, respectively. Notably, *Ac*Xyn30B_12 treatment of NOPW yielded a moderate TSS of 3.5 mg/L and TDS of 8.5 mg/L which were lower than those of NaOH (Table 5.10).

Overall, treatment of both NEPW and NOPW with purified *Ac*Xyn30B_12 showed lower TSS and TDS as compared with chemical NaOH treatment. These findings suggested that *Ac*Xyn30B_12 treatment is more environment-friendly than chemical NaOH treatment, as it generates effluent with lower solid load and dissolved content, indicating reduced environmental burden and lower wastewater treatment requirements.

Table 5.10. TSS and TDS levels in released effluents of deinked NEPW and NOPW by enzyme *Ac*Xyn30B_12 and NaOH.

Deinked sample	TSS (mg/L)	TDS (mg/L)
NEPW		
Untreated	1.0 ± 0.1	5.5 ± 1.1
Crude treated	2.0 ± 0.1	7.5 ± 1.0
*Ac*Xyn30B_12 treated	3.0 ± 0.2	10.0 ± 0.5
NaOH treated	4.5 ± 0.3	13.0 ± 1.2
NOPW		
Untreated	0.3 ± 0.1	4.0 ± 0.3
Crude treated	1.0 ± 0.6	8.0 ± 0.5
*Ac*Xyn30B_12 treated	3.5 ± 0.3	8.5 ± 1.0
NaOH treated	5.5 ± 1.0	10.5 ± 0.7

5.4. Conclusion

Among different types of waste papers analyzed, newspaper (NEPW) and notebook paper (NOPW) were selected based on their relatively high hemicellulose and low lignin content. Statistical optimization using response surface methodology (RSM) identified the ideal deinking conditions for both 5.0% (w/v) NEPW and NOPW with enzyme (*Ac*Xyn30B_12) loadings of 46.4 U/g and 58.6 U/g, respectively in 10 mL reaction mixture at 70°C for 90 min. Under these optimized conditions, *Ac*Xyn30B_12 achieved deinking efficiencies of 81.3% for NEPW and 77.2% for NOPW at 10 mL reaction scale, as determined by ERIC measurements. The deinking efficiency results obtained for *Ac*Xyn30B_12 were comparable to that of NaOH treated papers (87.3% for NEPW and 87.7% for NOPW) at 10 mL reaction scale. Although, *Ac*Xyn30B_12 deinking preserved paper is better than that of NaOH (68% (w/w) for NEPW and 72% (w/w) for NOPW), with 78% (w/w) recovery for NEPW and 76% (w/w) for NOPW indicating the retention of fiber integrity making it more suitable for paper recycling. At higher reaction volumes (20 mL and 50 mL), *Ac*Xyn30B_12 maintained consistent deinking efficiencies (79.0% for NEPW and 72.1% for NOPW) and biomass recovery (77% (w/w) for NEPW and 76% (w/w) for NOPW), demonstrating its scalability and suitability for large-scale deinking applications. Structural analysis revealed that *Ac*Xyn30B_12 treatment increased the crystallinity index to 58.8% (NEPW) and 63.4% (NOPW), with corresponding increases in their apparent crystallite size (17.7% for NEPW and 22.8% for NOPW). ATR-FTIR analysis revealed that *Ac*Xyn30B_12 treatment significantly reduced the intensity of characteristic ink peaks (2900-2800 cm^{-1} for -CH_2 and -CH_3 vibration and 1315 cm^{-1} for -OH in hemicellulose), confirming effective removal of ink and targeted

hemicellulose hydrolysis, higher than that of crude enzyme and NaOH pretreated papers. FESEM imaging showed that *Ac*Xyn30B_12 treated fibers were more fragmented and exposed compared to untreated and crude enzyme-treated papers and comparable to that of NaOH treated papers. *Ac*Xyn30B_12 significantly improved deinked paper brightness up to 75.3% for NEPW and 48.0% for NOPW, representing 12.4% and 26.3% increases, respectively, over untreated samples. Water absorptivity (Cobb value) increased to 28.1 g/m² (NEPW) and 14.9 g/m² (NOPW) in case of *Ac*Xyn30B_12 as compared to that of NaOH (35.6% g/m² for NEPW and 24.6% g/m² for NOPW) showing higher fiber strength retention in papers deinked by *Ac*Xyn30B_12. The total reducing sugar (TRS) content in the effluent reached 1.8 mg/g for NEPW and 2.3 mg/g for NOPW with *Ac*Xyn30B_12, which was highest among all treatments. In contrast, the TRS released by NaOH was just 0.3 mg/g (NEPW) and 0.2 mg/g (NOPW). Effluent analysis showed *Ac*Xyn30B_12 generated lower Total Dissolved Solids (TDS: 10.0 mg/L NEPW, 8.5 mg/L NOPW) and Total Suspended Solids (TSS: 3.0 mg/L NEPW, 3.5 mg/L NOPW) compared to NaOH (TDS of 13.0 mg/L in NEPW and 10.5 mg/mL in NOPW; TSS of 4.5 mg/L in NEPW and 5.5 mg/mL in NOPW), demonstrating its eco-friendly nature. These results together conclude that *Ac*Xyn30B_12 effectively removes ink, enhances fiber properties and produces environmentally effluent, making it an efficient and sustainable biocatalyst for waste paper recycling.

5.5. References

Abd Wahab, N., Kamarudin, M.K.A., Toriman, M.E., Ata, F.M., Juahir, H., Ghazali, A. and Anuar, A. (2018) The evaluation of dissolved oxygen (DO), total suspended solids (TSS) and suspended sediment concentration (SSC) in Terengganu River, Malaysia. Int. J. Eng. Technol. *7*(3.14), pp.44-48.

Amobonye, A., Bhagwat, P., Singh, S., Pillai, S. (2021) *Beauveria bassiana* xylanase: characterization and wastepaper deinking potential of a novel glycosyl hydrolase from an endophytic fungal entomopathogen. Journal of Fungi. 7(8), 668.

APHA. (1998) Standard methods for the examination of water and wastewater (20th ed.). American Public Health Association, Washington, DC.

Bajpai, P. (2015) Green chemistry and sustainability in pulp and paper industry. Springer, Singapore.

Box, G.E.P., Behnken, D.W. (1960) Some new three level designs for the study of quantitative variables. Technometrics. 2, 455–475.

Chen, H., Venditti, R., Jameel, H., Park, S. (2012) Enzymatic hydrolysis of recovered office printing paper with low enzyme dosages to produce fermentable sugars. Applied Biochemistry and Biotechnology. 166, 1121–1136.

Chutani, P., Sharma, K.K. (2015) Biochemical evaluation of xylanases from various filamentous fungi and their application for the deinking of ozone treated newspaper pulp. Carbohydrate Polymers. 127, 54–63.

Desai, D.I., Iyer, B.D. (2016) Biodeinking of old newspaper pulp using a cellulase-free xylanase preparation of *Aspergillus niger* DX-23. Biocatalysis and Agricultural Biotechnology. 5, 78–85.

Dutt, D., Tyagi, C.H., Singh, R.P., et al. (2012) Effect of enzyme concoctions on fiber surface roughness and deinking efficiency of sorted office paper. Cellulose Chemistry and Technology. 46, 611–623.

Dzimbeg-Malcic, V., Barbarić-Mikočević, Ž., Itrić, K. (2011) Kubelka-Munk theory in describing optical properties of paper (I). Tehnički Vjesnik. 18(1), 117–124.

Gonzalez-Estrella, J., Asato, C.M., Stone, J.J., Gilcrease, P.C. (2017) A review of anaerobic digestion of paper and paper board waste. Reviews in Environmental Science and Bio/Technology. 16, 569–590.

Gupta, V., Garg, S., Capalash, N., Gupta, N., Sharma, P. (2015) Production of thermo-alkali-stable laccase and xylanase by co-culturing of *Bacillus* sp. and *B.*

halodurans for biobleaching of kraft pulp and deinking of waste paper. Bioprocess and Biosystems Engineering. 38, 947–956.

Heinze, T., Liebert, T. (2001) Unconventional methods in cellulose functionalization. Progress in Polymer Science. 26, 1689–1762.

Hubbe, M.A., Bowden, C. (2009) Handmade paper: a review of its history, craft, and science. BioResources. 4(4).

Jordan, B.D., Popson, S.J. (1994) Measuring the concentration of residual ink in recycled newsprint. Journal of Pulp and Paper Science. 20, J161–J167.

Kumar, V., Satyanarayana, T. (2014) Production of endoxylanase with enhanced thermostability by a novel polyextremophilic *Bacillus halodurans* TSEV1 and its applicability in waste paper deinking. Process Biochemistry. 49(3), 386–394.

Lee, C.K., Ibrahim, D., Omar, I.C. (2013) Enzymatic deinking of various types of waste paper: efficiency and characteristics. Process Biochemistry. 48(2), 299–305.

Lee, J., Kim, S.H., Cho, Y.J., Nam, Y.S., Lee, K.B., Lee, Y. (2014) Characterization and sequence determination of pen inks, red sealing inks, and laser toners by TOF-SIMS and ATR FTIR. Surface and Interface Analysis. 46(S1), 317–321.

Li, B., Wang, G., Chen, K., Vahey, D.W. and Zhu, J.Y. (2011) On quantification of residual ink content and deinking efficiency in recycling of mixed office waste paper. Industrial & engineering chemistry research. 50(11), pp.6965-6971.

Malhotra, G., Chapadgaonkar, S.S. (2023) Thermo-alkali stable bacterial xylanase for deinking of copier paper. Journal of Genetic Engineering and Biotechnology. 21(1), 107.

Manandhar, S., Shrestha, B., Sciortino, F., Ariga, K., Shrestha, L.K. (2022) Recycling waste paper for further implementation: XRD, FTIR, SEM, and EDS studies. Journal of Oleo Science. 71(4), 619–626.

Nelson, N. (1944) A photometric adaptation of the Somogyi method for the determination of glucose. Journal of Biological Chemistry. 3, 375–380.

Sango, C., Pathak, P., Bhardwaj, N.K., Dalal, S., Sharma, J. (2021) Partial purification of bacterial cellulo-xylanolytic enzymes and their application in deinking of photocopier waste paper. Environmental Science and Pollution Research. 28, 61317–61328.

Saxena, A., Singh Chauhan, P. (2017) Role of various enzymes for deinking paper: a review. Critical Reviews in Biotechnology. 37(5), 598–612.

Segal, L.G.J.M.A., Creely, J.J., Martin Jr, A.E., Conrad, C.M. (1959) An empirical method for estimating the degree of crystallinity of native cellulose using the X-ray diffractometer. Textile Research Journal. 29(10), 786–794.

Sluiter, A., Hames, B., Ruiz, R., Scarlata, C., Sluiter, J., Templeton, D., Crocker, D.L.A.P. (2008) Determination of structural carbohydrates and lignin in biomass. Laboratory Analytical Procedure. 1617(1), 1–16.

Somogyi, M. (1945) A new reagent for the determination of sugars. Journal of Biological Chemistry. 160, 61–68.

Soz, Ç. (2021) Hybrid paper sheets with improved barrier properties. Turkish Journal of Chemistry. 45(4), pp.1162-1172.

Virk, A.P., Puri, M., Gupta, V., Capalash, N., Sharma, P. (2013) Combined enzymatic and physical deinking methodology for efficient eco-friendly recycling of old newsprint. PLoS One. 8(8), e72346.

Weinstock, I.A., Reiner, R.A.R., Moen, M.A., Hammel, K.E., Hill, C.L., Houtman, C.J. (1995) In: Proceedings of the 1995 TAPPI Pulping Conference; 1995 October 1–5; Chicago, IL. TAPPI PRESS, Atlanta, GA. Book 1, 153–156.

Yang, M., Li, J., Wang, S., Zhao, F., Zhang, C., Zhang, C., Han, S. (2023) Status and trends of enzyme cocktails for efficient and ecological production in the pulp and paper industry. Journal of Cleaner Production. 418, 138196.

Published (From Thesis)

Research Articles

1. **Bipasha Choudhury**, Yumnam Robinson Singh, Kaustubh Chandrakant Khaire, Nazneen Ahmed, Kedar Sharma, Carlos MGA Fontes and Arun Goyal (2025). Cellulosomal endo-1,4-β-D-xylanase (*Ac*Xyn30B_12) from *Acetivibrio clariflavus* acts synergistically with xylobiohydrolase (*Ac*GH30A) upon the hydrolysis of complex carbohydrates. ***International Journal of Biological Macromolecules*** 306, 141620. **(JIF: 8.5).**

2. **Bipasha Choudhury**, Akshay Kumar and Arun Goyal (2025). Structural, functional and biotechnological traits of GH30 endo-xylanases. ***International Journal of Biological Macromolecules,*** 148818 **(JIF: 8.5).**

3. **Bipasha Choudhury** and Arun Goyal (2025). Deciphering the structural insights and concentration-dependent dimerization of endo-β-1,4-xylanase (*Ac*Xyn30B_12) from *Acetivibrio clariflavus* by SAXS and computational methods. ***The FEBS Journal,*** **(JIF: 4.2)**.

4. **Bipasha Choudhury**, Akshay Kumar and Arun Goyal (2025). Efficient and eco-friendly enzymatic deinking of waste papers using endo-β-1,4-xylanase of glycoside hydrolase 30 family (*Ac*Xyn30B_12) from *Acetivibrio clariflavus* DSM 19732. ***Environmental sustainability,*** **(JIF: 2.8)**. **(Under review)**

Other Publications

1. Shyam Ji, Parmeshwar Vitthal Gavande, **Bipasha Choudhury** and Arun Goyal (2023). Computational design and structure dynamics analysis of bifunctional chimera of endoxylanase from *Clostridium thermocellum* and xylosidase from *Bacteroides ovatus*. ***3 Biotech*** 13 (2), 59.

2. Nilakshi Kakati **¥**, **Bipasha Choudhury**, Madhulika Shrivastava, Shreya Biswas, Carlos M.G.A. Fontes and Arun Goyal (2025). A GH43 β-1,4-xylosidase (ZgGH43A) from *Zobellia galactanivorans* exhibiting broad substrate specificity and exo-xylosidase activity. ***International Journal of Biological Macromolecules.*** (**¥ Equal Contribution**)

3. Priyanka Nath, Saquib Peerzade, **Bipasha Choudhury**, Arun Goyal and Shreyas Bapat (2025). Computational and structural insights into tRNA isoleucine lysidine synthetase from *Mycobacterium tuberculosis* and its interaction with a hyperbranched amoxicilloyl-poly-l-lysine inhibitor. Journal of Molecular Graphics and Modelling, (JIF: 3.0). **(To be submitted)**

Book chapters

1. **Bipasha Choudhury**, Akshay Kumar and Arun Goyal (2025). Insights of Hemicellulolytic Enzymes for Detoxification of Biomass Used as Animal Feed. In ***Lignocellulosic Biomass and Enzymes: Fundamentals, Emerging Technologies and Applications*** (pp. 211-236.2). Singapore: Springer Nature Singapore.

2. Akshay Kumar, **Bipasha Choudhury** and Arun Goyal (2025). Advancement in Pretreatment Technologies for Mixed Lignocellulosic Biomass. In ***Lignocellulosic Biomass and Enzymes: Fundamentals, Emerging Technologies and Applications*** (pp. 33-54). Singapore: Springer Nature Singapore.

Conferences/Symposia

1. **Bipasha Choudhury** and Arun Goyal (2025). Biochemical study of *Ac*Xyn30B_12 endo-xylanase with applications in renewable biomass utilization and waste paper deinking. International Carbohydrate Conference (CARBO XXXVI). November 21-23, 2025, Banaras Hindu University, India. **(Best poster award)**

2. **Bipasha Choudhury** and Arun Goyal (2025) Sustainable deinking of waste paper by a thermostable endo-β-1,4-xylanase from *Acetivibrio clariflavus* DSM 19732. Synthetic Biology and Future Food Networking Forum and IBA Subject Conference. November 05-07, 2025, Bangkok, Thailand. **(Best poster award)**

3. **Bipasha Choudhury** and Arun Goyal (2025) Biochemical, structure and functional analysis of an endo-β-1,4-xylanase (*Ac*Xyn30B_12) from *Acetivibrio clariflavus* DSM 19732 and its application in efficient deinking of waste papers. Research and Industrial Conclave (RIC-2024). Oct 10-12, 2025, Indian Institute of Technology Guwahati, Assam, India.

4. **Bipasha Choudhury** and Arun Goyal (2025) Enzymatic deinking of waste papers using thermostable endo-β-1,4-D-xylanase from glycoside hydrolase family 30 (*Ac*Xyn30B_12) from *Acetivibrio clariflavus* 19732. 5th International Conference on Waste Management. June 05-06, 2025, Indian Institute of Technology Guwahati, Assam, India. **(Best oral presentation award)**

5. **Bipasha Choudhury** and Arun Goyal (2024) A novel thermophilic, multi substrate specific, exo-/endo- β-1,4-xylanase of family GH30 glycoside hydrolase (*Ac*GH30B) from *Acetivibrio clariflavus.* IX International Conference on Sustainable Energy and Environmental Challenges. December, 13-15, 2024, IIT Mandi, Himachal Pradesh, India. **(Best Paper Award)**.

6. **Bipasha Choudhury** and Arun Goyal (2024) Structural and functional insights in exo-/endo- β-1,4-xylanase of family GH30 glycoside hydrolase (*Ac*GH30B) from *Acetivibrio clariflavus*. International Carbohydrate Conference (CARBO XXXVIII). December 04-06, 2024, Gauhati University, Assam, India.

7. **Bipasha Choudhury** and Arun Goyal (2024) Molecular and functional characterization of a thermophilic endo-xylanase of family GH30 glycoside hydrolase (*Ac*GH30B) from *Acetivibrio clariflavus* DSM 19732. Research and Industrial Conclave (RIC-2024). Aug 09-11, 2024, Indian Institute of Technology Guwahati, Assam, India.

8. **Bipasha Choudhury** and Arun Goyal (2023) Biochemical characterization and functional analysis of a xylanase of family GH30 glycoside hydrolase (*Ac*GH30B) from *Acetivibrio clariflavus.* International Conference on New Horizons in Biotechnology (NHBT-2023). November 26-29, 2023, Trivandrum, India.

9. **Bipasha Choudhury** and Arun Goyal (2023) Expression, purification and biochemical characterization of a xylanase of family GH30 glycoside hydrolase (*Cc*GH30B) from *Clostridium clariflavum*. Research and Industrial Conclave (RIC-2023). May 14-16, 2023, Indian Institute of Technology Guwahati, Assam, India.

10. **Bipasha Choudhury**, Parmeshwar Vitthal Gavande, Carlos M.G.A. Fontes, Arun Goyal (2022) Biochemical and functional characterization of a xylanase of family GH30 glycoside hydrolase (*Cc*GH30B) from *Clostridium clariflavum.* International Carbohydrate Conference (CARBO XXXVI). December 05-07, 2022, Indian Institute of Technology Powai, Mumbai, India.

Other Conferences/Symposia

1. Nilakshi Kakati, **Bipasha Choudhury** and Arun Goyal (2024) Structural insights of an endoglucanase of family GH5 glycoside hydrolase (*Ac*GH5) from *Acetivibrio clariflavus* DSM 19732 by computational methods. International Carbohydrate Conference (CARBO XXXVIII). December 04-06, 2024, Gauhati University, Assam, India.

2. Premeshworii Devi Maibam, **Bipasha Choudhury** and Arun Goyal (2021) Delignification of rice straw by deep eutectic solvent for enhancing saccharification of biofuel feedstock and extraction of lignin using RSM-CCD approach. International conference on advances in chemistry and biology of carbohydrates (CARBO XXXV) December 04-05, 2021, Forest Research Institute Dehradun, India.

Workshops

1. Online certification course on "Data Analytics with Python: From Fundamentals to Insights" co-organized by iHUB Divyasampark IIT Roorkee & Ritvij Bharat Pvt. Ltd. (RBPL), 18th August-26th September, 2025.

2. Hands on workshop on Optimization using Matlab/Python. Organized by Research and Industrial-Conclave, IIT Guwahati, 10th- 12th October, 2025.

VITAE

The author was born on December 14, 1996 in the town of Barpeta (Assam). She passed Secondary Examination (10th Class) conducted by Central Board of Secondary Examination, New Delhi in 2013 and Higher Secondary Examination (12th Class) conducted by Central Board of Secondary Examination, New Delhi in 2015. She completed Integrated M.Sc. (Bioscience and Bioinformatics) from Tezpur University, Tezpur, Assam, India in July, 2021 with a Gold Medal for securing first position.

Ms. Bipasha Choudhury joined the PhD program in July, 2022 at Department of Biosciences and Bioengineering, Indian Institute of Technology Guwahati, Guwahati 781039, Assam, India. She successfully completed the coursework with 9.0/10 CPI. She delivered the open (PhD Synopsis) Seminar on 10th June 2025 and presented her thesis work before the Doctoral Committee and her performance was satisfactory. She submitted the PhD thesis in June 2025.